ASME
SETTING THE STANDARD

Transactions of the ASME, Journal of Fluids Engineering (ISSN 0098-2202) is published monthly by The American Society of Mechanical Engineers, Three Park Avenue, New York, NY 10016. Periodicals postage paid at New York, NY and additional mailing offices.
POSTMASTER: Send address changes to Transactions of the ASME, Journal of Fluids Engineering, c/o THE AMERICAN SOCIETY OF MECHANICAL ENGINEERS, 22 Law Drive, Box 2300, Fairfield, NJ 07007-2300.
CHANGES OF ADDRESS must be received at Society headquarters seven weeks before they are to be effective. Please send old label and new address.
STATEMENT from By-Laws. The Society shall not be responsible for statements or opinions advanced in papers or ... printed in its publications (B7.1, Par. 3).

Journal of Fluids Engineering

Published Monthly by ASME

VOLUME 130 • NUMBER 3 • MARCH 2008

RESEARCH PAPERS

Flows in Complex Systems

Multiphase Flows

Techniques and Procedures

(Contents continued on inside back cover)

This journal is printed on acid-free paper, which exceeds the ANSI Z39.48-1992 specification for permanence of paper and library materials. ♾™
♻ 85% recycled content, including 10% post-consumer fibers.

(**Contents continued**)

Journal of Fluids Engineering **Volume 130, Number 3** **MARCH 2008**

TECHNICAL BRIEFS

The ASME Journal of Fluids Engineering is abstracted and indexed in the following:

Applied Science & Technology Index, Chemical Abstracts, Chemical Engineering and Biotechnology Abstracts (Electronic equivalent of Process and Chemical Engineering), Civil Engineering Abstracts, Computer & Information Systems Abstracts, Corrosion Abstracts, Current Contents, Ei EncompassLit, Electronics & Communications Abstracts, Engineered Materials Abstracts, Engineering Index, Environmental Engineering Abstracts, Environmental Science and Pollution Management, Excerpta Medica, Fluidex, Index to Scientific Reviews, INSPEC, International Building Services Abstracts, Mechanical & Transportation Engineering Abstracts, Mechanical Engineering Abstracts, METADEX (The electronic equivalent of Metals Abstracts and Alloys Index), Petroleum Abstracts, Process and Chemical Engineering, Referativnyi Zhurnal, Science Citation Index, SciSearch (The electronic equivalent of Science Citation Index), Shock and Vibration Digest, Solid State and Superconductivity Abstracts, Theoretical Chemical Engineering

Analysis of the Deterministic Unsteady Flow in a Low-Speed Axial Fan With Inlet Guide Vanes

Jesús Manuel Fernández Oro
e-mail: jesusfo@uniovi.es

Katia María Argüelles Díaz

Carlos Santolaria Morros

Eduardo Blanco Marigorta

Área de Mecánica de Fluidos,
Universidad de Oviedo,
Campus de Viesques,
33271 Gijón (Asturias), Spain

This paper is conceived as an extension in the analysis of the periodic stator-rotor interaction in a low-speed axial fan with inlet guide vanes. Here, the present work focuses on the deterministic fluctuations that occur in the axial gap between the blade rows. In particular, we present experimental data on the phase averaged velocity in the stator frame of reference. Detailed measurements of the flow field were obtained using hot-wire anemometry in a traverse sector that covered the whole span of the stage for a complete stator pitch. The blade-to-blade velocity gradient in the rotor passage is observed as an unsteady flow in the stator frame of reference due to the relative motion of the blades. As a consequence, this periodic fluctuation is superimposed on the steady vane-to-vane velocity distribution, resulting in a nonuniform unsteadiness with additional phase-dependent wake-blockage interaction. This phase-dependent interaction is determined by the difference between the overall deterministic fluctuation and the rotating spatial blade-to-blade distribution, when the latter is accurately transformed to the stator reference frame. The results revealed that high unsteadiness in the tip region is mainly derived from the radial increase of the blade-to-blade nonuniformities in the rotor, whereas the wake-blockage interaction exhibits a spanwise uniform distribution. Hence, the hub-to-tip torsion of the blades is responsible for setting off a major spatial distortion between the rows. Complementarily, we observed that a reduction in the rows' spacing or an increase in the blade loadings leads to a higher wake-blockage interaction, modifying the impingement of the incoming stator wakes. In addition, the deterministic stresses were calculated by time averaging the phase-dependent velocity correlations and compared to the turbulent stresses. The deterministic stresses were also segregated in temporal, spatial, and spatial-temporal correlations in order to analyze the dominant mechanisms involved in their generation. At this point, the deterministic kinetic energy levels were found to be generally lower than turbulent kinetic energy levels, with both temporal and spatial correlations being the most significant terms of the tensor.
[DOI: 10.1115/1.2844578]

Introduction

The description of the unsteady features of the flow inside the rotating passages of multistage turbomachinery is an extremely complex issue. A broad range of time and length scales is involved in the flow structure, resulting in an unsteady scenario composed of all-range fluctuations. Since all these unsteady patterns play a significant role in the mean-time performance of the machine, it is necessary to evaluate their particular impact on the total energy exchange.

A first approach is based on an overall decomposition of the flow field into two parts: a steady, time-averaged (or Reynolds averaged) term and a global (total) unsteadiness that includes all those fluctuations. This method, which provides the unsteady RANS equations, is useful to analyze general fluid dynamics problems but is unsuitable for addressing periodic fluctuations derived from the blade-passing frequency (BPF). Instead, the total unsteadiness can be considered as the contribution of both periodic (deterministic) and random (nondeterministic) components, producing an enhanced framework that allows the identification of the unsteadiness sources clocked with the shaft speed and the BPF (Fig. 1). Moreover, in the case of multistage turbomachinery, due to the presence of several rotors with different multiplicities in the number of blades, it is possible to isolate the influence of each row. To that end, an additional averaging operator needs to be introduced, leading to the establishment of the passage-to-passage average equations (PANS equations). Hence, this formulation is realized through a three-averaging sequence, resulting in a stationary framework in which periodic unsteadiness is addressed through additional terms, called "deterministic stresses." Clearly, this methodology, introduced by Adamczyk [1], constitutes a specific tool to analyze turbomachinery flows (an excellent overview of these modeling strategies is outlined in Adamczyk [2]). However, though the methodology was conceived as a full-3D, steady viscous equation system to simulate multistage turbomachinery flows, its basic assumptions can also be applied in the analysis of experimental data (Meneveau et al. [3], Uzol et al. [4]). Actually, the development of deterministic transport models requires an experimental database to validate them, so much effort has been placed on the calculation of deterministic correlations. In particular, the construction of the deterministic tensor from phase-averaged flow is well reported in the literature, especially from PIV measurements (Chow et al. [5], Uzol et al. [6]). The consideration of these deterministic stresses is important because its order of magnitude is similar to that of the Reynolds stresses in the interaction zones (Sinha et al. [7]). Other research has combined the experimental measurements of deterministic stresses with the establishment of transport models (Van de Wall et al. [8]). Even diverse physical phenomena, such as radial migration of momentum or wake recovery, have been linked to the deterministic kinetic energy budget (Van Zante et al. [9], Adamczyk [10]).

In the case of a single-stage axial turbomachine, most of the

Contributed by the Fluids Engineering Division of ASME for publication in the JOURNAL OF FLUIDS ENGINEERING. Manuscript received April 13, 2007; final manuscript received November 2, 2007; published online March 3, 2008. Assoc. Editor Chunill Hah. Paper presented at the 2005 ASME Fluids Engineering Division Summer Meeting and Exhibition (FEDSM2005), Houston, TX, June 19–23, 2005.

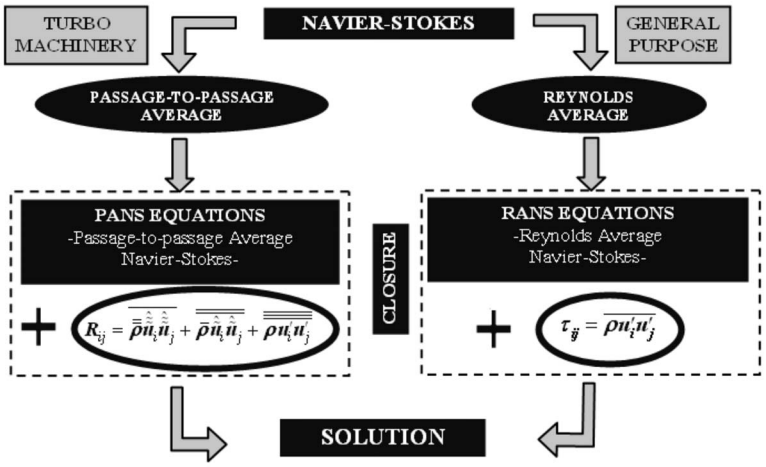

Fig. 1 Methodology framework

unsteadiness is due to the periodic motion of the rotor nonuniformities that interact with the stator flow structures. This deterministic unsteadiness and its effect on the time mean can be studied efficiently using the passage average model (Kirtley et al. [11]). In addition, the description of these deterministic fluctuations in any given row (either stator or rotor) is readily achieved through an accurate time-averaging operator in the corresponding frame of reference (Adamczyk et al. [12]). With this construction, it is possible to decouple spatial nonuniformities in the rotor frame of reference from deterministic fluctuations in the stator reference frame. Consequently, the unsteady part of the velocity field describing blade row interactions is finally identified. Thus, the deterministic fluctuations can be considered as the result of two components: a spatial blade-to-blade nonuniformity and a pure temporal stator-rotor interaction ([12], Chen et al. [13]). According to this, the deterministic tensor can be also decomposed into three different correlations: a spatial-spatial, a spatial-temporal, and a temporal-temporal term. Different authors have explored the physical mechanisms that are related to the transport and production of deterministic stresses in the tensor, either compactly [4] or decomposed (Leboeuf [14], Charbonnier et al. [15]). All these deterministic correlations explain the averaged consequences of the stator-rotor interaction phenomena on the steady flow field.

The present paper summarizes our efforts to provide insight into the analysis of the periodic stator-rotor interaction in a low-speed axial fan with inlet guide vanes. This time, we focus exclusively on the deterministic structures of the flow in the spacing between the rows. Using hot-wire anemometry intensively, experimental data on the phase averaged velocity are presented in the stator frame of reference. Next, the use of a deterministic scheme to analyze the velocity components in both absolute and relative reference frames allows us to segregate spatial unsteadiness induced by the rotor blades from pure nonlinear stator-rotor interaction. The nature of this temporal fluctuation and the influence of the axial gap and off-design conditions in the interaction are discussed in detail. In particular, this fluctuation is manifested as a shift of the wake structure and a cyclic variation of the wake deficit, perfectly described as a phase-dependent wake-blockage interaction. Afterwards, the deterministic stresses are introduced in order to show the location and intensity of the main unsteady sources. At this point, the deterministic stresses are compared to the turbulent stresses in terms of kinetic energy and shear stresses. Finally, this paper concludes by analyzing the spatial-spatial, spatial-temporal, and temporal-temporal correlations of the deterministic tensor. The most significant terms of these correlations are discussed and their behavior as a function of the axial spacing and the working point conditions is also presented.

Experimental Setup and Procedures

Experimental Facility. A low-speed axial fan with inlet guide vanes is operated in an open-loop facility that includes a throttle at the intake to provide off-design conditions. The fan analyzed presents a single stage composed of a 13-vane stator (IGV's) and a 9-blade rotor with hub and tip diameters of 380 mm and 820 mm, respectively (Fig. 2). The facility is conducted with the possibility of changing the axial spacing between the rows. In these experiments, two axial gap configurations were tested: a larger, nominal gap of 50% of the blade chord and a lower gap of 37% of the blade chord, both at the hub section. The rotational speed, 2400 rpm, presents maximum deviations of ± 2 rpm, when the fan is operated at nominal conditions: a volumetric flow rate of 16.5 m^3/s (Qn) for a total pressure rise of 1150 Pa. In addition, three different operating points were studied: "nominal" conditions, "partial-load" conditions for an 85% of the nominal flow rate, and "near-stall" conditions for a 70% of the nominal flow rate. Information related to the facility configuration and the operation of the axial fan can be found in Fernández Oro et al. [16].

Measuring Procedures. Dual hot-wire anemometry techniques were employed to measure both axial and tangential velocity fields between the rows. For that purpose, a two-wire anemometric probe, connected to a TSI IFA-100 CTA anemometer, was placed 15 mm downstream of the vanes' trailing edge (TE). The present database is composed of measurements taken in a traverse sector with a spatial discretization of 225 single points that covers the entire crossed area of the stator passage. Besides, 100 different rotor phases relative to the stator vanes (every 0.4 deg) were considered in order to describe the temporal variations in the flow. Therefore, a hundred phase-averaged flow fields, obtained each one by averaging 100 instantaneous samples, are used to calculate the average-passage flow field in the stator reference frame. Additional details about the probe and calibration setup, the data acquisition system and uncertainty estimates can be found in Blanco et al. [17].

Data Processing Techniques

Averaging Procedures: Phase Averaging and Passage-Averaging Operators. Deterministic (or periodic) unsteadiness is segregated from random (turbulent) unsteadiness by means of an ensemble averaging. Thus, using instantaneous data, the phase-averaged velocities are determined according to

	STATOR			ROTOR		
	Hub	Midspan	Tip	Hub	Midspan	Tip
Radius (mm)	190	300	410	190	300	410
Chord length (mm)	157.0	165.3	170.8	179.0	165.8	157.4
Solidity	1.71	1.14	0.86	1.35	0.792	0.55
Stagger angle (°)	18.11	12.97	10.77	48.64	59.70	66.45
Camber angle (°)	37.1	27.8	23.3	13.76	7.42	5.74
Thickness/Chord (%)	3.0	3.0	3.0	12	9.43	8
Pitch (mm)	91.8	145	198.1	132.6	209.4	286.2
Inlet flow angle (°)	0.0	0.0	0.0	59.61	64.7	69.36
Outlet flow angle (°)	31.17	20.73	15.68	47.73	60.07	67.16

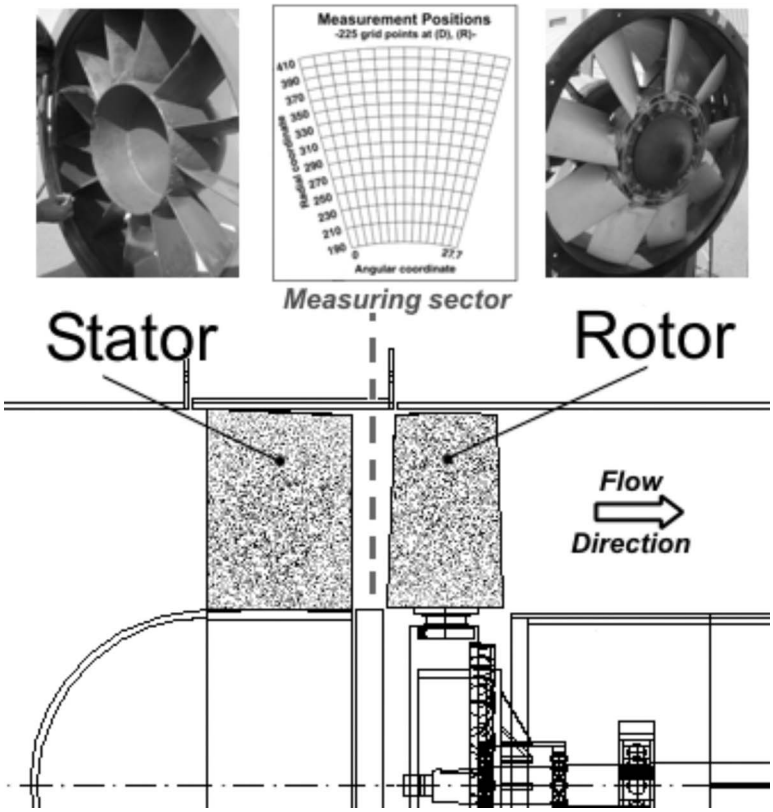

Fig. 2 Test section and vanes and blades geometrical parameters of the low-speed axial fan

$$\tilde{U}_i(r,\theta,t) = \frac{1}{M}\sum_{m=1}^{M} u_i(r,\theta,\tau)|_m, \quad \tau = t + \frac{2\pi}{\Omega B}(m-1) \tag{1}$$

where (r,θ) represent the spatial coordinates, t is the time for a rotor blade-passing period (i.e., phase angle of the rotor blades), B is the number of rotor blades, and τ computes the total acquisition time. In this case, $M=100$ is the number of instantaneous vector maps stored for each rotor phase. Typically, after subtracting the phase-averaged component of the velocity, the remaining term contains only the turbulent fluctuations. However, large-scale unsteadiness nonrelated to the BPF could not be filtered with the operator defined in Eq. (1). Therefore, it is necessary to keep this in mind when other phase-averaged quantities, such as the turbulent kinetic energy or the turbulent shear stresses, are determined through averaged differences of instantaneous realizations and phase-averaged distributions:

$$k_t(r,\theta,t) = \frac{3}{4}\frac{1}{M}\sum_{m=1}^{M}[(u_i(r,\theta,\tau)|_m - \tilde{U}_i(r,\theta,t))^2 + (u_j(r,\theta,\tau)|_m - \tilde{U}_j(r,\theta,t))^2] \tag{2}$$

$$T_{ij}(r,\theta,t) = \frac{1}{M}\sum_{m=1}^{M}[(u_i(r,\theta,\tau)|_m - \tilde{U}_i(r,\theta,t))\cdot(u_j(r,\theta,\tau)|_m - \tilde{U}_j(r,\theta,t))] \tag{3}$$

where (i,j) represent both axial and tangential velocity components and the $\frac{3}{4}$ coefficient of k is introduced to account for the variance of the out-of-plane velocity component according to Ref. [4].

The phase-averaged flow leads to the final passage-averaged flow field when the deterministic velocity is further decomposed into a mean value and a pure deterministic fluctuation. Hence, by applying a time-averaging operator, we obtain

$$\bar{U}_i(r,\theta) = \frac{1}{N}\sum_{n=1}^{N}\tilde{U}_i(r,\theta,t)|_n \tag{4}$$

where n represents every phase-averaged realization covering an entire rotor passage ($N=100$). Complementarily, in the absolute frame of reference, the deterministic kinetic energy and the deterministic shear stress are determined as

$$k_d(r,\theta) = \frac{1}{2}\frac{1}{N}\sum_{n=1}^{N}[(\tilde{U}_i(r,\theta,t)|_n - \bar{U}_i(r,\theta))^2 + (\tilde{U}_j(r,\theta,t)|_n - \bar{U}_j(r,\theta))^2] \quad (5)$$

$$D_{ij}(r,\theta) = \frac{1}{N}\sum_{n=1}^{N}[(\tilde{U}_i(r,\theta,t)|_n - \bar{U}_i(r,\theta)) \cdot (\tilde{U}_j(r,\theta,t)|_n - \bar{U}_j(r,\theta))] \quad (6)$$

Spatial and Temporal Components of the Phase-Averaged Flow. Additional analysis of the phase-averaged flow can be made if some considerations about both absolute and relative frames of reference are introduced at this point. For example, assuming that the flow is steady in the rotor frame of reference (relative), the periodic unsteadiness in the stator frame of reference (absolute) is caused by the circumferential displacement of the tangential blade-to-blade gradients in the rotor (Lyman [18]). In other words, the temporal fluctuations captured by the anemometric probe in the phase-averaged flow (i.e., the unsteadiness felt by the stator) are those spatial deviations from the axisymmetrical flow present in the rotor reference frame. However, the assumption of steady flow in the blade-to-blade flow distribution is not completely realistic. Indeed, there is an additional unsteadiness resulting from the nonlinear impact of the periodic spatial distortion of the stator wakes on the blade-to-blade flow structure that has to be considered. Thus, by including this phase-dependent (unsteady) stator-rotor interaction as a contribution to the deterministic fluctuation of the velocity fields in the absolute frame of reference, it yields

$$U_i(r,\theta,t) = U_i''^{(R)}(r,\theta-\Omega t) + \hat{u}_i(r,\theta,t) \quad (7)$$

where U_i is the difference between $\tilde{U}_i$ and $\bar{U}_i$, representing only the deterministic fluctuation. Besides, $U_i''^{(R)}$ is calculated as the difference between the passage-averaged distribution of the velocity in the relative reference frame and the axisymmetrical velocity component $U_i^{(ax)}$, a radial distribution that is independent of the reference frame. Finally, the pure unsteady part regarding stator-rotor interaction is denoted as $\hat{u}_i$ in Eq. (7). The decomposition is definitive: it divides the deterministic fluctuation into two parts and enables to obtain the temporal stator-rotor interaction as the subtraction of the spatial distortion of the rotor field from the deterministic fluctuation in the stator frame. Note that this procedure involves algebraic operations between velocity fields that refer to different frames of reference. With this constraint, it is necessary to convert the rotating coordinates fixed to the rotor into the stator coordinate system (Adamczyk et al. [19]). Notice that this transformation, which involves a rotation of coordinates expressed as $\theta_{abs}=\theta_{rel}+\Omega t$, is already included in the dependent variables of $U_i''^{(R)}$ in Eq. (7).

In order to facilitate the conversion, it is very useful to construct additional fields based on a linear interpolation of the experimental dataset. Furthermore, in order to provide an exact conversion between the angular and temporal discretizations of both stator and rotor frames, the original dataset of 15 tangential positions and 100 time instants in the stator reference frame has been, respectively, linear interpolated to 81 points covering the stator pitch and 117 instants describing the rotor blade-passing period (T_r). With this choice, the total number of interpolated circumferential positions and the interpolated time instants are exactly a multiple of the number of blades and vanes in each frame. Conversely, the velocity fields that are converted to the relative frame of reference present 117 circumferential points covering the rotor pitch and 81 temporal snapshots describing the stator vane passing period (T_s). Similar procedures to construct additional fields can be found in the literature (i.e., Ref. [4] introduces this method to prevent patchiness when transforming absolute velocities into the relative reference frame).

Finally, Eq. (8) gives the decomposition of the deterministic velocity field in its more compact form, as the contribution of the axisymmetric throughflow (a radial distribution independent of the tangential coordinate), both spatial vane-to-vane and blade-to-blade nonuniformities (each one steady in time when referring to their own reference frame) and a pure temporal, phase-dependent stator-rotor interaction:

$$\tilde{U}_i(r,\theta,t) = \underbrace{U_i^{(ax)}(r)}_{\text{Throughflow}} + \underbrace{\hat{u}_i(r,\theta,t)}_{\text{Temporal interaction}} + \underbrace{U_i''^{(S)}(r,\theta) + U_i''^{(R)}(r,\theta-\Omega t)}_{\text{Spatial nonuniformities}} \quad (8)$$

Deterministic Correlations. For a single-stage configuration, the time-averaged flow field associated with each blade row will be spatially periodic over the pitch of that blade row. Hence, the aperiodic part of the tensor in the PANS equations can be eliminated from the analysis, and the mixing stress tensor is composed only of deterministic and turbulent parts, giving

$$R_{ij} = \underbrace{\rho\overline{U_iU_j}}_{\text{Deterministic}} + \underbrace{\rho\overline{u_i'u_j'}}_{\text{Turbulent}} \quad (9)$$

Focusing on the deterministic part of the tensor, if deterministic fluctuations are replaced by their components, formerly segregated in Eq. (7), four deterministic correlations are again introduced:

$$D_{ij} = \underbrace{\rho\overline{(U_i''^{(R)}U_i''^{(R)})}}_{\text{Spatial-spatial}} + \underbrace{\rho\overline{(U_i''^{(R)}\hat{u}_j)}}_{\text{Spatial-temporal}} + \underbrace{\rho\overline{(\hat{u}_iU_j''^{(R)})}}_{\text{Temporal-spatial}} + \underbrace{\rho\overline{(\hat{u}_j\hat{u}_j)}}_{\text{Temporal-temporal}} \quad (10)$$

In the right-hand side of Eq. (10), the first term is the spatial correlation, completely steady, and phase independent. The second and third terms are temporal-spatial mixed correlations and the fourth term is the purely temporal correlation.

Experimental Results and Discussion

Since the paper introduces a deterministic framework to analyze the rotor-stator interaction, all the results are obtained in the axial gap between the rows. In the inter-row region, the averaging procedure defined in Eq. (1) provides accurate phase-averaged velocities. This is because in the gap of this particular turbomachine, there are no relevant contributions of large-scale unsteadiness that could be masked as large-scale eddies of random turbulence by the averaging operator. Therefore, the framework defined through Eqs. (1)–(6) presents no doubts about its accuracy to observe the deterministic flow. On the other hand, due to the stator-rotor configuration of the fan, there is always a swirl velocity at the stator exit giving a spanwise vortex-free prerotation. However, this tangential component is relatively small when compared to the axial velocity, so most of the results in the paper refer only to axial velocity, unless otherwise indicated.

Total Unsteadiness. A first approach to the deterministic unsteady flow of the fan is introduced in Fig. 3 with the representation of the radial distribution of total unsteadiness for the entire experimental database. Recall that this means that no filtering operator was used to process the raw traces of the velocity magnitude. Only the rms value of the signals—normalized by their overall mean value—is calculated to evaluate the fluctuation levels of velocity in the axial spacing of the stage. Also, the results have been pitch averaged in order to define a characteristic value for every radial position. The results exhibit a similar trend for all the test conditions: the unsteadiness induced by the rotor blades increases spanwise, especially at off-design conditions with higher values (see gray lines) in the case of a reduced axial gap. Typical values between 2% and 4% are encountered for all-range operat-

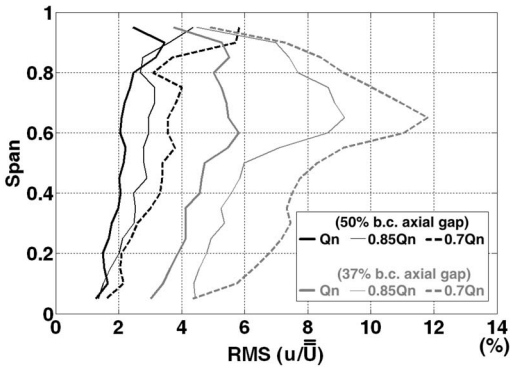

Fig. 3 Total unsteadiness at the stator exit

ing conditions in the case of a larger axial gap. On the contrary, when the axial gap is reduced, the unsteadiness is severely increased, reaching up to 10% for near-stall conditions.

Previous works by the authors ([16], Fernández Oro et al. [20]) have shown that an important unsteadiness (blockage) is activated from midspan to tip regions for this type of industrial fan with IGV's. In particular, the upstream propagation into the stator passage of the pressure field induced by the rotor loading was presented as the basic disturbing mechanism in the process, leading to the radial increase in the distributions. In addition, the measured unsteadiness was smaller in the case of the larger gap. However, since the distance between the vane's TE and the measuring sector (D) is maintained as a fixed reference for both axial gap configurations in the experiments, the description of the rotor blockage is obtained at different relative positions from the rotor blades when the gap is modified. Therefore, when analyzing the impact of the axial gap in the total unsteadiness, the comparison between both gap configurations must be done carefully.

This inconvenience can be avoided by introducing the phase-averaging framework for both absolute and relative reference frames that was discussed in the previous section. Using this methodology, the deterministic velocity fluctuations are segregated into a pure spatial distortion of the rotor field and a pure unsteady component regarding nonlinear, stator-rotor (wake-blockage) interaction. With this new scenario, the measuring location will only be modifying the levels of unsteadiness on the pure spatial part: i.e., at lower gaps, measuring closer to the rotor, the levels of spatial blade-to-blade nonuniformities increase severely. On the contrary, the pure temporal interaction will not be influenced by that effect because in this case the unsteadiness is spatially linked to the IGV wakes. Thus, this characteristic allows an accurate description of the wake-blockage interaction when the axial gap is modified.

Pure Unsteady Stator-Rotor Interaction. Figure 4 shows the spatial nonuniformities of the blade-to-blade velocity distribution in the rotor frame of reference. Note the circumferential periodicity linked to the rotor pitch (a second rotor pitch has been redrawn to obtain a clearer representation). Since these measurements were obtained upstream of the rotor, they present a clear potential characteristic. Also, these maps exhibit the same radial increase that was previously underlined in the total unsteadiness distribution of Fig. 3. Effectively, higher unsteadiness in the outer half of the passage is due to the blockage effect that propagates upstream with the pressure field induced by the rotor loading. Similar mechanisms were encountered by Arnaud et al. [21] in a high-speed, multistage, axial compressor. At nominal conditions, in the case of reduced axial gap, the spatial fluctuations increase from maximum values around 4% to maximum values of 8% near the tip, which clearly indicates the closer distance of the measuring sector from the rotor blades. Similar trends are observable at off-design conditions (Fig. 4, bottom), increasing the fluctuation from an 8% to 18% when operating at $0.7Qn$.

According to Eq. (7), the remaining unsteady part of the deterministic fluctuation contains in this case only the effect of the periodic influence of the rotor (blockage) in the vane-to-vane structures of the flow. This is because of the dominant role of the rotor loading over the pressure losses within the IGV wakes. Hence, it is possible to analyze the impact of the blockage in the structure of the stator wakes when the axial gap is modified. For example, Fig. 5 compares at midspan the evolution of the total

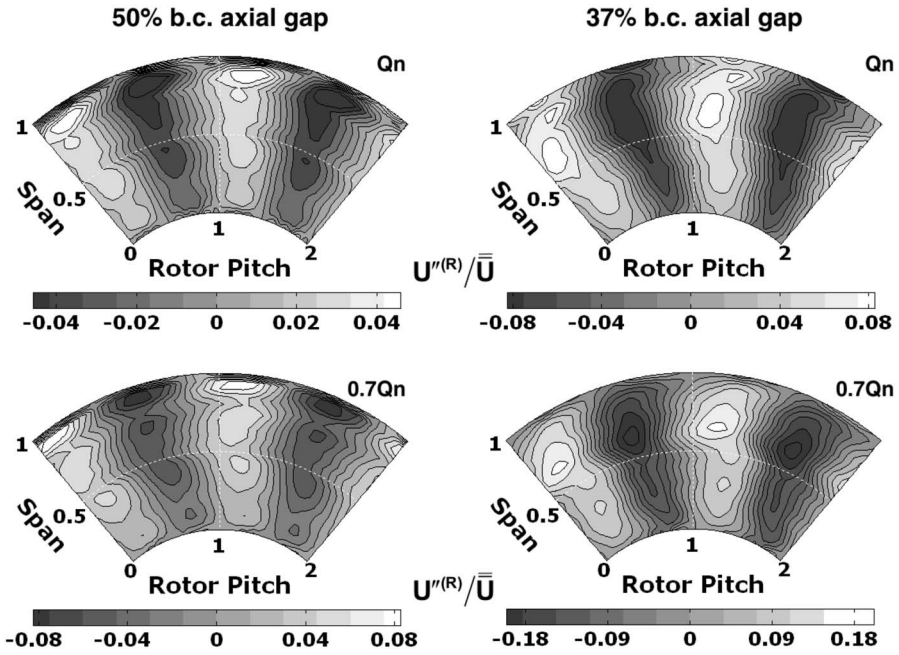

Fig. 4 Contours with spatial nonuniformities in the blade-to-blade, relative velocity, distributions between the rows

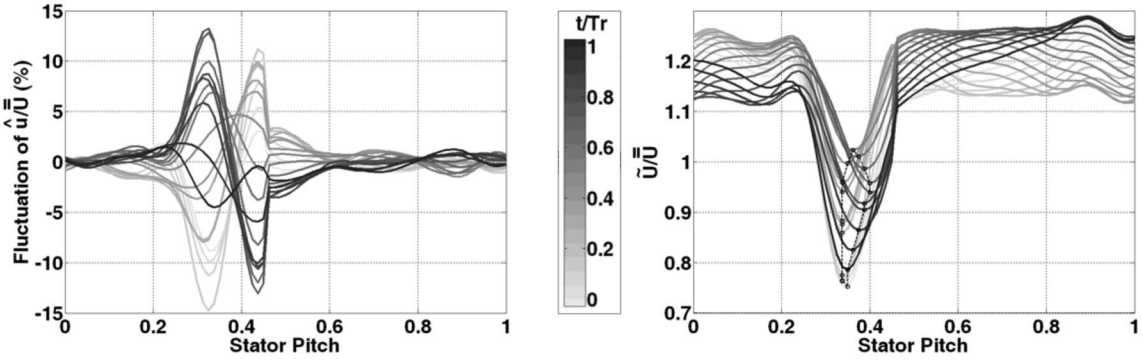

Fig. 5 Temporal evolution of the deterministic unsteady velocity (right) and its pure interaction component (left) at midspan

deterministic velocity ($\tilde{U}$ in the right-hand plot) and its inherent unsteady component ($\hat{u}$ in the left-hand plot) between the rows at nominal conditions for a complete rotor blade-passing period. Each line in the plots corresponds to the trace of the variable every $t/T_r=0.05$, colored in a gray scale to observe its temporal behavior. In other words, the colored lines represent a different rotor phase facing the stator passage.

Since these evolutions describe the flow structures of the vanes, the x axis represents the stator pitch. As is evident, the velocity deficit associated with the stator wake is influenced by the blades facing the vane's TE. Not only is the deficit of velocity modified (i.e., the amplitude of the wake) but also its position changes over time (marked with dashed lines in the right-hand plot). Considering that the pure unsteady component $\hat{u}$ of the deterministic unsteady flow contains only the influence of the rotor blades passing by, the stator wakes are vanished (i.e., the vane-to-vane flow structure) and just the difference between both steady and instantaneous evolutions of the phase-averaged velocity (absolute) is addressed here. Moreover, if there were no stator-rotor interaction, this component would be zero and no information of the flow could be obtained using the decoupling process between absolute and relative flow patterns.

When representing the deterministic velocity distributions at the stator exit (right-hand plot), it can be observed that the superimposition of the periodic blade-to-blade nonuniformities is inherently modifying the vane-to-vane structures. The stator wakes fluctuate in both amplitude and position, so it is expected to be $\hat{u}$ containing valuable information about the interaction features.

The left-hand plot shows the pulsating nature of this pure unsteady part. In particular, it behaves as a double-peak, oscillating wave (positive-negative or vice versa over time) that is centered on the tangential position of the mean-time stator wake (approximately at the stator pitch position of 0.36 in the figure). An exhaustive interpretation of this harmonic fluctuation, derived from the analysis of the flow physics behind this, will be introduced later in Fig. 8.

In order to examine the distributions and magnitudes of the pure stator-rotor interaction at midspan for other operating conditions of the turbomachine, the rms value of $\hat{u}$ is introduced in Fig. 6. The positive-negative oscillating peak in Fig. 5 turns into a double positive maximum value representing the maximum averaged intensity of that fluctuation. From the analysis of the results (two stator pitches plotted for convenience), the following observations can be easily made. First of all, the width of the oscillation seems to be quite independent with respect to both changes in the operating conditions and in the axial spacing. This characteristic is totally expected because the alternative oscillations of $\hat{u}$ take place along the wake thickness, which is barely influenced by reductions of the flow rate (especially at midspan) and hardly affected by modifications in the axial gap. On the contrary, the magnitude of the oscillation depends on both axial gap and operating conditions. For example, it has been quantified that at nominal conditions, a reduction in the gap leads to a sudden increase in the interaction values from 2% to almost 6%, while similar increments are also observed in the case of near-stall conditions. It is also quite interesting to observe how off-design conditions for a particular axial gap present higher values of pure unsteadiness than nominal operating modes. This is because the aerodynamic loads of the blades are increased at partial loads, inducing larger spatial nonuniformities and a major impact over the wake-jet structures at the stator exit.

Finally, the analysis of the features of the velocity component $\hat{u}$

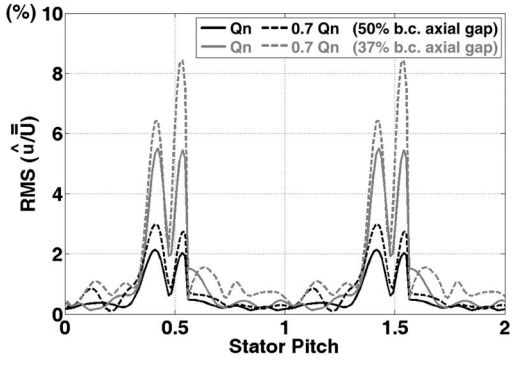

Fig. 6 Comparison of rms values of pure stator-rotor interaction at different operating conditions

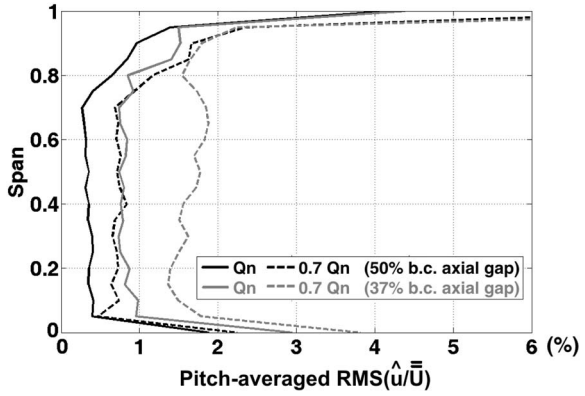

Fig. 7 Radial distribution of pure stator-rotor unsteadiness

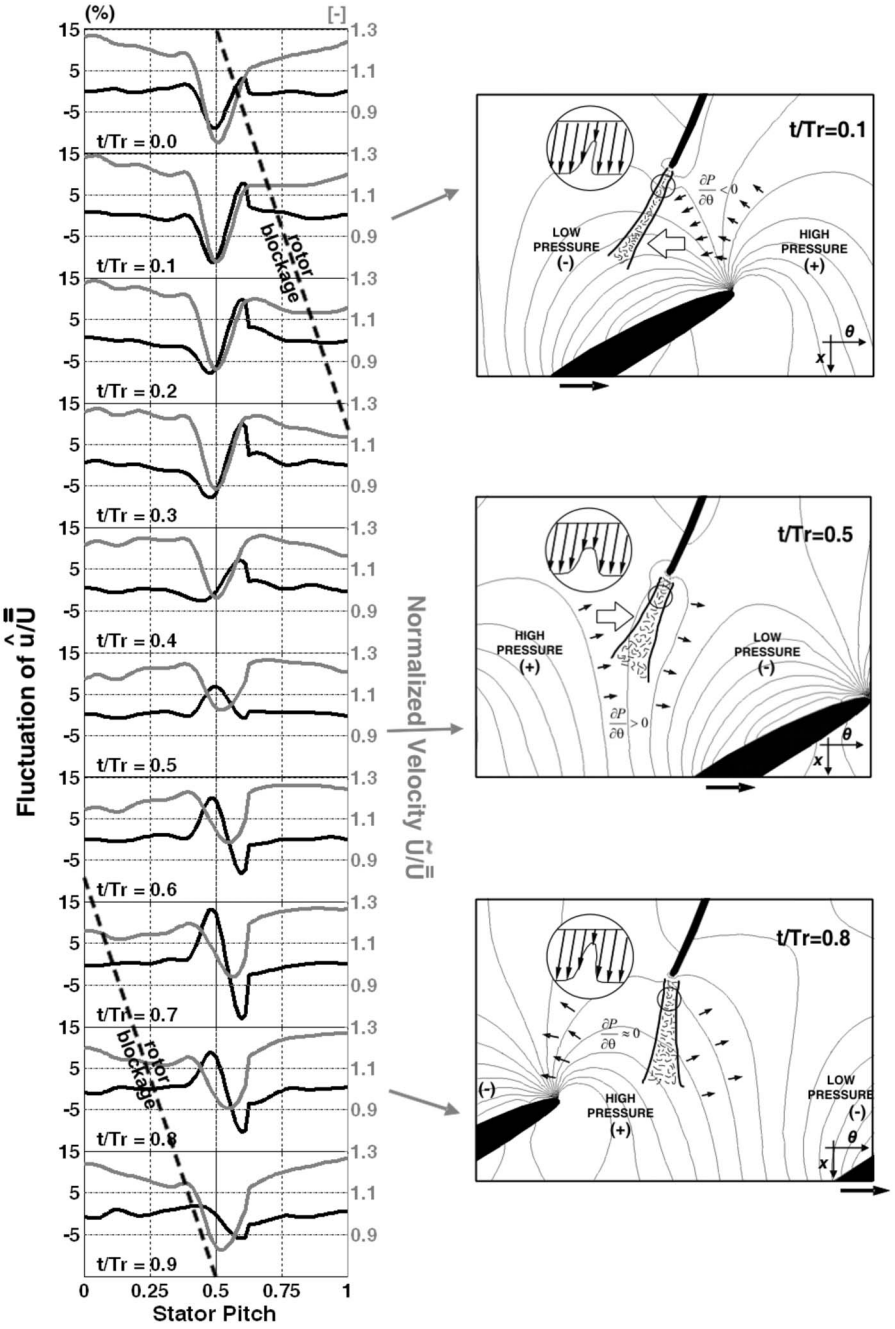

Fig. 8 Sketch of the stator-rotor interaction

is completed with the spanwise distribution of the mean value of the rms fluctuations (Fig. 7). This figure is obtained by pitch-averaging rms distributions for every measured radial position. Certainly, there are no significant variations in the results from hub-to-tip sections, which obviously derives in a uniform spanwise distribution of $\hat{u}$. This suggests that all the parameters that tend to increase the interaction are balanced with all those that tend to decrease it. For instance, the distance between the stator's TE and the rotor's LE is slightly increased spanwise, and also the blade thickness is reduced along the radial direction, causing a lower interaction, whereas the stagger angle of the rotor (Fig. 2) increases radially, inducing a higher interaction that compensates the former trend.

This section is concluded by illustrating the physical implications that are derived from the evolution of the pure wake-blockage interaction in Fig. 8. To do this, Fig. 5 is vertically stacked in order to track the shape of $\hat{u}$ over time (black line referred to the left axis) comparing it with the total deterministic unsteady velocity (gray line referred to the right axis) at different temporal snapshots. The dashed line crossing the plots diagonally represents the position of the rotor blockage.

At three particular instants, a sketch of the relative position of a rotating blade with respect to a fixed vane is introduced to analyze the influence of the stagnation conditions of the blades in the stator wake pattern. Distributions of static pressure are also included to provide insight of the potential mechanisms acting on the blockage. Such pressure contours have been calculated using a 3D-full unsteady numerical simulation (details of the simulation and its validation can be found in Refs. [20,22]), which are reproduced here simply as a reference for the discussion.

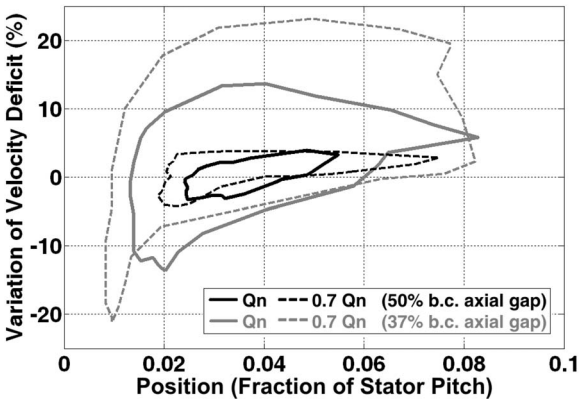

Fig. 9 Planar map of the stator wake trace

At $t/T_r=0.1$, the rotor blade has already passed along the vane TE. A region with negative pressure gradients induces the flow to overturn toward the θ-negative direction. Transported by the main flow, the instantaneous wake is displaced from the position of the mean-time wake, and moved toward the pressure side (PS) of the vane. Hence, the actual wake is reinforced (gains deficit) on the PS, while the intensity on the suction side (SS) of the vanes is now reduced. This situation determines the unsteady behavior of the stator-rotor interaction, with negative fluctuations (−10%) near the PS and positive fluctuations (+10%) near the SS (black line in the plot). Moreover, due to the geometrical blockage of the blades, the velocity (gray line in the plot) slows down, especially in the wake fluid, reducing the wake magnitude.

In phase $t/T_r=0.5$, the wake fluid is now convected through a positive pressure gradient, resulting in a net displacement toward the θ-positive direction (note the contour lines between the high and low pressure regions of the consecutive blades). In addition, the stator wake faces the blade passage, so the deficit is reduced and the wake thickens because of the flow acceleration when entering in the rotor passage (gray line in the plot). Also notice that maximum background values of velocity are obtained now over the stator wake position. Complementarily, because of the change in the wake displacement, the unsteady stator-rotor interaction is modified, showing positive values in the vane PS and negative values in the SS. This result thus starts to indicate the oscillating nature of this unsteady component (black line).

At $t/T_r=0.8$, when the next blade is beginning to interact with the vane, the wake fluid has completed its tangential shift, and it is ready to initiate a new displacement toward the opposite side. Then, the velocity component $\hat{u}$ evolves to the next cycle that is set off when the stator wake impinges on the rotor blade LE.

Therefore, the double-peak, oscillating nature of the interaction is revealed as a consequence of the periodic displacement of the wake, the main contributor being the rotor blockage. However, not only is the blockage responsible for this effect but it also modulates the wake deficit. In order to illustrate these fluctuations in the wake fluid, a representation of the relative variations in the velocity deficit as a function of the tangential position is depicted in Fig. 9. This planar map represents the closed loop followed by the wake for every blade-passing period at midspan. In particular, the figure summarizes the influence of the axial gap and the operating conditions on the temporal evolution of both position and magnitude of the velocity deficit. Important variations in the velocity deficit are found when the axial gap is reduced (up to a 20% in the gray lines). In any case, maximum tangential displacements are always lower than an 8% of the stator pitch. As expected, nominal conditions present less unsteadiness, so their paths are practically enclosed by the near-stall condition trace.

Comparison Between Turbulent and Deterministic Stresses. Further insight into the stator-rotor interaction of the low-speed axial fan is now completed through the comparison of distributions and magnitudes of both Reynolds and deterministic stresses measured between the rows.

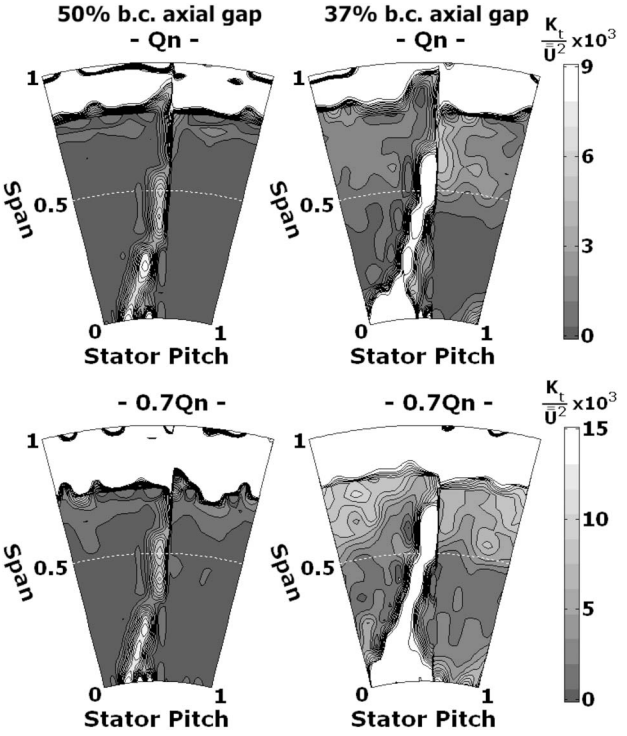

Fig. 10 Contours of turbulent kinetic energy for different gaps and operating conditions

Following Eqs. (3) and (6), the turbulent stresses have been calculated from the difference between the instantaneous and the phase-averaged velocity components, whereas the deterministic stresses were calculated from the difference between the phase averaged and the passage-averaged data. Some authors [4,5,7] have already reported that the deterministic stresses can be of similar or even higher magnitude than the turbulent stresses, especially in the interaction regions of multistage turbomachinery.

Figure 10 shows the results of turbulent kinetic energy for both large and low axial spacings at nominal and off-design conditions. These maps were made nondimensional by the square of the overall mean velocity in every operating point. In all the cases, turbulence associated with the casing boundary layer and with the stator wakes is clearly identified in the drawings. As expected, viscous regions of the casing are highly turbulent, presenting maximum values that are widely exceeding the colormap range (limited to improve the gradient of the wakes' disturbances). Moreover, when the mass flow rate is reduced for a particular axial gap configuration (i.e., left column), there is a significant enlargement of the turbulent boundary layer in the casing, while turbulence shed by the stator wakes maintains the same structure (though increasing the level as a consequence of a major disorder of the flow structures at off-design conditions). On the contrary, the axial spacing seems to be a critical parameter when controlling the turbulent kinetic energy associated with the stator wake fluid: for both nominal and near-stall conditions, there is a considerable increment of the turbulence level transported by the wakes, indicating the impact of the rotor blockage on the generation of small scale turbulence on the wakes shear layers.

Analogous figures showing deterministic stresses are added in Fig. 11. Notice that, outside the casing boundary layer, they show the similar overall trends that have been observed for the Reynolds stresses: regions with high deterministic stresses in the sta-

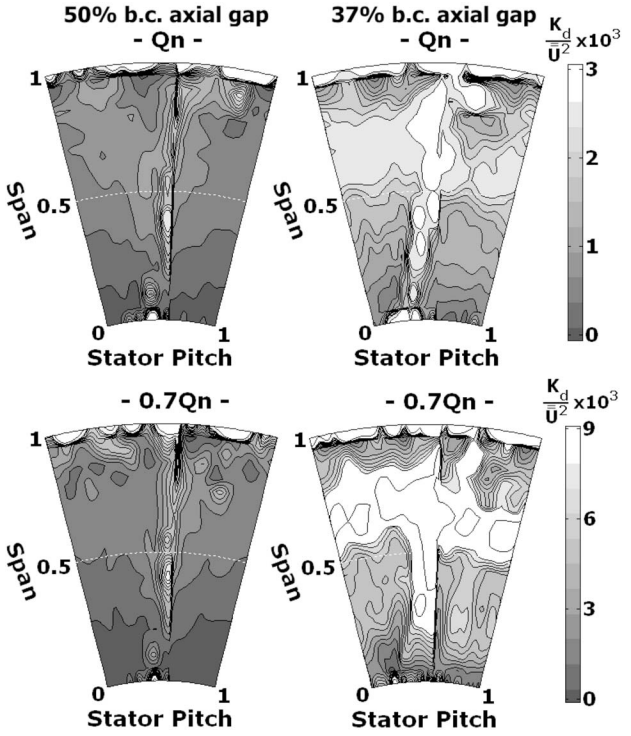

Fig. 11 Contours of deterministic kinetic energy for different operating conditions

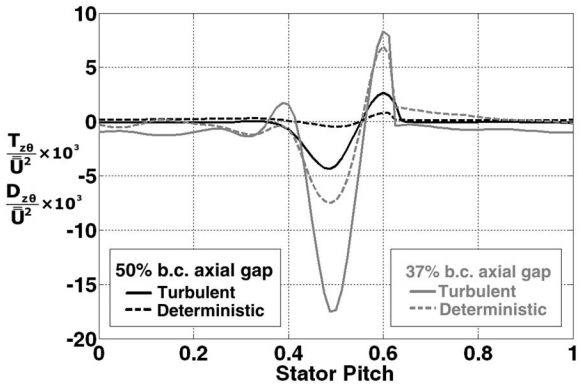

Fig. 12 Distribution of turbulent and deterministic shear stresses at midspan for nominal conditions

tor wakes are enlarged when the axial gap is reduced, and major unsteady disturbances appear (especially, the periodic blockage of the blades) at off-design conditions, increasing the global levels of deterministic stresses across the stator passage (up to three times).

The distributions of deterministic stresses reveal all the flow regions in which an important part of the unsteadiness consists of periodic phenomena, linked to the BPF. This means that wake-blockage interactions in addition to the rotating spatial nonuniformities of the blade can be perfectly described by these variables, whereas broadband, chaotic turbulence is completely filtered out. Effectively, as a result, the casing viscous region does not exhibit high levels of unsteadiness as before. Instead, it presents low disturbances at the BPF rate, in consonance with the background levels observed in the measuring sector. Also, these results show that the turbulent kinetic energy levels are significantly higher than the corresponding deterministic kinetic energy levels, indicating that the magnitude of the Reynolds and deterministic stresses differ substantially. These conclusions are similar to those found in the bibliography of axial turbomachinery, showing typical values that are also in reasonable agreement with former predictions (see Ref. [4]).

In order to understand the establishment of the deterministic stresses, we focus now on the physical mechanisms that produce them. Basically, the deterministic stresses are generated as a consequence of the dynamics of the circumferential nonuniformities of the rotor or even by a periodic modulation of the flow variables in a particular region of the vane-to-vane structures, constituting an ideal framework to address the unsteady sources of the flow by means of steady terms and correlations.

For example, in the case of the larger axial gap, notice the narrow band of unsteadiness associated with the wakes that breaks the circumferential uniformity of the deterministic distributions. Since the mathematical definition in Eq. (5) calculates a blade-passing averaged distribution of the unsteady deterministic variation of the squared velocities, this term reflects the mean deterministic energy for the wake-blockage interaction that is radially shifting from hub to tip during the rotor blade-passing period (this phenomenon is discussed in detail in Ref. [16]). On the contrary, when the axial gap is reduced, a high unsteadiness region is developed from midspan to tip sections as a consequence of the circumferential displacement of the rotor blockage. As a result of the mathematical construction, the rotor disturbance is swept out pitchwise, generating such a tangential band. This effect is even more severe at off-design conditions, as expected. In addition, the intersection of this blockage in the outer half of the sector and the radial migration of wake-blockage interaction reinforce the levels of unsteadiness, especially at 75% of the span.

In addition, the turbulent and deterministic shear stresses are also compared in terms of the crossed axial-tangential correlation in the case of nominal conditions at the midspan in Fig. 12.

A layer with elevated levels of positive and negative shear stress is developed in the wake of the stator vane for both turbulent and deterministic correlations. The appearance of layers of shear stresses with opposite signs is a fully expected feature when dealing with wakes (or jets) [4]. At large axial gaps, the fluctuating phase-averaged tangential velocity is weak, so the deterministic shear stress is almost negligible. On the contrary, the turbulent variable shows significant levels, suggesting appreciable correlation between axial and tangential randomness, which can be interpreted as an enhanced turbulent mixing.

In the case of a lower axial gap, turbulent and deterministic effects are both increased, with high negative levels toward the vane PS and positive values toward the SS. The explanation of this pattern in the shear stresses is based on the phase lag established between the spatial nonuniformities of both axial and tangential phase-averaged components, which are illustrated in Fig. 13.

The figure shows the temporal evolution of the product (thicker black line) of both axial and tangential deterministic fluctuations at midspan for nominal conditions. Every single component has also been introduced into the plots to explain the behavior of the correlation. Recall that the time-averaged distribution of the product of both components constitutes the deterministic shear stress of Fig. 12.

As noted before, the axial component presents a periodic, background fluctuation (i.e., $U_z''^{(R)}$) with a wavelength equal to the rotor pitch, in which a superimposed oscillation (i.e., $\hat{u}_z$) waves at the BPF rate. The transversal, dashed black line traces the displacement of the rotor blockage over time. In addition, the tangential positions influenced by the pure unsteady part of the deterministic fluctuations have been limited by the dashed, gray lines vertically crossing the plot. As expected, outside that region limited by the gray dashed lines, the tangential component shows a similar behavior to the axial one, reaching analogous levels of potential unsteadiness ($\pm 2.5\%$). On the contrary, inside that region, the pure unsteady part of the tangential component is sig-

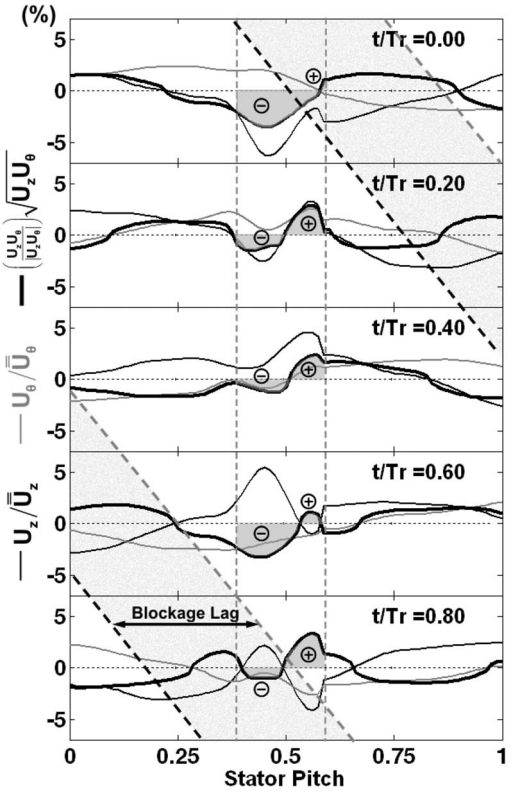

Fig. 13 Blockage lag effect on the instantaneous distribution of the axial and tangential deterministic fluctuations

nificantly lower than before (just a small superimposed oscillation is observed at $t/T_r=0.2$ and $t/T_r=0.8$), indicating a reduced influence of nonlinear interactions in the phase-averaged tangential component. This suggests that viscous mechanisms (induced by incoming wakes) have a reduced impact on the inflow conditions for the work exchange of the fan.

On the other hand, there is a clear phase lag in the displacement of the blockage between both velocity components. The blockage is first noticed by the deterministic flow in the tangential rather than in the axial direction, as a consequence of the early overturning of the flow, upstream of the stagnation conditions in the blade's LE.

Since potential fluctuations of both components are not in phase, their product always presents a positive value on the vane SS and a negative value on the PS (see shaded regions in the figure), leading to the time-averaged distribution of Fig. 12.

Spatial and Temporal Correlations of the Deterministic Stress Tensor. It is worth analyzing the relative importance of the diverse spatial and temporal terms involved in the definition of the deterministic tensor. Figure 14 shows all the correlations introduced in Eq. (10) in the case of nominal conditions for the lower axial gap configuration. This array of figures presents the axial-axial component in the first row and the tangential-tangential component in the second row. The columns correspond to the temporal correlation, the spatial-temporal correlation, and the spatial correlation, respectively. Also note that the horizontal sum for every component provides the total deterministic stress, as defined in Eq. (9).

Considering the axial-axial component, the temporal correlation exhibits a considerable uniformity for both radial and tangential directions, except for the wake fluid region, where two parallel layers (with elevated levels of stress) account for the unsteady wake-blockage interaction. Though not perfectly defined in this figure, both layers are clearly present in the distributions of every radial position, showing similar features to those in Fig. 6 (now

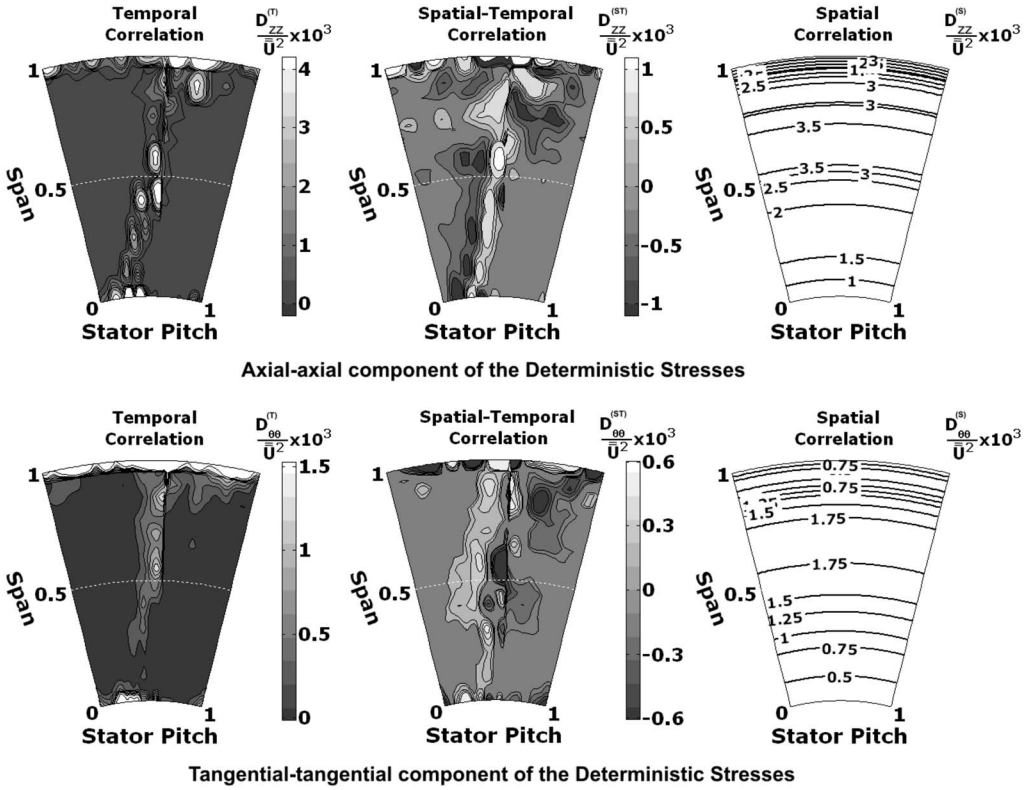

Fig. 14 Comparison of the correlations mixing to yield the global deterministic stresses

observed in the distributions of the deterministic stresses).

With respect to the spatial correlation, its value is constant along the tangential coordinate due to the relative motion of the blades in the absolute frame of reference. This means that the correlation introduces a phase-independent, radial gradient that is derived from the pitch-averaged nonuniformities in the blade passages (already shown in Fig. 4). Similar conclusions have been drawn in previous investigations in the case of transonic turbines [14], showing nearly uniform distributions for every component. However, in the present work, the correlation presents a perfect (inherent) axisymmetric pattern, because of the invariance of the time-averaged density in the case of this low-speed axial fan.

Finally, the spatial-temporal correlation of the axial component includes the influence of both temporal and spatial fluctuations. Its maximum values, which might be positive or negative, are small compared to the other correlations. However, they have to be considered twice according to Eq. (10). The contribution of the temporal fluctuations is mainly manifested with the presence of a two-sided band with opposite signs in the inner half of the passage. On the contrary, the influence of the spatial fluctuation is more significant in the outer half of the passage, where it leads to a higher dispersion of the correlation there.

The tangential-tangential component is also introduced in Fig. 14 to illustrate the distribution of the deterministic correlations in the case of the tangential velocity. Basically, the values of all the correlations are reduced in a half, though the overall trends are practically the same as that for the axial-axial components. Once again, both temporal and spatial correlations reach higher values than the spatial-temporal correlation, but now the mixed correlation inverts the sign of the two-sided band in the region of the stator wake fluid, because of the phase lag in the blockage between both velocity components.

Conclusions

The analysis of the deterministic unsteady flow, combined with a decomposition of the deterministic unsteadiness into pure temporal and rotating spatial parts, has proven to be a useful framework for investigating the periodic stator-rotor interaction inside a low-speed axial fan with inlet guide vanes. In this work, deterministic fluctuations are split into a rotating, spatial blade-to-blade nonuniformity (steady in the rotor reference frame) and a pure unsteady part that accounts for nonlinear wake-blockage interactions. This methodology has been developed using hot-wire anemometry measurements, already presented in previous works to explain the structure of the unsteady flow (see Ref. [16]), and now revisited to provide further insight into the underlying physics involved in the stator-rotor interaction.

This enhanced framework allows us to conclude that high unsteadiness in the tip region is mainly derived from the radial increase of the blade-to-blade spatial distortions in the rotor. Hence, the hub-to-tip torsion of the blades is responsible for setting off a major spatial distortion between the rows. In addition, it has been perfectly observed how this component is obviously independent of the axial spacing, whereas changes in the operating conditions significantly increase the deterministic unsteadiness.

Complementarily, a reduction in the axial gap contributes to increasing the wake-blockage interaction, i.e., the pure unsteady part of the deterministic fluctuations. This trend is also observable at off-design conditions since higher blade loadings induce major impact on the vane-to-vane flow structures. Therefore, this unsteady, nonlinear component has revealed a perfect suitability to address pure stator-rotor interaction in the absolute frame of reference, that is, to observe distortions of the stator wake fluid due to the rotor blockage.

Finally, the deterministic stresses have been calculated by time averaging the phase-dependent velocity correlations and compared to the turbulent stresses. The turbulent terms have shown higher values than the deterministic ones, but in any case, all of them within the same order of magnitude, as expected from previous investigations in the literature. Also, the same segregation used for the deterministic velocities was used for the stresses in order to compare the different parts of the deterministic correlations. Once again, higher levels were found for both temporal and spatial correlations, as is usual in the interaction zones of multistage turbomachinery.

Acknowledgment

This work was supported by the Research Projects "Modeling of Deterministic Stresses in Axial Turbomachinery," Reference No. DPI2003-09712, CICYT, and "Characterization of the Generation of Aerodynamic Noise due to the Interaction between the Rotor Blades and the Guide Vanes in Axial Flow Fans," Reference No. DPI2006-15720, CICYT.

Nomenclature

B = number of rotor blades
BPF = blade-passing frequency (s^{-1})
D = deterministic stresses
LE = leading edge
IGV = inlet Guide Vane
k_d = deterministic kinetic energy (m^2/s^2)
k_t = turbulent kinetic energy (m^2/s^2)
M = total number of stored rotor blades periods
N = number of samples per blade-passing period
P = pressure
PANS = passage averaged Navier–Stokes equations
PIV = particle image velocimetry
PS = pressure side
Q, Qn = flow rate and nominal flow rate (m^3/s)
RANS = reynolds averaged Navier–Stokes equations
$\vec{r}$ = spatial position in cylindrical coordinates
r = radial coordinate (m)
SS = suction side
t = time (s)
T_r = rotor blade-passing period (absolute) (s)
T_s = stator vane passing period (relative) (s)
T = Reynolds stresses (m^2/s^2)
TE = trailing edge
u = instantaneous velocity (m/s)
u' = random velocity fluctuation (m/s)
$\tilde{U}$ = deterministic velocity component (m/s)
U = deterministic velocity fluctuation (m/s)
$\bar{U}$ = mean velocity (m/s)
$\bar{\bar{U}}$ = overall mean velocity (m/s)
U'' = blade-to-blade spatial distortion (m/s)
$\hat{u}$ = pure temporal interaction (m/s)
z = axial coordinate (m)

Greek Letters

θ = angular coordinate (rad)
ρ = density (kg/m^3)
τ = total acquisition time (s)
φ = rotor blade phase (deg)
Ω = rotational speed (rad/s)

Superscripts and Subscripts

$\tilde{}$ = ensemble averaging.
$\bar{}$ = time averaging
(ax) = pitch averaging
t = tip
i, j = axial and tangential components
(R) = rotor reference frame (relative)
(S) = stator reference frame (absolute)

References

[1] Adamczyk, J. J., 1986, "Model Equation for Simulating Flows in Multistage Turbomachinery," ASME Paper No. 85-GT-226.

[2] Adamczyk, J. J., 2000, "Aerodynamic Analysis of Multistage Turbomachinery Flows in Support of Aerodynamic Design," ASME J. Turbomach., **122**, pp. 189–217.

[3] Meneveau, C., and Katz, J., 2002, "A Deterministic Stress Model for Rotor-Stator Interaction in Simulations of Average-Passage Flow," ASME J. Fluids Eng., **124**, pp. 550–554.

[4] Uzol, O., Chow, Y.-C., Katz, J., and Meneveau, C., 2002, "Experimental Investigation of Unsteady Flow Field Within a Two-Stage Axial Turbomachine Using Particle Image Velocimetry," ASME J. Turbomach., **124**, pp. 542–552.

[5] Chow, Y.-C., Uzol, O., and Katz, J., 2002, "Flow Non-Uniformities and Turbulent "Hot Spots" Due to the Wake-Blade and Wake-Wake Interactions in a Multistage Turbomachine," *Proceedings of ASME Turbo Expo, 2002, Amsterdam*, Netherlands.

[6] Uzol, O., Chow, Y.-C., Katz, J., and Meneveau, C., 2003, "Average Passage Flow Field and Deterministic Stresses in the Tip and Hub Regions of a Multistage Turbomachine," ASME J. Turbomach., **125**, pp. 714–725.

[7] Sinha, M., Katz, J., and Meneveau, C., 2000, "Quantitative Visualization of the Flow in a Centrifugal Pump With Diffuser Vanes.—II: Addressing Passage-Averaged and Large-Eddy Simulation Modeling Issues in Turbomachinery Flows," ASME J. Fluids Eng., **122**, pp. 108–116.

[8] Van de Wall, A. G., Kadambi, J. R., and Adamczyk, J. J., 2000, "A Transport Model for the Deterministic Stresses Associated With Turbomachinery Blade Row Interactions," ASME J. Turbomach., **122**, pp. 593–603.

[9] Van Zante, D. E., Adamczyk, J. J., Strazisar, A. J., and Okiishi, T. H., 2002, "Wake Recovery Performance Benefit in a High-Speed Axial Compressor," ASME J. Turbomach., **124**, pp. 275–284.

[10] Adamczyk, J. J., 1996, "Wake Mixing in Axial Flow Compressors," ASME Paper No. 96-GT-029.

[11] Kirtley, K. R., and Beach, T. A., 1992, "Deterministic Blade Row Interactions in a Centrifugal Compressor Stage," ASME J. Turbomach., **114**, pp. 304–311.

[12] Adamczyk, J. J., Beach, T. A., Celestina, M. L., Mulac, R. A., and To, W. M., 1989, "The Numerical Simulation of Multistage Turbomachinery Flows," *Proceedings of the AGARD Conference on Secondary Flows in Turbomachinery*.

[13] Chen, J. P., Celestina, M. L., and Adamczyk, J. J., 1994, "A New Procedure for Simulating Unsteady Flows Through Turbomachinery Blade Passages," ASME Paper No. 94-GT-151.

[14] Leboeuf, F., 2002, "Unsteady Flow Analysis in Transonic Turbine and Compressor Stages," *VKI Lecture Series*, 2002–01.

[15] Charbonnier, D., and Leboeuf, F., 2005, "Steady Flow Simulation of Rotor-Stator Interactions With an Unsteady Deterministic Model," *Proceedings of the Sixth European Conference on Turbomachinery*, Lille, France.

[16] Fernández Oro, J. M., Argüelles Díaz, K. M., Santolaria Morros, C., and Blanco Marigorta, E., 2007, "Unsteady Flow and Wake Transport in a Low-Speed Axial Fan With Inlet Guide Vanes," ASME J. Fluids Eng., **129**, pp. 1015–1029.

[17] Blanco, E., Ballesteros, R., and Santolaria, C., 1998, "Angular Range and Uncertainty Analysis of Non-Orthogonal Crossed Hot Wire Probes," ASME J. Fluids Eng., **123**, pp. 90–94.

[18] Lyman, F. A., 1993, "On the Conservation of Rothalpy in Turbomachines," ASME J. Turbomach., **115**, pp. 520–526.

[19] Adamczyk, J. J., Celestina, M. L., Beach, T. A., and Barnett, M., 1990, "Simulation of Three-Dimensional Viscous Flow Within a Multistage Turbine," ASME J. Turbomach., **112**, pp. 370–376.

[20] Fernández Oro, J. M., Argüelles Díaz, K. M., Santolaria Morros, C., and Ballesteros Tajadura, R., 2006, "Upstream Potential Propagation Effects of Unsteady Rotor-Stator Interaction in an Axial Flow Blower," ASME-FEDSM-98244.

[21] Arnaud, D., Ottavy, X., and Vouillarmet, A., 2004, "Experimental Investigation of the Rotor-Stator Interactions, Within a High Speed, Multi-Stage, Axial Compressor. Part 2—Modal Analysis of the Interactions," ASME Paper No. GT2004-53778.

[22] Fernández Oro, J. M., 2005, "Unsteady Rotor-Stator Interaction in an Axial Turbomachine," Ph.D. thesis, University of Oviedo, Spain.

Effects of Corrugated Roughness on Developed Laminar Flow in Microtubes

Zhipeng Duan

Y. S. Muzychka

Faculty of Engineering and Applied Science,
Memorial University of Newfoundland,
St. John's, NL, A1B 3X5, Canada

The effects of corrugated surface roughness on developed laminar flow in microtubes are investigated. The momentum equation is solved using a perturbation method with slip at the boundary. Novel analytical models are developed to predict friction factor and pressure drop in corrugated rough microtubes for continuum flow and slip flow. The developed model proposes an explanation on the observed phenomenon that some experimental pressure drop results for microchannel flow have shown a significant increase (15–50%) due to roughness. The developed model for slip flow illustrates the coupled effects between velocity slip and small corrugated roughness. Compressibility effect has also been examined and simple models are proposed to predict the pressure distribution and mass flow rate for slip flow in corrugated rough microtubes. [DOI: 10.1115/1.2842148]

Keywords: corrugations, roughness, perturbation, slip flow, microtubes

1 Introduction

Fluid flow in microchannels has emerged as an important research area. This has been motivated by their various applications such as medical and biomedical use, computer chips, and chemical separations. The advent of microelectromechanical systems (MEMSs) has opened up a new research area where noncontinuum behavior is important. MEMSs are one of the major advances of industrial technologies in the past decades. MEMSs refer to devices that have a characteristic length of less than 1 mm but greater than 1 μm, which combine electrical and mechanical components and which are fabricated using integrated circuit fabrication technologies.

Microchannels are the fundamental part of microfluidic systems. Understanding the flow characteristics of microchannel flows is very important in determining pressure drop, heat transfer, and transport properties of the flow. Microchannels can be defined as channels whose characteristic dimensions are from 1 μm to 1 μm. Above 1 μm, the flow exhibits behavior that is the same as continuum flows.

Some researchers have reported on deviations between microscale flow behavior and conventional macroscale flow theory. For laminar fully developed flow through microchannels, researchers have observed significant increases in the pressure drop from the macroscale flow theoretical values, as data appear up to 50% above the theoretical values [1–18]. Some publications indicate that flows on the microscale are different from that on macroscale. Several theories and models have been proposed to explain the observed deviations, but an indisputable conclusion has not yet been reached.

In macroscale flow theory, the friction factor is independent of relative roughness in the laminar region. However, some researchers proposed that the friction factor depends on the relative roughness of the walls of the microchannels also in the laminar region and the relative roughness cannot be neglected for microchannels in the laminar region [1,10,11,15–25].

Due to limitations in current micromachining technology, the microfabricated microchannel walls typically exhibit some degree of roughness. Roughness plays an increasingly important role in microchannel flows, but it is difficult to characterize its effects theoretically or numerically. It can be characterized using stylus-type surface profilometer, optical measurement, scanning electron microscope (SEM), atomic force microscope (ATM), and scanning tunneling microscope (STM). There is a need for a better understanding of the effects of wall roughness on fluid characteristics in microchannels.

Hu [26] employed the method of conformal mapping and Green's function in solving fully developed continuum flow through corrugated tubes. This approach is general, applicable to many irregular configurations although the procedure is lengthy.

Mala and Li [12] measured the friction factor of water in microtubes with diameters ranging from 50 μm to 254 μm. They proposed a roughness-viscosity model to explain the increase in the friction factor.

Kleinstreuer and Koo [27] proposed a numerical model to consider the effect of wall roughness on liquid continuum flow in microchannels. They modeled roughness by considering a porous medium layer (PLM) near the wall. The PML approach is able to mimic some details of the velocity profiles and of the effect of the roughness height.

Wang et al. [28] numerically investigated the friction factors of single phase continuum flow in microchannels with various roughness elements. The two-dimensional numerical solution shows significant influence of surface roughness including the height and spacing of the roughness elements on the Poiseuille number. The Poiseuille number increases with an increase of roughness height and decreases with an increase of the roughness spacing.

Bahrami et al. [14] developed a model to predict the pressure drop of the fully developed laminar continuum flows in roughness microtubes. In this model, the wall roughness is assumed to possess a Gaussian isotropic distribution.

Priezjev and Troian [29] investigated the influence of periodic surface roughness on the slip behavior of a Newtonian liquid in steady planar shear. However, the physics of liquid slip is complicated and not completely understood.

Li et al. [30] studied the effects of surface roughness on the slip flow in long microtubes. The rough surface was represented as a porous film based on the Brinkman-extended Darcy model, and the core region of the flow utilized velocity slip to model the rarefaction effects. By using the appropriate matching conditions at the gas/porous interface (velocity slip and stress continuity), the governing equation of pressure distribution was derived.

Contributed by the Fluids Engineering Division of ASME for publication in the JOURNAL OF FLUIDS ENGINEERING. Manuscript received October 19, 2006; final manuscript received November 18, 2007; published online March 3, 2008. Assoc. Editor: Ali Beskok.

Sun and Faghri [31] investigated the effects of surface roughness on nitrogen flow in a microchannel using the direct simulation Monte Carlo method. The surface roughness was modeled by an array of rectangular modules placed on two surfaces of a parallel plate channel. The effects of relative surface roughness, roughness distribution, and gas rarefaction on flow were studied. It was found that the effect of surface roughness is more pronounced at low Knudsen numbers. The roughness distribution represented by the ratio of the roughness height to spacing of the modules has a significant effect on the friction factor. The friction factor increases not only as the roughness height increases but also as the distance between the roughness modules decreases. This is consistent with the conclusions of Wang et al. [28].

In the slip flow regime ($0.001 \leqslant \mathrm{Kn} \leqslant 0.1$), the no-slip boundary conditions are not valid, and a kinetic boundary layer on the order of one mean free path [32,33], known as the ordinary Knudsen layer, starts to become dominant between the bulk of the fluid and the wall surface. The flow in the Knudsen layer cannot be analyzed using the Navier–Stokes equations, and it needs special equations of Boltzmann equation. The contributions of the Knudsen layer to the velocity field are of order Kn^2. However, for $\mathrm{Kn} \leqslant 0.1$, the Knudsen layer covers less than 10% of the tube diameter, and this layer can be neglected by extrapolating the bulk gas flow toward the walls [32]. The contribution of the Knudsen layer is small.

For a flow past a convex body, the kinetic boundary sublayer due to curvature is present in the moments. This boundary sublayer is formed by points that cannot be reached from the boundary along straight lines much longer than the mean free path. The curvature of the boundary sublayer appears in the second-order boundary conditions (Kn^2). This fact was discovered by Sone [34]. Details can be found in Refs. [35,34]. The kinetic boundary sublayer is a portion of the Knudsen layer. For $\mathrm{Kn} \leqslant 0.1$, the boundary sublayer covers much less than 10% of the tube diameter, and this boundary sublayer can be neglected. Using the first-order slip boundary conditions is expected to yield good approximations for $\mathrm{Kn} \leqslant 0.1$.

As analytical models derived using the first-order slip boundary condition have been shown to be relatively accurate up to Knudsen numbers of approximately 0.1 [36], the first-order slip boundary condition is employed in this paper. A variety of researchers have attempted to develop second-order slip models, which can be used in the early transition regime. However, there are large variations in the second-order slip coefficient [32,36]. The lack of a universally accepted second-order slip coefficient is a major problem in extending Navier–Stokes equations into the transition regime [36].

2 Theoretical Analysis

In this paper, we examine a simple approach to modeling surface roughness in the slip flow regime. In order to simplify the roughness problem, we can consider flow inside a microtube with a rough surface that is approximately sinusoidal corrugation, $r = R + R\varepsilon \sin(\lambda\theta)$, as illustrated in Fig. 1, where R is the mean radius of the rough microtube, λ is the wave number ($\lambda = 2\pi R/l$), relative roughness $\varepsilon = b/R \ll 1$, and b and l are the amplitude and wavelength of the rough corrugated walls, respectively. It is convenient to normalize the axial velocity u with $-(dp/dz)/\mu$. When the tubes are long enough ($L/D \gg 1$) and Reynolds number is relatively low, the momentum equation reduces to the Poisson equation. We will consider continuum flow first.

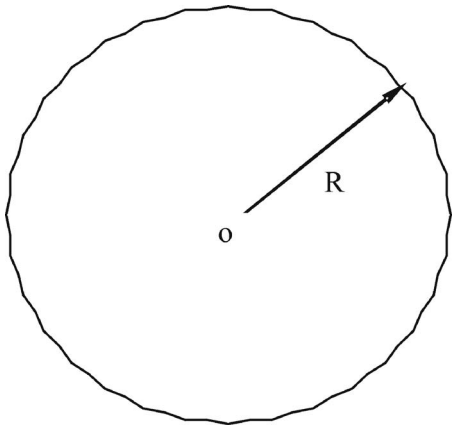

Fig. 1 A sinusoidal wave rough microtube

Continuum Flow.

$$\nabla^2 u = -1 \tag{1}$$

and

$$\nabla^2 = \frac{\partial^2}{\partial r^2} + \frac{1}{r}\frac{\partial}{\partial r} + \frac{1}{r^2}\frac{\partial^2}{\partial \theta^2} \tag{2}$$

The boundary conditions are

$$u \neq \infty \quad \text{at } r = 0 \tag{3}$$

$$u = 0 \quad \text{at } r = R + R\varepsilon \sin(\lambda\theta) \tag{4}$$

Using perturbation methods, we expand the velocity in terms of ε

$$u = u_0(r,\theta) + \varepsilon u_1(r,\theta) + \varepsilon^2 u_2(r,\theta) + \cdots \tag{5}$$

Equation (1) yields

$$\nabla^2 u_0 = -1, \quad \nabla^2 u_1 = 0, \quad \nabla^2 u_2 = 0 \tag{6}$$

and for the boundary conditions, we can expand $u(R + \varepsilon R \sin(\lambda\theta), \theta)$ in a Taylor series to obtain

$$u(R + \varepsilon R \sin(\lambda\theta), \theta) = u(R,\theta) + \varepsilon\left[R \sin(\lambda\theta)\frac{\partial u}{\partial r}(R,\theta)\right] + \varepsilon^2\left[\frac{[R \sin(\lambda\theta)]^2}{2}\frac{\partial^2 u}{\partial r^2}(R,\theta)\right] + \cdots = 0 \tag{7}$$

Substitution of Eq. (5) into Eq. (7) gives

$$u(R + \varepsilon R \sin(\lambda\theta), \theta) = u_0(R,\theta) + \varepsilon\left[u_1(R,\theta) + \frac{\partial u_0}{\partial r}(R,\theta)R \sin(\lambda\theta)\right] + \varepsilon^2\left[u_2(R,\theta) + \frac{\partial u_1}{\partial r}(R,\theta)R \sin(\lambda\theta) + \frac{1}{2}\frac{\partial^2 u_0}{\partial r^2}(R,\theta)R^2 \sin^2(\lambda\theta)\right] + O(\varepsilon^3) = 0 \tag{8}$$

Then, the boundary conditions become, respectively,

$$u_0(R,\theta) = 0 \tag{9}$$

$$u_1(R,\theta) + \frac{\partial u_0}{\partial r}(R,\theta)R \sin(\lambda\theta) = 0 \tag{10}$$

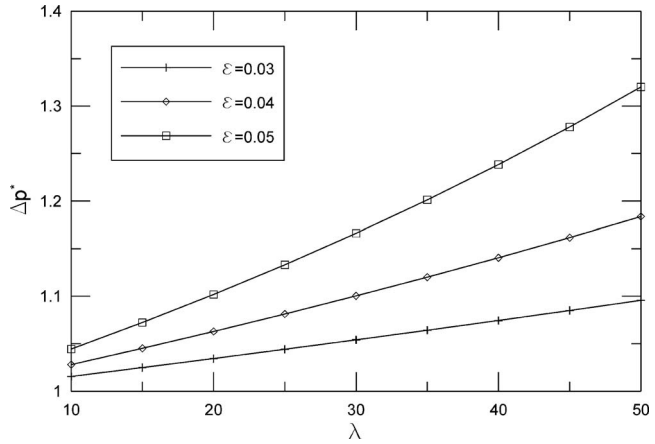

Fig. 2 Effect of relative roughness ε and wave number λ on pressure drop of microtubes for continuum flow

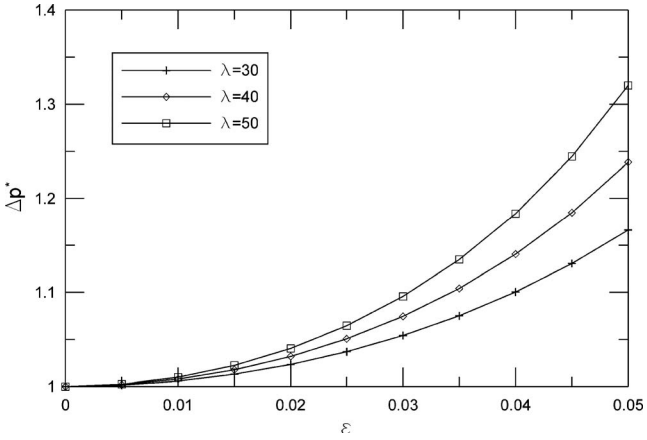

Fig. 3 Effect of relative roughness ε and wave number λ on pressure drop of microtubes for continuum flow

$$u_2(R,\theta) + \frac{\partial u_1}{\partial r}(R,\theta)R\sin(\lambda\theta) + \frac{1}{2}\frac{\partial^2 u_0}{\partial r^2}(R,\theta)R^2\sin^2(\lambda\theta) = 0 \tag{11}$$

The solutions of this problem yield

$$u_0 = \frac{R^2 - r^2}{4} \tag{12}$$

$$u_1 = \frac{1}{2}R^2\left(\frac{r}{R}\right)^{\lambda}\sin(\lambda\theta) \tag{13}$$

$$u_2 = \frac{1-2\lambda}{8}R^2 - \frac{1-2\lambda}{8}R^2\left(\frac{r}{R}\right)^{2\lambda}\cos(2\lambda\theta) \tag{14}$$

The total flow rate is given by

$$Q = -\frac{dp/dz}{\mu}\lambda \times \int_0^{2\pi/\lambda}\int_0^{R+\varepsilon R\sin(\lambda\theta)} (u_0 + \varepsilon u_1 + \varepsilon^2 u_2 + \varepsilon^3 u_3 + \cdots) r dr d\theta$$
$$= -\frac{\pi R^4 dp/dz}{8\mu}[1 - (2\lambda - 3)\varepsilon^2 + O(\varepsilon^4)] \tag{15}$$

It is seen that the periodic solution cannot be related to flow rate along z.

$$\frac{Q}{Q_{\text{sm}}} = 1 - (2\lambda - 3)\varepsilon^2 + O(\varepsilon^4) \tag{16}$$

where Q_{sm} is the flow rate for smooth microtubes. The flow rate decreases with an increase in λ, as $2\lambda - 3$ is always positive for practical applications, indicating a decrease in the flow rate with wall roughness.

After integrating Eq. (15), the pressure drop along the length of the pipe (L) may be determined to be

$$\Delta p = \frac{8\mu L Q}{\pi R^4}\frac{1}{1 - (2\lambda - 3)\varepsilon^2 + O(\varepsilon^4)} \tag{17}$$

It can also be shown that the effect of wall roughness on the pressure drop is given by the following equation:

$$\Delta p^* = \frac{\Delta p}{\Delta p_{\text{sm}}} = \frac{1}{1 - (2\lambda - 3)\varepsilon^2 + O(\varepsilon^4)} \tag{18}$$

where Δp_{sm} is the pressure drop for smooth microtubes.

Figures 2 and 3 demonstrate the effect of wave number λ and relative roughness ε on pressure drop of microtubes. As $2\lambda - 3$ is always positive, the pressure drop increases with wall roughness.

The friction factor Reynolds product can be obtained simply by substituting Eq. (15) into the definition of $f\text{Re}$.

$$f\,\text{Re} = \frac{2\left(-\frac{A}{P}\frac{dp}{dz}\right)D_h}{\mu\bar{u}} = \frac{2\left(-\frac{A}{P}\frac{dp}{dz}\right)D_h A}{\mu Q}$$
$$= 16\left(\frac{D_h}{2R}\right)^2\frac{1 + \frac{1}{2}\varepsilon^2}{1 - (2\lambda - 3)\varepsilon^2 + O(\varepsilon^4)} \tag{19}$$

where $A = \pi R^2(1 + \frac{1}{2}\varepsilon^2)$ and the perimeter can be evaluated numerically, see Shah and London [37]. The friction factor Reynolds product is presented in Table 1. The numerical value determined by conformal mapping and Green's function from Shah and London [37] is also included for comparison. It is found that Eq. (19) agrees with the numerical results of $f\text{Re}$ from Shah and London. The difference decreases with a decrease in ε. The present method would yield excellent result for small ε for continuum flow.

Slip Flow. Rarefaction effects must be considered in gases in which the molecular mean free path is comparable to the channel's characteristic dimension. The continuum assumption is no longer valid and the gas exhibits noncontinuum effects such as velocity slip and temperature jump at the channel walls. Traditional examples of noncontinuum gas flows in channels include low-density applications such as high-altitude aircraft or vacuum technology. The recent development of microscale fluid systems has motivated great interest in this field of study. There is strong

Table 1 $f\text{Re}$ for developed laminar flow in corrugated microtubes

λ	ϵ	$D_h/2R$	$f\text{Re}$ (Eq. (19))	$f\text{Re}$ [37]	Difference
6	0.02	0.9966	15.952	15.952	0.00%
	0.04	0.9863	15.805	15.806	0.00%
	0.06	0.9689	15.551	15.559	0.05%
8	0.02	0.9938	15.888	15.887	0.00%
	0.04	0.9747	15.536	15.542	0.04%
	0.06	0.9418	14.915	14.943	0.19%
12	0.02	0.9856	15.677	15.679	0.01%
	0.04	0.9402	14.647	14.671	0.16%
	0.06	0.8583	12.774	12.872	0.77%

evidence to support the use of Navier–Stokes and energy equations to model the slip flow problem, while the boundary conditions are modified by including velocity slip and temperature jump at the channel walls.

The Knudsen number (Kn) relates the molecular mean free path of gas to a characteristic dimension of the duct. Knudsen number is very small for continuum flows. However, for microscale gas flows where the gas mean free path becomes comparable with the characteristic dimension of the duct, the Knudsen number may be greater than 10^{-3}. Microchannels with characteristic lengths on the order of 100 μm would produce flows inside the slip regime for gas with a typical mean free path of approximately 100 nm at standard conditions. The slip flow regime to be studied here is classified as $10^{-3} < \mathrm{Kn} < 10^{-1}$. The flow is assumed to be isothermal. As the pressure drop is owing to viscous effects and not to any free expansion of the gas, the isothermal assumption should be reasonable.

We will first examine smooth microtubes. When the tubes are long enough ($L/D \gg 1$) and Reynolds number is relatively low, the continuum flow momentum equation is

$$\mu\left(\frac{d^2u}{dr^2} + \frac{1}{r}\frac{du}{dr}\right) = \frac{dp}{dz} \tag{20}$$

The boundary conditions for smooth microtubes are therefore

$$u \neq \infty \quad \text{at } r = 0 \tag{21}$$

$$u = -\lambda_f \frac{2-\sigma}{\sigma}\frac{du}{dr} \quad \text{at } r = R \tag{22}$$

where σ denotes the tangential momentum accommodation coefficient, which is usually between 0.87 and 1 [38]. Although the nature of the tangential momentum accommodation coefficients is still an active research problem, almost all evidence indicates that for most gas-solid interactions, the coefficients are approximately 1.0. Therefore, σ may be assumed to have a value of unity. The same procedure is valid even if $\sigma \neq 1$, defining a modified Knudsen number as $\mathrm{Kn}^* = \mathrm{Kn}(2-\sigma)/\sigma$. λ_f is the molecular mean free path. The characteristic length scale in the present analysis is defined as the microtube mean diameter. It is convenient to introduce the Knudsen number

$$\mathrm{Kn} = \frac{\lambda_f}{2R} \tag{23}$$

A solution of velocity distribution is obtained:

$$u = -\frac{1}{4\mu}\frac{dp}{dz}\left(R^2 - r^2 + \frac{2-\sigma}{\sigma}4\mathrm{Kn}R^2\right) \tag{24}$$

The mean velocity is found by integrating Eq. (24) across the section

$$\bar{u} = \frac{1}{A}\int udA = \frac{1}{\pi R^2}\int_0^R u 2\pi r dr = -\frac{R^2}{8\mu}\frac{dp}{dz}\left(1 + \frac{2-\sigma}{\sigma}8\mathrm{Kn}\right) \tag{25}$$

Then, we can obtain

$$f\,\mathrm{Re} = \frac{16}{1 + \frac{2-\sigma}{\sigma}8\mathrm{Kn}} \tag{26}$$

In addition, the volume rate of flow in the microtube is given by

$$Q = \pi R^2 \bar{u} = -\frac{\pi R^4}{8\mu}\frac{dp}{dz}\left(1 + \frac{2-\sigma}{\sigma}8\mathrm{Kn}\right) \tag{27}$$

The above equation indicates that the slip velocity boundary condition increases the volume rate of flow through the microtube.

Now, we will consider the coupled effects due to velocity slip and corrugated roughness on the channel walls. The only difference with no-slip case is the boundary condition

$$u = -\lambda_f \frac{2-\sigma}{\sigma}\frac{\partial u}{\partial n} \quad \text{at } r = R + R\varepsilon\sin(\lambda\theta) \tag{28}$$

where n is the outer direction normal.

We can expand $u(R+\varepsilon R\sin(\lambda\theta), \theta)$ in a Taylor series to obtain the boundary conditions

$$\begin{aligned} u(R + \varepsilon R\sin(\lambda\theta), \theta) &= u(R,\theta) + \varepsilon\left[R\sin(\lambda\theta)\frac{\partial u}{\partial r}(R,\theta)\right] \\ &\quad + \varepsilon^2\left[\frac{[R\sin(\lambda\theta)]^2}{2}\frac{\partial^2 u}{\partial r^2}(R,\theta)\right] + \cdots \\ &= -\lambda_f\frac{2-\sigma}{\sigma}\frac{\partial u}{\partial n} \end{aligned} \tag{29}$$

and

$$\begin{aligned} \frac{\partial u}{\partial n} &= \frac{\partial u}{\partial r}\cos\alpha + \frac{1}{r}\frac{\partial u}{\partial \theta}\cos\beta \\ &= \frac{\nabla u \cdot \nabla[r - R - R\varepsilon\sin(\lambda\theta)]}{|\nabla[r - R - R\varepsilon\sin(\lambda\theta)]|} \\ &= \left[\frac{\partial u}{\partial r} - \frac{\partial u}{\partial \theta}\varepsilon\frac{\lambda R}{r^2}\cos(\lambda\theta)\right]\left[1 + \varepsilon^2\frac{\lambda^2R^2}{r^2}\cos^2(\lambda\theta)\right]^{-1/2} \end{aligned} \tag{30}$$

Following a procedure similar to the no-slip case (the derivation is quite space consuming and omitted here), we may obtain the solution as follows:

$$u_0 = \frac{R^2 - r^2}{4} + \frac{2-\sigma}{\sigma}\mathrm{Kn}R^2 \tag{31}$$

$$u_1 = \text{periodic solution} = \cdots \times (\sin(\lambda\theta)) \tag{32}$$

$$\begin{aligned} u_2 &= \frac{R^2}{8}\left[1 - \frac{2\lambda(1+2\mathrm{Kn}^*)(1+4\lambda\mathrm{Kn}^* - 2\mathrm{Kn}^*)}{1+2\lambda\mathrm{Kn}^*}\right] \\ &\quad + \text{periodic solution} \\ &= \frac{R^2}{8}\left[1 - \frac{2\lambda(1+2\mathrm{Kn}^*)(1+4\lambda\mathrm{Kn}^* - 2\mathrm{Kn}^*)}{1+2\lambda\mathrm{Kn}^*}\right] \\ &\quad + \cdots \times (\cos(2\lambda\theta)) \end{aligned} \tag{33}$$

The total flow rate is given by

$$\begin{aligned} Q &= -\frac{dp/dz}{\mu}\lambda\int_0^{2\pi/\lambda}\int_0^{R+\varepsilon R\sin(\lambda\theta)}(u_0 + \varepsilon u_1 + \varepsilon^2 u_2 + \varepsilon^3 u_3 + \cdots) \\ &\quad \times r dr d\theta \\ &= -\frac{\pi R^4 dp/dz}{8\mu}\left[1 + 8\mathrm{Kn}^*\right. \\ &\quad - \left(1 + \frac{2\lambda(1+2\mathrm{Kn}^*)(1+4\lambda\mathrm{Kn}^* - 2\mathrm{Kn}^*)}{1+2\lambda\mathrm{Kn}^*} - 4\mathrm{Kn}^*\right. \\ &\quad \left.\left. - 4\frac{1+2\mathrm{Kn}^*}{1+2\lambda\mathrm{Kn}^*}\right)\varepsilon^2 + O(\varepsilon^4)\right] \\ &= -\frac{\pi R^4 dp/dz}{8\mu}[1 - B\varepsilon^2 + O(\varepsilon^4)](1 + 8\mathrm{Kn}^*) \end{aligned} \tag{34}$$

where

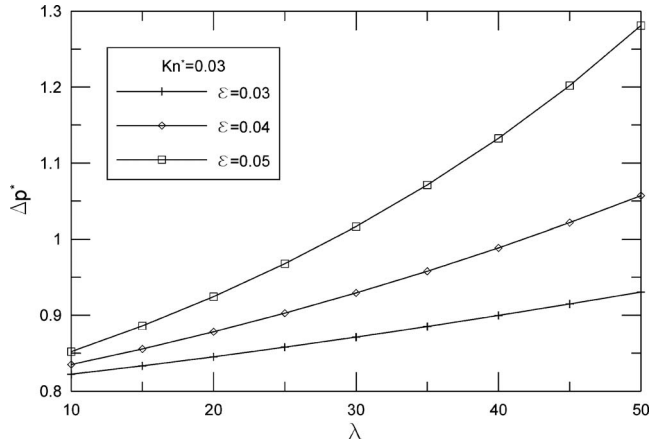

Fig. 4 Effect of relative roughness ε, wave number λ, and Knudsen number K*n* on pressure drop of microtubes

$$B = \frac{1 + \dfrac{2\lambda(1+2\mathrm{Kn}^*)(1+4\lambda\mathrm{Kn}^*-2\mathrm{Kn}^*)}{1+2\lambda\mathrm{Kn}^*} - 4\mathrm{Kn}^* - 4\dfrac{1+2\mathrm{Kn}^*}{1+2\lambda\mathrm{Kn}^*}}{1+8\mathrm{Kn}^*} \tag{35}$$

B is a function of wave number λ and modified Knudsen number Kn*.

$$\frac{Q}{Q_{\mathrm{sm}}} = [1 - B\varepsilon^2 + O(\varepsilon^4)]\left(1 + \frac{2-\sigma}{\sigma}8\mathrm{Kn}\right) \tag{36}$$

where Q_{sm} is the flow rate for continuum flow in smooth microtubes, as B is always positive, indicating a decrease in the flow rate with wall roughness.

After integrating Eq. (34), the pressure drop for incompressible flow along the length of the pipe (L) may be determined to be

$$\Delta p = \frac{\dfrac{8\mu LQ}{\pi R^4}}{[1 - B\varepsilon^2 + O(\varepsilon^4)]\left(1 + \dfrac{2-\sigma}{\sigma}8\mathrm{Kn}\right)} \tag{37}$$

It can also be shown that the effect of wall roughness on the pressure drop is given by the following equations:

$$\Delta p^* = \frac{\Delta p}{\Delta p_{\mathrm{sm}}} = \frac{1}{[1 - B\varepsilon^2 + O(\varepsilon^4)]\left(1 + \dfrac{2-\sigma}{\sigma}8\mathrm{Kn}\right)} \tag{38}$$

where Δp_{sm} is the pressure drop for continuum flow in smooth microtubes.

Figure 4 demonstrates the effect of wave number λ, relative roughness ε, and Knudsen number Kn on pressure drop of microtubes. Velocity slip decreases pressure drop and corrugated roughness increases pressure drop. Pressure drop depends on ε, λ, and Kn and it can be less than, equal to, or greater than unity. The coupled effects between small corrugated roughness and velocity slip propose a possible explanation on the observed phenomenon that Chung et al. [39] and Kohl et al. [40] found that the friction factors for slip flow in microchannels can be accurately determined from conventional theory for large channels.

Using the similar procedure as continuum flow, the friction factor Reynolds product for slip flow can be obtained as follows:

$$f\,\mathrm{Re} = 16\left(\frac{D_h}{2R}\right)^2 \frac{1 + \dfrac{1}{2}\varepsilon^2}{[1 - B\varepsilon^2 + O(\varepsilon^4)]\left(1 + \dfrac{2-\sigma}{\sigma}8\mathrm{Kn}\right)} \tag{39}$$

Now, we take account of the compressibility of the gas. For compressible flow, the mass flow rate in the microtube is given by employing the equation of state $p=\rho\Re T$,

$$\dot{m} = \rho\bar{u}A = -\frac{\pi R^4}{8\mu\Re T}[1 - B\varepsilon^2 + O(\varepsilon^4)]\frac{dp}{dz}\left(p + 8\frac{2-\sigma}{\sigma}p\mathrm{Kn}\right) \tag{40}$$

We can use $p\mathrm{Kn}=p_o\mathrm{Kn}_o$ since $p\mathrm{Kn}$ is constant for isothermal flow. Integrating Eq. (40), we obtain

$$\dot{m} = \rho\bar{u}A \cong \frac{\pi R^4 p_o^2}{16\mu\Re Tz}[1 - \bar{B}\varepsilon^2 + O(\varepsilon^4)] \times\left[\frac{p_i^2}{p_o^2} - \frac{p_z^2}{p_o^2} + 16\frac{2-\sigma}{\sigma}\mathrm{Kn}_o\left(\frac{p_i}{p_o} - \frac{p_z}{p_o}\right)\right] \tag{41}$$

where $\bar{B}$ denotes the average value of $B(\lambda, \mathrm{Kn}_i^*)$ and $B(\lambda, \mathrm{Kn}_z^*)$.

Letting $z=L$ gives

$$\dot{m} = \rho\bar{u}A \cong \frac{\pi R^4 p_o^2}{16\mu\Re TL}[1 - \bar{B}\varepsilon^2 + O(\varepsilon^4)] \times\left[\frac{p_i^2}{p_o^2} - 1 + 16\frac{2-\sigma}{\sigma}\mathrm{Kn}_o\left(\frac{p_i}{p_o} - 1\right)\right] \tag{42}$$

The continuum flow mass flow rate is given by

$$\dot{m}_c = \rho\bar{u}A = \frac{\pi R^4 p_o^2}{16\mu\Re TL}[1 - \bar{B}\varepsilon^2 + O(\varepsilon^4)]\left(\frac{p_i^2}{p_o^2} - 1\right) \tag{43}$$

The effect of slip may be illustrated clearly by dividing the slip flow mass flow equation (Eq. (42)) by the continuum mass flow equation (Eq. (43))

$$\frac{\dot{m}}{\dot{m}_c} \cong 1 + \frac{16\dfrac{2-\sigma}{\sigma}\mathrm{Kn}_o}{\dfrac{p_i}{p_o} + 1} \tag{44}$$

It is seen that the rarefaction increases the mass flow and that the effect of rarefaction becomes more significant when the pressure ratio decreases. This could be interpreted as a decrease of the gas viscosity.

Combining Eqs. (41) and (42), we obtain the expression for pressure distribution

$$\frac{p_z}{p_o} \cong -8\frac{2-\sigma}{\sigma}\mathrm{Kn}_o + \sqrt{\left(8\frac{2-\sigma}{\sigma}\mathrm{Kn}_o + \frac{p_i}{p_o}\right)^2 - \left[\frac{p_i^2}{p_o^2} - 1 + 16\frac{2-\sigma}{\sigma}\mathrm{Kn}_o\left(\frac{p_i}{p_o} - 1\right)\right]\frac{z}{L}} \tag{45}$$

The pressure distribution exhibits a nonlinear behavior due to the compressibility effect. Pressure drop required is less than that in a conventional channel. The deviations of the pressure distribution from the linear distribution decrease with an increase in Knudsen number. The nonlinearity increases as the pressure ratio increases. The effects of compressibility and rarefaction are opposite as Karniadakis et al. [32] demonstrated. The incompressibility assumption (linear pressure distribution) is valid for small pressure drop in the microtubes.

3 Summary and Conclusion

The influences of corrugated surface roughness on the developed laminar flow in microtubes are studied and novel models are proposed to predict friction factor and pressure drop for continuum flow and slip flow. Compressibility effect has also been examined and simple models are proposed to predict the pressure distribution and mass flow rate for slip flow in corrugated rough microtubes.

It is observed that the normalized pressure drop Δp^* is a function of relative roughness ε and wave number λ for continuum flow, i.e., $\Delta p^* = F(\varepsilon, \lambda)$. The present model exhibits the influence of corrugated roughness. For most conventional microtubes ($\varepsilon \approx 0.03-0.05$, $\lambda = 30-50$), the present model proposes an explanation on the observed phenomenon that pressure drop results for continuum flow have shown a striking increase (15–50%) due to roughness.

For slip flow, Δp^* is a function of relative roughness ε, wave number λ, and Knudsen number Kn, i.e., $\Delta p^* = F_1(\varepsilon, \lambda, \mathrm{Kn})$. There exist coupled effects between velocity slip and corrugated roughness. Velocity slip decreases pressure drop and increases flow rate. Corrugated roughness increases pressure drop and decreases flow rate. These two effects can have a canceling effect in some systems.

The friction factor Reynolds product depends on the relative roughness of the walls of the microchannels also in the laminar region and the relative roughness cannot be neglected for microchannels in the laminar region.

Common practice is to specify surfaces with a single parameter, average roughness as it is well established and understood. It is obvious that one parameter is not enough to describe the complete nature of a surface. The roughness spacing is another important parameter to describe surface roughness. The friction factor Reynolds product increases not only as the roughness height increases but also as the roughness spacing decreases.

The developed simple models may be used by the research community to estimate roughness and velocity slip effects for the practical engineering design of microtubes.

Acknowledgment

The authors acknowledge the support of the Natural Sciences and Engineering Research Council of Canada (NSERC).

Nomenclature

A = flow area, m^2
b = amplitude, m
D_h = hydraulic diameter, $=4A/P$
f = Fanning friction factor, $=\tau/(\frac{1}{2}\rho\bar{u}^2)$
Kn = Knudsen number, $=\lambda_f/2R$
Kn* = modified Knudsen number, $=\mathrm{Kn}(2-\sigma)/\sigma$
L = tube length, m
l = wavelength, m
$\dot{m}$ = mass flow rate, kg/s
n = outer direction normal
P = perimeter, m
p = pressure, N/m^2
Δp^* = normalized pressure drop
Q = volume flow rate, m^3/s
R = mean radius of a rough microtube, m
$\Re$ = specific gas constant, J/kg K
Re = Reynolds number, $=\bar{u}D_h/\nu$
r = radial coordinate in the cylindrical coordinate system, m
T = temperature, K
u = velocity, m/s
$\bar{u}$ = average velocity, m/s
z = coordinate in flow direction, m

Greek Symbols

ε = relative roughness, b/R
θ = angular coordinate in the cylindrical coordinate system, rad
λ = wave number
λ_f = molecular mean free path, m
μ = dynamic viscosity, $N\,s/m^2$
ν = kinematic viscosity, m^2/s
σ = tangential momentum accommodation coefficient
τ = wall shear stress, N/m^2

Subscripts

c = continuum
i = inlet
o = outlet
sm = smooth

References

[1] Wu, P., and Little, W. A., 1983, "Measurement of Friction Factors for Flows of Gases in Very Fine Channels Used for Microminiature Joule-Thompson Refrigerators," Cryogenics, **23**, pp. 273–277.
[2] Wu, P., and Little, W. A., 1984, "Measurement of the Heat Transfer Characteristics of Gas Flow in Fine Channel Heat Exchangers Used for Microminiature Refrigerators," Cryogenics, **24**, pp. 415–420.
[3] Harley, J., Bau, H., Zemel, J. N., and Dominko, V., 1989, "Fluid Flow in Micron and Submicron Size Channels," *Proceedings Workshop on Micro Electro Mechanical Systems*, Salt Lake City, UT, pp. 25–28.
[4] Peng, X. F., and Peterson, G. P., 1996, "Convective Heat Transfer and Flow Friction for Water Flow in Microchannel Structures," Int. J. Heat Mass Transfer, **39**, pp. 2599–2608.
[5] Peng, X. F., Peterson, G. P., and Wang, B. X., 1994, "Frictional Flow Characteristics of Water Flowing Through Rectangular Microchannels," Exp. Heat Transfer, **7**, pp. 249–264.
[6] Wilding, P., Shoffner, M. A., and Kircka, L. J., 1994, "Manipulation and Flow of Biological Fluids in Straight Channels Micromachined in Silicon," Clin. Chem., **40**, pp. 43–47.
[7] Wu, S., Mai, J., Zohar, Y., Tai, Y. C., and Ho, C. M., 1998, "A Suspended Microchannel With Integrated Temperature Sensors for High Pressure Flow Studies," *Proceedings IEEE Workshop on Micro Electro Mechanical Systems*, Heidelberg, Germany, pp. 87–92.
[8] Urbanek, W., Zemel, J. N., and Bau, H., 1993, "An Investigation of the Temperature Dependence of Poiseuille Numbers in Microchannel Flow," J. Micromech. Microeng., **3**, pp. 206–209.
[9] Papautsky, I., Brazzle, J., Ameel, T. A., and Frazier, A. B., 1998, "Microchannel Fluid Behavior Using Micropolar Fluid Behavior," *Proceedings of the 1998 IEEE 11th Annual International Workshop on Micro Electro Mechanical Systems*, Heidelberg, Germany, pp. 544–549.
[10] Pfund, D., Rector, D., Shekarriz, A., Popescu, A., and Welty, J., 1998, "Pressure Drop Measurements in a Microchannel," *Proceedings of the 1998 ASME International Mechanical Engineering Congress and Exposition: DSC Micro-Electro-Mechanical Systems*, Vol. 66, pp. 193–198.
[11] Qu, W., Mala, G. M., and Li, D., 1999, "Pressure-Driven Flows in Trapezoidal Silicon Microchannels," Int. J. Heat Mass Transfer, **43**, pp. 353–364.
[12] Mala, G. M., and Li, D., 1999, "Flow Characteristics of Water in Microtubes," Int. J. Heat Fluid Flow, **20**, pp. 142–148.
[13] Kulinsky, L., Wang, Y., and Ferrari, M., 1999, "Electroviscous Effects in Microchannels," *SPIE Conference on Micro and Nanofabricated Structures and Devices for Biomedical Environment Applications II*, San Jose, CA, Vol. 3606, pp. 158–168.
[14] Bahrami, M., Yovanovich, M. M., and Culham, J. R., 2006, "Pressure Drop of Fully Developed, Laminar Flow in Rough Microtubes," ASME J. Fluids Eng., **128**, pp. 632–637.
[15] Ding, L. S., Sun, H., Sheng, X. L., and Lee, B. D., 2000, "Measurement of Friction Factor for R134a and R12 Through Microchannels," *Proceedings of Symposium on Energy Engineering in the 21st Century*, Vol. 2, pp. 650–657.
[16] Li, Z. X., Du, D. X., and Guo, Z. Y., 2000, "Characteristics of Frictional Resistance for Gas Flow in Microtubes," *Proceedings of Symposium on Energy Engineering in the 21st Century*, Vol. 2, pp. 658–664.

[17] Kandlikar, S. G., Joshi, S., and Tian, S., 2001, "Effect of Channel Roughness on Heat Transfer and Fluid Flow Characteristics at Low Reynolds Numbers in Small Diameter Tubes," *Proceedings of 35th National Heat Transfer Conference*, Anaheim, CA, Paper No. 12134.
[18] Li, Z. X., Du, D. X., and Guo, Z. Y., 2003, "Experimental Study on Flow Characteristics of Liquid in Circular Microtubes," Microscale Thermophys. Eng., **7**, pp. 253–265.
[19] Yu, D., Warrington, R., Barron, R., and Ameel, T. A., 1995, "Experimental and Theoretical Investigation of Fluid Flow and Heat Transfer in Microtubes," *Proceedings of the 1995 ASME/JSME Thermal Engineering Joint Conference*, Maui, HI, Vol. 1, pp. 523–530.
[20] Pfund, D., Shekarriz, A., Popescu, A., and Welty, J. R., 2000, "Pressure Drop Measurements in a Microchannel," AIChE J., **46**, pp. 1496–1507.
[21] Celata, G. P., Cumo, M., Guglielmi, M., and Zummo, G., 2000, "Experimental Investigation of Hydraulic and Single Phase Heat Transfer in 0.130 mm Capillary Tube," *Proceedings of International Conference on Heat Transfer and Transport Phenomena in Microscale*, G. P. Celata, ed., Begell House, New York, pp. 108–113.
[22] Li, Z. X., Du, D. X., and Guo, Z. Y., 2000, "Experimental Study on Flow Characteristics of Liquid in Circular Microtubes," *Proceedings of International Conference on Heat Transfer and Transport Phenomena in Microscale*, G. P. Celata, ed., Begell House, New York, pp. 162–168.
[23] Bucci, A., Celata, G. P., Cumo, M., Serra, E., and Zummo, G., 2003, "Fluid Flow and Single-Phase Flow Heat Transfer of Water in Capillary Tubes," *Proceedings of the International Conference on Minichannels and Microchannels*, Rochester, NY, Paper No. ICMM-1037.
[24] Tu, X., and Hrnjak, P., 2003, "Experimental Investigation of Single-Phase Flow Pressure Drop Through Rectangular Microchannels," *Proceedings of the International Conference on Minichannels and Microchannels*, Rochester, NY, Paper No. ICMM-1028.
[25] Baviere, R., Ayela, F., Le Person, S., and Favre-Marinet, M., 2004, "An Experimental Study of Water Flow in Smooth and Rough Rectangular Micro-Channels," *Proceedings of the Second International Conference on Minichannels and Microchannels*, Rochester, NY, Paper No. ICMM2004-2338.
[26] Hu, M. H., 1973, "Flow and Thermal Analysis for Mechanically Enhanced Heat Transfer Tubes," Ph.D. thesis, State University of New York at Buffalo, New York.
[27] Kleinstreuer, C., and Koo, J., 2004, "Computational Analysis of Wall Roughness Effects for Liquid Flow in Micro-Conduits," ASME J. Fluids Eng., **126**, pp. 1–9.
[28] Wang, X. Q., Yap, C., and Mujumdar, A. S., 2005, "Effects of Two-Dimensional Roughness in Flow in Microchannel," ASME J. Electron. Packag., **127**, pp. 357–361.
[29] Priezjev, N. V., and Troian, S. M., 2006, "Influence of Periodic Wall Roughness on the Slip Behaviour at Liquid/Solid Interfaces: Molecular-Scale Simulations Versus Continuum Predictions," J. Fluid Mech., **554**, pp. 25–46.
[30] Li, W. L., Lin, J. W., Lee, S. C., and Chen, M. D., 2002, "Effects of Roughness on Rarefied Gas Flow in Long Microtubes," J. Micromech. Microeng., **12**, pp. 149–156.
[31] Sun, H., and Faghri, M., 2003, "Effects of Surface Roughness on Nitrogen Flow in a Microchannel Using the Direct Simulation Monte Carlo Method," Numer. Heat Transfer, Part A, **43**, pp. 1–8.
[32] Karniadakis, G. E., Beskok, A., and Aluru, N., 2005, *Microflows and Nanoflows*, Springer, New York.
[33] Hadjiconstantinou, N. G., 2005, "Validation of a Second-Order Slip Model for Dilute Gas Flows," Microscale Thermophys. Eng., **9**, pp. 137–153.
[34] Sone, Y., 2000, *Kinetic Theory and Fluid Dynamics*, Birkhäuser, Boston.
[35] Cercignani, C., 1988, *The Boltzmann Equation and Its Applications*, Springer, New York.
[36] Barber, R. W., and Emerson, D. R., 2006, "Challenges in Modeling Gas-Phase Flow in Microchannels: From Slip to Transition," Heat Transfer Eng., **27**, pp. 3–12.
[37] Shah, R. K., and London, A. L., 1978, *Laminar Flow Forced Convection in Ducts*, Academic, New York, Chap. 10.
[38] Rohsenow, W. M., and Choi, H. Y., 1961, *Heat, Mass, and Momentum Transfer*, Prentice-Hall, Englewood Cliffs, NJ.
[39] Chung, P., Kawaji, M., and Kawahara, A., 2002, "Characteristics of Single-Phase Flow in Microchannels," *Proceedings of ASME 2002 Fluids Engineering Division Summer Meeting*, Montreal, Canada.
[40] Kohl, M. J., Abdel-Khalik, S. I., Jeter, S. M., and Sadowski, D. I., 2005, "An Experimental Investigation of Microchannel Flow With Internal Pressure Measurements," Int. J. Heat Mass Transfer, **48**, pp. 1518–1533.

Influence of Staggering Angle of a Rotating Rod on Flow Past a Circular Cylinder

T. Ayyappan
Research Scholar

S. Vengadesan[1]
Assistant Professor
e-mail: vengades@iitm.ac.in

Department of Applied Mechanics,
IIT Madras,
Chennai 600036, India

The influence of the staggering position of a rotating rod on flow past a main circular cylinder is investigated numerically. The rod is rotated at a constant speed ratio of 3. The effect of the diameter ratio of the rotating rod is studied by considering two different diameter ratios. The investigation is carried out at a fixed pitch length of 1. The study is carried out for two Reynolds number, viz., 100 and 500. The momentum injection from the rod is found to alter the flow characteristics behind the main cylinder. For a certain arrangement of stagger angle and diameter ratio, the vortex shedding behind the main cylinder gets suppressed. The corresponding configuration for which minimum drag coefficient is achieved is suggested from this study. [DOI: 10.1115/1.2842224]

Keywords: rotating rod, staggered arrangement, drag reduction, circular cylinder

1 Introduction

Flow past a circular cylinder is of interest to fluid mechanics researchers as it has the application in many fields, and it features many behaviors observed in complex flows. Details of earlier studies are available in Blevins [1] and Zdravkovich [2]. It is well known that due to vortex shedding, the circular cylinder experiences flow induced vibration. To control the vortex shedding phenomena and to reduce the drag force on the cylinder, various techniques have been tried. The control techniques are broadly classified into active and passive. In active control, an external energy is supplied to the flow by means of mechanical devices such as jet blowing, acoustic excitation, rotating cylinder, and so on. In a passive control technique, the vortex shedding is suppressed by means of passive devices, which do not require any external driving forces. Different types of passive devices, such as circular cylinder, splitter plates, etc., were used for this purpose.

Barnes et al. [3] used a circular rod to control the flow past a cylinder. They investigated base pressure and Strouhal number for the angle of stagger (α) between 0 deg and 45 deg. In a tandem arrangement for pitch length $1.32D$ to $1.94D$ (D is the diameter of the main cylinder), shear layers from the upstream rod reattaches onto the downstream cylinder at ± 45 deg, and no vortex shedding from the upstream rod was observed. For larger gap distances, vortex shedding from both cylinders occurred.

Luo and Gan [4] experimentally studied the effect of the upstream circular rod of $d/D=0.33$ for Re in the range of $3.15 \times 10^4 - 8.8 \times 10^4$ in tandem arrangement. Lee et al. [5] experimentally investigated the effect d/D in the range of 0.133–0.267 for $\mathrm{Re}=2 \times 10^4$ in tandem arrangement. They proposed a relation for a critical pitch length (L_{cr}/D), which is defined as the pitch length beyond which the vortex shedding from the rod starts to happen. They found that flow quantities change abruptly at this pitch length. From a flow visualization study, they found a cavity mode for a lower pitch length and a wake impingement mode for a larger pitch length.

Zhao et al. [6] numerically studied the flow around two cylinders of different diameters at $\mathrm{Re}=500$. They investigated the effect of L/D and stagger angle with the stationary rod of $d/D=0.25$. Recently, Zhao et al. [7] simulated the turbulent flow past a main cylinder with the rod of the diameter ratio ranging from 0.1 to 0.5 by using a $k-\omega$ turbulence closure. Wang et al. [8] used an upstream rod of $d/D=0.5$ to reduce the drag on the main cylinder for $\mathrm{Re}=8.2 \times 10^3$. They obtained maximum drag reduction due to the shielding effect of a separated shear layer of the upstream rod on the downstream cylinder at lower L/D. They found that the upstream rod can reduce the drag until the stagger angle reaches 10 deg. In all the above discussed literatures, the rod is stationary. It is well known that the rotation of an isolated circular cylinder results in the acceleration and deceleration of fluid particles on opposite sides of the cylinder based on the direction of rotation. These phenomena result in the reduction of drag, increase in lift, and vortex suppression. A brief review of the work on an isolated rotating circular cylinder is discussed below.

The basic phenomenon of the rotating circular cylinder is explained by means of the *Magnus* effect. The potential flow theory proposed by Prandtl gives the closed streamlines only when $\omega > 2.0$ (ω is the speed ratio), at which the stagnation point is detached from the cylinder. Ingham and Tang [9] numerically investigated the steady two-dimensional flow past a rotating circular cylinder for $\mathrm{Re}=5$ and 20, and found that the mean drag force decreases and the mean lift force increases with an increase in speed ratio. They observed that the closed streamline pattern exists for all nonzero speed ratios. Takada and Tsutahara [10] simulated flow around an impulsively rotating two-dimensional circular cylinder using the Lattice–Boltzmann method for the Reynolds number of 200 and 500 for speed ratios of 0.5 and 1.

Kang et al. [11] simulated a two-dimensional flow past an isolated circular cylinder for three different low Reynolds numbers, $\mathrm{Re}=60$, 100, and 160, and investigated the effect of speed ratio on aerodynamic characteristics. They found that vortex shedding exists for low rotational speed, but completely suppressed beyond a certain speed ratio.

From previous studies reported so far, it is observed that the use of passive devices changes the flow pattern behind the main cylinder and results in drag reduction for some configuration. It is also known that the isolated rotating cylinder results in the suppression of vortex shedding, decrease of mean drag coefficient, and increase in mean lift coefficient. In this sense, it will be interesting to investigate the effect of an upstream rotating rod on a stationary cylinder. In the present study, the effect of a staggering angle of a constantly rotating rod on flow past a main cylinder of diameter D is analyzed numerically. In this study, rods of two

[1]Corresponding author.

Contributed by the Fluids Engineering Division of ASME for publication in the JOURNAL OF FLUIDS ENGINEERING. Manuscript received January 22, 2007; final manuscript received October 27, 2007; published online March 3, 2008. Assoc. Editor: Rajat Mittal.

diameter ratios $d/D=0.2$ and 0.5 are considered. The study is carried out for two different Reynolds numbers, viz., 100 and 500. The Reynolds number is defined based on the incoming uniform velocity and diameter of the main cylinder.

2 Numerical Details

2.1 Governing Equations. The two basic fluid flow equations, viz., continuity and momentum equations in general index notations, are given as

$$\frac{\partial(u_i)}{\partial x_i} = 0 \tag{1}$$

$$\frac{\partial(u_i)}{\partial t} + \frac{\partial(u_j u_i)}{\partial x_j} = -\frac{\partial p}{\partial x_i} + \frac{1}{\mathrm{Re}}\frac{\partial}{\partial x_j}\left[\frac{\partial u_i}{\partial x_j} + \frac{\partial u_j}{\partial x_i}\right] \tag{2}$$

where the indices i and j each go through x, y, and z taken to denote the streamwise, cross-stream and spanwise velocities (u, velocity; x, spatial coordinate; t, time; p, pressure).

2.2 Computational Domain and Grid. In this section, the computational domain and numerical details used for simulating flow past an isolated circular cylinder is discussed. The commercially available computational fluid dynamics preprocessor GAMBIT is used for generating the grid. A box-type computational domain size of $27D \times 16D$ with a structured grid in a Cartesian coordinate system is used. The streamwise direction is along the x axis, and the cross-streamwise direction is along the y axis with the origin positioned at the center of the cylinder. The upstream boundary is placed at $7D$ from the origin. This extent is slightly less than that used by Engelman and Jamina [12] and Behr et al. [13], who used an inlet boundary at $8D$, whereas Mittal et al. [14] used one at $5D$ for both isolated as well as interference cases. The outlet boundary is specified at $20D$ downstream from the origin. The same length was used by Engelman and Jamina [12] and Burbeau and Sagaut [15]. In the y direction, the boundary is kept at $8D$ from the origin. This distance is the same as the one used by Behr et al. [13] and Mittal et al. [14].

For Reynolds number Re=500, a three-dimensional grid with a z axis along the spanwise direction, with $z=0$ being the midspan of the cylinder, is used. Previous numerical studies for Re=200 and 500 (Takada and Tsutahara [10]) and for Re=1000 (Jester and Kallinderis [16]) were carried out with a two-dimensionality assumption. However, the instability experiment reported by Prasad and Williamson [17] and the three-dimensional floquet stability analysis performed by Barkley and Henderson [18] at subcritical Reynolds numbers showed that the dominant spanwise scales having a wavelength of approximately three to four times the cylinder diameters exist in the range $180 < \mathrm{Re} < 240$. After this Reynolds number, the wavelength shortens to nearly one diameter. Hence, present three-dimensional simulations are carried out with the spanwise length of $3D$ along the z direction.

2.3 Numerical Approach. The governing equations are solved using a commercial solver FLUENT 6.2. The equations are discretized using a finite volume method on a collocated grid in a fully implicit form. The convective terms in momentum equations are solved using the QUICK scheme, and the SIMPLE algorithm is used for coupling the pressure and velocity terms. The second order implicit scheme is used for the time integration of each equation. At the inlet, a uniform velocity is specified. A convective boundary condition is applied at outlet the boundary. In lateral boundaries, a symmetry boundary condition is prescribed. On the cylinder wall, a no-slip boundary condition is applied. For a three-dimensional grid, a periodic boundary condition is enforced in the spanwise direction.

Table 1 Mesh independent study and comparison of bulk parameters for Re=100

Re=100	Mesh size ($N_x \times Ny \times N_\theta$)	St	$C_{d\ \mathrm{mean}}$	$C_{l\ \mathrm{rms}}$
Grid A	$76 \times 51 \times 60$	0.156	1.34	0.145
Grid B	$110 \times 71 \times 100$	0.160	1.38	0.241
Grid C	$135 \times 105 \times 140$	0.163	1.39	0.253
Kang et al. [11]		0.164	1.34	0.236
Engelman and Jamina [12]		0.170	1.40	0.257
Mittal et al. [14]		0.164	1.32	0.230
Meneghini et al. [19]		0.165	1.37	0.257

2.4 Validation Details

2.4.1 Grid Independence Test for a Single Stationary Cylinder. Mesh sensitivity studies are carried out for Reynolds number Re=100 for the case of flow past a stationary isolated cylinder with three different grids. The comparison details are given in Table 1. In that table, $Nx \times Ny \times N\theta$ denotes the number of grid points used along the streamwise, cross-stream, and circumference of the cylinder. In Grid A, the first grid point is placed at a distance of $0.05D$ from the cylinder wall. In Grids B and C, the first grid point is placed at $0.01D$ and $0.007D$, respectively. The solution is initiated and allowed to march in time with an increment of $dt=2\times10^{-2}$ until the vortex shedding becomes periodic. The simulation is continued for some more vortex shedding cycles to attain the stationary flow condition, after which the time averaging is done over 20 vortex shedding cycles to obtain both bulk and field quantities. Bulk parameters such as mean drag coefficient ($C_{d\ \mathrm{mean}}$), root mean square value of lift coefficient ($C_{l\ \mathrm{rms}}$), and Strouhal number (St) reported in Table 1, showed a good agreement with numerical data. The $C_{d\ \mathrm{mean}}$ value in literature shows a scatter from 1.32 to 1.40, and present simulation results fall within this range. From the table, we also observe that the bulk parameters for Grids B and C agree well with the quoted references. Considering the computational time, the improvement showed by Grid C is negligible. Hence, further calculations are performed with Grid B. Figure 1 shows the typical grid used for isolated stationary cylinder case.

2.4.2 Rotating Isolated Circular Cylinder at Re=100. As reported in Sec. 1, many numerical and experimental studies are available for a single cylinder rotating with constant angular speed for Reynolds numbers such as Re=5, 20, 60, 100, and 200. The flow past a circular cylinder started impulsively from rest to rotation reaches a steady or an unsteady state depending on the Reynolds number and speed ratio. The flow past a circular cylinder rotating with constant angular speed is simulated to validate the numerical schemes adopted in the study.

The solver, discretization schemes, domain, construction of grid, and boundary conditions on all directions are the same as those used for the case of a stationary isolated circular cylinder. For the rotating case, on a cylinder surface, constant angular speed is applied with respect to its own axis. The angular speed is nondimensionalized by using freestream velocity and is given as a speed ratio $\omega = \phi D/2U_\infty$. This speed ratio indicates the tangential speed of the cylinder periphery with respect to the freestream velocity.

The medium grid used for the stationary isolated cylinder is used for this simulation as well, and results are compared with Kang et al. [11]. The variation of mean aerodynamic coefficients and wall pressure coefficient with respect to speed ratio is shown in Fig. 3. For the stationary cylinder, the value of $C_{l\ \mathrm{mean}}$ is zero because of the symmetric nature of vortex shedding for each cycle. With increasing speed ratio, the magnitude of $C_{l\ \mathrm{mean}}$ increases linearly toward the negative direction. This same trend is reported by Kang et al. [11]. The mean drag coefficient obtained

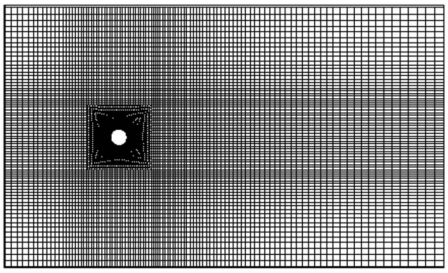

a) Complete domain

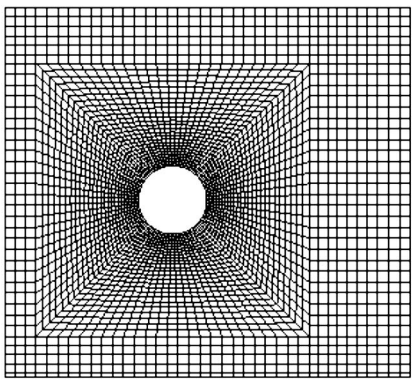

b) Enlarged view of the grid near the cylinder

Fig. 1 Typical grid used for flow over an isolated circular cylinder. (*a*) Complete domain. (*b*) Enlarged view of the grid near the cylinder.

by the present simulation (Fig. 3(*b*)) shows the decreasing trend with increasing speed ratio. When compared with Kang et al. [11], the magnitude deviates constantly for all the speed ratios, but the same trend was obtained. The wall pressure coefficient is also found to be in good agreement with the reported references.

2.4.3 Two Circular Cylinder in Tandem Arrangement at Re=100. As the influence of the upstream rotating rod on flow past bluff bodies is our interest, it is necessary that we have to validate our solver, domain, computational scheme, and grid construction for the interference case as well. For this, the simulation of flow past two identical stationary circular cylinders in a tandem arrangement for various pitch lengths is carried out. The construction of mesh is done in the same way as it was done for the isolated case, except for the region in between two cylinders. The value of L/D at which the $C_{d\ \mathrm{mean}}$ of downstream cylinder changes abruptly is called critical pitch length (L_{cr}/D). The data from the present simulation along with those from various literatures are reported in Table 2. It is found to agree well with the experimental result of Huhe et al. [20]. The numerical results of Sharman et al. [21] and Li et al. [22] predicted lower values of L_{cr}/D.

Table 2 Comparison of critical pitch length (L_{cr}/D) for two identical cylinders in tandem arrangement at Re=100

References	L_{cr}/D	
Present	$4.25 \leqslant L_{\mathrm{cr}}/D \leqslant 4.75$	Numerical
Huhe et al. [20]	$4.5 \leqslant L_{\mathrm{cr}}/D \leqslant 5$	Experimental
Sharman et al. [21]	$3.75 \leqslant L_{\mathrm{cr}}/D \leqslant 4$	Numerical
Li et al. [22]	$3 \leqslant L_{\mathrm{cr}}/D \leqslant 4$	Numerical

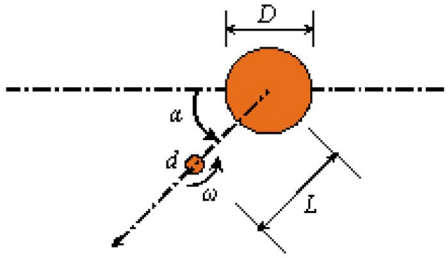

Fig. 2 Schematic arrangement of the present study

2.5 Schematic Arrangement and Other Details for the Present Study. The schematic arrangement of the present study is shown in Fig. 2. The circular cylinder having diameter D is used as the stationary main cylinder. A rod is a small circular cylinder of diameter d and is positioned on the upstream side of the main cylinder. The center-to-center distance between the rod and the main cylinder is denoted as L, which is nondimensionalized with the diameter of the main cylinder (D). The extension of computational domain from the center of the rod and the main cylinder is same as the one used for the isolated cylinder. The strategies adopted for the construction of grids in upstream, downstream, and two sidewise regions are the same as those adopted in the case of the isolated cylinder. Along the circumference of rod (θ), 60 and 80 number of grid points are taken, respectively, for $d/D=0.2$ and 0.5. For the rod, the first point is kept at a distance of $0.005D$ from the wall.

The angle of stagger (α) is varied nonuniformly from the tandem arrangement to the side-by-side arrangement. From Barnes et al. [3] and Wang et al. [8], it is observed that for a stationary rod at a lower staggering angle, the influence of rod is greater compared to that of the higher staggering angle. Hence, in this study, near by tandem line stagger angle is changed by a small value. The staggering angles used for the present simulation are 0 deg, 3 deg, 5 deg, 10 deg, 45 deg, and 90 deg. In the present study, the speed ratio is kept constant at $\omega=3$, where $\omega=\phi D/2U_{\infty}$ and (ϕ) is the angular velocity.

3 Results and Discussion

There are many ways to present the results obtained by current simulations. Luo and Gan, [4], Tsutsui and Igarashi, [23] and Lee et al. [5] presented their results with respect to the effect of L/D as their investigations were limited to the tandem arrangement. On the other hand, Barnes et al. [3] and Wang et al. [8] explained theirs by means of the influence of stagger angle as they did not study the influence of the speed ratio. In this paper, the results are presented as the effect of stagger angle for a constant speed of rotation $\omega=3$. The characteristics of aerodynamic coefficients, profiles of velocity at different wake stations, and streamline patterns are discussed in the following section.

3.1 Simulation Results at Re=100. The flow Reynolds number based on the main cylinder diameter for this case is 100. In this section, the effect of the diameter ratio of rod is analyzed by using the rod of diameter ratios 0.2 and 0.5.

3.1.1 Aerodynamic Coefficients

3.1.1.1 Variation of $C_{d\ \mathrm{mean}}$. The variation of the mean drag coefficient of the main cylinder is shown in Fig. 4(*a*). For the rod of $d/D=0.2$, the mean value of $C_{d\ \mathrm{mean}}$ increases continuously up to the stagger angle of 45 deg and then decreases for a side-by-side arrangement. The magnitude of $C_{d\ \mathrm{mean}}$ alternatively decreases and increases for the rod of $d/D=0.5$. The minimum value of the drag coefficient is observed at the staggering angle of 10 deg for $d/D=0.5$. For both diameter ratios, the drag acting on

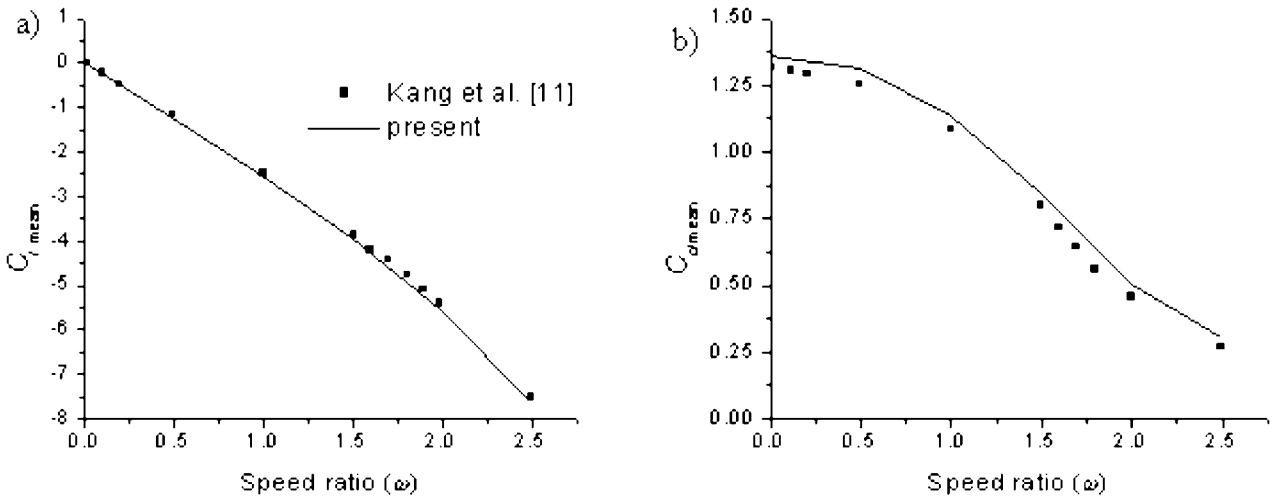

a) Variation of Mean lift coefficient, **b)** Variation of Mean drag coefficient

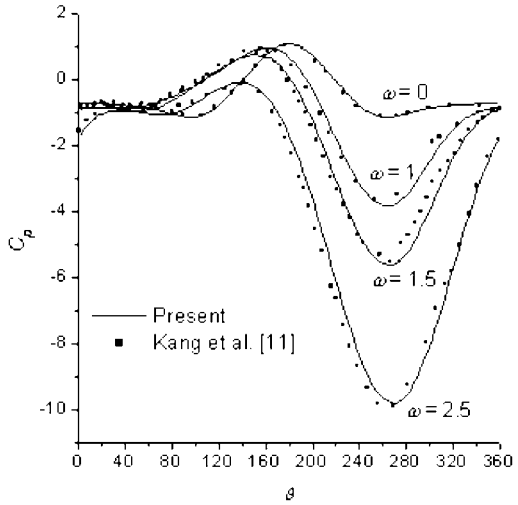

c) Variation of wall pressure coefficient with speed ratio.

Fig. 3 Results for the isolated rotating cylinder. Legends are the same in both plots. (*a*) Variation of mean lift coefficient. (*b*) Variation of mean drag coefficient. (*c*) Variation of wall pressure coefficient with speed ratio.

the main cylinder is less than the value of the isolated stationary cylinder (Table 1). This drastic change in the $C_{d\ \mathrm{mean}}$ can be explained with the help of the mean streamline plot shown in Fig. 5 for $\alpha=0$ deg and 10 deg. Because of the rotation of the rod, the fluid in the gap region gets decelerated and creates a recirculation bubble in front of the main cylinder. This causes negative pressure distribution in that area. For both tandem and 10 deg stagger angles, the negative region extends to the wake behind the main cylinder and forms a dumbbell shape. This dumbbell shape is not observed for the rod of $d/D=0.2$. For the sake of completeness, the mean drag coefficients of the rod for both diameter ratios are also given in Fig. 4(*d*). For both d/D, it shows a decreasing trend with increasing stagger angle up to 45 deg and then almost stays constant.

3.1.1.2 Variation of $C_{l\ \mathrm{mean}}$. Figure 4(*b*) shows the variation of the mean lift coefficient of the main cylinder with respect to the positioning of the rotating rod. For lower stagger angles, the value continuously decreases with the rod of $d/D=0.2$. Whereas for the rod of $d/D=0.5$, this magnitude slightly increases for lower stagger angles' and then it decreases continuously. For all the cases considered in this study, the $C_{l\ \mathrm{mean}}$ value stays nonzero. This is due to the asymmetry nature of pressure distribution on the main cylinder because of the rotation of the rod.

3.1.1.3 Variation of $C_{l\ \mathrm{rms}}$. The variation of the root mean square value of lift coefficient ($C_{l\ \mathrm{rms}}$) shown in Fig. 4(*c*) depicts a favorable trend in vortex suppression. With the rotating rod of $d/D=0.2$, a magnitude of $C_{l\ \mathrm{rms}}$ decreases continuously with increasing stagger angle. This value attains zero for $\alpha=90$ deg, and the flow behind the main cylinder is steady. This steady flow behind the main cylinder can be observed in the instantaneous vorticity contour. Figure 6(*a*) shows the instantaneous vorticity plot for $d/D=0.2$ at the 90 deg stagger angle. This vorticity contour is at a time instant corresponding to the maximum positive lift of the main cylinder. For a better comparison, the simulation is carried out for the stationary rod of the same d/D and is given in Fig. 6(*a*). (i) Nice periodic counter rotating vortices are observed behind the main cylinder for the stationary rod, whereas at $\omega=3$

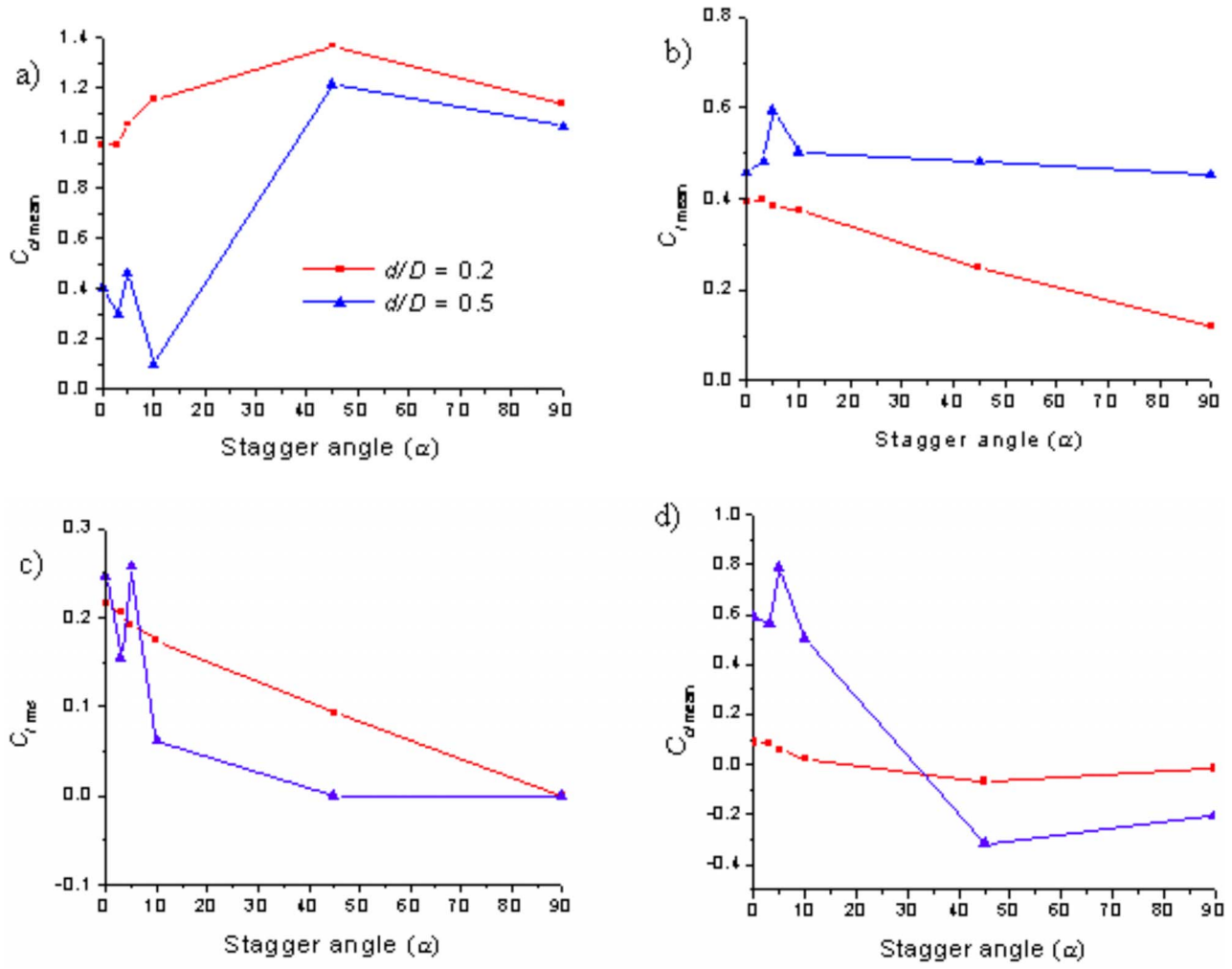

Fig. 4 Variation of aerodynamic coefficients. (*a*) Mean drag coefficient of the main cylinder. (*b*) Mean lift coefficient of the main cylinder. (*c*) rms lift coefficient of the main cylinder. (*d*) Mean drag coefficient of the rod. Legends are the same in all plots.

(Fig. 6(*a*) (ii)), the contours are stretched. The flow does not show features changing with respect to time, and the vortex shedding behind the main cylinder is suppressed. A similar behavior is observed for both 45 deg and 90 deg with the rod of diameter ratio 0.5, as shown in Figs. 6(*b*) and 6(*c*), respectively. The contours of

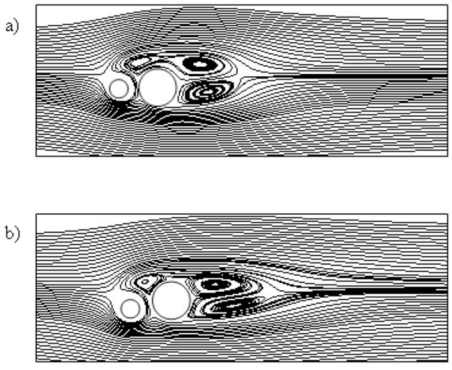

Fig. 5 Mean streamline contours for $d/D=0.5$. (*a*) Tandem arrangement. (*b*) Staggering angle of 10 deg.

u_{rms} shown in Fig. 7 for a typical case also confirm the trend. The value is very low when the rod is subjected to rotation.

3.1.2 Variation of Mean Velocity. The variation of mean velocity in the field shows how the supplied momentum through the rotation of the rod is convected to various regions of the flow field. Figure 8(*a*) shows the variation in mean streamwise velocity along the wake centerline of the main cylinder for the rotating rod of $d/D=0.2$. For the tandem arrangement, a small positive velocity region is observed in front of the main cylinder. This indicates that the direction of flow crosses the centerline. For small staggering angles, negative velocity is observed in the gap region. This is because of the continuous deceleration of flow in the positive y direction. The velocity profile behind the main cylinder is not affected for tandem and small stagger angles. However, for 45 deg and 90 deg, the flow is considerably affected behind the main cylinder. In the side-by-side arrangement, the recirculation region is not observed behind the main cylinder. The velocity profile becomes almost flat without any negative velocity, and the freestream recovery is delayed.

The respective velocity variation for the rotating rod of $d/D=0.5$ is shown in Fig. 8(*b*). For the tandem arrangement and for other lower stagger angles, a negative velocity region is observed in between gaps. Behind the main cylinder, the velocity profile changes considerably for each staggering angle. However, for the

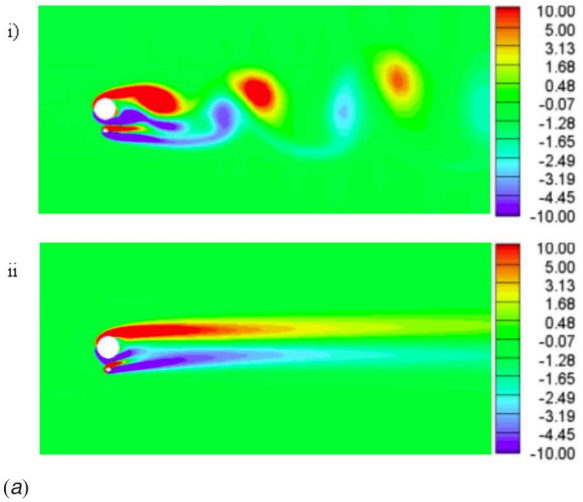

(*a*)

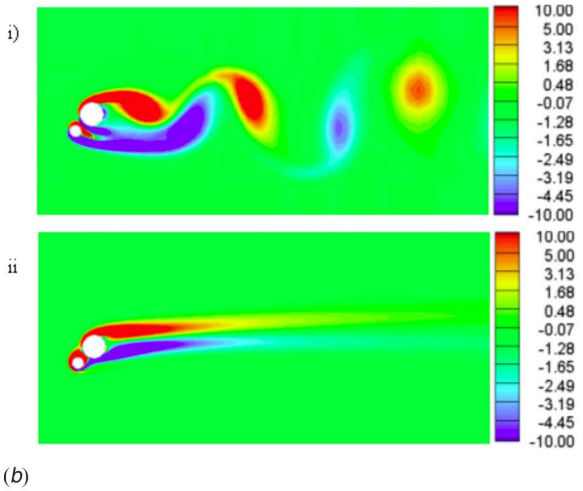

(*b*)

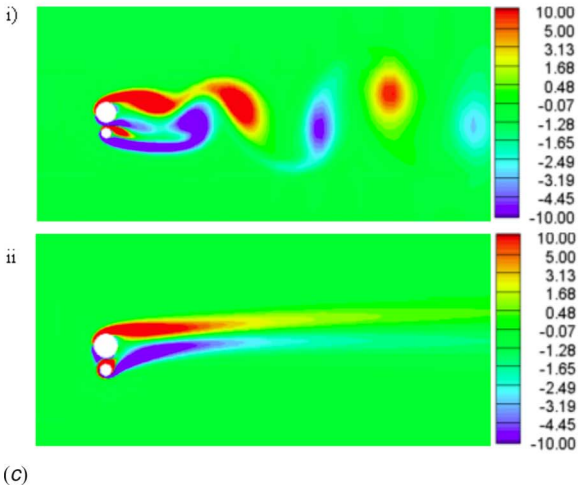

(*c*)

Fig. 6 (*a*) Instantaneous vorticity contour for d/D=0.2 and α =90 deg: (i) ω=0 and (ii) ω=3. (*b*) Instantaneous vorticity contour for d/D=0.5 and α=45 deg: (i) ω=0 and (ii) ω=3. (*c*) Instantaneous vorticity contour for d/D=0.5 and α=90 deg: (i) ω=0 and (ii) ω=3.

rod of diameter ratio 0.2 in tandem as well as low staggering angles, the velocity profile coincides with one another. For the rod of d/D=0.2, the velocity profile along the normal plane at x=0 is shown in Fig. 9(*a*). In this plot, the velocities in the positive y direction (i.e., above the cylinder) coincide with each other for all

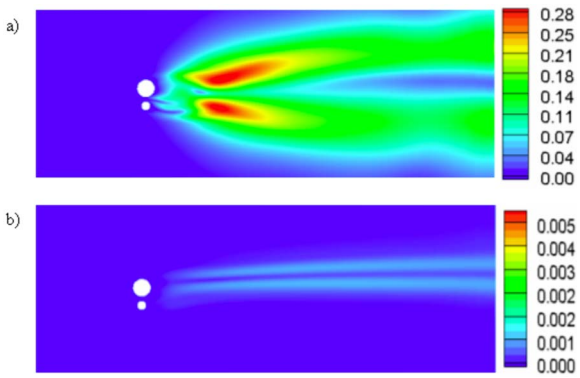

Fig. 7 u_{rms} contour for (*a*) d/D=0.5, α=0 deg, and ω=0 and (*b*) d/D=0.5, α=0 deg, and ω=3

the cases. On the other hand, for the rod of d/D=0.5, which is shown in Fig. 9(*b*), a negative velocity profile is observed for lower staggering angles. This could be again due to the formation of the recirculation region in front of the main cylinder.

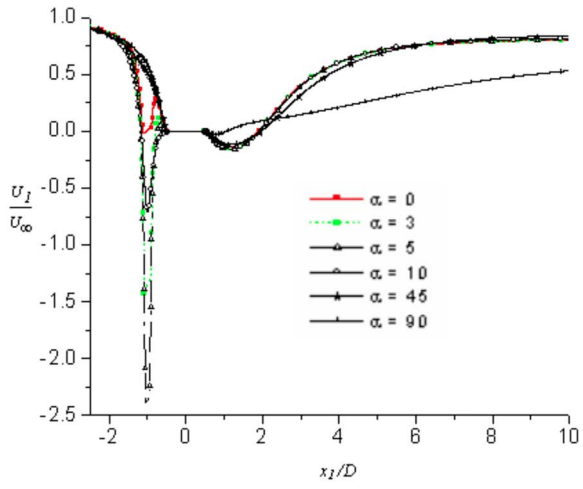

(*a*)

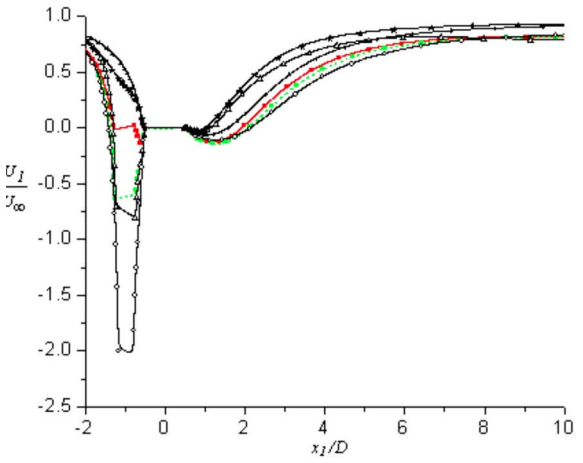

(*b*)

Fig. 8 Mean streamwise velocity along the wake centerline for (*a*) d/D=0.2 and (*b*) d/D=0.5. Legends are the same in both plots.

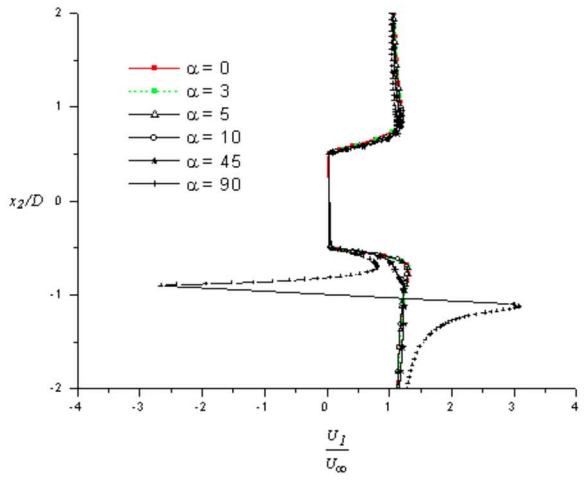

(*a*)

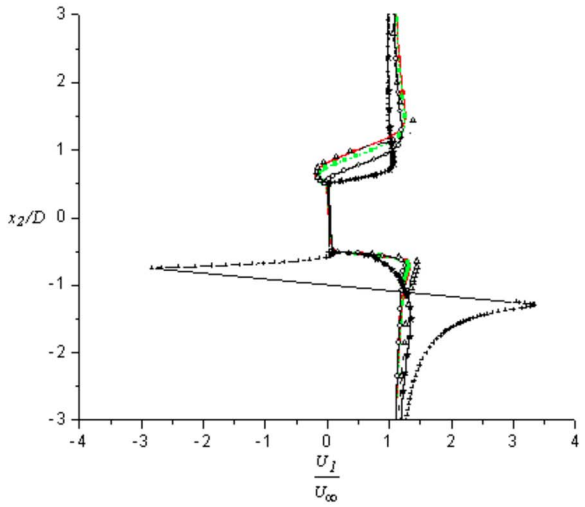

(*b*)

Fig. 9 (*a*) Variation of mean streamwise velocity along a normal line at $x_1/D=0$ for Re=100 and $d/D=0.2$. (*b*) Variation of mean streamwise velocity along a normal line at $x_1/D=0$ for Re=100 and $d/D=0.5$. Legends are the same in both plots.

3.2 Simulation Results at Re=500. To investigate the effect of Reynolds number, the present study is extended to Re=500. Though the flow becomes turbulent at this Re, from available literature there is no clear information about what is the good or right turbulence model even for flow past an isolated circular cylinder as they all show some kind of discrepancy in predictions. Large eddy simulation (LES) or direct numerical simulation (DNS) techniques are computationally expensive methods for the present study. Hence, we perform simulations for this case also with the laminar flow model as this assumption may not have any serious influence on aerodynamic quantities and mean velocities, and, hence, on the conclusions with respect to the objective of the present study.

However, for reasons mentioned in Sec. 2.2, three-dimensional simulations are carried out. A mesh independent study is carried out for this case as well. The grid size in the streamwise and cross-streamwise directions are kept the same as the one used for Re=100 case. In the spanwise direction, the domain is chosen as $3D$ (Ayyappan [24]) and the number of mesh points is varied as 20, 26, and 32, respectively, for three grids, namely, Grids D, E, and F. Drag coefficients computed by these grids for the case of flow past an isolated cylinder are compared in Table 3. From the table, we observe that there is a 10% variation between Grids D and E and a 3% variation between Grids E and F. Hence, further calculations are run with Grid F. The contours of streamwise vorticity are presented in Fig. 10 for two representative cases. They show the presence of a vortical structure in the spanwise direction, which indicates the need for carrying out three-dimensional calculations. For this Reynolds number also, a control rod with two different diameter ratios is considered. The results are also compared with those for Re=100.

Table 3 Comparison of bulk parameters for Re=500

Re=500	Mesh size ($x\times y\times\theta\times z$)	$C_{d\ \mathrm{mean}}$
Grid D	$110\times71\times100\times20$	1.217
Grid E	$110\times71\times100\times26$	1.114
Grid F	$110\times71\times100\times32$	1.085
Wen et al. [25]		1.143

3.2.1 Aerodynamic Coefficients

3.2.1.1 Variation of $C_{d\ \mathrm{mean}}$. The variation of the mean drag coefficient of the main cylinder with respect to the angular position of the rotating rod is given in Fig. 11(*a*). With the rod of $d/D=0.2$, the drag value slightly increases for lower stagger angles and decreases for higher stagger angles. The opposite behavior of drag coefficient is found to occur with the rod of $d/D=0.5$. A minimum mean drag value is observed at a 10 deg stagger angle with the rod of diameter ratio of 0.5. It is observed that for both Re=100 and 500, the trend is the same for both diameter ratios. Once again, the mean drag of the rod for both diameter ratios is also given in Fig. 11(*d*). For both ratios, it shows a decreasing trend with increasing stagger angle up to 45 deg and then a marginal rise.

3.2.1.2 Variation of $C_{l\ \mathrm{mean}}$. Figure 11(*b*) shows the variation of the mean lift coefficient of the main cylinder by the influence of the staggering angle. This value constantly decreases for the main cylinder when the rod of $d/D=0.2$ is placed at various staggering angles. For the rod of $d/D=0.5$, the $C_{l\ \mathrm{mean}}$ value slightly increases at lower staggering angles. This value decreases with further increase in staggering angle and reaches a minimum value for the side-by-side arrangement, which is also observed for the Reynolds number of 100.

3.2.1.3 Variation of $C_{l\ \mathrm{rms}}$. The variation of $C_{l\ \mathrm{rms}}$ of the main cylinder with respect to the positioning of the rotating rod is shown in Fig. 11(*c*). For the rod of $d/D=0.2$, this value slightly increases first and then decreases. Again, this value increases in the side-by-side arrangement, whereas this value for the rod of $d/D=0.5$ slightly oscillates for lower stagger angles and then constantly decreases as the stagger angle increases. A minimum $C_{l\ \mathrm{rms}}$ of magnitude 0.05 is observed in the side-by-side arrangement. The suppression of vortex shedding observed for the Re=100 case is not observed here.

3.2.2 Variation of Velocity. The variation of the mean streamwise velocity component along the normal plane at $x=0$ for $d/D=0.5$ is shown in Fig. 12(*a*). At $x=0$, a maximum negative velocity in the region closer to the positive y direction is observed for the tandem arrangement. As the angle of stagger increases, the negative velocity region in the positive y direction changes to a positive magnitude. A small wake is observed behind the main cylinder for the 45 deg stagger angle. For the side-by-side arrangement, a steep velocity gradient is observed near the rotating rod. The same velocity component at $x/D=1$ is shown in Fig. 12(*b*). The reduction in width of the wake is observed as the stagger angle increases. The velocity gradient behind the rod disappears, and the wakes from the cylinder and the rod merge.

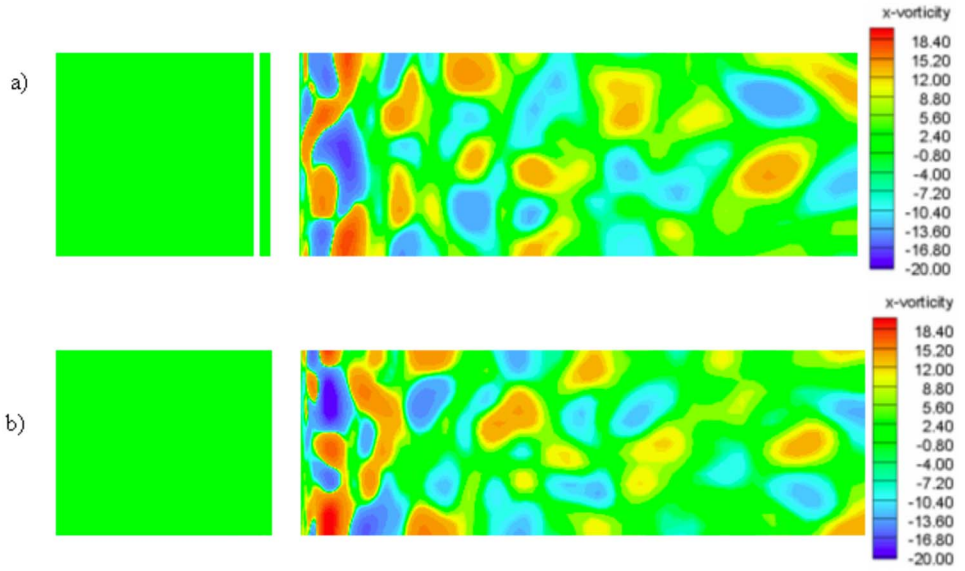

Fig. 10 Contours of streamwise vorticity for the case of d/D=0.2 and ω=3. (*a*) α=0 deg; (*b*) α=90 deg.

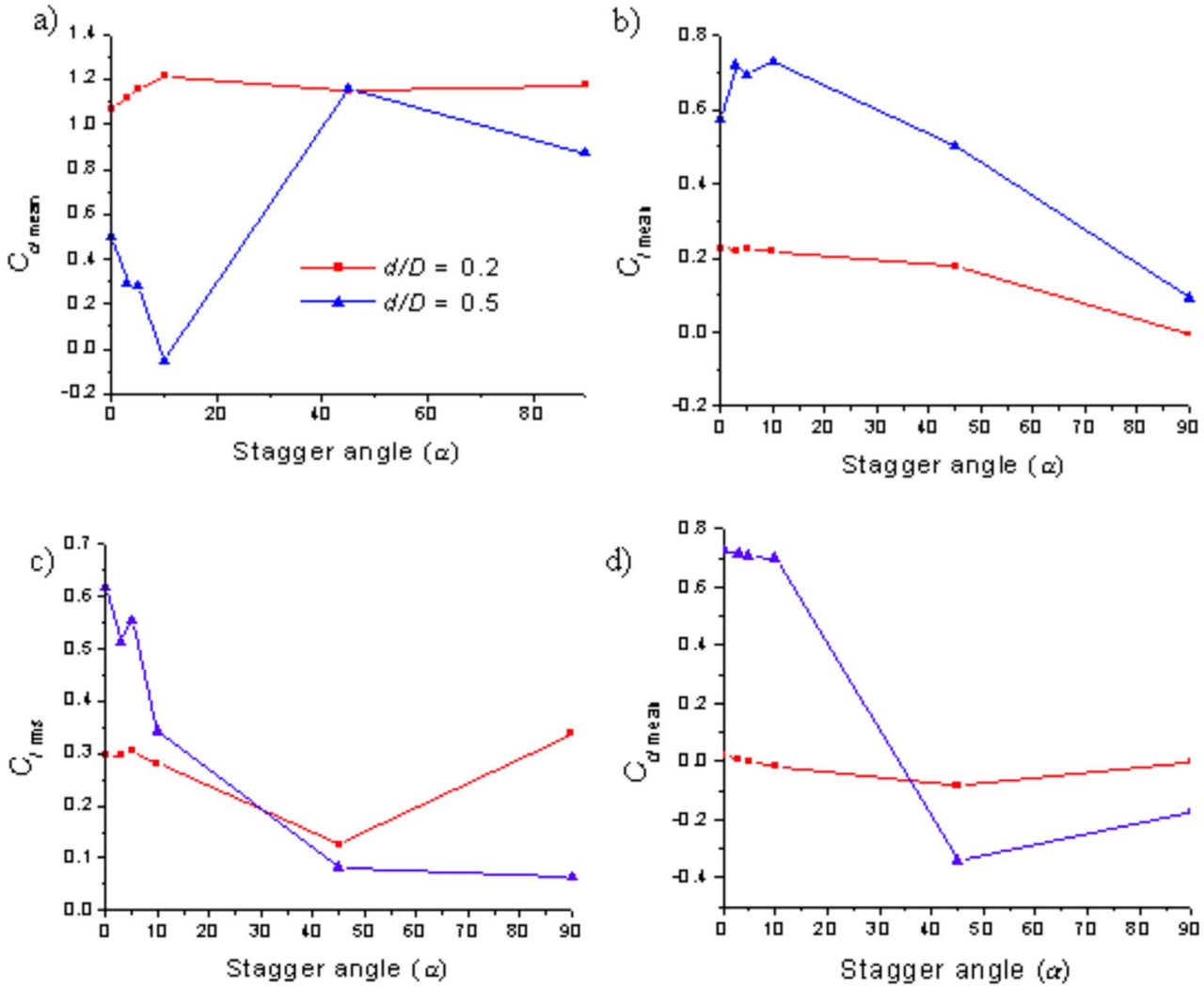

Fig. 11 Variation of aerodynamic coefficients. (*a*) Mean drag coefficient of the main cylinder. (*b*) Mean lift coefficient of the main cylinder. (*c*) rms lift coefficient of the main cylinder. (*d*) Mean drag coefficient of the rod. Legends are the same in all plots.

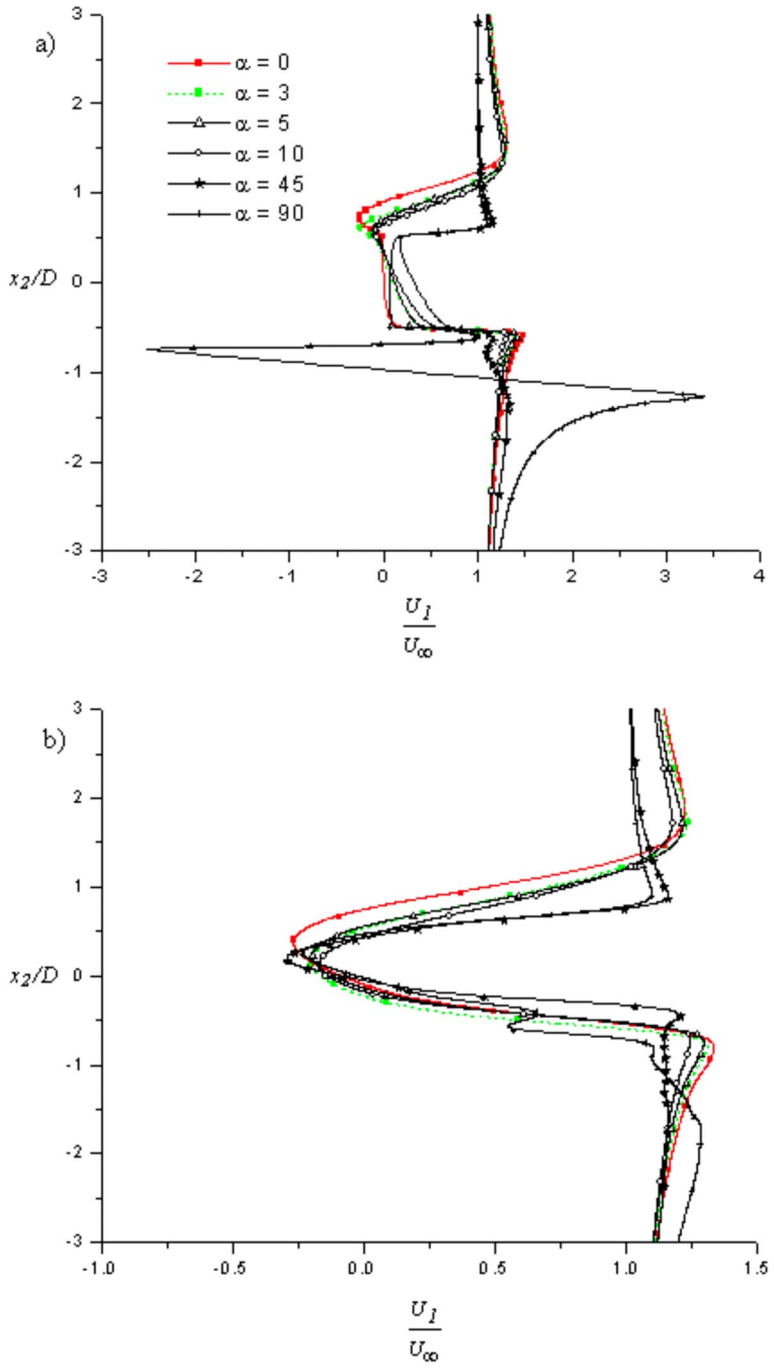

Fig. 12 Variation of mean streamwise velocity along a normal line for $d/D=0.5$ and Re=500. (*a*) $x/D=0$; (*b*) $x/D=1$. Legends are the same in both plots.

3.3 Maximum Drag Reduction. In previous sections, the variation of aerodynamic coefficients of the main cylinder and velocity profile in the flow field with respect to the positioning of the rotating rod is discussed. The variation of the mean drag of the control rod is also observed independently. However, the drag acting on the rod contributes a small increase when considered as a system along with the main cylinder. Hence, the mean system drag ($C_{d\ \mathrm{sys}}$) is calculated by using the formula $C_{d\ \mathrm{sys}}=C_{d\ \mathrm{main}}+d/D\mathrm{x}(C_{d\ \mathrm{rod}})$, as reported by Luo and Gan [4]. This formula is a simple arithmetic addition of mean drag for the main cylinder and the rod nondimensionalized by the main cylinder diameter (D), and the variation for all the cases considered is shown in Fig. 13(*a*). The optimum configuration in comparison with drag in the corresponding stationary case is listed in Table 4. As can be observed, at Re=100 for the $d/D=0.2$ case, a minimum system drag observed is at the stagger angle of 3 deg, whereas this position is 10 deg for the $d/D=0.5$ rod. However, based on the magnitude of drag, maximum reduction is observed with the rod of $d/D=0.5$. The minimum system drag obtained for this Reynolds number is 0.598, corresponding to the case $d/D=0.5$ and $\alpha=10$ deg. The $C_{d\ \mathrm{sys}}$ obtained for the Reynolds number Re=500 is 0.647, corresponding to the case $d/D=0.5$ and $\alpha=10$ deg. The same arrange-

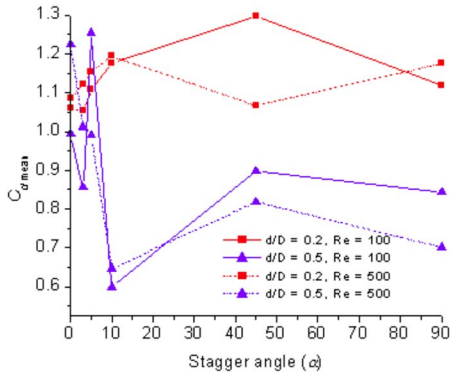

(*a*)

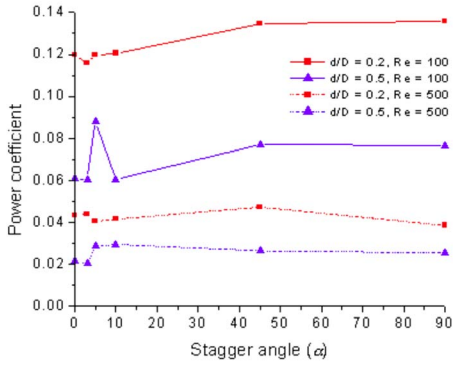

(*b*)

Fig. 13 Variation of system drag for both diameter ratios and Reynolds numbers

ment and speed ratio are found to give a minimum drag for both Reynolds numbers considered in the present study.

3.4 Power Coefficient. The total power required (P_{tot}) for any particular configuration is the summation of translational (P_{trans}) and rotational power (P_{rot}). P_{trans} is the drag coefficient of the system and P_{rot} is the power coefficient of the rotating rod. Power coefficient (P_{rot}) is calculated from the nondimensionalized wall shear stress acting on the rod (σ_W), speed ratio (ω), and diameter ratio (d/D) as $P_{tot}=\sigma_w\omega(d/D)$. The power coefficient required to rotate the rod is given in Fig. 13(*b*). The magnitude of power coefficient for a particular configuration is the same for all the stagger angles. In the near tandem arrangement, the magnitude slightly fluctuates. This is because of the presence of the main cylinder. For the rod of $d/D=0.2$ at Re=100, the power coefficient calculated lies closer to 0.12. This value reduces to 0.06 for the rod of $d/D=0.5$ for the same Reynolds number. This reduction in power required to rotate the rod with the increase in d/D is observed for Re=500 also. The total power coefficient of the minimum drag coefficient configuration is 0.718 for Re=100 and 0.697 for Re=500. This value is less when compared to the system drag (Table 4) for the corresponding case of the stationary rod.

Table 4 Optimum configuration for drag reduction

Re	d/D	α (deg)	$C_{d\,sys}$	For stationary rod
100	0.2	3	1.053	1.105
	0.5	10	0.598	1.014
500	0.2	45	1.066	1.127
	0.5	10	0.647	0.869

4 Conclusions

The influence of the rotating rod on flow past a main circular cylinder is investigated numerically. The effect of the staggering position of the rod on aerodynamic coefficients is analyzed. A common phenomenon of increase in the velocity behind the rotating rod is observed, and the reason is attributed to the momentum transfer. With the rod of diameter ratio of 0.2, vortex suppression behind the main cylinder is observed for Re=100 in the side-by-side arrangement. This vortex suppression phenomenon is observed for 45 deg stagger angle and in the side-by-side arrangement with the rod of diameter ratio of 0.5. The optimum position for a maximum drag reduction is calculated by considering system drag. The staggering position is found to be at 10 deg from the stagnation point of the isolated cylinder. The same position of the staggering angle and speed ratio is obtained for both the Reynolds numbers considered in this study. It is observed that the total power required for the minimum system drag configuration is less than that for the stationary rod case.

Nomenclature

D = diameter of the main cylinder
f = frequency of vortex shedding
d = diameter of the upstream rod
L = pitch length
L_{cr} = critical pitch length
ω = speed ratio ($\phi D/2U_\infty$)
ϕ = angular velocity
α = stagger angle
U = freestream velocity
St = Strouhal number
x_i = spatial coordinate
p = pressure
ν = kinematic viscosity
Re = Reynolds number ($U_\infty D/\nu$)
C_d = coefficient of drag

Subscripts

rms = root mean square
main = main cylinder
sys = system
rod = upstream rod
trans = translational
rot = rotational

References

[1] Blevins, R. D., 1977, *Flow Induced Vibrations*, Van Nostrand Reinhold, New York.
[2] Zdravkovich, M. M., 1997, *Flow Around Circular Cylinders*, Oxford University Press, New York.
[3] Barnes, F. H., Baxendale, A. J., and Grant, I., 1985, "The Flow Past Two Cylinders Having Different Diameters," Aeronaut. J., **89**, pp. 125–134.
[4] Luo, S. C., and Gan, T. L., 1992, "Flow Past Two Tandem Circular Cylinders of Unequal Diameter," Aeronaut. J., **96**, pp. 105–114.
[5] Lee, S. J., Lee, S. I., and Park, C. W., 2004, "Reducing the Drag on a Circular Cylinder by Upstream Installation of a Small Control Rod," Fluid Dyn. Res., **34**, pp. 233–250.
[6] Zhao, M., Cheng, L., Teng, B., and Liang, D., 2005, "Numerical Simulation of Viscous Flow Past Two Circular Cylinders of Different Diameters," Appl. Ocean. Res., **27**, pp. 39—55.
[7] Zhao, M., Cheng, L., Teng, B., and Dong, G., 2007, "Hydrodynamic Forces on Dual Cylinders of Different Diameters in Steady Currents," J. Fluids Struct., **23**, pp. 59–83.
[8] Wang, J. J., Zhang, P. F., Lu, S. F., and Wu, K., 2006, "Drag Reduction of a Circular Cylinder Using an Upstream Rod," Flow, Turbul. Combust., **76**, pp. 83–101.
[9] Ingham, D. B., and Tang, T., 1990, "A Numerical Investigation Into the Steady Flow Past a Rotating Circular Cylinder at Low and Intermediate Reynolds Numbers," J. Comput. Phys., **87**, pp. 91–107.
[10] Takada, N., and Tsutahara, M., 1998, "Evaluation of Viscous Flow Around a

Suddenly Rotating Circular Cylinder in the Lattice Boltzmann Method," Comput. Fluids, **27**, pp. 807–828.
[11] Kang, S., Choi, H., and Lee, S., 1999, "Laminar Flow Past a Rotating Circular Cylinder," Phys. Fluids, **11**(11), pp. 3312–3321.
[12] Engelman, S. M., and Jamnia, M. A., 1990, "Transient Flow Past a Circular Cylinder: A Bench Mark Solution," Int. J. Numer. Methods Fluids, **11**, pp. 985–1000.
[13] Behr, M., Liou, J., Shih, R., and Tezduyar, T. E., 1991, "Vorticity-Stream Function Formulation of Unsteady Incompressible Flow Past a Cylinder: Sensitivity of the Computed Flow Field to the Location of the Outflow Boundary," Int. J. Numer. Methods Fluids, **12**, pp. 323–342.
[14] Mittal, S., Kumar, V., and Raghuvanshi, A., 1997, "Unsteady Incompressible Flows Past Two Cylinders in Tandem and Staggered Arrangements," Int. J. Numer. Methods Fluids, **25**, pp. 1315–1344.
[15] Burbeau, A., and Sagaut, P., 2002, "Simulation of a Viscous Compressible Flow Past a Circular Cylinder With High-Order Discontinuous Galerkin Methods," Comput. Fluids, **31**, pp. 867–889.
[16] Jester, W., and Kallinderis, Y., 2003, "Numerical Study of Incompressible Flow About Fixed Cylinder Pairs," J. Fluids Struct., **17**, pp. 561–577.
[17] Prasad, A., and Williamson, C. H. K., 1997, "The Instability of the Shear Layer Separating From a Bluff Body," J. Fluid Mech., **333**, pp. 375–402.
[18] Barkley, D., and Henderson, D. R., 1996, "Three-Dimensional Floquet Stability Analysis of the Wake of a Circular Cylinder," J. Fluid Mech., **322**, pp. 215–241.
[19] Meneghini, J. R., Saltara, F., Siqueria, C. L. R., and Ferrari, J. A., 2001, "Numerical Simulation of Flow Interference Between Two Circular Cylinders in Tandem and Side-By-Side Arrangements," J. Fluids Struct., **17**, pp. 561–577.
[20] Huhe, A., Tatsuno, M., and Taneda., S., 1985, "Visual Studies on Wake Structure Behind Two Cylinders in Tandem Arrangement," Rep. Res. Inst. Appl. Mech. (Kyushu Univ.), **32**(99), pp. 1–20 (data taken from Sharman et al., Ref. 21).
[21] Sharman, B., Lien, F. S., Davidson, L., and Norberg, C., 2005, "Numerical Predictions of Low Reynolds Number Flows Over Two Tandem Circular Cylinders," Int. J. Numer. Methods Fluids, **47**(5), pp. 427–447.
[22] Li, J., Chambarel, A., Donneaud, M., and Martin, R., 1991, "Numerical Study of Laminar Flow Past One and Two Cylinders," Comput. Fluids, **19**, pp. 155–170.
[23] Tsutsui, T., and Igarashi, T., 2002, "Drag Reduction of a Circular Cylinder in an Air Stream," J. Wind. Eng. Ind. Aerodyn., **90**, pp. 527–541.
[24] Ayyappan, T., 2007, "Influence of Staggering Angle and Speed Ratio of Upstream Rotating Rod on Flow Past a Circular Cylinder," MS thesis, IIT Madras.
[25] Wen, C. Y., Yeh, C. L., Wang, M. J., and Lin, C. Y., 2004, "On the Drag of Two Dimensional Flow About a Circular Cylinder," Phys. Fluids, **16**(10), pp. 3828–3831.

Numerical and Experimental Studies of Oscillatory Airflows Induced by Rotation of a Grass-Cutting Blade

F. Abbasian
Doctoral student
e-mail: fabbasia@ryerson.ca

J. Cao
Associate Professor
e-mail: jcao@ryerson.ca

S. D. Yu
Associate Professor
Mem. ASME
e-mail: syu@ryerson.ca

Department of Mechanical and Industrial Engineering,
Ryerson University,
350 Victoria Street,
Toronto, ON, M5B 2K3, Canada

Three-dimensional oscillatory airflows induced by a rotating grass-cutting blade in a cylindrical chamber are studied experimentally and numerically in this paper. Experimental pressure results are obtained using a sound pressure transducer and a data acquisition system. The measured pressure data contain background noise and high-frequency sound signals due to the blade vibrations. The background noise is separately measured; its effect on the signal is determined from a spectral subtraction algorithm. A time-accurate finite volume numerical solution to the three-dimensional incompressible unsteady Navier–Stokes equations is also sought using the sliding frame technique and the unstructured tetrahedral mesh. Convergence studies are conducted using various combinations of mesh sizes and time increments to ensure the stability of the numerical scheme. The experimental and numerical pressure results are in good agreement.
[DOI: 10.1115/1.2842225]

Keywords: computational fluid dynamics (CFD), cutting blade, oscillatory airflow, sliding frame, air pressure, rotation

1 Introduction

In the lawn care industry, cutting blades are designed to cut grass, draw air into the cutting chamber, and propel the air and grass-clipping mixture into a collector. Oscillating airflows generated by one or more rotating blades inside a cutting chamber can be a source of noise and vibrations. Because of the high demand of sufficient airflow rate for propelling a grass-clipping mixture through the chamber, significant turbulence may occur in regions trailing the blade tips, which increases the power consumption and affects the quality of cut. In designing cutting blades for multiple functions, it is important to study the aerodynamics inside the cutting chamber.

In this paper, the airflow in a cutting-discharge lawn care system is investigated experimentally and numerically for a physical setup shown in Fig. 1. The system consists of a rotating blade driven by a 10 hp ac motor, a cutting chamber, and a side discharge tunnel. The airflows examined in this study is generated by the rotating blade in an off-load laboratory condition. A sound pressure transducer is used to measure the oscillatory air pressure at various locations. Kaupert and Staubli [1] reported a successful application of piezoelectric transducers in measuring the unsteady pressure.

To compute the oscillatory flows generated by blade rotation, a time-accurate scheme with continuous mesh movement must be adopted. In dealing with the moving mesh problem, the whole computational domain is divided into rotary and stationary subdomains; the two subdomains are separated by an interface mesh. Among various moving mesh approaches, the sliding mesh technique is widely used in various applications [2–6] and is employed in this paper for studying the oscillatory airflows generated by the grass-cutting blade rotations. When solving the time-dependent Navier–Stokes (NS) equations, the time derivative terms are discretized using an implicit scheme. An upwind second-order space discretization scheme is adopted in conjunction with the flux difference splitting method to calculate the pressure fluctuations using the vertex-average method.

If the interactions between the two subdomains are negligible, a steady-state solution can be sought with sufficient accuracy. In a steady flow analysis, the circumferentially averaging method [7] and the frozen-rotor method [8] have been used in the literature. Although the capability of the two approaches has been improved over the past decade [9,10], they still lack the sufficient accuracy, especially when the interactions between the rotary and stationary parts are significant. To capture the instantaneous interactions, the unsteady NS equations must be solved. When dealing with rotating-blade problems, the predictability of the blade movement is a priori, which allows the NS equations to be solved in frames with prescribed rotating coordinates. This provides a reference frame for the rotary and stationary subdomains, eliminates the need for remeshing, and enhances the solution accuracy and convergence. Chen et al. [11] and Chen and Barter [12] compared the fixed and rotating coordinate approaches in a turbomachinery application and revealed that the data communication between the two subdomains via the interface is of critical importance.

The experimental and numerical results obtained in this paper for oscillatory air pressures at various locations are in good agreement. The experimental data and the validated computer models have been utilized by a lawn care equipment manufacturer for designing its cutting blades.

2 Experimental Procedure

The entire experimental setup is illustrated in Fig. 2. To measure the oscillatory air pressure, a Bruel & Kjaer 4188 microphone is installed near the blade tip with the support of a tripod. The orientation of the microphone was carefully chosen so that the flow was kept parallel to the microphone. The pressure signal was recorded using a data acquisition system and processed using a personal computer. The experimental setup is calibrated using a standard sound generator. The air pressure can be found with re-

Contributed by the Fluids Engineering Division of ASME for publication in the JOURNAL OF FLUIDS ENGINEERING. Manuscript received February 3, 2007; final manuscript received July 4, 2007; published online March 3, 2008. Assoc. Editor: Chunill Hah.

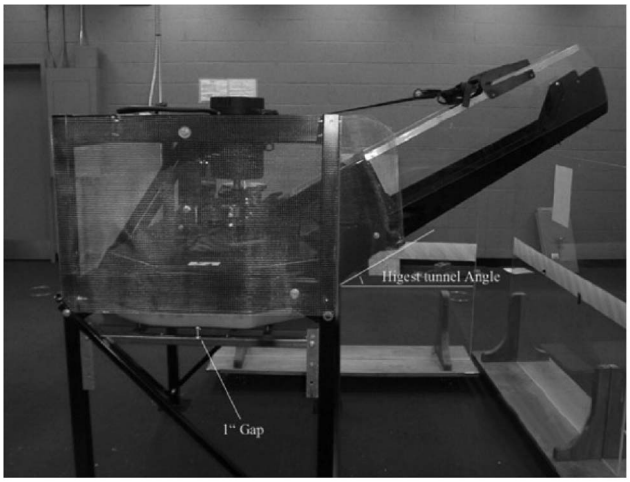

Fig. 1 The experimental setup for studying aerodynamics of a lawn care system

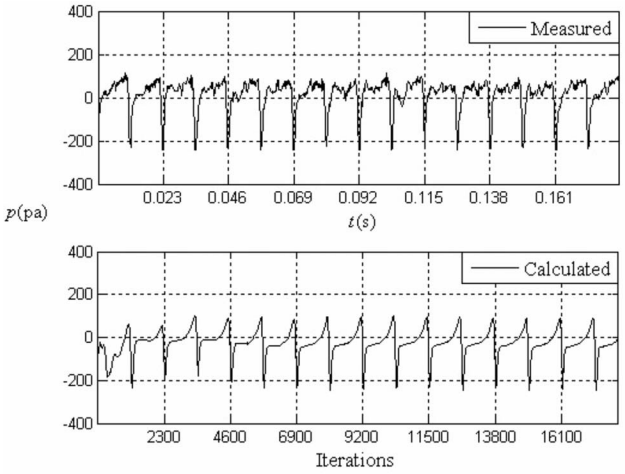

Fig. 3 Measured and calculated pressures versus elapsed time and iterations

spect to the sound level using $\mathrm{SPL}=20\log_{10}(p/p_r)$, where SPL is the sound pressure level in decibel, p is the pressure in pascal, and $p_r=20$ μPa is the reference pressure.

The uncertainty of the microphone with 95% confidence level is 0.35% according to the manufacturer. After 15 repetitions, the uncertainty was found to be 2.2%. Using the Lindeberg central theorem [13–15], the overall uncertainty is 2.23%.

When setting up the experimental apparatus, a tiny vertical gap was kept between the blade tip and the location where the pressure transducer was placed. The experimental data were taken at a location 4 cm underneath the blade tip where the pressure transducer was installed, as shown by a cross in Fig. 2. The pressure data obtained from the experiments are shown in Fig. 3. A review of the pressure data indicates that the measured signal contains some high-frequency components and noise. The high-frequency pressure components of relatively small magnitudes, picked up by the microphone, are largely structure borne. A study of the structure-borne sound pressure is outside the scope of this paper. The effect of background noise on the signal can be studied by the spectral subtraction method [16]. The background noise was recorded while the system was not in operation. It is evident from Fig. 4 that the amplitude of the background noise is very small compared to the overall pressure signal. In this paper, the following subtraction method is applied to the noisy signal:

$$S(\omega)=X(\omega)-N(\omega)=\left(1-\frac{N(\omega)}{X(\omega)}\right)X(\omega)=H(\omega)X(\omega) \qquad (1)$$

where $S(\omega)$, $X(\omega)$, and $N(\omega)$ are the noise-free signal, noisy signal, and background noise. Equation (1) is used to derive $H(\omega)$, which is the subtraction filter, and is applied to the noisy signal in order to derive the noise-free signal. The power spectral density (PSD) of the background noise in Fig. 5 shows that the main spike occurs at 300 Hz, which is believed to be caused by a cooling fan in a power supply located in the laboratory. The dominant frequency of the signal, as expected, is twice the blade passing frequency or $2\omega_0$, where ω_0 is the blade passing frequency. All peaks and troughs of the pressure signal occur when a tip of the blade meets the designated spot. Since the blade has two tips, the dominant frequency is twice the blade passing frequency.

After the noise-free signal is obtained, the signal to noise ratio (SNR) is calculated for different sampling rates. The SNR is defined using $\mathrm{SNR}=20\log(A_{\mathrm{signal}}/A_{\mathrm{noise}})$, where A_{signal} and A_{noise} are rms values of the signal and noise amplitudes. In the experimental data grouped in Table 1, different time intervals are examined, and the corresponding SNR values are also calculated. The optimal sampling rate for high SNR is 3500, and the correspond-

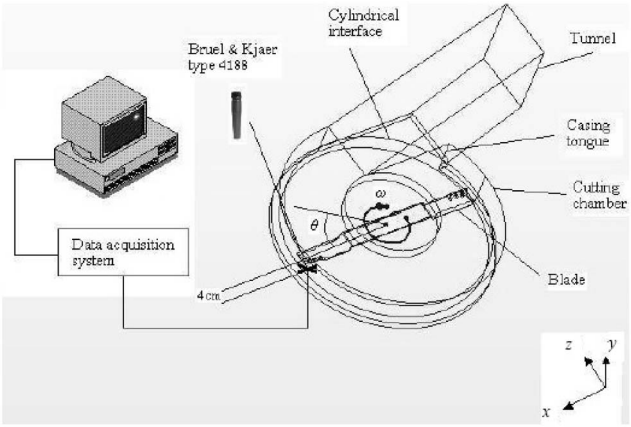

Fig. 2 Illustration of experimental setup and coordinate systems

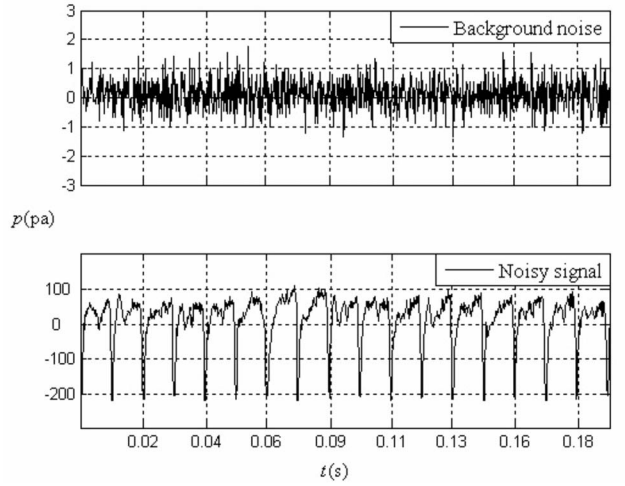

Fig. 4 Comparison between the background noise and the noisy signal

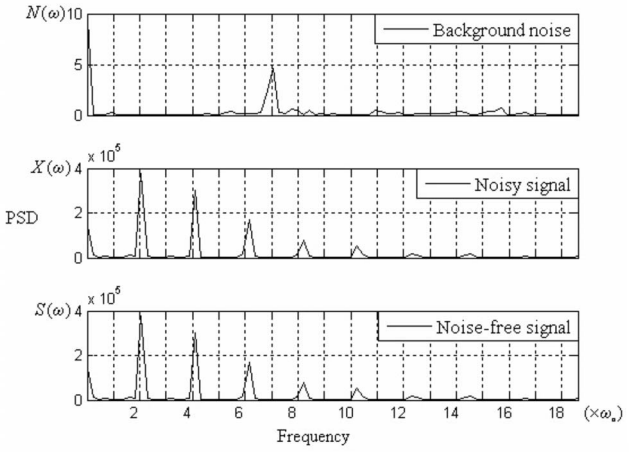

Fig. 5 Fast Fourier transform of the experimental data normalized to the blade passing frequency ω_0

ing time interval is $\Delta t = 0.000\,28$ s. This value will be used for further comparison and validation of the calculated results.

3 Computational Model and Simulation Results

The computational model, illustrated in Fig. 6, consists of a blade and a cutting chamber. The actual tunnel has been shortened in the computational model to reduce the model size and the CPU time. The air is sucked into the system through a 1 in. (2.54 cm) gap beneath the cutting chamber. The blade with a diameter of 0.71 m is designed to rotate at a speed of 2616 rpm or 43.61 Hz. Under the normal operating conditions, the blade tip has a nominal velocity of 97.3 m/s. The static pressure and total pressure are specified as the inlet and outlet boundary conditions, respectively. Hydraulic diameter and turbulence intensity are prescribed at the boundaries. The grid for the whole domain and the rotating part, used in the computational fluid dynamics (CFD) models, are shown Fig. 6.

In the simulations, the blade is inside a cylinder, the surfaces of which separate rotary and stationary subdomains. The blade and adjacent cells are defined to have a prescribed rotational velocity; the rest of the outer part is stationary.

Because of the complex geometry of the blade (teeth and curvatures in various directions), a three-dimensional analysis is necessary. The numerical simulation is performed using FLUENT, a finite volume CFD code. A cell-centered finite volume method is used to solve the 3D NS equations. The continuity and momentum equations for a three-dimensional flow are

$$\partial_t \rho + \nabla \cdot (\rho \mathbf{v}) = 0 \tag{2}$$

$$\partial_t (\rho \mathbf{v}) + \nabla \cdot (\rho \mathbf{v}\mathbf{v}) = -\nabla p + \nabla \cdot (\boldsymbol{\tau}) \tag{3}$$

where $\mathbf{v}$ is the velocity vector, $\boldsymbol{\tau}$ is the stress tensor, and p is the static pressure. Body forces and all other possible source terms are neglected.

3.1 Governing Equations of Airflow in the Stationary Zone. The nondimensional form of Eqs. (2) and (3) for an incompressible flow may be written as

$$\partial_t \mathbf{Q} + \partial_x \mathbf{E} + \partial_y \mathbf{F} + \partial_z \mathbf{G} = \frac{1}{\mathrm{Re}}[\mathbf{M}]\nabla^2 \cdot \mathbf{Q} \tag{4}$$

where Re is the Reynolds number and

$$\mathbf{Q} = \begin{bmatrix} p^* \\ u^* \\ v^* \\ w^* \end{bmatrix}, \quad \mathbf{E} = \begin{bmatrix} a^2 u^* \\ u^{*2} + p^* \\ v^* u^* \\ w^* u^* \end{bmatrix}, \quad \mathbf{F} = \begin{bmatrix} a^2 v^* \\ u^* v^* \\ v^{*2} + p^* \\ w^* v^* \end{bmatrix},$$

$$\mathbf{G} = \begin{bmatrix} a^2 w^* \\ u^* w^* \\ v^* w^* \\ w^{*2} + p^* \end{bmatrix}, \quad \mathbf{M} = \begin{bmatrix} 0 & 0 & 0 & 0 \\ 0 & 1 & 0 & 0 \\ 0 & 0 & 1 & 0 \\ 0 & 0 & 0 & 1 \end{bmatrix}$$

where a is the pseudocompressibility. Note that in Eq. (4), the superscript * denotes nondimensional quantities defined as follows:

$$u^* = \frac{u}{V_\infty}, \quad v^* = \frac{v}{V_\infty}, \quad w^* = \frac{w}{V_\infty}, \quad t^* = \frac{tV_\infty}{L}, \quad p^* = \frac{p}{\rho V_\infty^2}$$

where L is the length scale and V_∞ is the freestream velocity. Equation (4) is applied to the stationary region of the computational volume. The stress tensor has been simplified as a result of the incompressibility assumption.

3.2 Governing Equations of Airflow in the Moving Zone. In the moving subdomain, Eq. (4) may be written in the following integral form:

$$\partial_t \int\int\int_V \mathbf{Q} \cdot dV + \int\int_A [(\mathbf{E} - U_g) \cdot \mathbf{n}_x + \mathbf{F} \cdot \mathbf{n}_y + (\mathbf{G} - W_g) \cdot \mathbf{n}_z - \mathbf{H}] \cdot dA = 0 \tag{5}$$

where $\mathbf{Q}$ is the variable matrix; $\mathbf{E}$, $\mathbf{F}$, and $\mathbf{G}$ are the inviscid flux vectors; $\mathbf{H}$ is the viscous flux vector; and $\mathbf{U}_g$, and $\mathbf{W}_g$ are grid velocities in the x and z directions associated with the mesh motion, as illustrated in Fig. 2. In the present study, the y component of grid velocity vanishes since the blade is rotating around the y axis.

3.3 Sliding Mesh Technique. When using the sliding frame technique, cells at the interface are not deformed but can slide with respect to their adjacent cells with the grid velocity to maintain the initial shape. The sliding frame strategy requires that the mesh be duplicated along the interface. Thus, two face meshes are generated, one for the stationary subdomain and the other for the rotary subdomain. The sliding frame scheme developed in this paper is illustrated in Fig. 7, where diagram (*a*) shows the radial interface, (*b*) shows the radial and axial interfaces, and (*c*) shows a portion of the radial interface for demonstrating the relative mesh movement at the radial interface of the rotating and fixed frames. In Fig. 7, point *A* belongs to the stationary subdomain and

Table 1 SNR for different sampling rates

Sample length	5000	4500	4000	3500	3000	2500	2000	1500
Sample rate	5000	4500	4000	3500	3000	2500	2000	1500
Time domain (s)	1	1	1	1	1	1	1	1
Time interval (s)	0.0002	0.00022	0.00025	0.00028	0.00033	0.0004	0.0005	0.00067
Frequency (Hz)	5000	4545	4000	3571	3030	2500	2000	1492
SNR (dB)	15.5	15.66	16.41	18	17.74	17.24	16.36	15.72

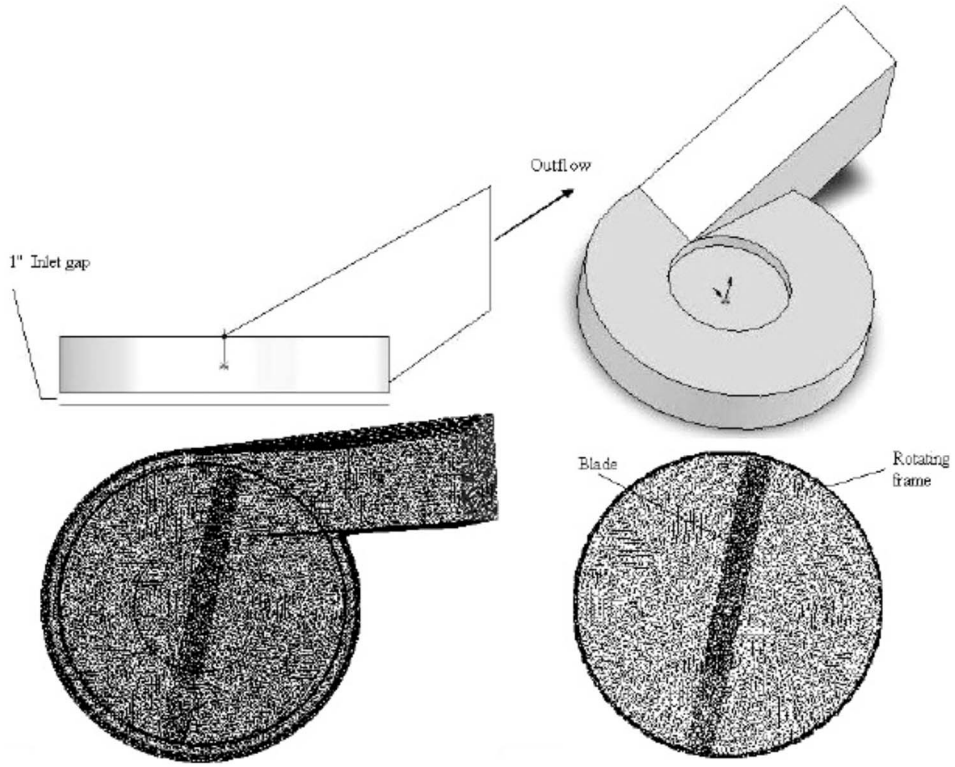

Fig. 6 Computational model (top right), front view of the model (top left), top view of the associated grid (bottom left), and grid of rotating part (bottom right)

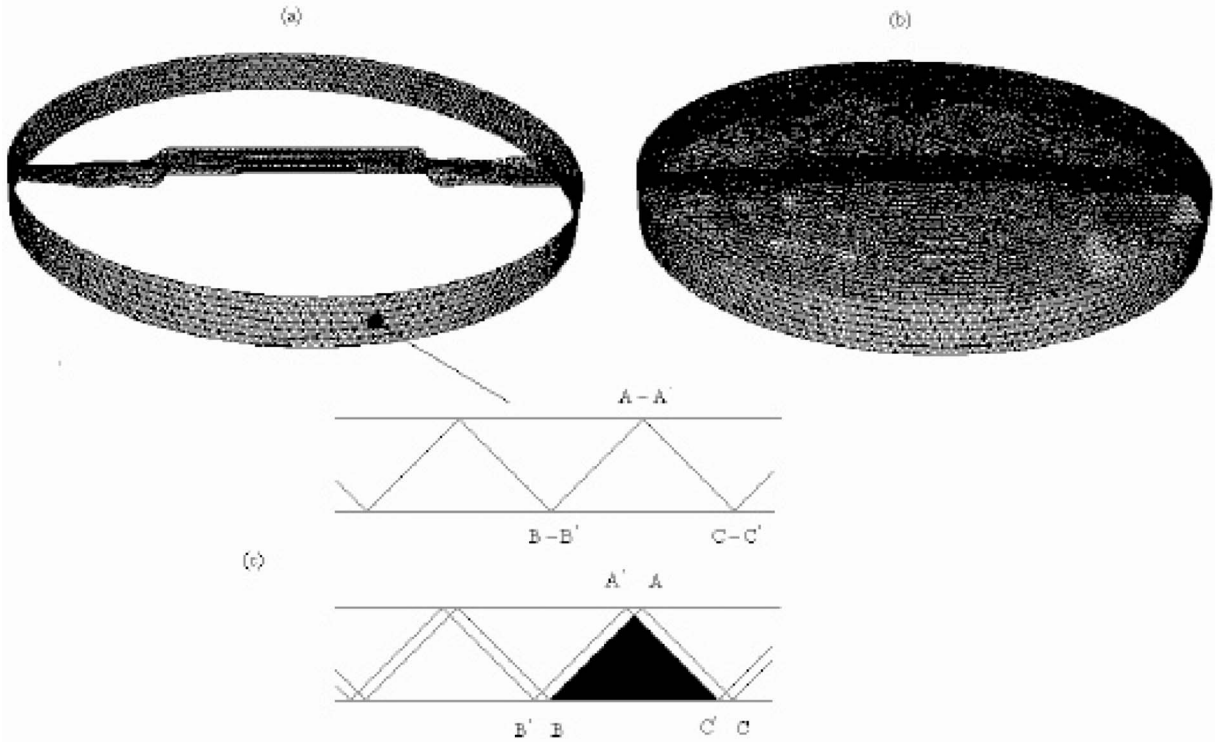

Fig. 7 Illustration of sliding mesh scheme: (*a*) radial interface only, (*b*) both radial and axial interfaces, and (*c*) movement of the radial rotating interface relative to the stationary frame

Table 2 Summary of different meshes used in convergence studies

Meshes	Number of elements	Elapsed time (h)	Time step (s)	Number of time steps per cycle	Number of iterations
I	153,000	35	0.0002	115	16,000
II	302,500	61	0.0002	115	16,000
III	583,000	109	0.0002	115	16,000

point A' belongs to the rotating subdomain. The top of the zoomed part describes the onset of iteration when the points corresponding to the fixed and rotating frames coincide on a pair-by-pair basis over the interface. During the solution process, A', B', and C' belonging to the rotating frame have all slid, while A, B, and C belonging to the stationary subdomain remain fixed. The triangular shape of the mesh itself does not change. However, the overlapped area (shaded) keeps changing during time iteration. This shared face is used for data communication between the two adjacent cells located in the two different subdomains. The overlapped face may become a pentagonal shape depending on the motion direction. This eliminates the need for updating the mesh connectivity during time iterations.

3.4 Discretization. The first-order implicit time discretization scheme is adopted in the computational model. This allows for an unconditionally stable and speedy solution. For the space discretization, a second-order upwind spatial formulation is used. The second-order accuracy is achieved by employing the linear reconstruction method [17]. Roe's flux difference splitting method [18] is employed to propagate information throughout the computational domain.

3.5 Simulation Results. Three computational models in Table 2 were created for three mesh sizes, which contain 153,000, 302,500 and 583,000 tetrahedral cells, respectively. All numerical simulations were performed on an UltraSparc IIe workstation.

The pressures obtained using the three meshes are grouped in Fig. 8. As expected, the finer mesh yielded more accurate numerical solutions compared to the experimental data. However, the computational model for Mesh II provides numerical predictions with good accuracy, stability, and much shorter computing time. Three sets of pressure results are shown in Fig. 9 for the time steps of 0.0002 s, 0.0004 s, and 0.0012 s, respectively. The time step of 0.0002 s is the most promising one. When the time step is doubled, the solution seems to be experiencing a lingering instability. When the time step is increased to 0.0012 s, the solution failed to capture the deep pressure drop caused by the local sucking effect of the blade tip. The time step size is $\Delta t = 0.0002$ s, and 20 iterations were used for each time step. Since the period of blade rotation is 0.023 s, there are 115 time steps in each cycle. A typical run took about 100 h to complete.

The 3D flow patterns are shown in Fig. 10 for two angular positions $\theta = 0$ and $\theta = \pi/2$. The angular position is measured relative to the initial position when blade tips and the microphone line up. In Fig. 11, the detailed flow pattern around the blade in the form of velocity vectors is shown from a top view. The maximum velocity is 98.9 m/s, corresponding to a Mach number of 0.3, which arises only in the localized regions near the tip. Hence, the incompressibility assumption is justified.

4 Comparisons and Discussions

One of the interesting locations is the circumference just underneath the blade tip. At this location, both numerical solutions and experimental measurements were carried out. The pressure value was calculated using the vertex-average method. The principle of the method is to use a weighted average to determine values of field variables. Since a cell-centered method is used, the NS equations are solved for all cells. The numerical solution is obtained on a cell-by-cell basis for each of the variables involved in the NS equations. The values of each variable are calculated at nodes by averaging the variable over all neighboring cells where the weights are the inverses of the distances between the nodes and the cell centroid.

The numerical solution becomes convergent and stable after one to three cycles depending on the mesh quality. For instance, the numerical part of Fig. 3 indicates that only one cycle is taken to reach a stable pressure solution. A time increment $\Delta t = 0.0002$ s and 20 iterations per time step are defined for the simulation. The pressure is plotted against the angular position of the

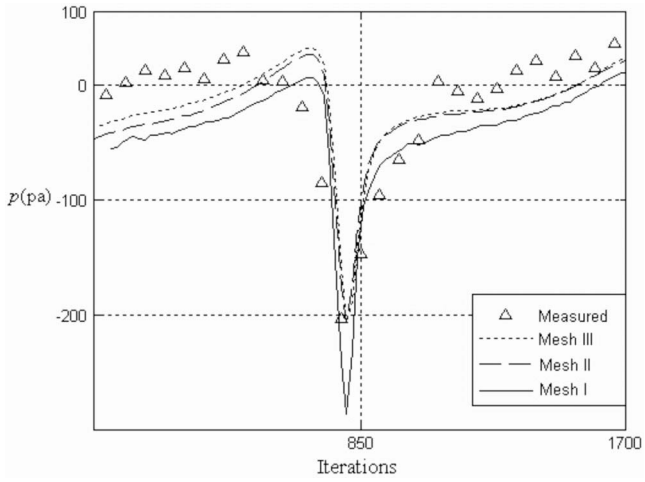

Fig. 8 Pressures near the largest dip obtained using different meshes

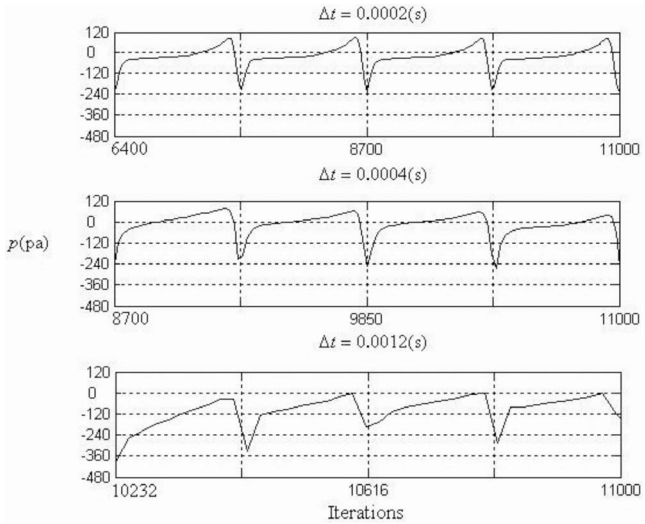

Fig. 9 Pressure obtained using different time increments

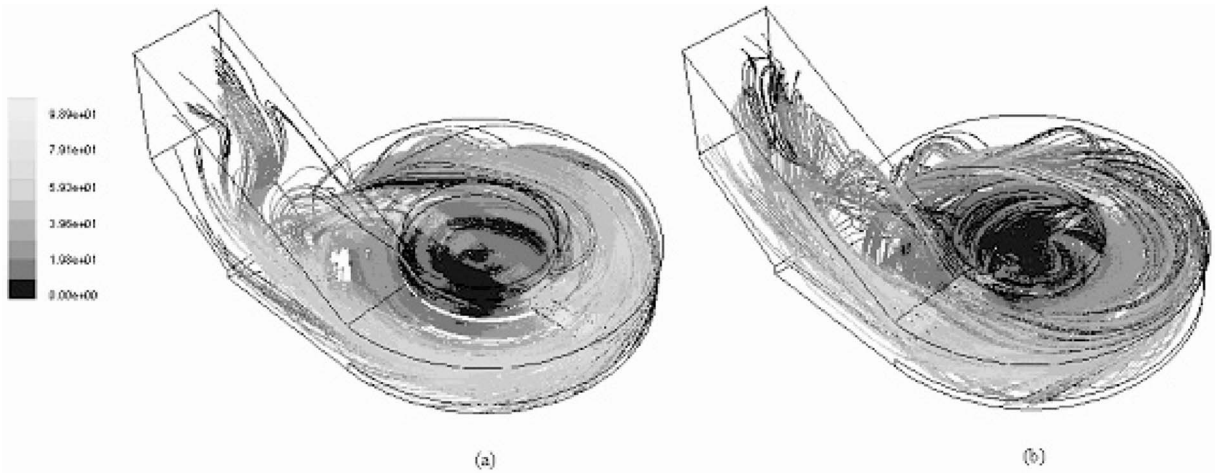

Fig. 10 Velocity path lines (m/s) on the blade surface at different angular positions: (*a*) $\theta=0$ and (*b*) $\theta=\pi/2$

blade with reference to the radial plane containing the point of measurement. Immediately after the tip passes over the spot, the pressure drops as the air is vacuumed in the suction region. According to Figs. 3 and 8, the experimental and numerical results are in good agreement. The structural borne sound and vibrations may have contributed to the presence of high-frequency components in the measured signal between the peaks and may have induced some errors. Though the pressure during a cycle is slightly underpredicted, the pressure pulsation amplitude, which is of the greatest importance, is well predicted by the computer simulation.

Next, the pressure pulsation in regions closer to the blade tips is examined only through numerical simulation since the *in situ* measurements are unfeasible. In Fig. 12, pressure is calculated at three different locations: 2 mm underneath the tip, 2 cm underneath the tip, and 2 cm underneath the tip near the casing tongue, as illustrated in Fig. 2. The pulsation amplitude has significantly increased for the spots closer to the tip compared to the case where the 4 cm gap was used. The maximum dynamic pressure can be determined using $p_d=1/2\rho V^2$, where V is the maximum flow velocity calculated at the outlet passage. The calculated dynamic pressure is 1531 Pa when taking $\rho=1.225$ kg/m^3 and $V=50$ m/s, which are used in our study. As shown in the upper part of Fig. 12, when the gap between the blade tip and the sound pressure transducer is 2 mm, the pressure pulsation amplitude is 3000 Pa, which is twice the maximum dynamic pressure. This indicates that the pressure fluctuation at the blade tip is significant. The lower part of Fig. 12 shows a different signal pattern, revealing a perturbation in the peaks. This is attributable to the tip-casing interaction, which is most pronounced in the casing tongue area and appears in the plot in the form of pressure drop. Wherever $\theta=(2k-1)\pi/2$ (k is an integer) or any of the blade tips meets the casing tongue, a pressure drop is evident as a result of the tongue-blade interaction.

As the blade rotates, the aerodynamic force acting on the blade varies with blade positions in a periodic manner. Values of the x and y components of the aerodynamic force, and the y component of the moment at many blade positions, are computed using the computer model. The results are shown in Fig. 13 for three cycles of blade rotations, where the blade angular position is measured clockwise from the x axis and the y axis is normal to the blade rotational plane. All the force calculations are based on pressure and viscous force integration on the blade surface and have been done in a fixed coordinate in order to capture the periodicity that accords with the frequency of the system. The aerodynamic force components, F_x and F_z, acting on the blade surface in the plane of rotation have a peak value of about 3 N. The tangential compo-

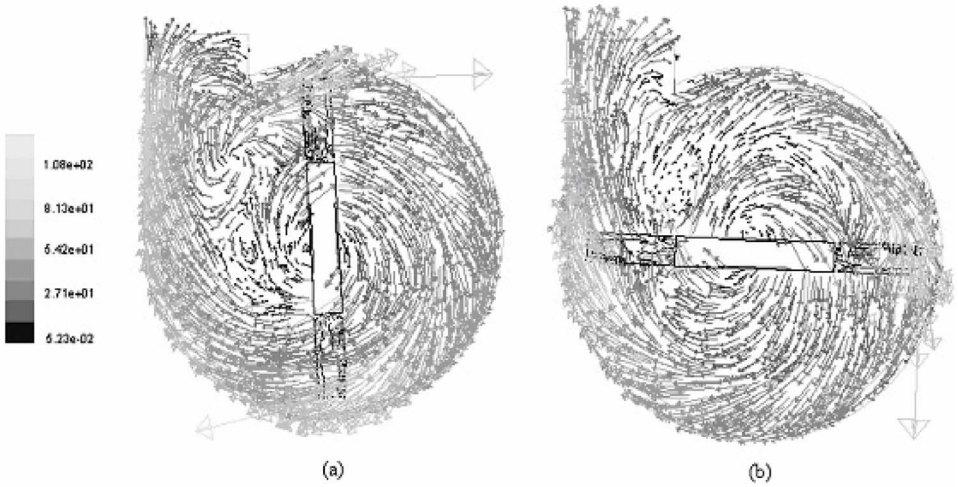

Fig. 11 Velocity vectors (m/s) around the blade from the top view at different angular positions: (*a*) $\theta=0$ and (*b*) $\theta=\pi/2$

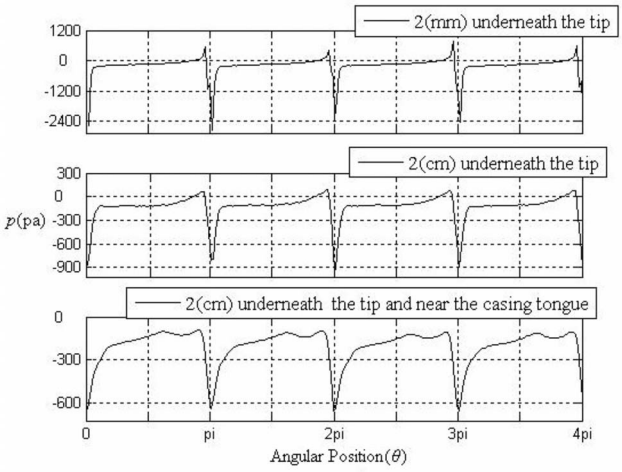

Fig. 12 Calculated pressure with different vertical gaps between the blade tip and the observation spot

nent of the resultant of the two components acts as a drag force and resists the blade rotation. The radial component of the resultant aerodynamic force is the result of radial airflow and is expected to be much smaller than the tangential component. When the blade takes on the positions $\pi/2$, $3\pi/2$, $5\pi/2$, etc., the aerodynamic force component F_x becomes tangent to the blade tip circular path. Therefore, values of F_x at $\theta=(2k-1)\pi/2$, $k=1,2,\ldots$, are the drag forces, which are responsible for power consumption. When the blade takes on the positions 0, π, 2π, etc., the aerodynamic force component F_x becomes collinear with the blade. In these cases, F_x represents the radial component of the aerodynamic force. The negative value (about –0.75 N) indicates that the net radial force component of the aerodynamic force acts toward the chamber exit. A greater lift force F_y of 30 N in magnitude acts downward on the blade from the high pressure region to the low pressure region. The high amplitude of the lift force is an indication of the high rate of pressure fluctuations that is counterbalanced by the relatively large lift force. The asymmetric shape of the casing and position of the tunnel can also cause the fluctuation of the lift force. During operation, the blade rotation plane divides the cutting chamber into two regions. Because of the suction in the lower region, a downward lift force along the y axis is observed. Due to the asymmetry of the cutting chamber, the lift force fluctuates with the periodicity proportional to the blade position. From the diagram, it can be described that the maximum pressure difference between the top and bottom of the cutting chamber occurs at $\theta=k\pi$ $(k=0,1,2,\ldots)$ or when the blade is along the x axis. At $\theta=(2k-1)\pi/2$, $k=1,2,\ldots$, or when the blade tip meets the tunnel, this pressure difference is minimum. The physical meaning of this is that when the tip meets the tunnel, the tunnel acts as a pressure relief valve and weakens the suction from the bottom of the cutting chamber. As a result, pressure difference and F_y are minimum. A higher amplitude of F_y compared with other forces means that the pressure effect is much greater than the viscosity effect. Finally, the moment on the blade as shown in Fig. 13 is almost constant and always positive, which suggests a nearly constant consumption of power throughout a cycle. The source of the moment about the y axis is the forces in the rotation plane (i.e., F_x or F_z). The power consumption is an important design criterion in evaluating blade design in the lawn care industry.

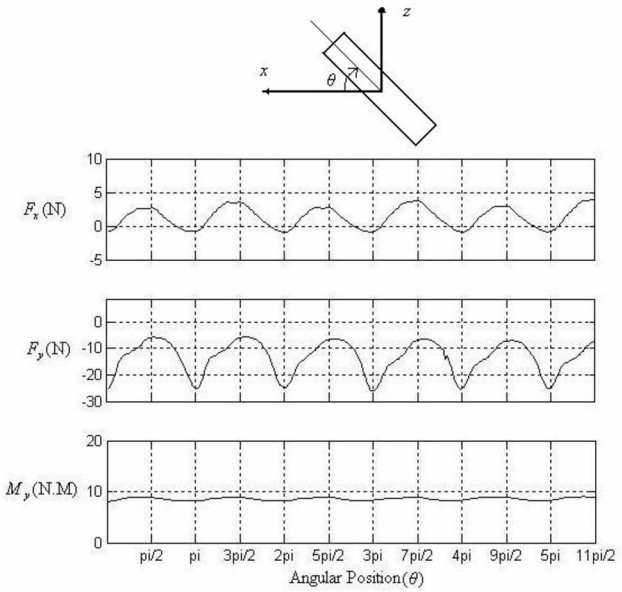

Fig. 13 Aerodynamic forces on the blade surface versus blade angular positions

5 Conclusions

Experimental and numerical studies of oscillatory flows induced by a rotating blade in a lawn care cutting system are presented in this paper. The experiments were conducted in the laboratory conditions without grass-cutting operation to evaluate blade performance and design. The oscillatory pressure at locations of interest was measured using a microphone and a data acquisition system. To develop a computational tool for a speedy cutting system design by a lanwcare manufacturer, comprehensive three-dimensional computational models were also developed and presented in this paper. The numerical and experimental pressure data obtained in this study are in good agreement, especially for pressure peaks and troughs that signify the pressure pulsations. The pressure pulsations are well predicted by the computational model though there is a 5.8% discrepancy mostly emerging between the peaks, which is believed to be caused by the structure-borne sound and inevitably picked up by the microphone. The experimental data and the computational models have been used by a Canadian lawn care manufacturer in designing a multifunctional grass-cutting blade for optimal performance.

Acknowledgment

The authors wish to thank the Ontario Centre of Excellence for Materials and Manufacturing Ontario, and GP-Turfcare Inc. for their financial support through a collaborative research grant, Evan Davidge and Piotr Bulski for their help with the computational modeling and experiments during this study, and Evan Martin, Chris Siemecki, Joseph Amankrah, Roy Churaman, Andrew Heim, Alan Machin, and Devin Ostrom for setting up the experimental facilities.

Nomenclature

a = pseudocompressibility
$\mathbf{E},\mathbf{F},\mathbf{G}$ = inviscid flux vectors
F_x, F_y = aerodynamic forces in the x and y directions (N)
$\mathbf{H}$ = viscous flux vector
M_y = aerodynamic torque about the y axis (N m)
$\mathbf{n}_x, \mathbf{n}_y, \mathbf{n}_z$ = normal unit vectors of control volume
ω_0 = blade passing frequency (Hz)
p = pressure (Pa)
p_d = dynamic head (Pa)
p_r = reference pressure (Pa)

$\mathbf{Q}$ = variable vector
Re = Reynolds number
t = elapsed time (s)
U_g = grid velocity in the x direction (m/s)
U_0 = velocity of blade tip (m/s)
u, v, w = velocity components in the x, y, and z directions (m/s)
W_g = grid velocity in the z direction (m/s)
$\partial_x, \partial_y, \partial_z$ = spatial derivatives with respect to the x, y, and z directions
∂_t = temporal derivative
ρ = density (kg/m^3)
θ = angular position of blade (rad or deg)
$\boldsymbol{\tau}$ = stress tensor (Pa)
Δt = time increment (s)

References

[1] Kaupert, K. A., and Staubli, T., 1999, "The Unsteady Pressure Field in High Specific Speed Centrifugal Pump Impeller. Part I: Influence of the Volute," ASME J. Fluids Eng., **121**, pp. 621–626.

[2] Jaworski, Z., Wyszynski, M. L., Moore, I. P. T., and Nienow, A. W., 1997, "Sliding Mesh Computational Fluid Dynamics: A Predictive Tool in Stirred Tank Design," Proc. Inst. Mech. Eng., Part E: J. Process Mechanical Engineering, **211**(3), pp. 149–156.

[3] Shi, F., and Tsukamoto, H., 2001, "Numerical Study of Pressure Fluctuations Caused by Impeller-Diffuser Interaction in a Diffuser Pump Stage," ASME J. Fluids Eng., **123**(3), pp. 466–474.

[4] Liu, Q., Qi, D., and Mao, Y., 2006, "Numerical Calculation of Centrifugal Fan Noise," Proc. Inst. Mech. Eng., Part C: J. Mech. Eng. Sci., **220**(8), pp. 1167–1177.

[5] Fenwick, C. L., and Allen, C. B., 2006, "Development and Validation of Sliding and Nonmatching Grid Technology for Control Surface Representation," Proc. Inst. Mech. Eng., Part G: J. Aerospace Eng., **220**(4), pp. 299–315(17).

[6] Ballesteros-Tajadura, R., Velarde-Suarez, S., Hurtado-Cruz, J. P., and Santolaria-Morros, C. P., 2006, "Numerical Calculation of Pressure Fluctuations in the Volute of a Centrifugal Fan," ASME J. Fluids Eng., **128**(2), pp. 359–369.

[7] Daws, W. N., 1992, "Towards Improved Throughflow Capability: The Use of Three-Dimensional Viscous Flow Solvers in Multistage Environment," ASME J. Turbomach., **114**, pp. 8–17.

[8] Liu, Z., Biba, Y., and Hill, D. L., 1999, "Aerodynamic and Noise Aspects of a Pipeline Compressor: A Benchmark Study," *Proceedings of Fall Pacific Energy Association Conference*.

[9] Busby, J., Sondak, D., Staubach, B., and Davis, R., 2000, "Deterministic Stress Modeling of Hot Gas Segregation in a Turbine," ASME J. Turbomach., **122**, pp. 62–67.

[10] Meakhail, T., and Park, S. O., 2000, "A Study of Impeller-Diffuser-Volute Interaction in a Centrifugal Fan," ASME J. Turbomach., **127**(1), pp. 84–90.

[11] Chen, J. P., Ghosh, A. R., Sreenivas, K., and Whitfield, D. L., 1997, "Comparison of Computations Using Navier-Stokes Equations in Rotating and Fixed Coordinates for Flow Through Turbomachinery," AIAA Paper No. 97-0878.

[12] Chen, J. P., and Barter, J., 1998, "Comparison of Time-Accurate Calculations for the Unsteady Interaction in Turbomachinery Stage," *Proc. of the 27th Aerospace Sciences Meeting*, Reno, Nevada, AIAA Paper No. 98-3292.

[13] Kline, S. J., and McClintock, F. A., 1953, "Describing Uncertainties in Single-Sample Experiments," Mech. Eng. (Am. Soc. Mech. Eng.), **75**, pp. 3–8.

[14] Kline, S. J., 1985, "The Purposes of Uncertainty Analysis," ASME J. Fluids Eng., **107**, pp. 153–160.

[15] Abernethy, R. B., Benedict, R. P., and Dowdell, R. B., 1985, "ASME Measurement Uncertainty," ASME J. Fluids Eng., **107**, pp. 161–164.

[16] Boll, F. F., 1979, "Suppression of Acoustic Noise in Speech Using Spectral Subtraction," IEEE Trans. Acoust., Speech, Signal Process., **27**, pp. 113–120.

[17] Barth, T. J., and Jespersen, D., 1989, "The Design and Application of Upwind Schemes on Unstructured Meshes," *Proc. of the 34th AIAA/ASME/SAE/ASEE Joint Propulsion Conference*, Cleveland, Ohio, AIAA Paper No. 89-0366.

[18] Roe, P. L., 1986, "Characteristic Based Schemes for the Euler Equations," Annu. Rev. Fluid Mech., **18**, pp. 337–365.

Unsteady Vortex Flows Produced by Trailing Edge Articulation

Stephen A. Huyer
David Beal

Naval Undersea Warfare Center,
Newport, RI 02841

Daniel Macumber
Anuradha Annaswamy

Massachusetts Institute of Technology,
Cambridge, MA 02139-4307

The unsteady vortex flows produced by biologically inspired tail articulation are investigated. The application is to provide active means of reducing tonal noise due to upstream wake interaction with downstream propellers on underwater vehicles. By reducing the wake velocity defect, the periodic unsteady propeller blade pressure fluctuations that are the source of the noise should be reduced. Accordingly, experiments to measure the flows produced by an upstream stator fitted with a movable trailing edge were carried out in a water tunnel for Reynolds numbers in the range 75,000 $<Re<$ 300,000. A stator model with a hinged flapping trailing edge section operated at frequencies up to 21 Hz corresponding to a range of Strouhal number 0.0 $<St<$ 0.18. Velocity measurements of the articulating stator wake were carried out by laser Doppler velocimetry (LDV) and particle image velocimetry (PIV). Reduced mean and rms LDV data show that trailing edge articulation generates vortex structures with dependence on both Strouhal number and articulation amplitude. Estimates of the time mean stator drag that were obtained by integrating the mean wake profiles were used to estimate optimal Strouhal numbers in terms of wake elimination. Instantaneous phase-averaged measurements via PIV show a transition in the unsteady stator wake flow regimes as St is increased, from a deflected vortex sheet to a series of rolled up, discrete vortices. Measurements of the wake highlight the characteristics of the vortex structures and provide a means to estimate the impact on downstream propellers. [DOI: 10.1115/1.2844579]

Introduction

A significant source of noise generation by propulsors and turbomachinery is due to the tonal component caused by the interaction of the rotor with periodic disturbances generated by upstream control surfaces and appendages. The underlying physics that produce the tonals have been documented (e.g., Refs. [1–4]) and relatively well understood. Due to the no-slip boundary condition that exists for any viscous fluid, a boundary layer is produced on upstream appendages. A velocity wake deficit is then produced downstream that is dependent, among other factors, on the flow Reynolds number and the surface area of the appendage. As the downstream rotor blades encounter the wake deficit, an unsteady force is produced. For rotors spinning at a constant rpm, radiated noise can be characterized by the resulting blade rate tonals. The radiated noise is then a function of the characteristics of the velocity defect. In order to reduce the tonal radiated noise, it follows that the characteristics of the velocity defect must be altered or eliminated.

As a propeller blade passes through regions of varying inflow velocity, the effective angle of attack on the blade changes and the blade experiences unsteady forces. These unsteady fluid forces acting on the propeller blade are a major source of directly radiated noise [5]. If the most significant unsteady force acting on the propeller blade section is the lift L, then the expression for directly radiated noise in the acoustic far field may be written as

$$P'(\vec{r},t) = \frac{1}{4\pi} \nabla \cdot \vec{F}(t - r/c_0) \approx k_0 \dot{L}(t - r/c_0) \tag{1}$$

where P' is the acoustic pressure, $\vec{F}$ is the blade force per unit span, r is the radius from blade to observer, $t - r/c_0$ is the retarded time, k_0 is a constant, and $\dot{L}$ is the derivative of L with respect to time. The above expression assumes the source region is acoustically compact. Because the motion of the propeller is periodic in time, the noise generated by the wake blade interaction is tonal noise, with harmonics of the blade passing rate. This component of noise is particularly disadvantageous in military applications as it can be used to identify or locate the vehicle. Unsteady blade forces are also undesirable as they may excite structural vibrations of the vehicle and contribute to fatigue of the blades and propeller assembly. Noise radiated by secondary vibrations in the vehicle assembly is referred to as indirectly radiated noise.

One method that has been used in an attempt to reduce or eliminate the velocity defect was the use of trailing edge blowing [6]. Fluid was pumped through a slot in the trailing edge to add momentum to the fluid to counteract the momentum lost due to the boundary layer. Time-averaged velocity profiles in the wake indeed show that the wake defect can practically be eliminated using this methodology. Tonal noise reduction as high as 8 dB was seen for lower fan rpm. These effects were diminished as fan rpm was increased. These experiments were conducted in air. For undersea vehicles, trailing edge (TE) blowing may not be practical due to a variety of mechanical limitations.

An alternative approach is inspired by thrust generation by biological entities that swim or fly. These creatures utilize unsteady flow generated by pitching and heaving wings or fins to produce thrust. The effectiveness with which swimming animals use fins for propulsion and trajectory control has led scientists to believe that the motion of a fish's fin is optimally tuned to interact with the surrounding fluid. It is therefore possible that a biologically inspired method of fluid actuation may provide a more effective and more efficient manner of blade tonal noise reduction than traditional engineering solutions such as TE blowing.

Engineering efforts have been made to replicate the motions of swimming fish in order to exploit the same fluid interactions that fish use so effectively. Much of this work has focused on the use of fins oscillating in pitch and heave for efficient propulsion and has been modeled after body/caudal fin undulating motions by swimming fish. Propulsive forces and efficiencies of hydrofoils moving in both heave and pitch have been studied extensively [7–9]. A key result of this work has been the identification of a nondimensional number common to many types of oscillating propulsive motions. The Strouhal number St may be defined as

Contributed by the Fluids Engineering Division of ASME for publication in the JOURNAL OF FLUIDS ENGINEERING. Manuscript received February 9, 2007; final manuscript received January 3, 2008; published online March 11, 2008. Assoc. Editor Hamid Johari.

$$\mathrm{St} = \frac{fA_{\mathrm{disp}}}{U} \tag{2}$$

where f is the tail frequency, A_{disp} is the maximum peak-to-peak tail tip displacement, and U is the freestream velocity. The Strouhal number provides a measure of the relative spacing of vortices in the wake. Studies have shown that many fish and swimming animals propel themselves for effective Strouhal numbers in the range of $0.25 < \mathrm{St} < 0.35$ [10]. It was also found in Ref. [11] that a wide variety of bats, birds, and insects also flap their wings in this same range during cruising flight. Experimental tests have shown that flapping foils produce their most efficient thrust when operating in this Strouhal number range [10].

Transition from the biological to the mechanical world requires thrust generation by pitching and oscillating wings. With that in mind, an extensive database has been previously established to characterize the unsteady flows produced by unsteady wing oscillations [12]. The application here was to examine the effect of dynamic stall and the production of unsteady flows. It was shown that this phenomenon produced significant amounts of transient lift on wings. It also showed the characteristics of the unsteady vortex structures produced and shed into the wake. These vortices were characterized by large velocity excursions where the instantaneous velocities could be as large as two to three times freestream. These tests showed that simple wing oscillations can provide a significant amount of momentum to the fluid.

For present requirements, however, the biological and mechanical world shows that the large scale unsteady forces produced would have the opposite of the desired effect in terms of reducing noise. If the wake velocities are characterized by a significant velocity excess, as occurs for propulsion, the resulting unsteady blade forces will likely be higher than the base line steady wake. The key is then to provide just enough momentum to counter the velocity defect, but not so much as to generate increased velocities. In addition, if the unsteady flows produced result in instantaneously large velocity excursions, the unsteady blade forces and resultant noise still would not be reduced. They may, in fact, increase.

The use of tail articulation for blade tonal noise reduction was first proposed and studied numerically by Krol et al. [13] and with initial experiments by Bandyopadhyay et al. [14]. Krol et al. modeled tail articulation as an arbitrary vorticity source at the stator TE and the shed vorticity was assumed to advect with the freestream velocity. With these assumptions, a second order differential equation describing the propeller lift due to vorticity shed into the wake by tail articulation was written and solved with the fluctuating lift component set to zero. The ideal vorticity input predicted by this model resulted in noise reduction up to 40 dB at some frequencies.

The experiments presented here examine the unsteady vortex flows produced by an articulating TE. A wing with a NACA 0020 airfoil section was fabricated and placed in a water tunnel. The aft 1/3 portion of the wing section could then oscillate sinusoidally (or with a modified sinusoid) in order to produce the biologically inspired articulating motion. The nominally two-dimensional flow field was measured using laser Doppler velocimetry (LDV) and particle image velocimetry (PIV). LDV was used to provide data for the mean and rms axial and normal velocity components. PIV provided representations of the instantaneous vortex dominated flow field. Both methods were used to provide insight into the unsteady flows produced and their potential impact on a downstream rotor blade. The hydrodynamic quantities measured provided the needed velocity data for simulations to estimate the resulting unsteady blade forces and radiated noise produced as a downstream rotor blade encounters these unsteady wakes.

Methodology

Experimental Apparatus. Experiments were conducted in the research water tunnel (Fig. 1) at the Naval Undersea Warfare Center in Newport, RI. The tunnel has a 30.48 cm^2 cross section and a maximum flow speed of 9.1 m/s. The facilities are equipped with closed loop velocity control and have removable Plexiglas windows for tunnel access. The width of the NUWC water tunnel slowly expands in the downstream direction to account for boundary layer growth on the walls, minimizing the acceleration of fluid in the 3.05 m long test section. The tunnel has a 3:1 ratio contraction section and a 15.25 cm thick honeycomb mesh with 7.6 mm cells, giving 0.5% maximum turbulence intensity in the center of the tunnel. The tunnel is powered by a 61 cm single stage impeller with a 448 kW electric motor. Two 13.25 kl water storage tanks, one for fresh water and the other for salt, are used for filling and draining the tunnel. Fresh water is used for all experiments in this work.

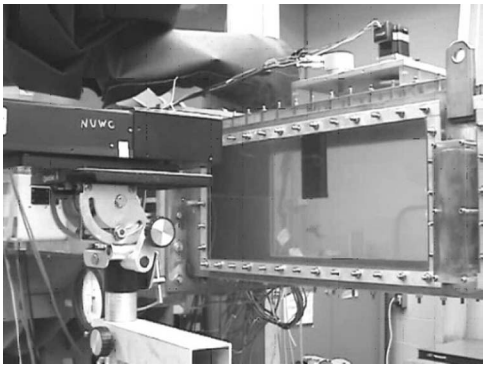

Fig. 1 Research water tunnel and experimental setup

Flow speeds $1 < U < 4$ m/s corresponding to $75{,}000 < \mathrm{Re} < 300{,}000$ over a 7.62 cm long stator model were examined. Flow velocities can be set using propeller rpm as a reference within 0.5% of the desired values. A 1/3 chord length (2.54 cm) stator TE section was selected to perform sinusoidal and nonsinusoidal flapping motions of 5 deg, 10 deg, and 20 deg. Only sinusoidal results are presented here. An actuator capable of direct sinusoidal oscillation at these frequencies could not be found. Instead, a four bar linkage was designed to implement sinusoidal tail motions (Fig. 2). The orientation of the experimental coordinate system is also shown in Fig. 2; the origin is taken to be at midspan on the stator's TE. The four bar linkage converts a constant angular velocity input to a sinusoidal output of the same frequency. Amplitude of the output motion is set pinning one of the linkage arms through holes drilled in the input disk. Due to slight imperfections in the mechanism, there were deviations from actual sinusoidal motion. Measurements of actual angle of attack at the maximum and minimum positions demonstrated a maximum error of 5% in actual versus desired stator angle of attack. This bias can result in slight deviation of the desired sinusoidal motion as well as slight

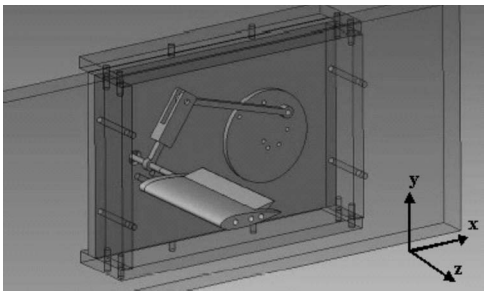

Fig. 2 Four bar linkage and stator with TE flap

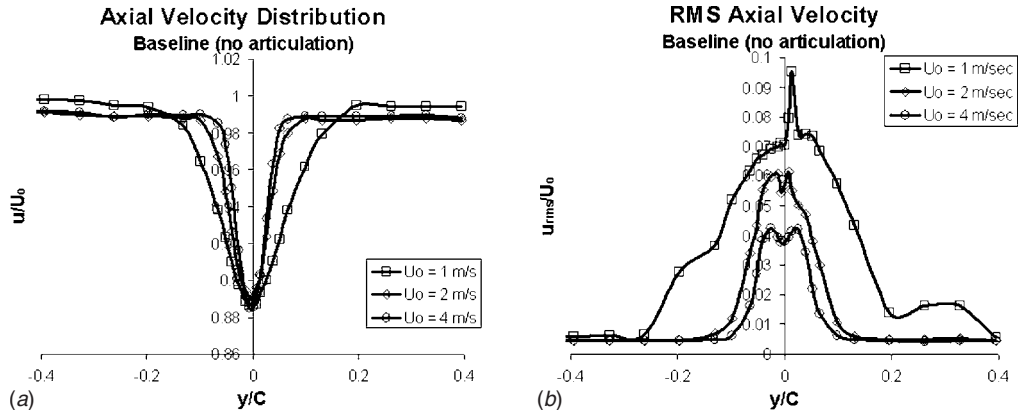

Fig. 3 Base line axial velocity wake profiles for $A=0$ deg, $U_0=1$ m/s, 2 m/s, and 4 m/s, and St=0

asymmetry (e.g., nonzero mean pitch angle) in the overall articulation motion history. Further discussion of the articulation mechanism may be found in Ref. [17].

LDV Measurements. Two-component LDV was used to measure the axial and normal velocity components. The flow was assumed to be two dimensional with velocity measurements taking place at midspan. Because the passage of a particle through the measurement volume is a random event in time, velocity data are averaged over a large number of bursts to obtain mean and rms velocity data. In this experiment, velocity data are collected at each point for 100 s before the traverse carrying the laser head is moved and data collection in the next measurement volume begins. Effective sampling rate was on the order of 600 Hz, resulting in approximately 60,000 data points to obtain the statistics. By comparison, the maximum articulation frequency was approximately 21 Hz. Measurements are made one chord length downstream of the stator TE at stator midspan and at 25 points in the y direction. The measurement range generally extended 0.4 chord lengths above and below the stator centerline.

An initial calibration of the freestream velocity (U_0) to tunnel impeller speed by LDV with no stator in the tunnel showed a very linear relationship at speeds $U_0 > 0.3$ m/s. The two-dimensional stator wake assumption was then tested by installing the stator and aligning the laser head to measure flow in the spanwise (z) direction at one chord length downstream. For sinusoidal motions up to $f=1252$ rpm (21 Hz) and with $A=10$ deg, the maximum normalized w component of velocity in the active wake was found to be between 1% and 2% of maximum freestream velocities, thereby justifying a two-dimensional analysis.

Unsteady PIV Measurements. While the LDV analysis provides valuable insight into the time mean effect of tail articulation, an unsteady measurement technique is required to study the instantaneous stator wake. PIV is another noninvasive fluid velocity measurement technique, which works by measuring the displacement of fluid seed particles using an optical imaging system [15,16]. In order to convert particle displacement to velocity measurements, two closely timed laser pulses are used to illuminate particles in rapid succession. A synchronized two laser system with 200 μs delay between laser pulses was used in this work. Because the maximum single laser pulse rate of the system was 10 Hz, continuous velocity measurements were not possible. Instead, articulation frequencies were chosen to beat with the laser repetition frequency and the velocity field behind the stator was phase averaged, with 30 phase bins per revolution. Velocity data were collected until at least eight velocity measurements were acquired for each phase bin. The data in each bin were then averaged. The final PIV grid size is 16×16 pixels, which relates to a 0.9×0.9 mm^2 grid resolution in real world units. The total viewing area extended from 0.25 to 1.75 chord lengths downstream of the TE and 0.3 chord lengths above and below the stator centerline. Base line stator wake velocity data were found to compare well with wake data taken by LDV. By constructing finite differences of the grid velocities, it was possible to estimate the spanwise flow vorticity. For a two-dimensional flow, vorticity is in the spanwise direction only, which allows for a basic representation of the flow physics. Vorticity is defined as

$$\omega = \nabla \times \vec{u} = \left(\frac{dv}{dx} - \frac{du}{dy}\right)\hat{z} \tag{3}$$

Results

Laser Doppler Velocimetry. Figure 3 shows the base line mean and rms wake velocity profiles at the three freestream velocities of 1 m/s, 2 m/s and 4 m/s. Immediately apparent is the increasingly thick profiles for reduced freestream velocities. Wake thickness for the 2 m/s and 4 m/s is nearly equivalent. For all three cases, the minimum nondimensional velocity is on the order of 0.885. The rms velocities also demonstrate decreased wake thickness for increased velocity. Peak rms velocities are reduced with increased freestream from 0.08 for 1 m/s to 0.04 for 4 m/s. The more drastic change in the wake profiles is from 1 m/s to 2 m/s and a more modest change from 2 m/s to 4 m/s suggests turbulent boundary layer transition from 1 m/s to 2 m/s. At $U_0=2$ m/s, the Reynolds number is 150,000. For a flat plate, boundary layer transition occurs on the order of $(1-3)\times10^6$. However, considering freestream turbulence, the fact that the airfoil section is a relatively thick NACA 0020 and accounting for surface roughness effects, turbulent transition for this case for Re=150,000 is not unreasonable [18]. The velocity profiles appear symmetric although some asymmetry is noted in the rms velocity for $U_0=1$ m/s.

Cases for sinusoidal wake articulation for a constant Strouhal number and velocity range are shown in Fig. 4. At this Strouhal number, the wake defect is nearly eliminated with minimum velocities on the order of 0.97. Mean velocities exhibit a significantly thicker wake compared with the base line cases. Varying velocity for a given Strouhal number and oscillation amplitude does not appear to significantly change the wake thickness, however. The mean and rms profiles are slightly different from 1 m/s to 2 m/s but appear similar for 2 m/s and 4 m/s. Notice that the rms profile exhibits two humps, indicating the induced velocities due to shed vortices from the upper and lower surfaces. Overall, the rms profiles appear symmetric except for the 1 m/s freestream test case. The mean velocity profiles do not appear symmetric. For this Strouhal number, however, near total wake

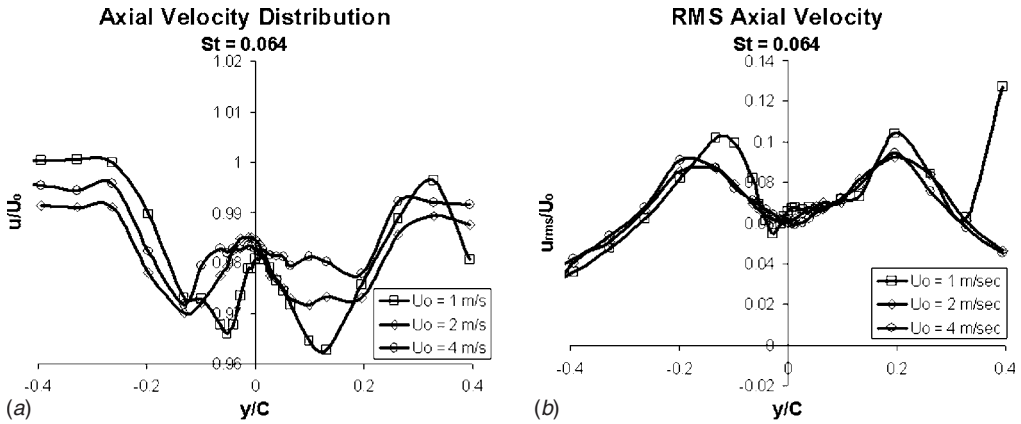

Fig. 4 Axial velocity wake profiles for A=10 deg, U_0=1 m/s, 2 m/s, and 4 m/s, and St=0.064

filling is achieved and the differences may be attributable to slight errors in the oscillating mechanism. Again, at lower speeds, the water tunnel test section expansion may also produce slight flow asymmetries.

Alternatively, oscillation amplitude has a significant effect on the flow for a given velocity and Strouhal number. Figure 5 shows the wake profiles examining a range of amplitudes from 5 deg to 20 deg. As can be seen, for A=20 deg, mean and rms profiles show maximum wake thickness and rms velocities; for A=5 deg, the wake is thinnest and the rms velocities are lowest. In addition, it appears that for A=20 deg, wake filling is less efficient as wake velocities are approximately 2% lower compared with A=5 deg and 10 deg.

Effects of Strouhal number on the axial and vertical wake profiles are shown in Figs. 6 and 7, respectively. In this case, freestream velocity and oscillation amplitude were held constant at 2 m/s and 10 deg. Immediately apparent in the axial velocity distribution is the fact that for even small Strouhal numbers, there is an increase in the centerline mean wake velocity. The deficit is reduced and nearly eliminated by St=0.089. For the higher Strouhal number (0.122), a significant peak in wake velocity (1.1) demonstrates that at this point, the articulating TE is producing thrust. Interestingly, the increase in overall wake thickness is not seen in the mean velocity distribution, but rather in the rms data. Here, the

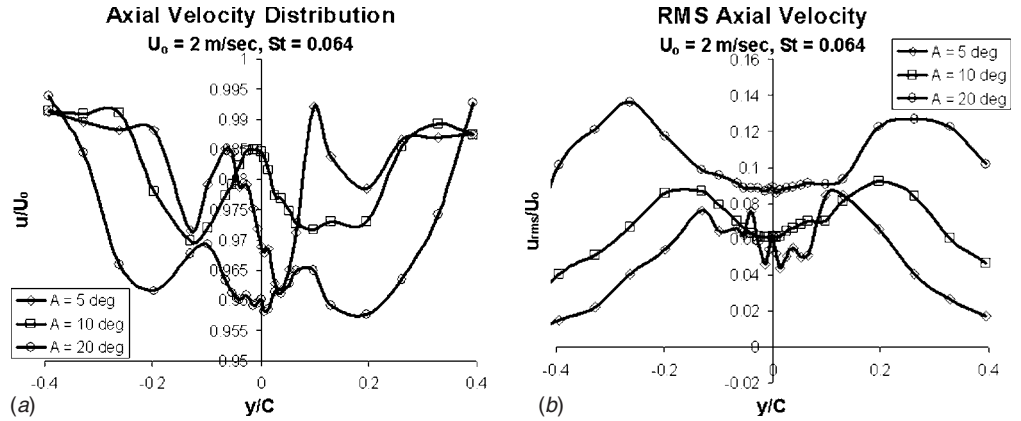

Fig. 5 Axial velocity wake profiles for A=5 deg, 10 deg, and 20 deg, U_0=2 m/s, and St=0.064

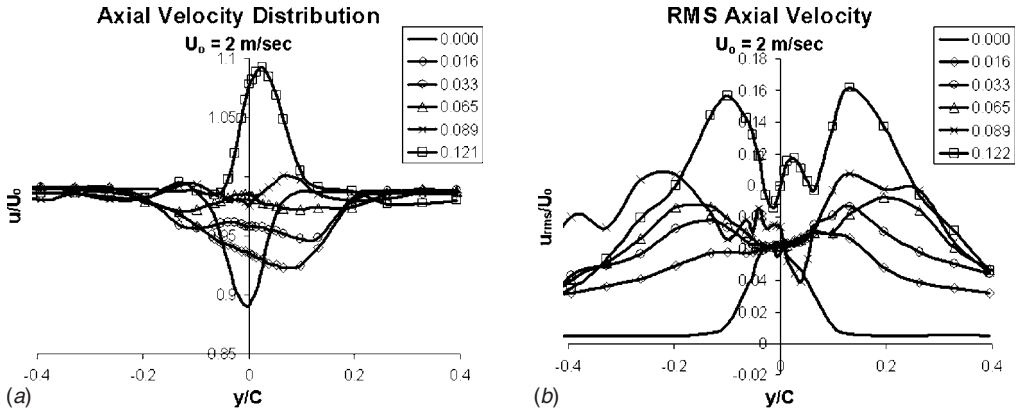

Fig. 6 Axial velocity wake profiles for A=10 deg, U_0=2 m/s, and St=0.0, 0.016, 0.033, 0.065, 0.089, and 0.122

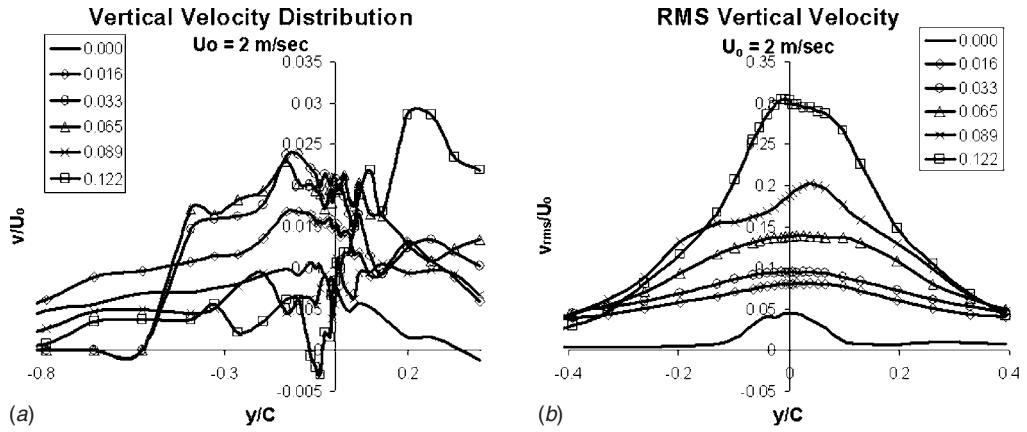

Fig. 7 Vertical velocity wake profiles for $A=10$ deg, $U_0=2$ m/s, and St=0.0, 0.016, 0.033, 0.065, 0.089, and 0.122.

extent of the unsteady velocity perturbations can be seen. rms velocities consistently increase with Strouhal number. For St >0.033, two rms peaks are seen indicative of upper and lower vortices shed into the wake. For St=0.016, only a single defined rms peak was seen.

Mean vertical velocities shown in Fig. 7 remain relatively small and asymmetric with respect to the wake. The reason for this is unclear and may be caused by a slight bias in mean TE angle of attack. Base line peak mean vertical velocities of 0.01 were recorded increasing only to 0.03 for the highest Strouhal number. rms vertical velocities, on the other hand, demonstrate significant variations in vertical velocity. Unlike the axial rms velocities, the vertical rms velocities exhibit only a single peak along the stator centerline. Peak rms velocities increase with Strouhal number and appear to become more spread out as well. Based on the rms velocities, the unsteady wake extends to +40% of the stator chord.

Figure 8 shows the estimate of total drag for a range of Strouhal number up to 0.25 and for articulation amplitudes of 5 deg, 10 deg, and 20 deg. Drag coefficient was estimated by integrating the wake velocity defect. The purpose of the drag estimate was to provide an approximation for optimal tail articulation in terms of filling the wake without generating an overall velocity increase due to thrust production. The following classical formula was used for the drag estimate:

$$C_d = \frac{2D}{\rho U^2 \mathrm{Sc}} = \frac{2}{c}\int_{y\,\min}^{y\,\max}\left[\left(\frac{u}{U}\right)^2 - \left(\frac{u}{U}\right)\right]dy \qquad (4)$$

As can be seen, there is an initial increase in drag versus St followed by a decrease as effective thrusting is produced. As articulation amplitude is increased, an increased Strouhal number is needed to reach the point of optimal articulation (e.g., where overall drag is zero). Using this measure, it appears that for $A=5$ deg, St=0.06, for $A=10$ deg, St=0.1, and for $A=20$ deg, St=0.15. As C_d becomes negative, velocity surpluses are seen in the wake.

Particle Image Velocimetry. PIV was used to measure the instantaneous velocity field associated with the articulating TE. Figure 9 shows out of plane vorticity plots (obtained by differencing the u and v velocity fields) for Strouhal numbers of 0.033, 0.092, and 0.184 with $A=10$ deg and $U_0=2$ m/s. The vertical line is shown as a reference for velocity measurements presented in later figures and the horizontal line shows the position of the TE. For the low Strouhal number of 0.033, the vorticity field is characterized by an oscillating type of wake. The wake does not appear to significantly roll up, rather the shed vorticity remains concentrated in the thin wake and forms a sinusoidal pattern downstream. For the near optimal Strouhal number of 0.092 (suggested from drag

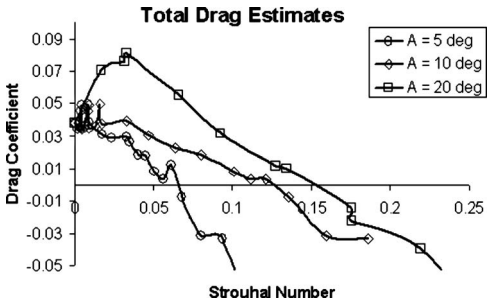

Fig. 8 Total drag estimates derived from wake profile integration as a function of Strouhal number for articulation amplitudes of 5 deg, 10 deg, and 20 deg

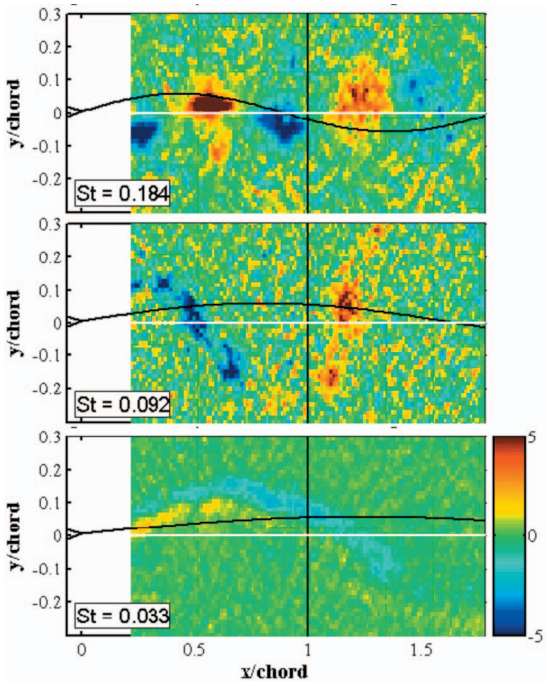

Fig. 9 Downstream vorticity plots derived from PIV data for $A=10$ deg and St=0.033, 0.092, and 0.184. The line at $x/c=1.0$ refers to the velocity measurement rake in later figures and the horizontal line plots the location of the TE

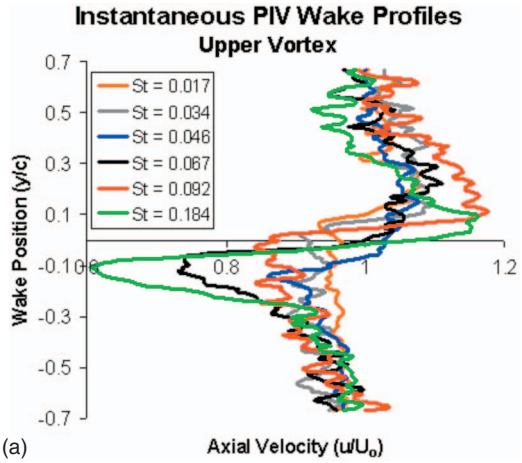

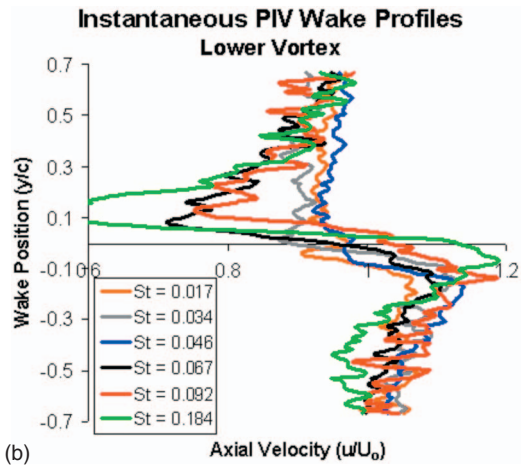

Fig. 10 Instantaneous axial velocity wake profiles taken one chord length downstream of the articulating TE highlighting the induced velocity due to the upper and lower vortices for St =0.017, 0.034, 0.046, 0.067, 0.092, and 0.184

data presented in Fig. 8), opposite signed vorticity now appears distinguishable with weak vortex rollup. The wake remains in a sinusoidal pattern, however, with opposite signed vorticity elongated. For St=0.184, strong vortex rollup is evident with alternating compact circular vortex cores clearly distinguishable in the wake. There are also twice as many vortices in the near wake compared with St=0.092 (as expected due to the doubling of St). Judging by the lighter colors, the vortex cores appear to become diffused as they are advected downstream.

Instantaneous axial wake velocities were measured one chord length downstream of the articulating TE with results plotted in Figs. 10 and 11 for a range of Strouhal numbers. These profiles highlight the induced velocities due to the vortices shed from the upper and lower surfaces. As can be seen, maximum and minimum velocities are seen to increase with Strouhal number. Maximum vortex velocities of 120% freestream and minimum velocities of 60% freestream are seen for the highest St. For the optimal case, these values are on the order of 110% and 70% freestream, respectively. For the lowest St plotted (0.017), these values are 105% and 90%. The velocity profiles presented between the upper and lower vortices appear to be independent of St (Fig. 11). The profiles appear to be characterized by random fluctuations in axial velocity reminiscent of turbulent fluctuations. There does not appear to be a spatially defined wake velocity deficit/increase.

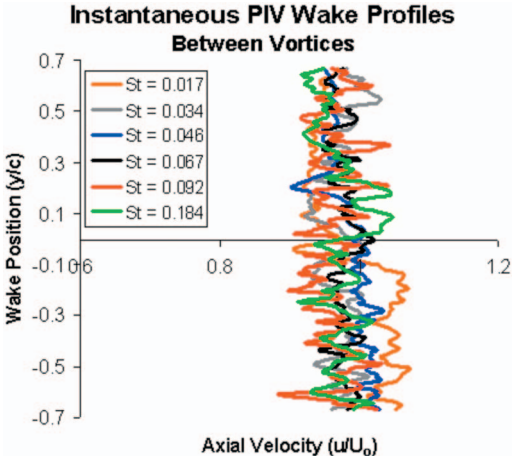

Fig. 11 Instantaneous axial velocity wake profiles taken one chord length downstream of the articulating TE highlighting the induced velocity between the upper and lower vortices for St =0.017, 0.034, 0.046, 0.067, 0.092, and 0.184

Discussion

Based on PIV data, there appears to be three distinct flow regimes that are a function of Strouhal number. For the lowest Strouhal numbers, an oscillating wake pattern appears. In this case, the shed vorticity does not appear to roll up into defined vortex structures. Rather, the vorticity remains concentrated in a thin wake that is displaced due to tail articulation. Corresponding LDV data for the St=0.016 case for the axial velocity distribution show that there is a single minima. Likewise, the rms axial velocity shows a single distinct peak. In addition, drag estimates show that this regime can be characterized by an initial increase in drag caused by quasi-static deflection of the flap at these low frequencies. This increased drag is worse for higher flap amplitudes because the drag due to the quasi-static deflection is correspondingly higher. In fact, the higher Strouhal number required to cancel the wake deficit at higher amplitudes may be due to the flapping having to overcome this effect.

As Strouhal number is increased, a new regime that can be classified as weak vortex rollup emerges. PIV data show that the opposite signed vorticity is distinct. However, there does not appear to be a sign of distinct vortex cores. Rather, the same sign vorticity appears elongated. It is in this regime where total body drag begins to decrease. LDV data show two distinct maxima in the rms axial velocity profiles corresponding to distinct shed vortices. PIV wake profiles of the upper and lower vortices also clearly display more coherent vortices.

The upper Strouhal numbers elicit a strong vortex rollup regime. This can be clearly seen in the PIV derived vorticity plots where the opposite signed vorticity is concentrated in distinct vortex cores. In this regime, thrust (e.g., negative drag) is produced. The strong vortex rollup regime shows two strong peaks in the rms axial velocity profile with PIV data demonstrating induced vortex velocities as great as 30% in excess of freestream values.

A common characteristic of the three flow regimes is the periodic fluctuations in velocity due to the spatial distribution and advection of the vorticity. This was highlighted in Figs. 10 and 11. Maximum and minimum velocities became more pronounced with increased Strouhal number. However, as illustrated in Fig. 11, there is a point in the cycle (specifically between the two shed vortices) where the velocity fluctuations and wake defect/increase are minimal. Hypothetically, if a downstream propeller blade was timed so that it encounters the stator wake at these optimal points in the articulation cycle, then it may be possible to reduce the unsteady blade fluctuations and radiated noise.

Mean and rms velocity profiles exhibited cases of mild asym-

metry for certain test cases. The base line (St=0.0) cases exhibited very symmetric behavior in both mean and rms profiles. For nonzero Strouhal numbers, asymmetry increased as a function of Strouhal number and articulation amplitude. This can be explained by the bias in the oscillating mechanism, which was stated to be on the order of 5%. The asymmetry was very slight for St =0.064 and was seen mostly in the mean profiles. As this was an optimum Strouhal number for wake filling, however, the velocity scales were compressed highlighting small differences that may also be attributable to random error. As St was increased to the higher values (0.089 and higher), consistent asymmetry was seen with the peak velocity and rms values shifted slightly in the positive direction. This suggests that the bias for this mechanism was in this direction.

For an actual vehicle, strong asymmetry would be present due to the fact that the upstream stator is a lifting surface. Both swirl and axial velocity differentials will be generated relative to each side of the stator. A detailed analysis of stator wakes typical to undersea vehicles was presented by Huyer and Snarski [4]. The change in axial and swirl velocity due to the lifting stators varied gradually between the stators. The velocity wake defects were localized, strong, and persistent. Equation (1) shows that increased acoustic pressure is mostly a function of the force gradients. Increased force gradients produce increased noise. Therefore, the flow asymmetry would be a lower order effect compared to the wake defects. The current methodology aims to reduce not only the magnitude of the encountered velocity defect but by spreading out the effect would reduce the gradient as well, thereby reducing noise. Experiments are currently underway to measure the unsteady propeller forces and will be reported in a future article.

Conclusions

The unsteady vortex flows produced by an articulating TE have been examined. A simplified stator model was modified so that the aft 1/3 chord was allowed to oscillate. PIV and LDV were used to characterize the unsteady wakes produced by the resulting tail articulation. The resulting flows were predominantly two dimensional in nature and axial and normal velocities were measured. LDV data provided mean and rms velocity data along a profile one chord length downstream of the TE and PIV provided an instantaneous velocity field over an area extending from 0.25 to 1.75 chord lengths downstream of the TE and 0.3 chord lengths above and below the stator centerline. Velocity data demonstrated a clearly defined wake defect for the base line case with no articulation. It is the interaction of a downstream propulsor with this defect that produces the tonal radiated noise seen for actual propulsor configurations.

Strouhal number was defined based on freestream velocity, articulation amplitude, and frequency and individually varied. Increased freestream velocity resulted in thinner wakes and reduced rms velocities for the nonarticulating case. This was likely due to transition to turbulent flow from 1 m/s to 2 m/s. Little effect was seen for the articulating cases. Increases in oscillation amplitude resulted in larger flow disturbances at a given Strouhal number, suggesting larger vortex structures. Examination of Strouhal number at constant articulation amplitude and freestream velocity revealed three separate flow regimes. At the lowest Strouhal numbers, an oscillating wake regime was observed where the vorticity does not appear to coalesce. A weak vortex rollup regime was seen for more moderate Strouhal numbers where the vorticity distribution was spatially elongated. At the highest Strouhal numbers, a strong vortex rollup regime resulted with vorticity concentrated in a relatively well defined core. System drag was estimated by integrating the wake momentum according to classical formula. The oscillating wake regime resulted in an initial increase in system drag. The weak vortex rollup regime resulted in decreased system drag with the optimum case defined as zero drag. For the strong vortex rollup regime, a thrusting effect was produced.

PIV data showed that a common characteristic of all three regimes was a minimum in velocity perturbations and wake defects/increases. This suggested a potential optimum position in the articulation cycle where unsteady propeller forces due to impact of the unsteady wakes would be minimal. Recently, completed experimental data measuring the unsteady forces on a downstream propeller in the wake of the current articulating TE configuration will be analyzed and presented in future work.

Acknowledgment

This work was supported under the ONR-ULI Program (Dr. Kam Ng and Dr. David Drumheller program managers).

References

[1] Satyanarayana, B., 1977, "Unsteady Wake Measurements of Airfoils and Cascades," AIAA J., **15**(5), pp. 613–618.
[2] Jessup, S. D., 1990, "Measurement of Multiple Blade Rate Unsteady Propeller Forces," David Taylor Research Center, Report No. DTRC-90/015.
[3] Muench, J. D., 2001, "Periodic Acoustic Radiation From a Low Aspect Ratio Propeller," Ph.D. thesis, University of Rhode Island, New Port, RI.
[4] Huyer, S. A., and Snarski, S. R., 2003, "Analysis of Turbulent Propeller Inflow," ASME J. Fluids Eng., **125**, pp. 533–542.
[5] Ross, D., 1987, *Mechanics of Underwater Noise*, Peninsula, Los Altos, CA.
[6] Leitch, T., Saunders, C., and Ng, W., 2000, "Reduction of Unsteady Stator-Rotor Interaction Using Trailing Edge Blowing," J. Sound Vib., **235**(2), pp. 235–245.
[7] Anderson, J. M., 1996, "Vorticity Control for Efficient Propulsion," Ph.D. thesis, Massachusetts Institute of Technology, Cambridge.
[8] Read, D. A., Hover, F. S., and Triantafyllou, M. S., 2003, "Forces on Oscillating Foils for Propulsion and Maneuvering," J. Fluids Struct., **17**, pp. 163–183.
[9] Triantafyllou, G. S., Triantafyllou, M. S., and Grosenbaugh, M. A., 1993, "Thrust Development in Oscillating Foils With Application to Fish Propulsion," J. Fluids Struct., **7**, pp. 205–224.
[10] Triantafyllou, M. S., and Triantafyllou, G. S., 1995, "An Efficient Swimming Machine," Sci. Am., **272**(3), pp. 64–70.
[11] Taylor, G. K., Nudds, R. L., and Thomas, A. L. R., 2003, "Flying and Swimming Animals Cruise at a Strouhal Number Tuned for High Power Efficiency," Nature (London), **425**, pp. 707–711.
[12] McCroskey, W. J., 1982, "Unsteady Airfoils," Annu. Rev. Fluid Mech., **14**, pp. 285–311.
[13] Krol, W. P., Annaswamy, A. M., and Bandyopadhyay, P. R., 2002, "A Biomimetic Propulsor for Active Noise Control: Theory," NUWC-NPT Technical Report No. 11,350.
[14] Bandyopadhyay, P. R., Krol, W. P., Thivierge, D. P., Nedderman, W. H., and Mojarrad, M., 2002, "A Biomimetic Propulsor for Active Noise Control: Experiments," NUWC-NPT Technical Report No. 11,351.
[15] Westerweel, J., Dabiri, D., and Gharib, M., 1997, "The Effect of a Discrete Window Offset on the Accuracy of Cross-Correlation Analysis of Digital PIV Recordings," Exp. Fluids, **23**, pp. 20–28.
[16] Willert, C. E., and Gharib, M., 1991, "Digital Particle Image Velocimetry," Exp. Fluids, **10**, pp. 181–193.
[17] Macumber, D. L., 2005, "Blade Tonal Noise Reduction Using Tail Articulation at High Reynolds Number," MS thesis, Massachusetts Institute of Technology, Cambridge.
[18] Schlichting, H., 1979, *Boundary Layer Theory*, 7th ed., McGraw-Hill, New York.

A Numerical and Experimental Study on the Effect of the Cone Angle of the Spindle in Murata Vortex Spinning Machine

Huifen Guo
Xianglong An
Zhaosheng Yu
Chongwen Yu[1]
e-mail: yucw@dhu.edu.en

College of Textiles,
Donghua University,
Shanghai 201620, P. R. China

To study the effect of the cone angle of the hollow spindle in the nozzle of Murata vortex spinning (MVS) on yarn properties, the k-ε turbulence model is employed to simulate the airflow patterns inside the different nozzles with different spindle cone angles. A set of corresponding spinning experiments is designed to verify numerical predictions. The simulation results show that some factors, such as the counter-rotating vortex pair (CVP) over the spindle, high supersonic zone in the inlet of the swirling chamber, and the distribution of wall shear stress (WSS) along the outer wall of the spindle caused by variation of the cone angle of the spindle, are significantly related to fluid flow, and consequently to MVS yarn properties. A rational cone angle (Case 2) can form an axisymmetric CVP and high WSS, which can ensure sufficient twisting of the yarn and produce high quality yarn. The experimental results, which yarn properties spun using 100% cotton, 100% polyester, and polyester 70/cotton 30 blends with different nozzles, are well consistent with the numerical study. [DOI: 10.1115/1.2844582]

Keywords: fiber, hollow spindle, counter-rotating vortex pair (CVP), WSS, MVS

1 Introduction

It is well known that Murata vortex yarn is formed by air vortex to entangle the fibers. There are several claimed advantages of Murata vortex spinning (MVS) system such as "ringlike" structure, low hairiness and fabric pilling, better abrasion resistance, higher moisture absorption, better color fastness, and fast drying characteristics [1,2]. So, it is accepted as one of the most promising new technologies and can offer advantages with respect to processing speed and cost.

At present, most of the information available in the literature on MVS is related to the yarn structure [3–5], the principle of yarn formation [6,7], and the effects of various parameters on yarn quality [4,8–10]. All these mainly depend on the fiber motion, which is closely related to the flow characteristics, so it is important to study the airflow in the nozzle. However, no work has been reported regarding flow characteristics in the nozzle of MVS so far.

Based on the above reason, this work aims to report airflow characteristics in the nozzle of MVS and cone angle of the hollow spindle effects on yarn properties using the numerical and experimental methods. The remainder of this paper is organized as follows. In Sec. 2, a standard k-ε turbulence model [11] is adopted to simulate the fluid flow. Simulation results are presented in Sec. 3 and the influence of flow characteristics on yarn properties are also discussed. Finally, in Sec. 4, we conduct a set of corresponding experiments to verify our numerical predictions.

2 Numerical Simulation of Fluid Flow

2.1 Nozzle Structure. According to the principle of the MVS [6,7], the bulk of the swirling chamber is an important parameter. In order to machine easily, the cone angle of the spindle is designed to alter the bulk of the swirling chamber. Figure 1 shows the longitudinal sectional profile of the nozzle structures with different cone angles of the spindle. Case 1 is an original nozzle with cone angle $\alpha=16$ deg. Cases 2 and 3 are remodeled nozzles with two-cone angle. Their first cone angles are 12 deg and 8 deg, respectively, and the second cone angles are the same, viz., $\beta=16$ deg.

2.2 Method of Numerical Simulation. Ignoring the influence of the fibers or strands, airflow in the nozzle will be a classical fluid flow problem. As high-velocity compressed air is forced into the nozzle through the jet orifices from the air reservoirs, part of airflow comes into hollow spindle and others into the swirling chamber. Therefore, the flow is very complex. As a preliminary study, only two-dimensional flow is calculated. In addition, since the twisting process occurs in a very short time and the fluid flow in texturing nozzle is supersonic, turbulent [12–14], a two-dimensional, steady, supersonic, viscous turbulent flow of a perfect gas (air) in the absence of body forces is considered. The fluid viscosity, the thermal conductivity, and the specific heat ratio are assumed to be constant. To close Reynolds-averaged equations, a standard k-ε turbulence model [11] is adopted. Therefore, the governing equations are expressed as follows [15]:

Continuity equations,

$$\nabla \cdot (\rho V) = 0 \tag{1}$$

Momentum equations,

$$\nabla \cdot (\rho V u - \mu_{\text{eff}} \nabla u) = -\frac{\partial p}{\partial x} + \frac{\partial}{\partial x}\left(\mu_{\text{eff}} \frac{\partial u}{\partial x}\right) + \frac{\partial}{\partial y}\left(\mu_{\text{eff}} \frac{\partial v}{\partial x}\right) \tag{2}$$

$$\nabla \cdot (\rho V v - \mu_{\text{eff}} \nabla v) = -\frac{\partial p}{\partial y} + \frac{\partial}{\partial x}\left(\mu_{\text{eff}} \frac{\partial u}{\partial y}\right) + \frac{\partial}{\partial y}\left(\mu_{\text{eff}} \frac{\partial v}{\partial y}\right) \tag{3}$$

Energy equations,

[1]Corresponding author.

Contributed by the Fluids Engineering Division of ASME for publication in the JOURNAL OF FLUIDS ENGINEERING. Manuscript received March 29, 2007; final manuscript received November 28, 2007; published online March 11, 2008. Assoc. Editor: Ye Zhou.

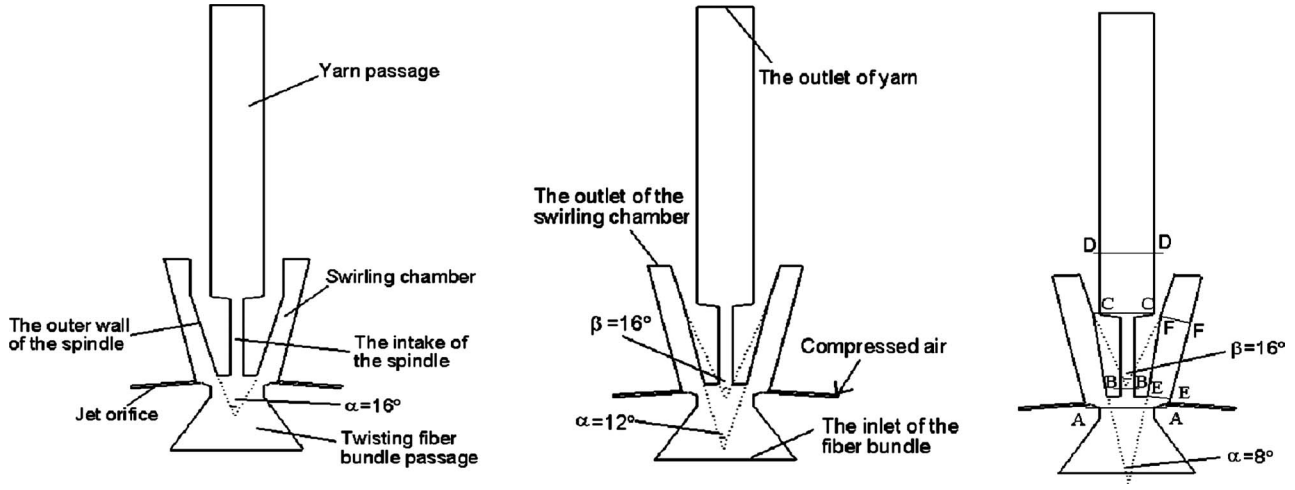

Fig. 1 The longitudinal sectional profile of the nozzle structures, in order from left to right: Cases 1, 2, and 3

$$\nabla \cdot (\rho V T) - \nabla \cdot \left[\left(\frac{\mu}{\mathrm{Pr}} + \frac{\mu_t}{\sigma_T} \right) \nabla T \right] = G_k + \rho \left(u \frac{\partial p}{\partial x} + v \frac{\partial p}{\partial y} \right) \quad (4)$$

Turbulence kinetic energy k equation,

$$\nabla \cdot (\rho V k) - \nabla \cdot \left[\left(\mu + \frac{\mu_t}{\sigma_k} \right) \nabla k \right] = G_k - \rho \varepsilon - Y_M \quad (5)$$

Turbulence rate of dissipation ε equation,

$$\nabla \cdot (\rho V \varepsilon) - \nabla \cdot \left[\left(\mu + \frac{\mu_t}{\sigma_\varepsilon} \right) \nabla \varepsilon \right] = C_{1\varepsilon} G_k \frac{\varepsilon}{k} - \rho C_{2\varepsilon} \frac{\varepsilon^2}{k} \quad (6)$$

The equation of state of a perfect gas ($p=\rho RT$) is added to complete the system of the equations. In these equations, ρ, p, V (u,v), γ, T, and Pr are the air density, pressure, velocity vector, the ratio of specific heats, temperature, and Prandtl number, respectively. The effective viscosity μ_{eff} is the sum of the laminar μ and turbulent viscosities $\mu_t=(C_\mu \rho k^2/\varepsilon)$ of the fluid. G_k represents the generation of turbulence kinetic energy due to the mean velocity gradients. Y_M represents the contribution of the fluctuating dilatation in compressible turbulence to the overall dissipation rate. σ_k, σ_ε, and σ_T are the turbulent Prandtl numbers for k, ε, and T, respectively. The model constants are $C_{1\varepsilon}=1.44$, $C_{2\varepsilon}=1.92$, $\sigma_k=\sigma_T=1.0$, $\sigma_\varepsilon=1.3$, and $C_\mu=0.09$ [11].

A finite volume technique is used to discretize the governing equations inside the computational domain. Due to the compressible effects, the coupled implicit approach is adopted. The conservation equations are solved using the second-order upwind scheme, and the other (k and ε) equations use the QUICK scheme [16] to minimize numerical diffusion. In order to accelerate the convergence of the solver, a block Gauss–Seidel algorithm is used in conjunction with an algebraic multigrid (AMG) method [17] to solve the discretized equations.

2.3 Boundary Conditions. The airflow in the nozzle is a more complex flow with multiple fluid inlets and outlets. Because the pressure of the air reservoir is known, pressure inlet condition is used at the jet orifices. However, at the fiber-bundle inlet, while the fibers or strands output from the front roller and go into the nozzle, the outer air is supplied into the nozzle, so the velocity inlet boundary can be set. At the outlets of spindle and swirling chamber, the pressures are supposed to be the external pressure. In addition, nonslip and adiabatic condition is imposed on the wall.

3 Numerical Results and Discussion

In all the cases, the jet orifice pressure of 5 kg/cm^2 is used as the initial conditions according to spinning experiments [10]. The geometrical configuration of the nozzle is very complex due to the existence of the spindle. The grid construction should be very carefully selected in order to meet the convergence and accuracy requirements. Nonuniform grids are generated, and grid refinements in the regions of expected high gradients, e.g., near the wall and at the zones with large geometrical structure change, are applied. The total numbers of grid points of Cases 1, 2, and 3 are 31, 515, 32, 128, and 33, 248, respectively. The best grid structures of the three cases are shown in Fig. 2.

Figure 3 shows the contour plots of streamline in the three cases. Impinging turbulent jet [18,19] is formed as compressed air through the jet orifice impinges on the outer wall of the spindle. The high velocity airflow jets into three areas: the swirling chamber, the hollow spindle, and the region between the spindle and twisting fiber-bundle passage. The recirculation zone in the swirling chamber is formed due to the impingement on the spindle outer wall. Vortices are generated in intake of the spindle due to the sudden contraction of the cross section (see Fig. 4). Obviously, some parameters, such as the low velocity cross flow, the wall of the spindle, and jet flow from different jet orifices, affect flow field over the spindle, and consequently to form a counter-rotating vortex pair (CVP). In addition, flow separation and subsequent reattachment are caused by sudden expansion cross section in yarn passage of the spindle. These vortices mentioned above prolong the residence time of the fibers, which are helpful to twist sufficiently for fibers. CVP over the spindle makes fibers separate from each other and twine over the spindle to be twisted. It is worthy to note that the CVP in Cases 1 and 3 are asymmetric and eccentric, especially in Case 1. However, the CVP is almost axisymmetric on the core axis in Case 2, which makes fibers twine evenly over the hollow spindle and twist evenly. Therefore, high quality yarn can be produced in Case 2. For fibers with lower flexural rigidity (e.g., polyester fiber), it is easy to block the swirling chamber in Case 1 due to the large eccentric vortex, furthermore, influence twisting and the quality of the resultant yarn.

The distributions of the mean axial velocities at different loca-

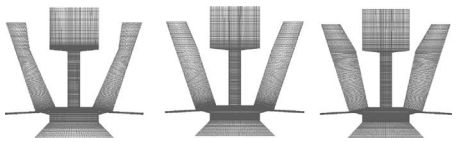

Fig. 2 The grid structures in three cases, in order from left to right: Cases 1, 2, and 3

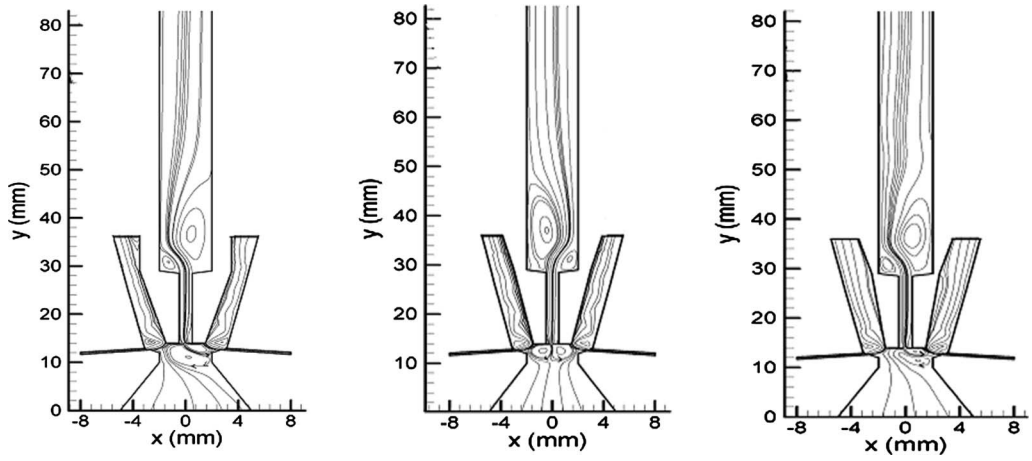

Fig. 3 Contour plots of streamline in three cases, in order from left to right: Cases 1, 2, and 3

tions are plotted in Fig. 4 for different cases. It is obvious that the flow is asymmetric near the jet orifice (Cross section A-A), especially in Cases 1 and 3. This coincides with previously published results by Acar et al. [13,20], Bock and Lunenschloss [12], and Versteeg et al. [14]. The variations in flow velocity across the spindle intake are smooth and supersonic. It may indirectly induce the leading ends of all fibers to be drawn into the hollow spindle. The recirculation zone in the spindle intake, on the other hand, prevents the fibers twined over the spindle from drawing into the hollow spindle early. The velocity of Case 3 is the lowest in the spindle. In the inlet of the twisting chamber, there are supersonic zones in the vicinity of the spindle outer wall in all cases. It is helpful to eliminate short fibers. In Case 2, owing to high velocity and suitable supersonic zone, short fibers can be eliminated sufficiently and big fiber loss rate can be avoided. Because the supersonic zone in Case 3 is bigger than any of the others. Fiber loss may be increased for sliver with high short-fiber content. Consequently, yarn tenacity is decreased. In contrast with Cases 2 and 3, the velocity of Case 1 is the smallest. Therefore, Case 1 can spin staple fiber yarn because it may avoid too more short-fiber loss.

Regarding the principle of yarn formation in MVS, wall shear stress (WSS) can affect greatly the twisting degree of fiber twine over the spindle. The distributions of WSS across the outer wall of the hollow spindle in three cases are shown in Fig. 5. For the three cases, there are large WSS and the gradient of WSS near the inlet of the swirling chamber. After that, discontinuities occur, which verified the existence of the shock waves [12–14] and WSS decline quickly. Although WSS of Case 1 is the lowest in the inlet of

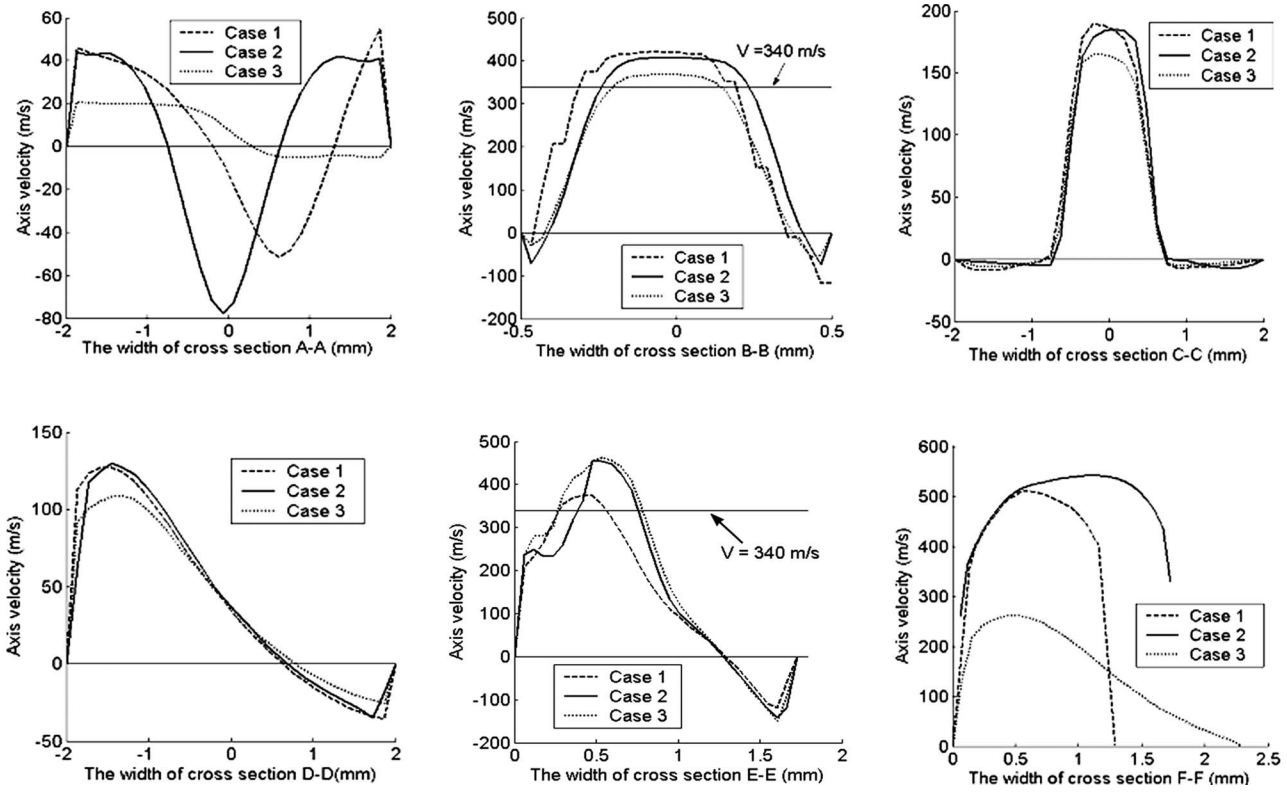

Fig. 4 Distributions of the axial velocities at different locations for three cases. For convenience to compare, a coordinate transformation is done to axial velocity at Section D-D in Case 2, but its magnitude keeps constant.

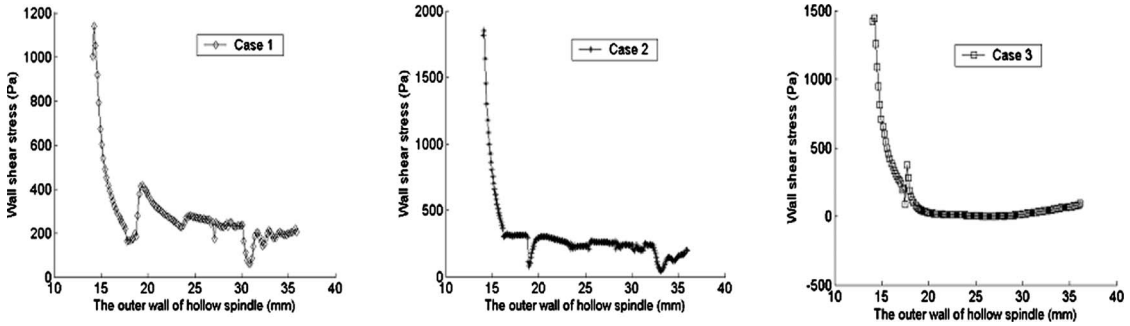

Fig. 5 The distributions of wall shear stress along the outer wall of the hollow spindle in three cases

the vortex chamber in three cases, WSS oscillates acutely after discontinuity. For fiber bundle (polyester) with longer mean length and lower cohesion force, this is disadvantageous to twist enough before they are drawn into the spindle. At the same time, in Case 3, it is difficult to get enough twisting for fibers with larger cohesion force due to the low WSS after discontinuity.

4 Experiment

For experimental purposes, three different nozzles, shown in Fig. 1, are used to spin pure cotton, pure polyester, and the polyester/cotton (T/C) blend with 30% of cotton ratio. After three passages of drawing, the slivers are transferred to MVS machine. To ensure comparison between the different mechanical performances of yarns, the optimized process parameters have the following specifications: the distance between front roller nip and nozzle inlet is 13 mm, the spinning speed is 180 m/min, the jet orifice angle (between the axis of jet orifice and x axis) is 80 deg, and the jet orifice pressure is 5 kg/cm^2.

All these yarns are tested on automatic single yarn strength tester with a testing speed of 200 mm/min under the test standard ISO2063–93. Mean tenacity and breaking extension are averaged from 50 observations for each yarn sample.

The properties of yarns, which spun by using 100% cotton, 100% polyester, and T70/C30 blends from different nozzles, are given in Table 1. Its experimental results show a similar trend for all the three kinds of yarns. Yarn tenacity increases with increasing polyester fiber content. The yarns spun by using Case 2 (α =12 deg) show the highest tenacity and the minimum irregularity values as compared with other yarns. However, when Case 1 is used to spin yarns, it is very easy to spin cotton fibers with high specific flexural rigidity and cohesion force [21], but it is difficult to spin polyester fiber. The reversed results can be obtained when Case 3 with bigger swirling chamber is used to spin yarns, that is, polyester fibers with low flexural rigidity and cohesion force [21] can be made. These results confirm the predictions deduced from our simulation.

Table 1 Effect of the cone angle of the spindle on yarn properties (Count, 21 tex)

Blend ratio T/C	Case	Strength (cN)	Tenacity (cN/tex)	Strength CV%	Elongation at break (%)	Elongation CV%
100/0	1	—	—	—	—	—
	2	480.0	22.9	12.1	8.5	6.5
	3	451.7	21.5	12.3	8.5	8.3
700/30	1	248.6	14.2	9.2	8.3	7.2
	2	325.3	18.6	9.3	8.1	6.6
	3	320.1	18.3	10.7	8.2	6.6
0/100	1	196.5	9.4	10.2	4.5	8.9
	2	204.5	9.6	10.4	4.6	9.1
	3	179.4	8.5	11.8	4.3	10.8

When the polyester fiber strand was processed, it is difficult to spin by using Case 1. Owing to small swirling chamber passage of Case 1, polyester fiber with low specific flexural rigidity [21] blocks easily the swirling chamber under the action of large eccentric vortex pair, and in turn, affects the twisting of yarn. However, after reducing the cone angle, swirling chamber passage enlarges and the asymmetry of CVP reduces. Therefore, polyester yarns can be produced when Cases 2 and 3 are used. Especially, for Case 2, yarn properties are improved obviously.

For the T70/C30 blend yarns spun by using the three nozzles, it is obvious that the performances, such as strength and elongation variations, are improved to a large extent. However, the strength CV% is increased. This may be because 70% polyester fiber mainly determines the yarn structure and affects the strength variation. On the other hand, the break elongation hardly changes.

Cotton vortex yarns that have the same fineness with polyester vortex yarn are also spun using the three nozzles. All properties of the yarn, which are spun by using Case 3 as nozzle, are the worst compared with that of two other cases. This may be due to the presence of a considerable amount of short fiber in cotton fibers and large supersonic zone in the inlet of the swirling chamber of Nozzle 3, to lead to a great deal of fibers loss.

5 Conclusions

A standard k-ε turbulence model is used to simulate the flow pattern inside the nozzle of MVS. The results in conjunction with the experimental data are analyzed. The analysis focuses on the influence of the cone angle of the hollow spindle on the flow characteristics in the nozzle and, consequently, yarn properties.

Our study demonstrates that the cone angle of the hollow spindle is an important parameter that affects yarn properties. Proper reduction in the cone angle of the spindle (α=12 deg, i.e., Case 2), which can increase the cross section area of the swirling chamber, is significant. In Case 2, flow characteristics, including axisymmetric CVP over the spindle, suitable high supersonic zone in the inlet of the swirling chamber, and the distribution of high and smooth WSS along the outer wall of the spindle, are propitious to spin high quality yarn. However, for too small cone angle of the spindle (Case 3), it is disadvantageous to spin staple fiber yarn because large and high supersonic zone and low WSS can lead to high fiber loss rate and insufficient twisting of the yarn. Simulation results also show that when using big cone angle of the spindle (Case 1), large eccentric CVP and high oscillation WSS will not ensure the sufficient twisting of the yarn for fibers with bigger flexural rigidity and longer principal length. The experimental works further confirm our predictions from the simulation.

Acknowledgment

This work is supported by the Specialized Research Fund for the Doctoral Program of Higher Education (SRFDP) in China under Grants No. 20040255009.

References

[1] Leary, R. H., 1997, "OTEMAS'97 Survey 1: Yarn Formation," Textile Asia, **28**(12), pp. 11–24.
[2] Örtlek, H. G., and Ülkü, S., 2005, "Pilling and Abrasion Performances of Murata Vortex Spun Cotton Yarns," Melliand International, **11**(4), pp. 287–289.
[3] Basal, G., and Oxenham, W., 2003, "Vortex Spun Yarn vs. Air-Jet Spun Yarn," Autex Research Journal, **3**(3), pp. 96–101.
[4] Ortlek, H. G., and Ulku, S., 2005, "Teffect of Some Variables on Properties of 100% Cotton Vortex Spun Yarn," Text. Res. J., **75**(6), pp. 458–461.
[5] Soe, A. K., Takahashi, M., Nakajima, M., Matsuo, T., and Matsumoto, T., 2004, "Structure and Properties of MVS Yarns in Comparison With Ring Yarns and Open-End Rotor Spun Yarns," Text. Res. J., **74**(9), pp. 819–826.
[6] Murata Machinery Limited, No. 851 Murata Vortex Spinner, Service Manual.
[7] Deno, K., 1996, "Spinning Apparatus With Twisting Guide Surface," U.S. Patent No. 5,528, 895.
[8] Tyagi, G. K., Sharma, D., and Salhotra, K. R., 2004, "Process Structure Property Relationship of Polyester Cotton MVS Yarns: Part I Influence of Processing Variables on Yarn Structural Parameters," Indian Journal of Fibre and Textile Research, **29**(4), pp. 419–428.
[9] Tyagi, G. K., Sharma, D., and Salhotra, K. R., 2004, "Process Structure Property Relationship of Polyester Cotton MVS Yarns: Part II Influence of Process Variables on Yarn Characteristics," Indian Journal of Fibre and Textile Research, **29**(4), pp. 429–435.
[10] Basal, G., and Oxenham, W., 2006, "Effects of Some Process Parameters on the Structure and Properties of Vortex Spun Yarn," Text. Res. J., **76**(6), pp. 492–499.
[11] Launder, B. E., and Spalding, D. B., 1972, *Lectures in Mathematical Models of Turbulence*, Academic, London.
[12] Bock, G., and Lunenschloss, J., 1981, "Air-Jet Stream and Loop Formation in Aerodynamic Texturing," Chemifasern/Textilinustrie, **31/83**(5), pp. 380–384.
[13] Acar, M., Turton, M. R., and Wray, G. R., 1986, "An Analysis of the Air Jet Yarn Texturing Process, Part II: Experimental Investigation of the Air-Flow," J. Text. Inst., **77**(1), pp. 28–43.
[14] Versteeg, H. K., Bilgin, S., and Acar, M., 1994, "Effects of Geometry on the Flow Characteristics and Texturing Performance of Air-Jet Texturing Nozzles," Text. Res. J., **64**(4), pp. 240–246.
[15] Patankar, S. V., 1980, *Numerical Heat Transfer and Fluid Flow*, McGraw-Hill, New York.
[16] Leonard, B. P., and Mokhtari., S., 1990, "ULTRA—SHARP Nanoscillatory Convection Schemes for High-Speed Steady Multidimensional Flow," NASA Lewis Research Center, NASA TM 1–2568 (ICOMP-90–12).
[17] Brandt, A., McCormick, S. F., and Ruge, J., 1982, "Algebraic Multigrid (AMG) for Automatic Multigrid Solution With Application to Geodetic Computations," Institute for Computational Studies, Colorado.
[18] Donaldson, C., and Snedeker, R. S., 1971, "A Study of Free Jet Impingement. Part 1: Mean Properties of Free and Impinging Jets," J. Fluid Mech., **45**, pp. 281–319.
[19] Beltaos, S., and Rajaratnam, N., 1974, "Impinging Circular Turbulent Jets," J. Hydr. Div., **B100**(HY10), pp. 1313–1328.
[20] Acar, M., Turton, M. R., and Wray, G. R., 1987, "Air Flow in Yarn Texturing Nozzles," ASME J. Eng. Ind., **109**(3), pp. 197–202.
[21] Morton, W. E., and Hearle, J. W. S., 1975, "Physical Properties of Textile Fibres," The Textile Institute, London.

Improvement of Hydrofoil Performance by Partial Ventilated Cavitation in Steady Flow and Periodic Gusts

Jim Kopriva

Roger E. A. Arndt

Saint Anthony Falls Laboratory,
University of Minnesota
Minneapolis, MN 55414

Eduard L. Amromin
Mechmath LLC,
Prior Lake, MN 55372

This paper describes a study of the response of a recently developed low-drag partially cavitating hydrofoil (denoted as OK-2003) to periodical perturbations of incoming flow. A two-flap assembly specially designed to simulate sea wave impact on the cavitating hydrofoil generates the perturbations. The design range of cavitation number was maintained by ventilation. Unsteady flow can be simulated over a range of ratios of gust flow wavelength to cavity length. The measurement of time-average lift and drag coefficients and their fluctuating values over a range of inflow characteristics allows a determination of hydrofoil performance over a range of conditions that could be expected for a prototype hydrofoil. Both regular interaction with practically linear perturbations and resonancelike singular interaction with substantial nonlinear effects were noted. The observations are accompanied by a numerical analysis that identifies resonance phenomena as a function of excitation frequency. [DOI: 10.1115/1.2842147]

1 Introduction

The theory of cavitation in an ideal fluid predicts a possibility to develop hydrofoils that have a significant decrease of drag and an increase in the lift in a partially cavitating flow regime. An example of such hydrofoil is the OK-2003 hydrofoil, which was first reported at the Cav-2003 Conference by Amromin et al. [1]. This study and subsequent research [2] identified a sharp peak of lift to drag ratio at design conditions. The hydrofoil OK-2003 shape was developed from the parent hydrofoil NACA-0015 on the basis of a solution of the problem of cavitation in an ideal fluid. The shape of both hydrofoils is shown in Fig. 1.

A cavity extends over a portion of the suction side of the foil and is designed to reattach smoothly at a fixed position (in this case at the 60% point). The essence of the design is the elimination of unsteady cavity dynamics by ensuring a smooth reattachment of the cavity. As shown in Figs. 2 and 3, the drag minimum and the mentioned peak of the lift to drag ratio takes place in a quite narrow range of cavitation number. In order to apply this design in practice, it would be necessary to keep such an increase in lift to drag ratio within a favorable range under diverse speed variations and periodic perturbations. Consideration must be given to the possibility of maintaining a favorable cavitation number by air ventilation into the cavity. Therefore, a reasonable extension of our previously reported studies [1,2] is an investigation of ventilated cavitation for both steady incoming flow and flow with a superimposed gust (to simulate wave impact).

There are two issues associated with ventilated partial cavitation. First, although ventilated cavitation is a very old topic of research, these studies mainly relate to supercavitation (e.g., Reichardt [3] and Kuklinski [4]), whereas ventilated partial cavitation has received little attention.

Second, although there are many towing tanks for the study of wave effects on ship models, few of these tanks are configured for testing ventilated hydrofoils. The use of a ventilated hydrofoil as a part of a tested model will introduce many side effects, and a confident determination of the wave effect on the hydrofoil itself would be a difficult problem. An exception to this are the many tow tank studies of ventilated hydrofoils carried out at the Saint Anthony Hydraulic Laboratory (now known as the Saint Anthony Falls Laboratory) [5,6].

In spite of the mentioned towing tank experience, water tunnels remain as the traditional facilities for testing of cavitating hydrofoils, but the simulation of a periodic inflow requires special attention. Although there are experimental studies of periodic perturbations of partial cavitation of marine propeller blades (by Weitendorf and Tanger [7], for example), our study required the development of special experimental tools because of the relatively low values of Strouhal number inherent to wave impact and the necessity to measure drag variations. These two issues are central to this paper.

2 Optimization of Airflow Rate

As illustrated in Figs. 2 and 3, the experiments have shown remarkably similar payoffs for both the natural and ventilated cases. However, natural cavities have lower shape/length pulsations and more transparent wakes. For these experiments, optimal air flux was associated with clear cavities. An increase in ventilation flow rate is generally required for a decrease of cavitation number. However, a decrease of σ by a gradual increase of Q for the partially cavitating hydrofoil OK-2003 has resulted in a jump of σ values over the range of lift maximum/drag minimum.

A comparison of the measurements of lift coefficient C_L and drag coefficient C_D at the same free stream velocity, $U_\infty = 8$ m/s, with various combinations of water tunnel pressure P_∞ and volumetric air flux Q have shown a gradual decrease of C_L with an increase in Q (shown in Fig. 4). On the other hand, C_D is only slightly changed with an increase in Q. These experiments yielded a reasonable flux minimum to obtain a favorable range of σ (as shown in Fig. 5). One can also note in Fig. 4 that for the maximum lift condition, natural cavitation has much lower force pulsations and that the amplitude of these pulsations increases with airflow rate.

An important need in experiments with partial cavities is the measurement of cavity pressure P_C. Usually, pressure measurement in cavities is quite difficult (see Arndt et al. [8]). However, because of the unusual stability of partial cavities on the hydrofoil OK-2003, successful measurements were made with a spanwise

Contributed by the Fluids Engineering Division for publication in the JOURNAL OF FLUIDS ENGINEERING. Manuscript received May 9, 2006; final manuscript received December 31, 2007; published online March 3, 2008. Review conducted by Georges L. Chahine.

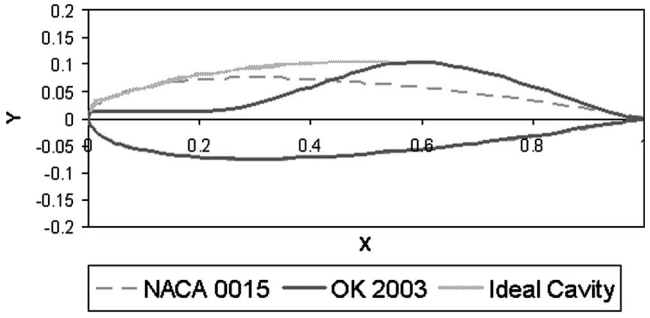

Fig. 1 Hydrofoil contours of the OK-2003 and NACA-0015. The ideal cavity shape predicted by theory is also shown.

distribution of several pressure taps just behind the cavity detachment line. These measurements yielded cavity pressure data as a function of upstream conditions and ventilation flow rate (P_∞, U_∞, and Q). These data were utilized for both steady and gust flow studies.

3 Gust Flow Generator

After reviewing known gust simulation concepts (described by Lorber and Covert [9], Neel et al. [10] and Delpero [11]), a gust generation apparatus was designed to model various sea conditions (see Fig. 6). Our approximate analytical estimation has shown that the concept described in Ref. [10] allows for a generation of incoming flow oscillations that are the best approximation of a sinusoidal velocity oscillation that might be experienced by hydrofoils in sea waves. With this concept in mind, a special flow apparatus was designed with two oscillatory flaps in the form of NACA-0020 hydrofoils. At the test Reynolds number, $\mathrm{Re}\sim 8\times 10^5$, flow separation is avoided up to angles of attack of 12 deg. The contour of these hydrofoils was also selected to avoid premature cavitation. In addition, the chord lengths of the two hydrofoils were selected to minimize unwanted blockage effects. The hydrofoils are oscillated in phase by a servomotor to provide uniform gusts. To allow for various gust amplitudes, an eccentric wheel provides offsets that allow for 2 deg, 4 deg, 6 deg, 8 deg, and 10 deg in flap oscillation amplitude. A flywheel and the ability to adjust the servomotor's proportional-integral-derivative (PID) gains allows the system to run smoothly under operation, keeping the speed of the motor within 3% of the desired rate. The servomotor can operate in the range 0–3500 rpm. Given this wide range of motor speed and the flow capabilities of the SAFL high-speed water tunnel (in excess of 20 m/s), a wide range of excitation Strouhal numbers can be obtained, allowing for the modeling of any desired sea state.

This water tunnel has a 0.19×0.19 m^2 cross section allowing for a hydrofoil span of 0.19 m. The stationary hydrofoil chord length used in this study is 0.081 m and can be viewed from the two side and bottom test section windows.

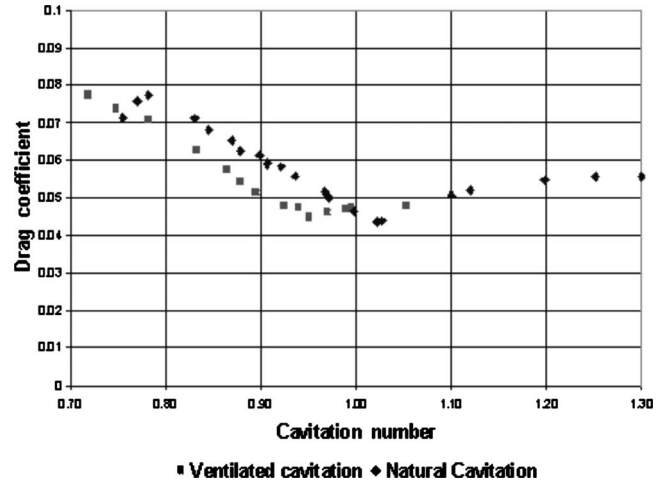

Fig. 2 Drag coefficient for natural and ventilated cavitations of the hydrofoil OK-2003 at α=6 deg

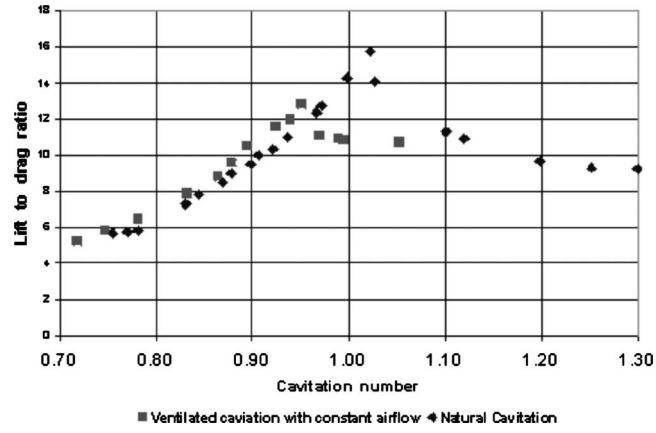

Fig. 3 Lift to drag ratio for natural and ventilated cavitations of the hydrofoil OK-2003 at α=6 deg

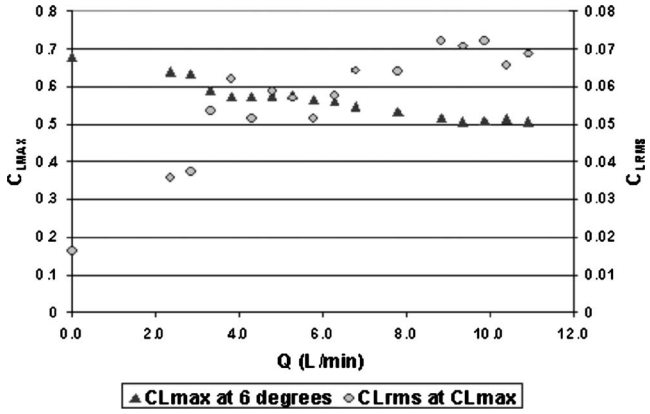

Fig. 4 Effect of airflow rate on the maximum values of average lift and fluctuating (rms) lift coefficients. U_∞=8 m/s, while P_c and P_∞ were tuned to maintain the maximum C_L.

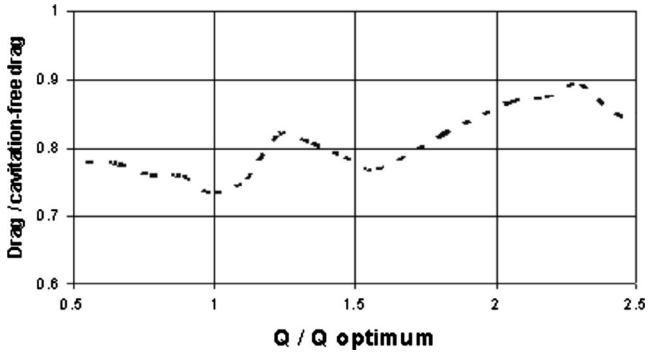

Fig. 5 Correlation between airflow rate Q and the total drag coefficient for cavitating hydrofoil OK-2003

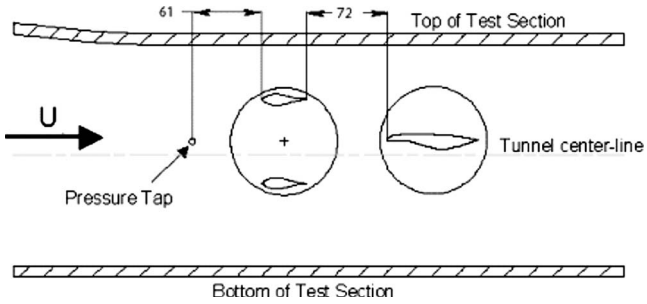

(*a*)

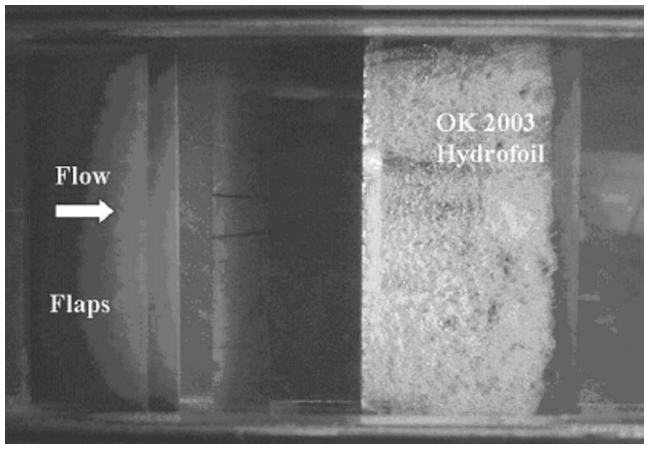

(*b*)

Fig. 6 Schematic of two-flap gust generator (top) and view from the bottom of the apparatus in place. Note that the OK-2003 hydrofoil is cavitating in the absence of cavitation on the gust generator.

Measurements of the gust obtained with laser Doppler velocimetry (LDV) have shown that the time-varying velocity amplitude and frequency can be represented with a sine function. In addition, LDV measurements have shown that the frequency of the gust is equal to the upstream oscillation frequency of the hydrofoils (see Fig. 7). Further details can be found in Ref. [12].

The gust flow characteristics in the water tunnel are also illustrated in Fig. 8. These data show the level of uniformity of the gust flow obtained for the modeling of wave impact in the water tunnel conditions. The gust angle of attack can be approximated as $\alpha_G = A_0 + A_1 \sin(\omega_t)$, but one can see in Fig. 7 that the real α_G is not a pure sinusoid because of the vortex sheet interaction behind the flaps. As a result of the simplified approximation of real flow by this single-frequency gust, $A_0 \neq 0$.

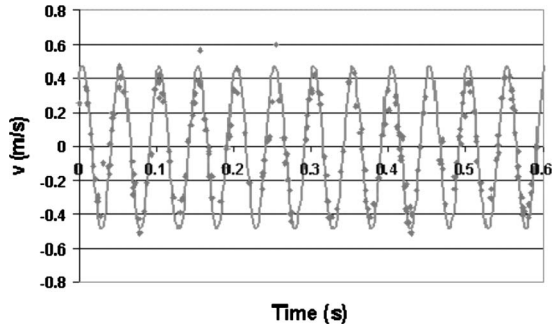

Fig. 7 Comparison of measured vertical velocity component (symbols) with its sinusoidal approximation (line)

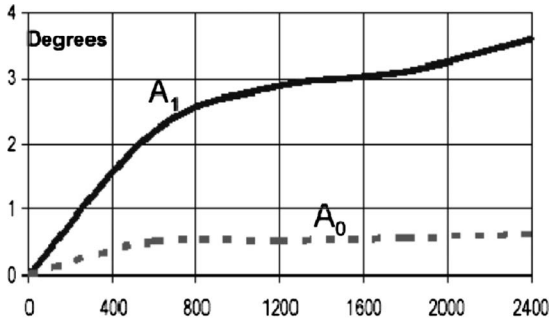

(*a*)

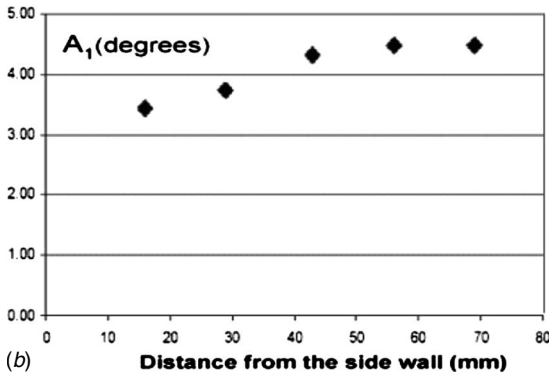

(*b*)

Fig. 8 Dependencies of coefficients A_0 and A_1 on flap rpm for β=3 deg flap oscillation amplitude shown on the top plot. Spanwise variation in oscillation amplitude A_1 for β=4 deg at 2400 rpm shown on the bottom plot.

As stated earlier [2] for a steady incoming flow, very stable cavities with clear reattachment lines and transparent wakes are observed over the range of σ where drag reduction occurs. As shown clearly in Fig. 9, this feature is retained in oscillatory flow as well.

4 Gust Impact on Average Forces

A series of experiments were carried out under periodic flow perturbations to estimate the possibility to use ventilation as a drag reduction technology under encounters with waves. All measurements in gust flow have been carried out with an air flux rate, Q=5 l/min, that was optimal in this study. It was assumed that the time-averaged dependency of the cavity pressure P_C on Q at the fixed P_∞ was not affected by the incoming flow perturbations described in Fig. 8.

The experimental study was carried out at two-flap angles of attack and two-flap frequencies corresponding to 1200 rpm and 2400 rpm (Fig. 10). The magnitude of flap oscillation was selected to be 2 deg and 4 deg. The corresponding excitation Strouhal numbers, based on hydrofoil chord c are St=0.2 and St=0.4. The measured data for lift, drag, and lift to drag ratio at St=0.2 are presented in Figs. 11–13.

The accuracy of the force balance for lift and drag is about 3% and 3.5%, respectively. This is based on full-scale measurements of 900 N lift and 100 N drag. All lift and drag data were recorded at a minimum of 2000 samples/s over a time interval of 2 s. This allowed for accurate statistical and frequency analysis. The actual angle of attack variation experienced by the hydrofoil is roughly half of the flap oscillation amplitude. The data indicate that there does not appear to be any substantial wave effect on the measured average forces at St=0.2. Note that a 4 deg flap oscillation corresponds to a 2 deg oscillation of the angle of attack for the down-

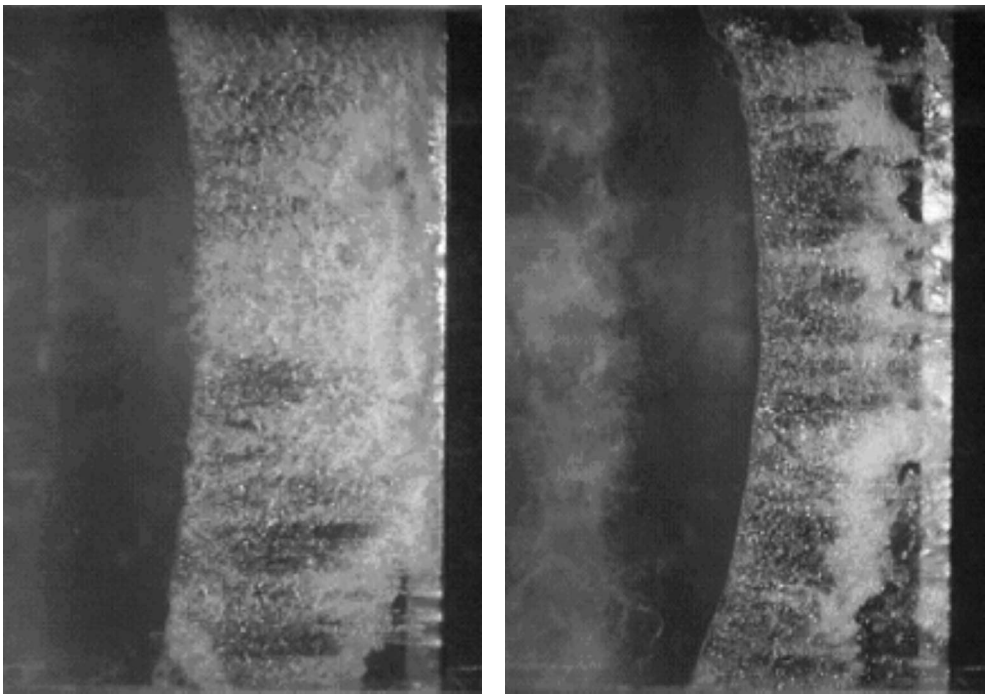

(*a*) (*b*)

Fig. 9 Opposite phases (left and right) of a ventilated cavity on the hydrofoil OK-2003 at α=6 deg and rpm=2400. The flow is from right to left.

stream hydrofoil, which is quite large for typical hydrofoils. The stationary hydrofoil, OK-2003, is placed at α=6 deg for all steady and oscillating flow cases unless otherwise specified (α is measured based on the steady flow case).

The measured data for drag, lift, and lift to drag ratio for St =0.4 are presented in Figs. 14–16. There is a similar correspondence between indices and flow parameters in these figures, but at this motor speed, a 4 deg flap oscillation induces a 2.5 deg oscillation of the angle of attack and a 2 deg flap oscillation induces a 1.25 deg oscillation of the angle of attack.

One can see that for St=0.4, the partially cavitating hydrofoil in unsteady flows exhibits greater lift and drag coefficients than it did in steady flow. The lift to drag ratio remains to be roughly the same, but the peak value and the σ range of drag reduction is

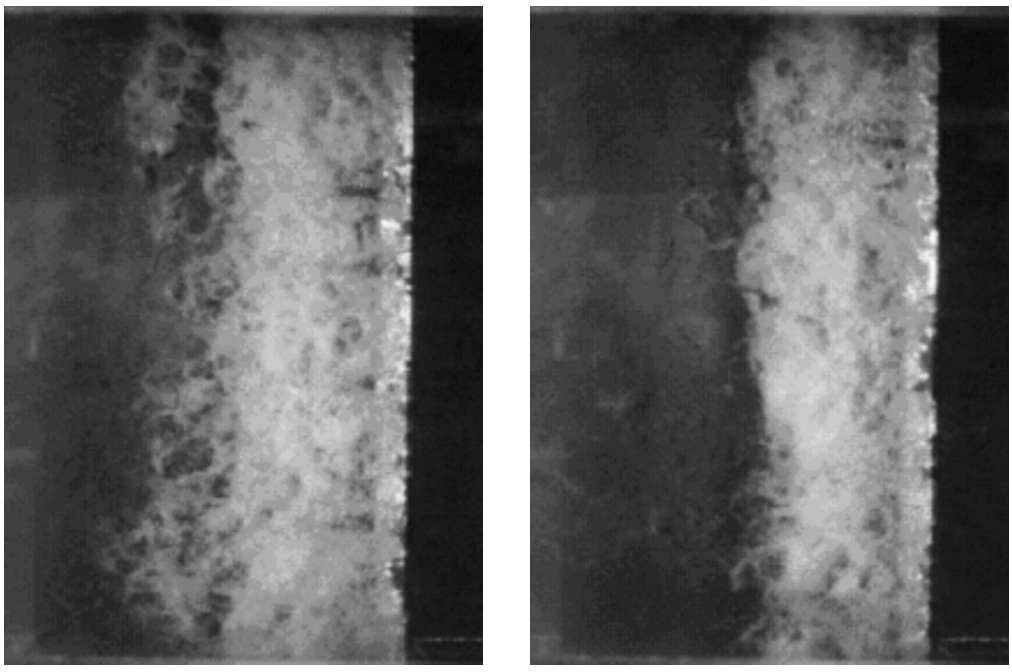

(*a*) (*b*)

Fig. 10 Opposite phases (left and right) of a ventilated cavity on the hydrofoil OK-2003 at α=7 deg and rpm=1200. The flow is from right to left.

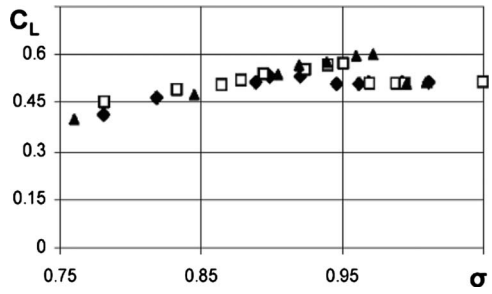

Fig. 11 Measured lift coefficient of the hydrofoil OK-2003 at St=0.2. Squares relate to steady flow, triangles to 2 deg of flap oscillation amplitude β, and rhombuses to β=4 deg.

shifted to a greater value of σ. The effect of incoming flow unsteadiness weakens with a decrease of σ corresponding to transition from partial cavitation to supercavitation.

For cavitating hydrofoils in gust flows, it is, however, necessary to separate the effects of a gust on a cavitation-free hydrofoil (with variations of its lift and drag that include the added mass influence as well) from cavitation-caused effects. In order to assess this distinction, the average drag of the cavitating hydrofoil is normalized by the average value of this cavitation-free hydrofoil in the same incoming flow (and presented in Fig. 17). Note that there is a certain jump of characteristics between St=0.2 and 0.4 in Fig. 17. Its nature can be possibly clarified with a force pulsation analysis.

5 Gust Impact on Pulsations

Figures 18 and 19 contain data for lift and drag pulsations at St=0.2 and St=0.4. It is necessary to keep in mind that the measured lift pulsation includes contributions from all oscillating sources, including a contribution caused by oscillations of the angle of attack during the wave period. The data in these plots show a qualitative effect of excitation frequency (Strouhal number) on the pulsation behavior.

There are lift pulsation minima at the design cavitation number, σ=0.95, for both values of excitation frequency used in this study. However, it is a flat minimum at St=0.2, and drag pulsation remains to be a flat function of σ at this excitation Strouhal number.

It should be noted in Fig. 19 that the data for St=0.4 do not display as smooth a dependency on σ. Note the deep minimum in the amplitude of lift pulsations at the design value of σ=1. A comparison with cavitation-free lift pulsations under the same perturbed incoming flow suggests some pitch damping by the partial cavitation at St=0.4 with an increase in pitch amplitude. A similar non-linearity is not shown at St=0.2. Other evidence of a strong nonlinearity at St=0.4 is the dependency of the time-averaged cavity length L with variations in St, as shown in Fig. 20. For linear perturbations, L should be independent of excitation frequency for any magnitude of its pulsation dL. In looking for the nature of this nonlinearity within the design range of σ, one can

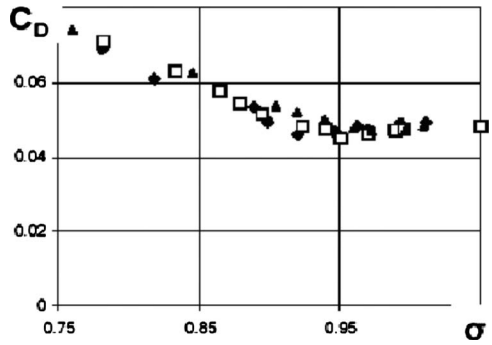

Fig. 12 Measured drag coefficient of the hydrofoil OK-2003 at St=0.2. Squares relate to steady flow, triangles to 2 deg of flap oscillation amplitude β, and rhombuses to β=4 deg.

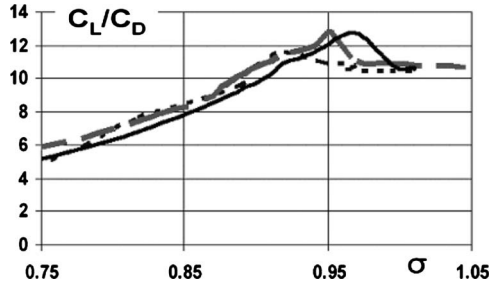

Fig. 13 Lift to drag ratio of the hydrofoil OK-2003 at St=0.2. Dashed line relates to steady flow, solid line relates to β =2 deg, and dotted line relates to β=4 deg.

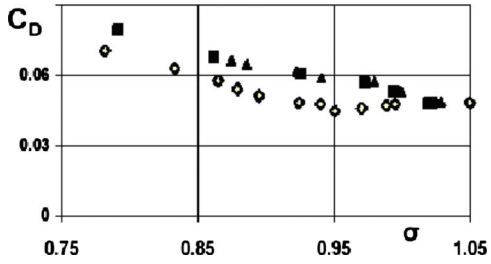

Fig. 14 Measured drag coefficient of the hydrofoil OK-2003 at St=0.4. Rhombuses relate to steady flow, squares relate to β =2 deg, and triangles relate to β=4 deg.

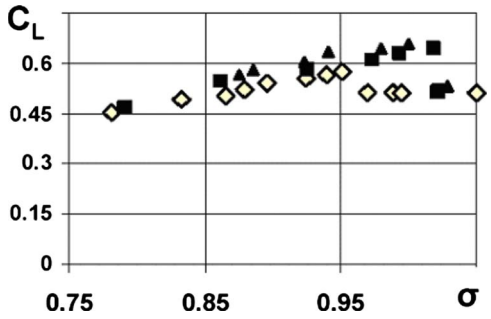

Fig. 15 Measured lift coefficient of the hydrofoil OK-2003 at St=0.4. Rhombuses relate to steady flow, squares relate to β =2 deg, and triangles relate to β=4 deg.

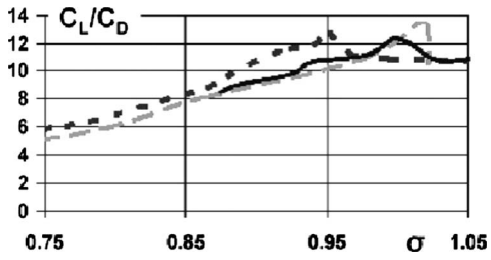

Fig. 16 Lift to drag ratio of the hydrofoil OK-2003 at St=0.4. Dotted line relates to steady flow, dashed line relates to β =2 deg, and solid line relates to β=4 deg.

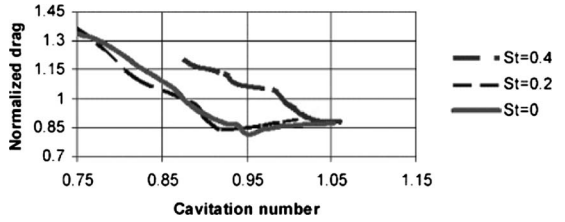

Fig. 17 Frequency effect on normalized drag reduction of the ventilated hydrofoil OK-2003 at α=6 deg and β=6 deg. Drag is normalized to drag for noncavitating flow.

note that for St=0.4, the assembly generates a gust of wavelength $\lambda \approx 4L$. This raises a suspicion that there may be some type of quarter-wave resonance in the wave-cavity interaction. Verification of such suspicion would require a detailed analysis of the effect of excitation frequency (Strouhal number), which would be quite difficult and time consuming experimentally because of the necessity to obtain data for numerous values of St. Therefore, a theoretical analysis was utilized to clarify the situation.

Such an analysis can be done in the framework of ideal fluid theory, with employment of an iterative numerical technique that was earlier applied (by Amromin and Kovinskaya [13]) to another unsteady problem on cavitation. A 2D incompressible periodic flow is considered. The velocity potential Φ is defined as the following sum:

$$\Phi(x,y,t) = \Phi_0(x,y) + \Phi_1(x,y)e^{i\omega t} + \Phi_2(x,y,\Gamma(x,t)) + \Phi_3(x,y,q(x,t)) \quad (1)$$

The term Φ_0 describes an unperturbed steady solution for the cavitating hydrofoil at a given pair of cavitation number σ and the angle of attack α. The term Φ_1 describes an incoming flow perturbation, while the terms Φ_2 and Φ_3 describe lift-variation-related and volume-variation-related hydrofoil hydrodynamic responses to this perturbation. Here, ω is the perturbation frequency, q is the density of sources distributed between points of cavity detachment X_1 and cavity end X_2, and Γ is the vortex intensity defined for $x>0$.

The potential Φ satisfies the Laplace equation $\Delta\Phi=0$ and four boundary conditions. The first condition is of the Newman kind. Because the hydrofoil is quite slender, the boundary condition may be written at its camber line,

$$-\frac{\partial\Phi}{\partial y} = \frac{\partial}{\partial t}\frac{H}{2} \quad (2)$$

Here, H is the cavity thickness. The second condition is the pressure constancy condition for the cavity for $X_1<x<X_2$. For the usual assumptions of potential theory, this condition can be written as

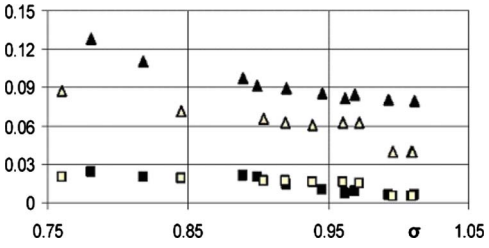

Fig. 18 Measured rms pulsation of lift and drag for the ventilated hydrofoil OK-2003 at St=0.2. Lift pulsations are shown by triangles; drag pulsations are shown by squares. Data for β =4 deg are shown by shaded symbols; data for β=2 deg are shown by open symbols.

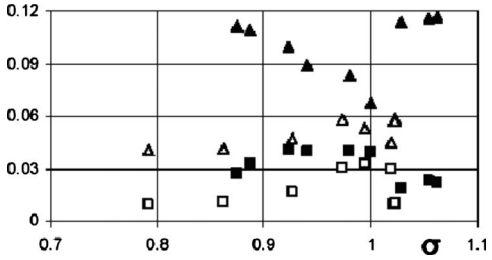

Fig. 19 Measured rms pulsation of lift and drag for the ventilated hydrofoil OK-2003 at St=0.4. Lift pulsations are shown by triangles; drag pulsations are shown by squares. Data for β =4 deg are shown by shaded symbols; data for β=2 deg are shown by open symbols.

$$\frac{U^2(x_1,t) - U^2(x,t)}{2} + \frac{\partial}{\partial t}(\Phi(x,Y,t) - \Phi(x_1,Y,t)) = 0 \quad (3)$$

Here, $U=\text{grad}(\Phi)$. The third and fourth conditions are the conservation law for Γ, also known as the Helmholtz theorem and the Kutta–Joukowski condition. Following Ref. [13], we obtain these conditions with a Birnbaum equation for Γ and represent q through H. The perturbation of the cavity thickness H is approximated by the following series:

$$H(x,t) = e^{i\omega t}\sum_{m=1} B_m \sin\left(\frac{\pi m}{2}\frac{(x-X_1)}{(X_2-X_1)}\right) \quad (4)$$

It is evident that odd coefficients of the series in Eq. (4) describe thickness oscillation of the cavity tail and is proportional to the pulsation of the drag coefficient.

Thus, solving a steady cavitation problem (described in Ref. [2]) for given L or σ allows computation of derivatives of Φ_0, whereas tuning of the function Φ_1 allows approximation of the profiles of the velocity perturbation corresponding to measurements in Fig. 3. Substitution of Eqs. (1) and (4) into Eqs. (2) and (3) with the assumption of small perturbations makes it possible to compute q, Γ, and other unknown quantities (there are intermediate transforms that are omitted here as a secondary detail). As shown in Fig. 20, computed pulsations of the cavity length are in the range of measured pulsations and reflect the general tendency, and it is a validation for these computations.

Further, the computed pulsation of the cavity thickness in Fig. 21 substantially depends on St and has a sharp maximum near St=0.45. However, there is the observed effect of St on the time-average cavity length L, and this effect was not taken into account

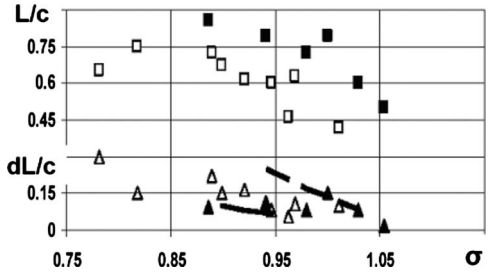

Fig. 20 Cavity length *L* and cavity length pulsation amplitude *dL* on the ventilated OK-2003 hydrofoil for β=4 deg. Squares show *L* values; triangles show *dL*. Shaded symbols relate to experimental data for St=0.4; open symbols relate to St=0.2. The dashed line for St=0.4 and the solid line for St=0.2 are computational results.

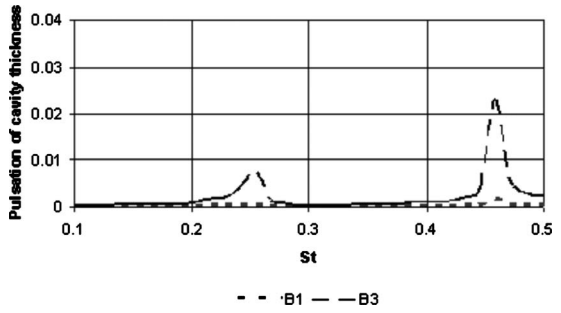

Fig. 21 Coefficients describing thickness oscillation of the cavity tail versus St. Computation made for 4 deg flap oscillations and σ=1.0.

in computations that underestimate it and, as a result, overestimate the chord-based St. Possibly, a more accurate computation would find the peak of B_3 at St$\approx$0.4.

On the other hand, the peak value of B_3 in Fig. 21 is of the same order with drag pulsation maximum in Fig. 19. Thus, according to the provided approximate numerical analysis, there is a resonance-similar anomaly in the wave effect on cavitation at St =0.4. A more significant resonance was experimentally detected at 60 Hz, but a hydroelastic analysis has shown that there is the first structural (bending) resonance at such frequency corresponding to St=0.6.

6 Conclusions

An experimental study of hydrofoil drag reduction by ventilated partial cavitation in steady and unsteady flows has been performed. It was determined that ventilated cavitation on the OK-2003 hydrofoil is effective in reducing drag and sharply increasing the lift to drag ratio. The measured maximum of L/D is slightly lower than that obtained with natural cavitation. The hydrofoil OK-2003 designed for cavitating flows exhibits lower lift to drag ratio for cavitation-free flow than the parent traditional hydrofoil has at Reynolds number of model tests. The Reynolds number effect on the performance of OK-2003 and similar hydrofoils was not studied yet.

The maximum L/D ratio corresponds to quite low airflow rates. Further increase in the ventilation flow rate leads to some increase of drag coefficient and a significant decrease of the lift coefficient. The ability of the OK-2003 hydrofoil to maintain high performance under moderate wave impact was demonstrated with a specially designed two-flap apparatus.

The experiments have also shown a substantially new effect of the perturbation frequency (Strouhal number, St) on pulsations of lift and drag as well as an effect on the time-average cavity length. As clarified by numerical analysis, a resonance in wave-induced cavity oscillation can take place with gust perturbations.

Acknowledgment

The authors appreciate the support of DARPA under Contract No. W31P4Q-04-C-R012 (contract monitors Capt. J. Kamp and Dr. T. Kooij).

Nomenclature

c = hydrofoil chord
C_D = drag coefficient
C_L = lift coefficient
C_Q = ventilation coefficient, Q/UA
H = oscillation of cavity thickness
L = cavity length
N = normal to S
P_C = pressure within cavity
P_∞ = unperturbed pressure
q = source strength distribution
Q = ventilation flow rate
s = span
S = boundary of inviscid flow
U = velocity in inviscid flow related to U_∞
U_∞ = free stream speed
α = angle of the attack
$\boldsymbol{\alpha_G}$ = gust angle of attack
β = amplitude of flap oscillation angle
δ_C = hydrofoil camber
δ_T = hydrofoil thickness
σ = $2(P_\infty - P_C)/(\rho U_\infty^2)$, cavitation number
ρ = water density
Φ = velocity potential
ω = frequency of gust

References

[1] Amromin, E. L., Hansberger, J., Arndt, R. E. A., and Wosnik, M., 2003, "Investigation of a Low-Drag Partially Cavitating Hydrofoil," *Cav-2003 Symposium*.
[2] Amromin, E. L., Kopriva, J., Arndt, R. E. A., and Wosnik, M., 2006, "Hydrofoil Drag Reduction by Partial Cavitation," ASME J. Fluids Eng., **128**, pp. 931–936.
[3] Reichardt, H., 1946, "The Law of Cavitation Bubbles at Axially Symmetric Bodies in a Flow," Ministry of Aircraft Production, Report and Translation No. 766.
[4] Kuklinski, R., Henoch, C., and Castano, J., 2001, "Experimental Studies of Ventilated Cavities on Dynamic Test Model." *Cav-2001 Symposium*, Pasadena.
[5] Schiebe, F. R., and Wetzel, J. M., 1964, "Further Studies of Ventilated Cavities on Submerged Bodies," University of Minnesota—SAFL, Project Report No. 72.
[6] Silberman, E., and Song, C. S., 1961, "Instability of Ventilated Cavities." J. Ship Res., **5**(1), pp. 13–33.
[7] Weitendorf, E.-A., and Tanger, H., 1994, "Cavitation Investigation in Two Conventional Tunnels and the Hydrodynamics and Cavitation Tunnel HYKAT," *ASME, FED*, Vol. 177, pp. 73–90.
[8] Arndt, R. E. A., Kawakami, D., and Wosnik, M., 2007, "Measurements in Cavitating Flows," *Handbook of Fluid Mechanics Measurements*, Springer-Verlag, Berlin, in press.
[9] Lorber, P. F., and Covert, E. E., 1982, "Unsteady Airfoil Pressure Produced by Aerodynamic Interference," AIAA J., **20**, pp. 1153–1159.
[10] Neel, R. E., Walters, R. W., and Simpson, R. L., 1998, "Computations of Steady and Unsteady Low-Speed Turbulent Separated Flows," AIAA J., **36**, pp. 1208–1215.
[11] Delpero, P. M., 1992, "Investigation of Flows Around a 2D Hydrofoil Subject to a High Reduced Frequency Gust Load," MS thesis, MIT.
[12] Kopriva, J., 2006, "Experimental Study of a High Performance Partial Cavitating Hydrofoil Under Steady and Periodic Flows," MS thesis, Department of Mechanical Engineering, University of Minnesota.
[13] Amromin, E. L., and Kovinskaya, S. I., 2000, "Vibration of Cavitating Elastic Wing in a Periodically Perturbed Flow: Excitation of Sub-Harmonics," J. Fluids Struct., **14**, pp. 735–751.

S. C. Li[1]
School of Engineering,
University of Warwick,
Coventry CV4 7AL, UK;
State Key Laboratory of Hydroscience
and Engineering,
Tsinghua University,
Beijing 100084, P.R.C.
e-mail: scl@eng.warwick.ac.uk

Z. G. Zuo
School of Engineering,
University of Warwick,
Coventry CV4 7AL, UK

S. H. Liu

Y. L. Wu

State Key Laboratory of Hydroscience
and Engineering,
Tsinghua University,
Beijing, 100084, P.R.C.

S. Li
School of Engineering,
University of Warwick,
Coventry CV4 7AL, UK

Cavitation Resonance

This article deals with a phenomenon named as cavitation resonance. Cavitation-associated pressure fluctuations in hydraulic systems affect their design, operation, and safety. Under certain conditions, the amplitude of a particular component of these fluctuations will be significantly magnified, causing a resonance. Here, the observed phenomenon from three different flow systems is briefly introduced. Based on the coupling of two subsystems, a hypothesis of (macroscopic) mechanism reduced from these experimental observations is presented. [DOI: 10.1115/1.2842149]

Keywords: cavitation, resonance, system instability, pressure fluctuations

1 Introduction

Low-frequency fluctuations in flow systems, such as power swing caused by pressure fluctuations in draft-tube (cavitating) flows of turbine systems, has been a research subject since 1940 by Rheingans [1]. Many contributions have been made to these pressure fluctuations, particularly for cavitating flows, such as the "water plug" model for simulating the free oscillations in the draft tube of Francis turbines induced by cavitation cloud there (e.g., Refs. [2–5]). For more information, about cavitation induced oscillations and vibrations in turbomachinery (turbines and pumps), readers are referred to, e.g., the reviews by Henry, Tsujimoto, Sato, Turton, Martin, and Tsukamoto in Ref. [6]. The recent work by the Grenoble group [7] supported by the French Space Agency Centre National d'Etudes Spatiales (CNES) was also a good contribution toward local instability study. However, it has been noticed that under certain flow conditions, a particular component of these pressure fluctuations would be manifested and significantly magnified with attributions similar to resonance, revealing as system instability. This feature was firstly noticed by Li et al. in 1983 and 1986 [8,9] when they were studying cavitating flows on the UM[2] Venturi.

Owing to its significance to the safety and reliability of hydraulic systems, this study has been systematically performed on three different systems, including the latest one by Zuo et al. [10], to verify the hypothesis of resonance proposed. That is, subject to system characteristics, a particular component of low-frequency pressure fluctuations[3] associated with cavitating flows will be significantly magnified through the coupling of cavitation cloud (i.e., the collective bubbles) with liquid phase of the flow system, leading to a resonance. It has also been experimentally proven that the frequency at which cavitation resonances occur is actually one of the frequencies of the liquid phase at noncavitation condition, which is not modified by the presence of cavitation and thus distinguishes itself from those cavitation-associated pressure fluctuations whose frequencies are modified with both the presence and the pattern/level of cavitation. In other words, the frequency of cavitation resonance is the system's frequencies when it is not cavitated. This frequency of cavitation resonant for these three systems can be accurately predicted by a numerical approach proposed based on this resonance concept.

Having done these experimental and numerical works, based on an understanding of cavitation cloud (as collective bubbles) being one of the subsystems and the liquid phase as the other, a *macromechanism* (in contrast to the mechanism at the level of individual bubbles, referred as *micromechanism*) has now been concretely established, and the phenomenon can be accurately predicted by using the approach proposed by Li [11]. Therefore, these results are thus to be published formally.

2 Features of Phenomenon

The features of this phenomenon were firstly revealed through the analysis of cavitating flow on the UM Venturi (Fig. 1).

[1]Corresponding author.
[2]The University of Michigan, USA.

Contributed by the Fluids Engineering Division of ASME for publication in the JOURNAL OF FLUIDS ENGINEERING. Manuscript received December 20, 2006; final manuscript received December 21, 2007; published online March 3, 2008. Assoc. Editor: Steven Ceccio.

[3]That is, in contrast to the natural (high) frequencies of individual bubbles, a low-frequency noise component is always observed. It is believed to be generated by the bubble cloud oscillating at its characteristic frequency.

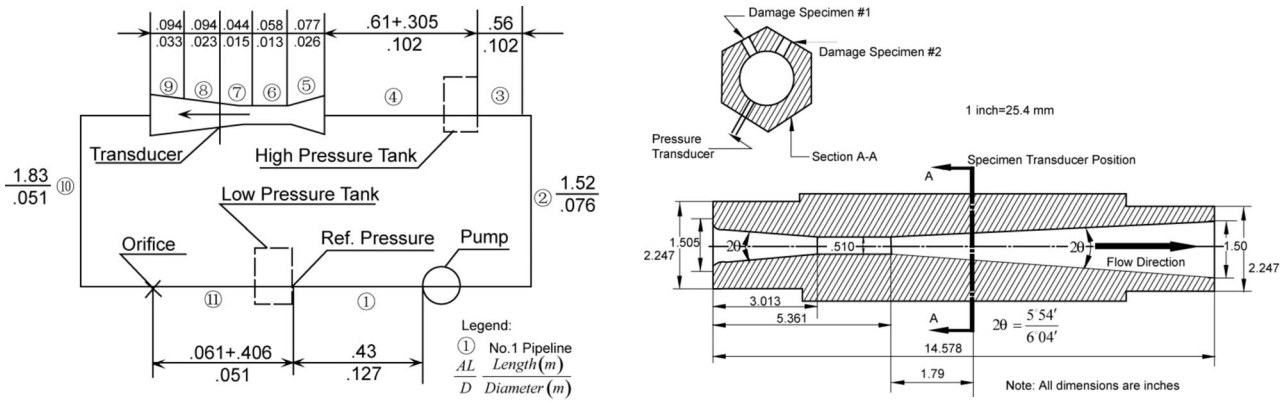

(*a*) (*b*)

Fig. 1 (*a*) Schematic of the UM Venturi. (*b*) Details of the Venturi section.

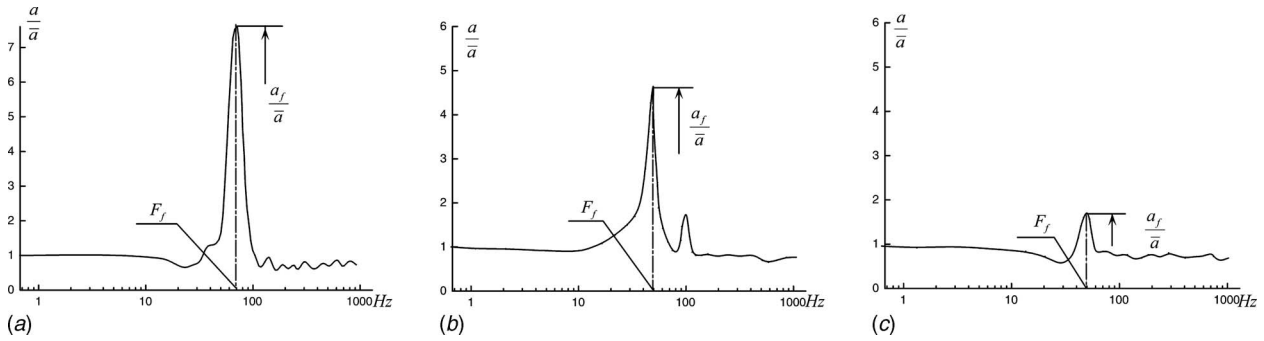

(*a*) (*b*) (*c*)

Fig. 2 FFT results of fluctuations for (*a*) σ=0.84, (*b*) σ=0.74, and (*c*) σ=0.69

When the pressure oscillation is sampled from the throat of the Venturi test section (location of the transducer is shown in Fig. 1), a particular component of low-frequency pressure fluctuations (f_0=50–60 Hz) was observed whenever cavitation appeared even if it was not visible yet. More details of the configuration and the nature of the data sampled are available [8,11]. The spectral analysis (Fig. 2) shows that for σ=0.84, 0.74, and 0.69, a particular component of fluctuations persistently appears at f_0=50–60 Hz. Its amplitude, not frequency, varies with cavitation number σ with a peak at σ=0.81, referring to Fig. 3.

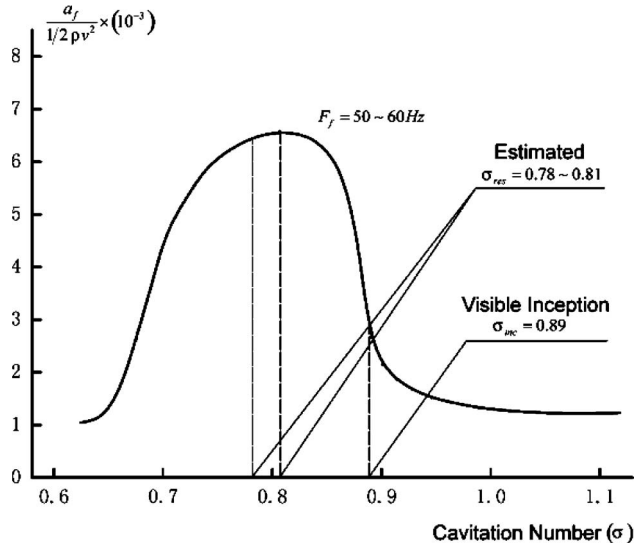

Fig. 3 Amplitude variation of the particular fluctuation-component with cavitation number

Hydraulic impedance approach is a method for free vibration analysis, which is a mean of identifying the oscillatory modes of nonforced vibration in a system. Therefore, it is useful in system analysis in which the forcing function is unknown. It is thus particularly useful for locating sources responsible for unknown vibrations in a flow system [12]. The frequency scan[4] reveals that the value of the first harmonic of the complex frequency $s=\sigma_f+i\omega$ is equal to $-1.03+i385.16$. That is, the first harmonic frequency of the (liquid phase) system (i.e., at noncavitating conditions), $f_{\text{liq}}=\omega/2\pi=61.3$ Hz agrees well with the observed value f_0=50–60 Hz with the presence of cavitation at the Venturi throat. More details of the nature of the signals are available in Ref. [11].

The mode shape analysis as shown in Fig. 5 reveals that for the first harmonic, i.e., $s=-1.03+i385.16$, the hydraulic impedance[5] at the throat and the diffuser of the Venturi section[6] reaches an extremely high level,[7] where it is just the location where the cavi-

[4]First, with an assumption of σ_f=0, it finds a number of minima of impedance ($Z12$) at the exit of the low-pressure tank. The results are then represented as a graph of modulus $|Z12|$ against ω, as shown in Fig. 4. Second, Newton's method is used to determine the exact values of $s=\sigma_f+i\omega$ to satisfy $Z12=0$.

[5]The impedance is defined as $Z(X)=H(X)/Q(X)$. The large value of $Z(x)$ indicates that a small flow-rate perturbation can trigger large pressure oscillation.

[6]By cross reference to Fig. 1(*a*), the corresponding component in the venture system can be identified. Here, sections 5–9 in Fig. 5 correspond to the sections 5–9 (divisions of venture section) in Fig. 1(*a*).

[7]From the definition of impedance, it is readily seen that a high impedance (say, at the throat) indicates a low flow-rate fluctuation $Q(x)$ and high-pressure fluctuation $H(x)$. In other words, any small flow-rate variation will trigger high-pressure fluctuations.

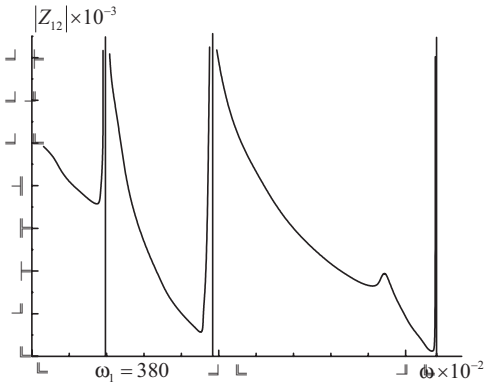

Fig. 4 Frequency scan of UM Venturi, with an assumption of σ_f=0. These results are to be fed as input to Newton's method for finding exact values of the natural frequencies of the non-cavitated system.

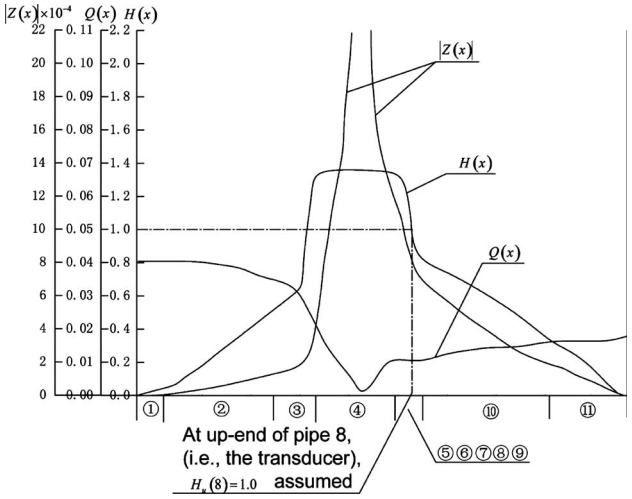

Fig. 5 Mode shape of UM Venturi for $s=-1.03+i385.16$

tation cloud appears. The unsteadiness of cavitation is actually a flow-rate oscillation that triggers and manifests significantly this particular component of pressure fluctuations owing to the high hydraulic impedance, particularly for this frequency f_0.

Similar features have been observed from the cavitating flows on a closed model turbine (Francis) system by Li in 1992 [13] and currently on the Warwick Venturi by Zuo et al. [10].

The instability caused by cavitating turbomachinery (pumps and turbines) is complicated. For turbines, a lumped parameter model (water plug) is most commonly used for cavitating draft-tube flow. It assumes that the cavitated portion functions only as a compliance (or capacitance), together with the water portion, in the draft tube as a local oscillating system, inducing instability locally. It treats the draft-tube flow as a tube closed at the tapered end (inlet) by the runner and opened with a zero impedance limit at the outlet, forming a water plug. Based on this concept, more accurate models have also been developed, e.g., by Jacob et al. in 1987, 1988, and 1992 [3–5]. For details, see review by Henry in Ref. [6]. However, the draft-tube flow in Francis turbines is complex, owing to its nature of swirling and bending. Under cavitation conditions (i.e., cavitating draft flow) from our model studies [13], the cavity itself in the draft tube can also serve as an exciter in some cases rather than simply a capacitor. In other words, the entire cavitated turbine system has two subsystems: One is the liquid phase and the other is the cavitation (bubble) cloud, which is different from the concept that the presence of cavitation simply adds a component (capacitor) into the liquid system.

The experiments were performed in 1980s on a Francis turbine model (HL-169-25) system, whose schematic configuration (including test rig) is shown in Fig. 6(*a*), and fuller descriptions of the experiment are available [13]. A series of transducers shown in Fig. 7(*b*) was employed to monitor the nature and variation of fluctuations in the flow system particularly for those in the draft tube and the spiral case. A particular component of fluctuations $f2$ with a frequency $f_0=52-88$ Hz has been sampled throughout the system for different guide-vane openings, a_0(mm), referring to Fig. 7(*a*). It always appeared at the system's natural frequency

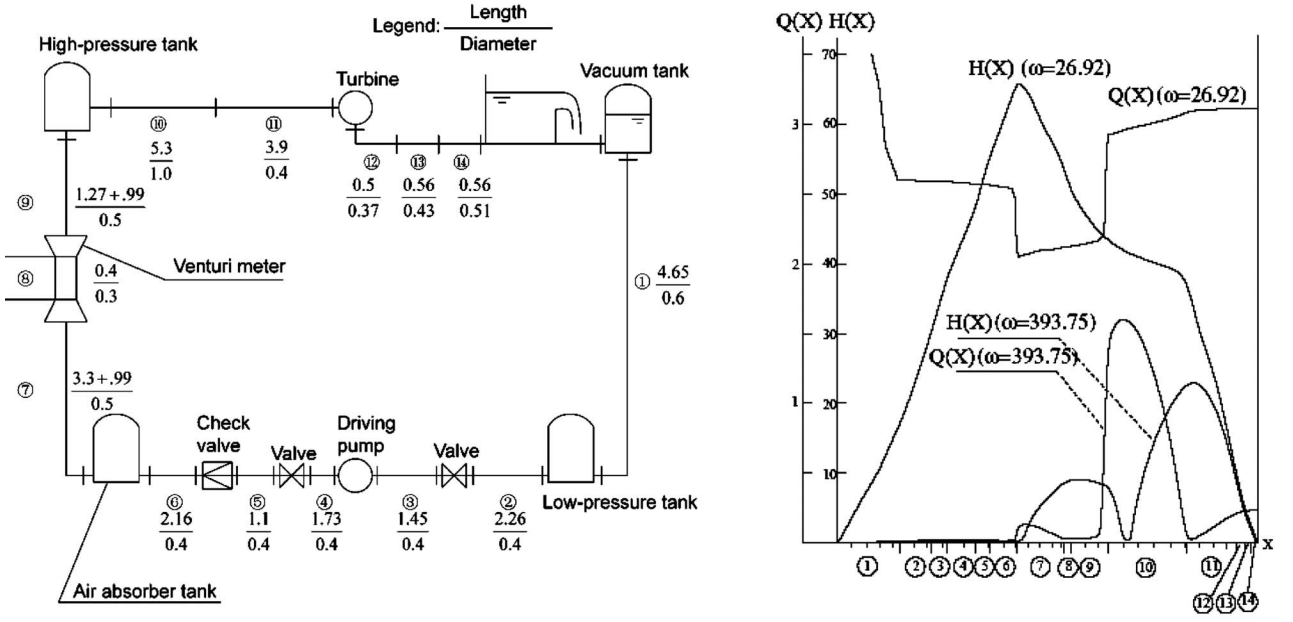

(*a*) (*b*)

Fig. 6 (*a*) Schematic of Francis turbine model HL-169-25 and its cavitation test rig. (*b*) Low-frequency fluctuations from HL-169-25 turbine: mode shape analysis.

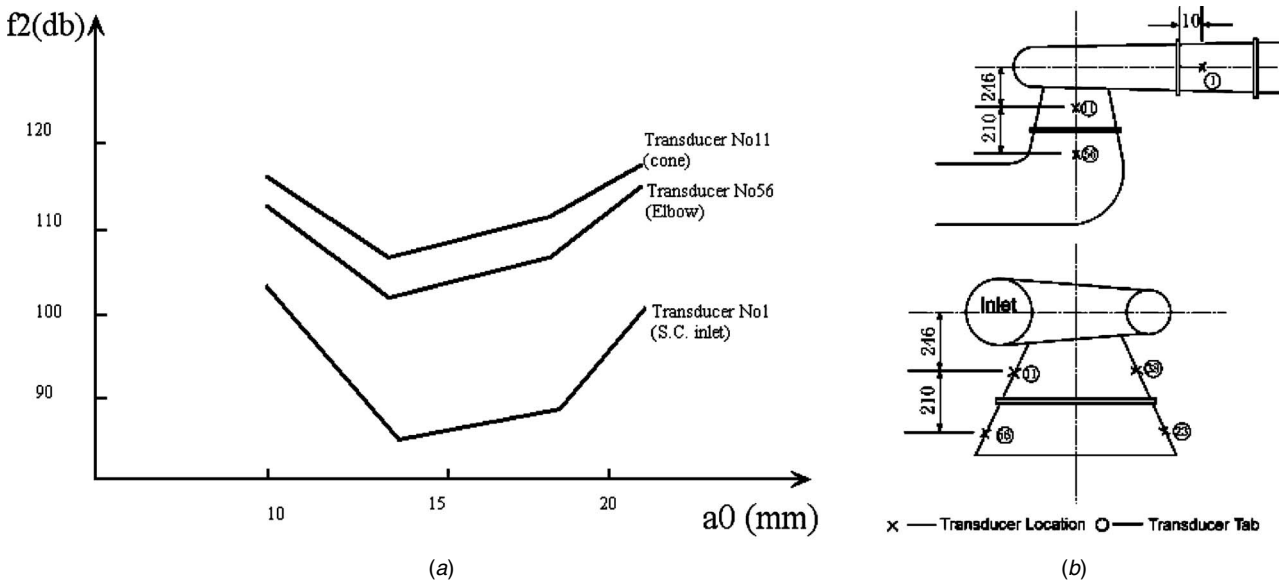

Fig. 7 (*a*) **The particular fluctuation component *f*2 (with frequency f_0=52–88 Hz) against the guide-vane openings a_0 measured in the cone (No. 11 transducer) and elbow (No. 56 transducer) of the draft tube and in the spiral case (No. 1 transducer), respectively: The same variation pattern with guide-vane opening for these three different locations indicates the propagation of the *f*2 component in the system under initial cavitation conditions.** (*b*) **The locations of the pressure transducer Nos. 1, 11, and 52 on the model turbine (distance unit: mm).**

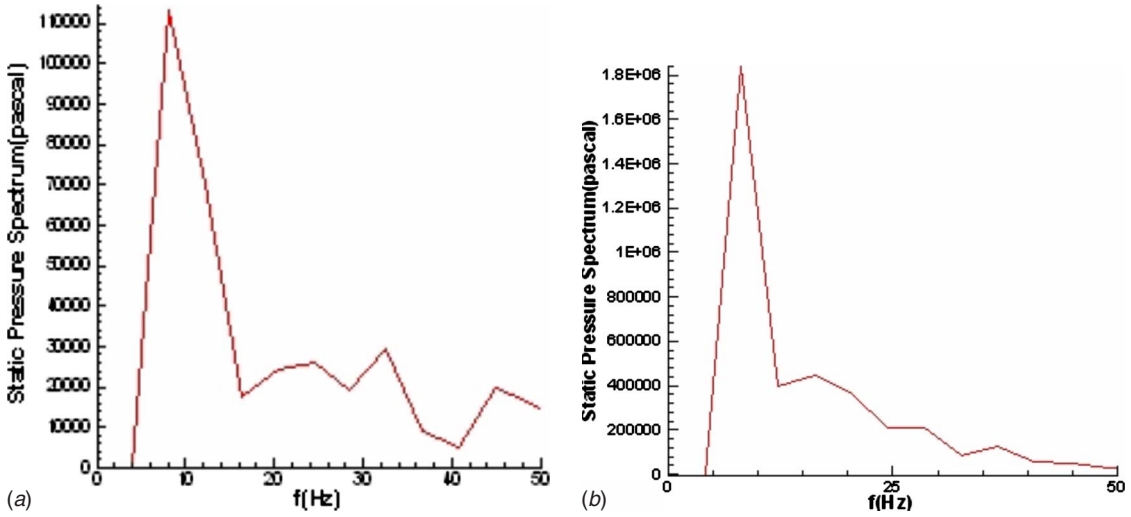

Fig. 8 The spectra at the inlet of spiral case and at the inlet of the draft tube, both showing a distinguishing component (around 10 Hz), indicate the propagation of this component throughout the system. (*a*) **Pressure fluctuations at the inlet of the spiral case.** (*b*) **Pressure fluctuations at the inlet of the draft tube.**

once cavitation occurs. Our numerical analysis confirmed the observed value of frequency f_0 (in this case, f_0=52–88 Hz) in agreement with the second harmonic frequency, s_2=−0.36 +*i*393.75 (note: not the first harmonic frequency, s_1=−0.8 +*i*26.92), of the system. The reason was that the impedance of the draft tube (corresponding to zone 12-14 on the abscissa) for s_2 reached its peak value (much higher than for s_1)[8] and thus provided an environment for the cavitation cloud to behave as a resonance exciter at this particular frequency, referring to Fig. 6.

Apart from similar features discovered from the UM Venturi, this study also confirms the nature of system instability rather than local instability. That is, it passes throughout the entire system, as shown in Fig. 7(*a*). Recently, for Three Gorge Power Station, a numerical study in 2004 by Liu et al.[9] [14] confirms the attribution that the draft-tube pressure unsteadiness is not a localized oscillation (Fig. 8), supporting the coupling hypothesis proposed through our experimental study.

Currently, we are further verifying this mechanism by using the third facility, i.e., a purposely designed and built Venturi at Warwick University. Apart from macroscopic behavior, with the advance made in the last two decades, we are now able to perform both the direct numerical simulation (DNS) and the experimental observations (using extremely high-speed camera[10]) at the level down to individual bubbles. This will open a door for searching

[8]Note: The value of impedance Z is not plotted in the figure. However, since $Z(x)=H(x)/Q(x)$, it is readily to see that $Z(12-14)_{S2}>Z(12-14)_{S1}$.

[9]This work was based on the true unsteadiness of rotor-stator interaction, enabling the propagation of pressure fluctuations throughout the entire flow system.

[10]The advance in high-speed photography has facilitated the observation of individual bubble behavior in cavitation cloud [17].

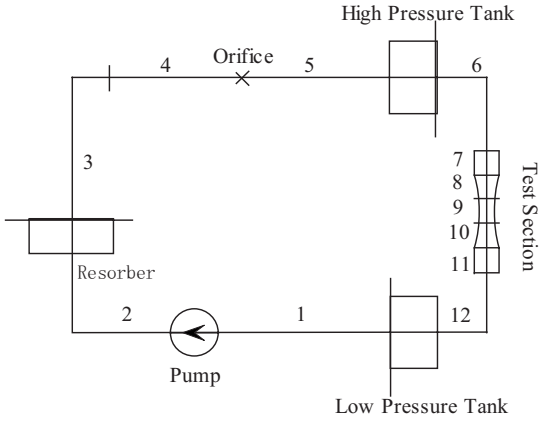

Fig. 9 Schematic of Warwick Venturi

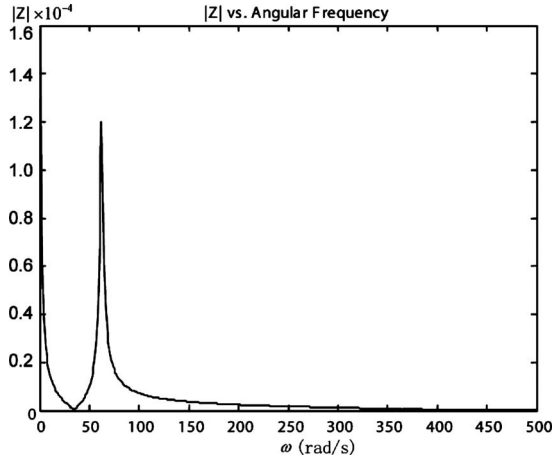

Fig. 10 Frequency scanning result showing the first harmonic frequency of f_0=5.4 Hz (i.e., ω=33.93 rad/s).

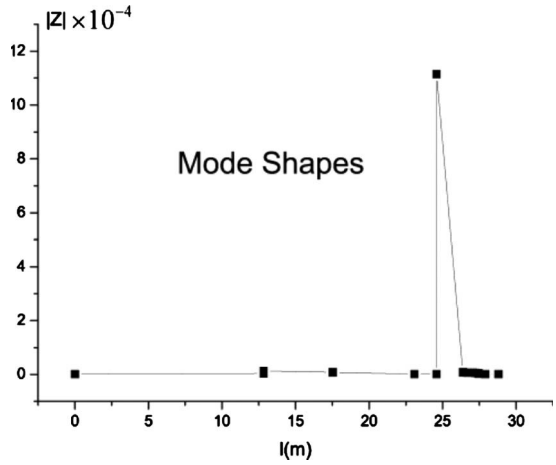

Fig. 11 Mode shapes of Warwick Venturi (hydraulic impedance)

the microscopic behavior (or mechanism) of this resonance, answering many unknowns raised from the observed phenomenon. The Warwick cavitating Venturi is a versatile facility for a stochastic study of bubble behavior near boundaries [15,16]. The initial results obtained by using the similar approach as for the UM Venturi confirm the hypothesis proposed despite the fact that these two Venturi systems are very different in size and layout, etc. The resonance frequency of Warwick Venturi can also be precisely predicted by using the approach proposed before. These are briefly cited below; for details, see Ref. [10].

A similar numerical analysis based on hydraulic impedance approach has been performed for the system (Fig. 9). For operating condition $\bar{Q}=0.044\ \mathrm{m}^3/\mathrm{s}$, the first harmonic frequency $f_0=5.4$ Hz and its corresponding mode shape have been obtained, as shown in Figs. 10 and 11, respectively. For this particular frequency, the impedance at the diffuser of the Venturi reaches extremely high level (presenting as a peak in Fig. 11), indicating the cavitation cloud there (i.e., in the diffuser) being very prone to self-excitation at the natural frequency for this system.

An initial experiment has evidenced that a peak component with a frequency very close to the predicted frequency emerges when cavitation is about to appear visually. This component is magnified significantly at inception point and further increases as the cavitation develops, and then disappears at a fully developed cavitation. This again gives strong support to the coupling hypothesis proposed. Figure 12(*a*) shows a typical pressure wave form for $\sigma=0.79$ (with reference pressure $p_\infty=1$ atm), with its fast Fourier transform (FFT) analysis in Fig. 12(*b*). The peak appears around 5 Hz, with all the attributions of the cavitation resonance described before, referring to Fig. 13. Here, the nondimensional amplitude is defined as

$$A_f = \frac{a_f}{\frac{1}{2}\rho v^2}$$

As mentioned before, in the work by the Grenoble group [7], as shown in Fig. 14, there is a frequency for the low-frequency fluctuation component, shown "as low pass (exp)," experimentally[11] observed to remain unchanged (i.e., ~40 Hz) throughout the range of σ variation. This is a clear sign of cavitation resonance, dominated by the system characteristics through the coupling mechanism. Unfortunately, they did not identify its resonance nature in their article, and no further investigations were reported. A hydraulic impedance analysis like the one performed by us will readily clarify the nature of this component.

3 Mechanism

A hypothesis of (macroscopic) mechanism, based on these three experimental observations and numerical analysis, has been proposed. The possible mechanism envisaged is that apart from behaving as a compliance, the bubbly cloud can function as an (pressure fluctuation) exciter with its own characteristic frequencies[12] and stimulate huge low-frequency pressure fluctuations in hydraulic systems through the double-oscillator[13] mechanism' [8,9]. The cavitation cloud is an exciter with its own range of characteristic frequencies rather than simply a lumped capacitance. Therefore, under certain condition, through frequency coincidence with one of the liquid-phase frequencies of the whole system, f_{liq}, resonance occurs. The diffuser of Venturi and the diffuser of draft tube, etc., all make the cavitation cloud there prone to self-oscillation, owing to their high impedance.[14] This resonance has the following attributions.

[11] And also numerical results shown in the plot but nothing mentioned.

[12] That is, the cloud itself is a complete oscillating system rather than a simply lumped-capacitive element in an oscillating system. Apart from compliance, it possesses, at least, the inertial mass, elasticity, and viscous resistance. For some cases, these parameters have a rather discrete nature than lumped parameters, subject to the geometric shape and properties of the cloud.

[13] One is the cloud; the other is the liquidphase in the system.

[14] That is, a small perturbation of flow rate (such as the cavity unsteadiness in this case) will trigger huge pressure fluctuations.

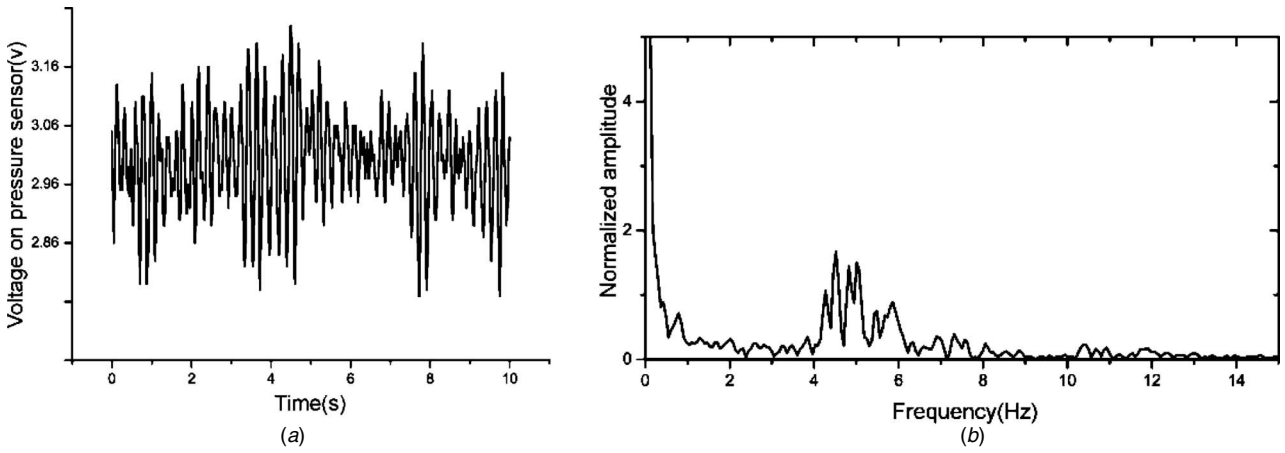

Fig. 12 Pressure fluctuations for σ=0.79. (*a*) The recorded pressure signals. (*b*) FFT analysis: The scale of the ordinate is a normalized amplitude in the FFT analysis.

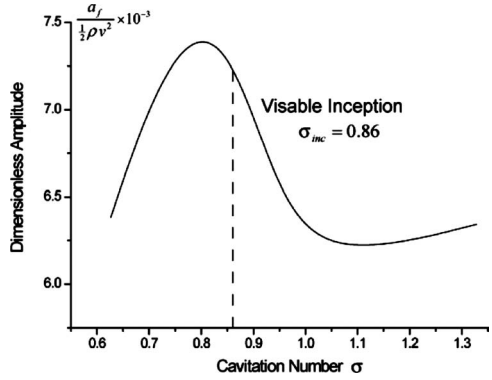

Fig. 13 Amplitude variation of the particular fluctuation-component with cavitation number

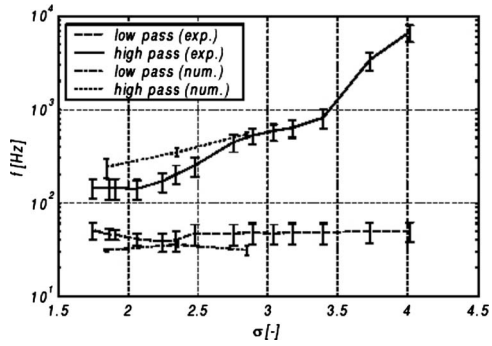

Fig. 14 Frequency variations of pressure fluctuations against cavitation number (Reboud et al. [7])

- The phenomenon is system instability, not local instability, because the fluctuation component presents/travels throughout the whole system.
- Despite the fact that in some cases the cavitation cloud (collective bubbles) can be simplified as a compliance, in the resonance mode, the cavitation cloud serves as an exciter interplaying with the whole liquid-phase system, not simply a lumped component (compliance or capacitor)[15] in the system.
- In the context of cavitation resonance, the cavitation cloud is considered as one of the subsystem and the liquid phase as the other subsystem, which are coupled to each other. A distinguishing feature is that one of the system's noncavitation frequencies, which serves as resonance frequency, does not modify/vary with cavitation presence and/or cavitating degree (i.e., the cavitation number) although it slightly varies with flow rate, etc. Indeed, it serves as resonance frequency for a certain range of cavitation numbers (as demonstrated by Figs. 3 and 13). This feature distinguishes itself from other components.

4 Remarks

The cloud as an exciter seems to possess a range of frequencies, adapting to the frequency of the (liquid-phase) system, creating a frequency coincidence and causing resonance under certain conditions. This still remains as a mystery, being a research topic in our ongoing study.

However, some clues have now been revealed from our ongoing DNS simulations,[16] which simulate the dynamic response of a column of bubble cloud to a step-rise pressure at one end of the column. In solid mechanics, we know that there are energy exchanges between different oscillation modes and subsystems owing to nonlinear effects.[17] For cavitated flows, much little is known although the energy exchange between two modes (shape oscillation and volume oscillation) through nonlinear effect for a single bubble has been known for a while, e.g., review by Feng and Leal [19]. Our results indicate that in a bubble cloud (as collective bubbles in a liquid), there is also an energy exchange between two modes of oscillations.[18] Hopefully, our ongoing research program searching for explanations at the microscopic level can lead to a step toward a better understanding of bubbly cloud in flow systems, involving cavitation resonance.

Acknowledgment

The authors acknowledge the following: UK EPSRC's Warwick-IMRC grants (R.ESCM.9001 and R.ESCM9004) awarded to S. C. Li; UK EPSRC (Instrumental Pool) technical

[15]Or local systems such as a water plug in a draft tube.

[16]See Ref. [18].

[17]For example, *The Mechanics of Nonlinear Systems With Internal Resonances* by A. I. Manevich and L. I. Manevich.

[18]One is the initial pressure propagation wave caused by a step pressure rise at the one end of a bubble column, and the other is the initially nonexisting volumetric oscillation (in-phase) of bubbles.

support on the high-speed camera loaned to S. C. Li; China State Key Laboratory of Hydroscience and Engineering, Open Grant (Sklhse-2006-E-01) awarded to S. C. Li, S. H. Liu, and Y. L. Wu; and China, Beijing Science Foundation Grant (No. 3073020) to S. H. Liu and Y. L. Wu. The Chinese government scholarship (1978) to S. C. Li as visiting scientist at the Cavitation & Multiphase Flow Lab, the University of Michigan, USA. They would also like to thank Mr. R. H. Edwards and Mr. S. Wallace of Warwick University for technical support.

Nomenclature

a = amplitude
a_0 = opening of guide vane of model turbine
a_f = amplitude at a particular frequency observed in UM Venturi and proven to be resonance frequency
$\bar{a}$ = averaged amplitude
A_f = nondimensional amplitude of pressure fluctuation
f_0 = resonance frequency (Hz)
f_{liq} = natural frequency of liquid phase of system
f_2 = amplitude of the second type of pressure fluctuation component observed in the HL-169-25 model turbine
F_f = mark for the condition where a particular frequency of pressure fluctuation was observed
$H(x)$ = head fluctuation at location x of system
p_∞ = reference pressure
$Q(x)$ = flow-rate fluctuation at location x of system
$\bar{Q}$ = average flow rate
s = complex frequency
$s_1, s_2, s_3, \ldots$ = harmonics of complex frequencies
v = velocity
$Z(x)$ = hydraulic impedance at location x of system
Z_{12} = hydraulic impedance at node 12 (low-pressure tank exit) of UM Venturi, a reference point
ρ = density
σ = cavitation number
σ_f = real par of the complex frequency for the particular fluctuation component (i.e., resonance) observed in UM Venturi
σ_{in} = cavitation inception number
ω = imaginary part of complex frequency, i.e., angular frequency

References

[1] Rheingans, W. J., 1940, "Power Swings in Hydroelectric Power Plants," Trans. ASME, **62**, pp. 171–184.
[2] Henry, P., 2001, *Cavitation of Hydraulic Machinery*, S. C. Li ed., ICP, London, UK, Chap. 7, Sec. 3.
[3] Jacob, T., Maria, D., and Prenat, J. E., 1987, "Comportement Dynanique D'une Turbine Francis 1 Forte Charge. Comparaisons modele-prototype," *SHF Comite Technique*, Paris, p. 134.
[4] Jacob, T., Prenat, J. E., and Grenier, R., 1988, "A Characterization Procedure for the Dynamic Behaviour of Francis Turbines: Practical Comparison of Elbow and Moody Type Draft Tubes," *IAHR Symposium*, Trondheim.
[5] Jacob, T., Prenat, J. E., and Vullioud, G., and Lopez Araguas, B., 1992, "Surging of a 140 MW Francis Turbine at High Load, Analysis and Solution," *IAHR Symposium*, Sao Paulo.
[6] 2001, in *Cavitation of Hydraulic Machinery*, S. C. Li, ed., ICP, London, Chaps. 7 and 8.
[7] Reboud, J. L., Coutier-Delgosha, O., Pouffary, B., and Fortes-Patella, R., 2003, "Numerical Simulation of Unsteady Cavitation Flows: Some Applications and Open Problems," *Fifth International Symposium on Cavitation*, Osaka, Japan.
[8] Li, S. C., Zhang, Y. J., and Hammitt, F. G., 1983, "Investigation of Low-Frequency Presure Fluctuation Associated With Cavitating Venturi Flow," University of Michigan, Report No. UMICH 014571–64-I.
[9] Li, S. C., Zhang, Y. J., and Hammitt, F. G., 1986, "Characteristics of Cavitation Bubble Collapse Pulses, Associated Pressure Fluctuations and Flow Noise," J. Hydraul. Res., **24**(2), pp. 109–122.
[10] Zuo, Z. G., Li, S. C., Carpenter, P. W., and Li, S., 2006, "Cavitation Resonance on Warwick Venturi," *CAV 2006*, Netherlands.
[11] Li, S. C., Boldy, A. P., Liu, Z. Y., and Zhou, H. F., 1989, "Cavitation Resonance in a Venturi Loop," *Proceedings of the Third Joint ASCE/ASME Mechanics Conference*, San Diego, USA, pp. 71–74.
[12] Wylie, E. B., and Streeter, V. L., 1978, *Fluid Transients*, Advanced Book Program, McGraw-Hill, New York.
[13] Li, S. C., 1992, "Pressure Fluctuations in Cavitating Draft-Tube Flows," FED (Am. Soc. Mech. Eng.), **136**, pp. 1–6.
[14] Liu, S. H., Shao, Q., and Yang, J. M., 2004, "Unsteady Turbulent Simulation of Three Gorges Hydraulic Turbine and Analysis of Pressure in the Whole Passage," J. Hydroelectric Engineering, **23**(5), pp. 97–101 (in Chinese).
[15] Li, S. C., and Carpenter, P. W., 1999, "A Device for Studying the Stochastic Behaviour of Bubbles Interacting With Compliant Wall," *Proceedings of the Eighth Asian Congress of Fluid Mechanics*, Shenzhen, China, pp. 263–266.
[16] Li, S. C., and Carpenter, P. W., 2000, "Note on an Envisaged Markov Model for Cavitation Bubble(s) Near Compliant Walls," *ASME Fluids Conference*, Boston, USA.
[17] Zuo, Z. G., Dunkley, P., Carpenter, P. W., Bryanston-Cross, P., and Li, S. C., 2005, "Visualization Method for Acquiring Statistical Characteristics of Cavitation Bubbles," *The Eighth International Symposium on Fluid Control, Measurement and Visualization*, Chen Du, China, Paper No. 4–10.
[18] Chen, H., Li, S. C., Zuo, Z. G., and Li, S., "DNS Simulation of Bubble-Cluster Response to Step-Rise Pressure Perturbation," The 1st International Colloquium on Dynamics, Physics and Chemistry of Bubbles and Gas-Liquid Boundaries, Niseko, Japan.
[19] Feng, Z. C., and Leal, L. G., 1997, "Nonlinear Bubble Dynamics," Annu. Rev. Fluid Mech., **29**, pp. 201–243.

An Assessment of the Influence of Environmental Factors on Cavitation Instabilities

Damien T. Kawakami
A. Fuji
Y. Tsujimoto
R. E. A. Arndt[1]

University of Minnesota,
Mississippi River at 3rd Ave. S.E.,
Minneapolis, MN 55414
e-mail: arndt001@umn.edu

Cavitation induced flow instabilities are of interest in numerous applications. Experimental and numerical investigations of this phenomenon are taking place at several institutions around the world. Although there is qualitative agreement among the numerous recent papers on the subject, there is a lack of agreement with regard to important details, such as the spectral content of unsteady lift oscillations. This paper summarizes observations of a cavitating NACA0015 foil in three different tunnels that revealed remarkably different cavity shedding appearances and behaviors. Some of the differences were attributed to system instabilities. However, in addition to a different cavitation behavior attributed to system instabilities, it was found that differences in gas content could significantly alter the lift spectrum of a cavitating foil. For a certain range of the composite parameter $\sigma/2\alpha$ near 4, the dominant frequency appears to double when the gas content is reduced by a half. It is also argued that surface effects can have a significant influence on fully wetted time during cavity shedding. Normally, surface effects are assumed to play an important role in the initial inception of a fully wetted hydrofoil with gas content being the primary factor governing developed cavitation behavior. However, the repetitive nature of the process implies that each shedding cycle is an individual inception process. Hence, the unexpected role of surface effects in partially cavitating hydrofoils. The conclusions reached have important ramifications concerning numerical code verification that is a topic of major concern. [DOI: 10.1115/1.2842146]

Introduction

A significant amount of information concerning unsteady cavitation on a hydrofoil is available in the literature. Examples include Kjeldsen et al. [1], who mapped the cavitation behavior for a NACA0015, Reisman et al. [2], who performed a detailed investigation of the shock waves caused by cavitation cloud collapse behind a stationary and oscillating hydrofoils, and Arndt et al. [3], who performed a joint experimental and numerical analysis of partial cavitation instabilities. In addition to studies of the dynamics associated with sheet/cloud cavitation, efforts have been made to control the phenomenon. Pham et al. [4] used high-speed video to investigate cavity shedding caused by a reentrant jet. Motivated by observations of a reentrant jet in sheet cloud cavitation, Kawanami et al. [5] found that simply putting an obstacle on the surface of the foil could significantly alter the cavitation behavior. Arndt et al. [6] used air injection to reduce the intensity of cloud collapse in an effort to prevent cavitation erosion. A different approach was taken by Amromin et al. [7] and Kopriva et al. [8], who found that cavity oscillations could be suppressed by tuning the local pressure gradient in the region of cavity closure. The modified foil has both improved lift/drag characteristics and dramatically reduced lift oscillations when operating in the cavitating regime.

An important feature of the problem is that the lift oscillations are highly periodic. This is illustrated in Fig. 1 where cavitation behavior over an envelope of angle of attack and cavitation number is depicted. The regions depicted by I and II correspond to sheet/cloud cavitation. Note that Regions I and II have different spectral characteristics, as shown in Fig. 2. A bifurcation in the data occurs at $\sigma/2\alpha=4$. When $\sigma/2\alpha\leqslant 4$, a strong spectral peak exists at a Strouhal number, fc/U, ranging from about 0.15 to 0.3 that is relatively independent of cavitation number. Under these conditions, the relative maximum cavity length is greater than 0.75 ($l/c>0.75$). At values of $\sigma/2\alpha\geqslant 4$, a different mode of oscillatory behavior (Regime II) is noted. This corresponds to cavity lengths that are less than 0.75, c, and peak frequency scales with cavity length l, $fl/U\approx 0.3$. A reentrant jet within the sheet is the mechanism for regular breakup of sheet cavitation into large cylindrically shaped bubble clouds. As a reentrant jet is formed, it moves forward to the leading edge of the cavity, colliding with the cavity interface and pinching off the cavity. The rearward part of the sheet forms a bubble cloud. The significance of the bifurcation at $\sigma/2\alpha=4$ is discussed by Watanabe et al. [9]. Their results, based on an inviscid analysis of flow over a flat plate, show that the flow becomes unstable when l/c is greater than 0.75. Although there is agreement on the oscillation frequency for $\sigma/2\alpha\geqslant 4$ (referred to herein as Type II oscillations), there is disagreement for $\sigma/2\alpha\leqslant 4$ (Type I oscillations). This is often attributed to system auto-oscillation (e.g., Callenaere et al. [10]). Another possibility is suggested here. The frequency of Type I oscillations is found to vary significantly with dissolved air content. Since the void fraction for a cavitating hydrofoil at a fixed angle of attack is a function of the cavitation number and gas content of the fluid, it is expected that a higher gas content will likely result in a larger void fraction. A larger void fraction results in a smaller collapse propagation velocity, and therefore a lower collapse frequency.

Although considerable work has been carried out to control cavitation and its damaging effects, relatively little emphasis has been placed on comparing observations carried out in different facilities. This is an important issue since the details of this complex flow require careful observation and comparison with other data. Several factors need to be considered. For example, Franc [11] notes the importance of distinguishing between system instabilities and intrinsic instabilities. System instabilities are caused by the interaction between the cavitating foil and the rest of the system. Intrinsic instabilities, however, are a result of the cavita-

[1]Corresponding author.

Contributed by the Fluids Engineering Division of ASME for publication in the JOURNAL OF FLUIDS ENGINEERING. Manuscript received July 3, 2005; final manuscript received December 28, 2007; published online March 10, 2008. Assoc. Editor: Joseph Katz.

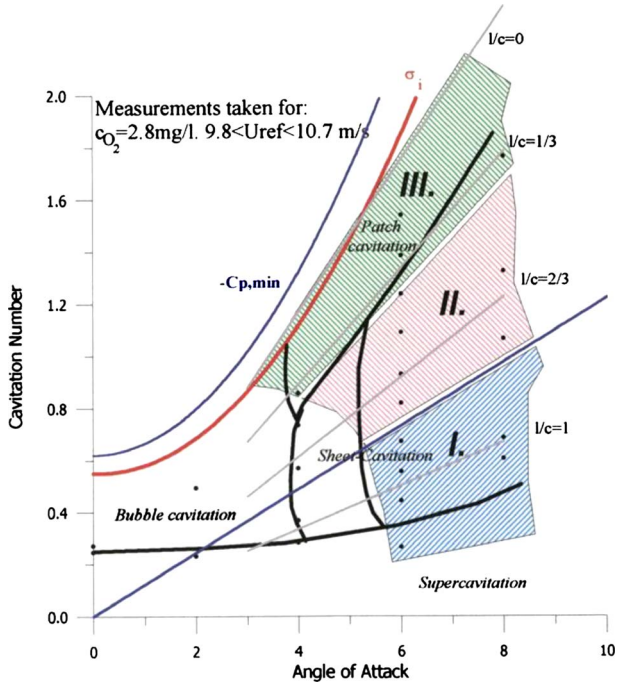

Fig. 1 Types of cavitation found on the NACA 0015 hydrofoil

tion behavior and are independent of the system. The reentrant jet mechanism (Refs. [3,5], and many others) discussed above is an intrinsic instability. Numerous researchers across the world have observed it and is a basic mechanism causing the cavity shedding. Watanabe et al. [9] compared the results of Sato et al. [12] for a flat plate hydrofoil, and the Arndt et al. [3] results for a NACA0015 foil. The comparison is reproduced in Fig. 3. The discrepancy between results could not be explained. The difference is most likely a result of system instabilities. What is not clear, however, and merits further discussion, is the cause and repercussions system instabilities have on cavitation behavior.

One factor that may explain many of the discrepancies is gas content. It is well known that gas content has an effect on inception. Little has been done, however, in direct examination of gas content effects on cavitation dynamics. Arndt and Keller [13] found that not only the gas content is crucial for the water quality in a circulating cavitation tunnel but also the prehistory of the test water. Developed cavitation was observed at two instances at identical gas contents of 95% at atmospheric conditions during an

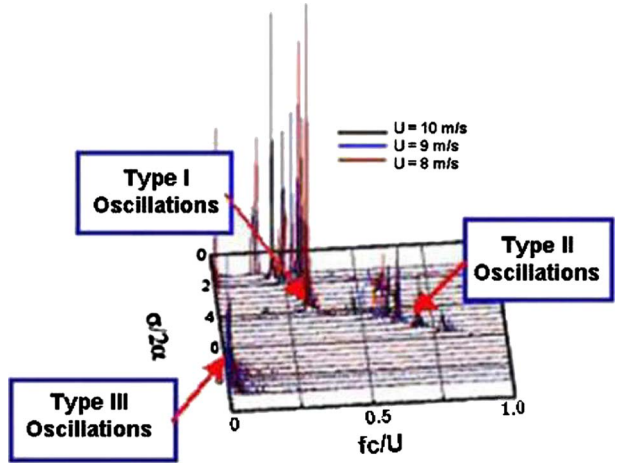

Fig. 2 Spectra of measured lift oscillations [3]

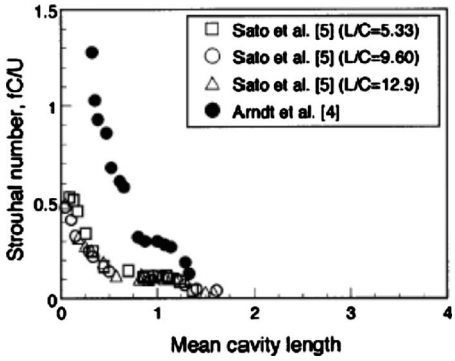

Fig. 3 Comparison between Sato et al. [12] and Arndt et al. [3] data for a cavitating hydrofoil. *l/c* is the ratio of upstream duct length to chord length.

experiment. The first observation was made immediately after reaching constant velocity. The second was made about 12 s later, i.e., after about one circulation of the test water in the tunnel was completed. In the interim, many bubble nuclei were created by the cavitating flow and circulated into the test section. The cavitation type changed dramatically from sheet cavitation with trailing cloud cavitation into bubble cavitation at the leading edge, followed again by cloud cavitation. The spectral content of the lift oscillations was also found to change markedly with the change in water quality.

Background

The NACA0015 hydrofoil was chosen for a comparative analysis of cloud cavitation observed in three different water tunnels. This foil was chosen because it has been widely studied ([1,14–16]). The mapping for the NACA0015 by Ref. [1] is shown in Figs. 1 and 2. Three shedding modes are found when the angle of attack is larger than 6 deg. Modes I and II have already been described. Mode III is characterized by localized areas of patch cavitation located at the minimum pressure point along the span of the foil. The experiments presented in the remainder of this section focus on the transitional sheet/cloud cavitation regime (Type I) where $\sigma/2\alpha \leqslant 4$, where both bubbly flow shock wave and reentrant jet phenomena can occur (as opposed to reentrant jet physics dominating for values of $\sigma/2\alpha$ greater than 4). This is a more complex form of sheet cloud cavitation that defies simple analysis. A dominant feature in Mode I cavity shedding appears to be a pressure wave that propagates upstream of the trailing edge of the cavitating foil and completely "snuffs out" the cavity resulting in a fully wetted leading edge.

Comparisons of data from the three facilities are made utilizing high-speed video taken over a wide range of σ values in Regions I and II. In addition to high-speed video, pressure fluctuations were measured either by lift, foil surface pressure, or pressure taps located in the vicinity of the cavitating foil.

Water Tunnels

The results from three water tunnels are compared. Sheet/cloud cavitation was observed in the 30×30 cm^2 cavitation channel in Obernach, Germany (Fig. 4). The foil for this study was made of anodized aluminum using a numerical milling process. The chord length is 128 mm. In these tests, unsteady lift data were also recorded using a piezoelectric quartz balance. High-speed video was taken at 4500 frames/s.

The second tunnel is the 19×19 cm^2 water tunnel at the University of Minnesota (Fig. 5). Three identically dimensioned NACA0015 foils were studied. The foils in this case are 81 mm in chord length. One foil (denoted "anodized foil") was made using a similar process as described for the Obernach tunnel. Both the

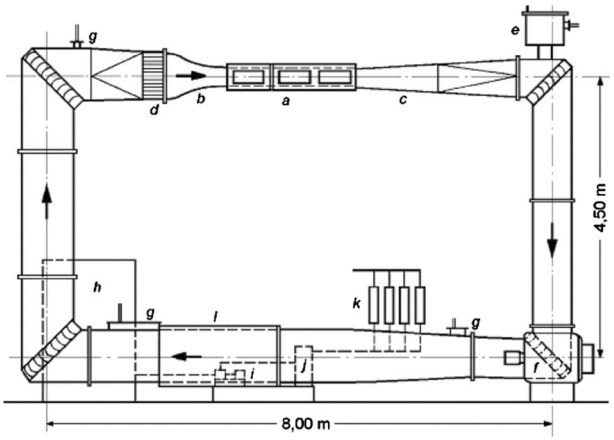

Fig. 4 Sketch of the Obernach cavitation tunnel and its essential components

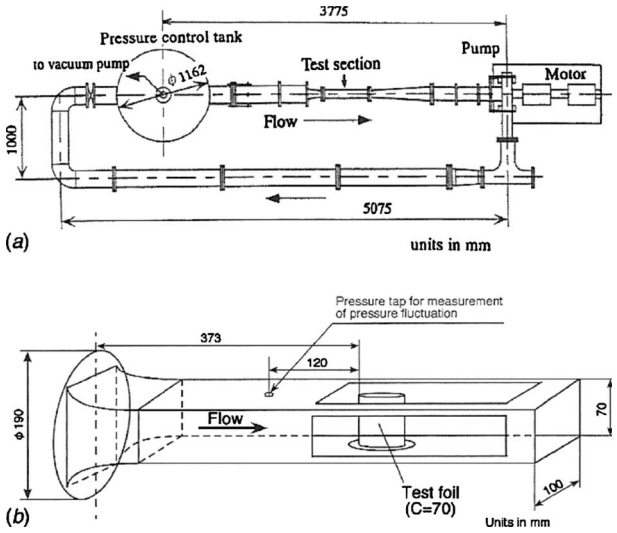

Fig. 6 Osaka water tunnel

Obernach and SAFL foils were manufactured in the same machine shop at the University of Minnesota. The second NACA0015 foil (denoted "polished foil") was made at Osaka University using the same process described below for the Osaka NACA0015 foil. The relative chord length and span, c/h and s/h, were identical to that used at Obernach. At this facility, unsteady lift is measured using both a force balance and by measuring the pressure difference between the suction and pressures sides of the foil [1]. Downstream pressure fluctuations were measured one chord length downstream the trailing edge of the foil. The third foil (denoted "instrumented foil"), a piezoelectric instrumented foil described in Arndt et al. [16] is used to measure unsteady pressure fluctuations at several locations on the suction surface of the NACA0015 foil. High-speed video was taken at 2500 frames/s, for a duration of approximately 1 s for the anodized and polished foils.

Sheet/Cloud cavitation was also studied in the 10×7 cm^2 tunnel at Osaka University, Japan (Fig. 6). A series of foils has been tested in this tunnel [17]. The NACA 0015 foil described in this paper are made of wire cut stainless steel, which is then polished to a roughness of $Ra\sim1.16$ μm. The chord length is 70 mm. Unsteady pressure fluctuations 120 mm upstream of the foil were measured. High-speed video was taken at 2250 frames/s and approximately 3 s of each run were recorded.

Numerous differences exist between the tunnels utilized in this study. Tunnel geometry and size, water properties, and foil properties all are likely to contribute to discrepancies in cavitation behavior. For instance, a perfectly smooth foil would be expected to be more resistant to cavitation since it is hypothesized that nuclei trapped on a cavitating surface promote cavitation inception. The same argument can be made for a flow with a dearth of nuclei. Table 1 summarizes the major differences between tunnels, foil dimensions and surface finish, and water quality.

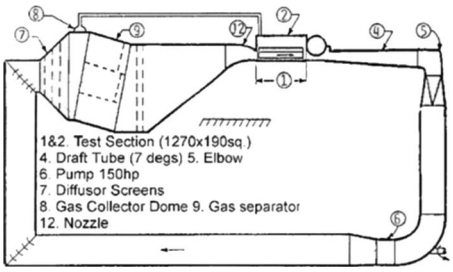

Fig. 5 Sketch of the SAFL water tunnel

Results

A comparison of a typical shedding cycle at $\sigma/2\alpha=3.58$ (Type I oscillations) for the NACA0015 foil observed in the three tunnels is shown in Figs. 7–9.

Some important observations can be made. While the cavitation number is identical for the three videos shown, the behavior is very different. Although not clear from the images, the Osaka video revealed instances of bubble cavitation occurring intermittently between shedding cycles. This is best seen in Frame 8 of Fig. 8 where the sheet cavity is beginning to form again and leading edge cavitation is localized along the span. Bubble cavitation has been observed on polished foils and is discussed by Guennoun et al. [18], but was not observed in either the Obernach or SAFL tunnel. In the case of the Osaka and Obernach tunnel, the leading edge is observed to be fully wetted during a certain period in a cycle of oscillation. In the case of the SAFL video, however, a fully wetted leading edge is never observed. Recall that the Obernach and Osaka foils were made with different manufacturing processes, but the SAFL and Obernach foils were made by the same machinist. The fully wetted time is plotted for the three tunnels in Fig. 10.

As previously mentioned, the Obernach foil and SAFL foil data shown above are made from anodized aluminum. The Osaka foil is made of polished stainless steel. Gas content at the SAFL tunnel was also much higher than both the Osaka and Obernach tunnels. The question arises whether the surface characteristics of the foil and gas content have an effect on the intrinsic instability of the cavity. A smooth surface will have smaller and less crevices available for nuclei to exist on the foil. Less and smaller nuclei will result in cavitation occurring at a later point in the shedding cycle. Preliminary video investigation of the smooth foil made at Osaka for the SAFL tunnel showed visible fully wetted time. High-speed video and unsteady lift was recorded at a number of points for $\sigma/2\alpha$ between 2 and 7. The results show that, under certain conditions, both a distinct period of fully wetted flow and bubble cavitation can be observed.

The shedding frequency was recorded visually for each video. The Strouhal number based on freestream velocity (U) and foil chord length (c) is plotted in Fig. 11 for the NACA0015 foils. All three tunnels show similar trends, but the Osaka tunnel varies significantly from the SAFL and Obernach tunnel. Recall that the SAFL and Obernach tunnels have identical aspect ratios. It has been observed by numerous researchers that a transition in shedding behavior occurs. The transition is observed to occur when the cavity length based on chord length (l/c) is approximately 0.75. It

Table 1 Summary of differences in each tunnel

Tunnel and foil	Tunnel dimensions (mm^2)	Foil mounting	Chord length (mm)	Aspect ratio	Re	Gas content (ppm)	Surface finish	Roughness (μm)
Obernach	300×300	Fixed at both ends	128	2.35	1.02*E*06	6.7	Anodized Aluminum	>1.16
SAFL-polished[a]						13 7	Polished Steel	1.16
Anodized[b]	190×190	Cantilever	81	2.35	6.48*E*05	13 7	Anodized Aluminum	>1.16
Instrumented foil[c]						13 7	Aluminum	>1.16
Osaka	100×70 (h×w)	Cantilever	70	1.43	3.5*E*05	3.5	Polished Steel	1.16

[a]Manufactured at Osaka University (polished foil).
[b]Manufactured at University of Minnesota (anodized foil).
[c]Instrumented foil manufactured at the University of Minnesota.

should be noted that shedding frequency is easy to observe only for values of $\sigma/2\alpha$ less than approximately 5, which may explain some of the discrepancy between data for larger $\sigma/2\alpha$ values.

In addition to video observation, unsteady lift data obtained at Obernach and SAFL are compared with unsteady pressure spectra obtained at Osaka in Fig. 12. While the data are obtained with different instruments at different locations in the flow for each tunnel, the results are expected to be similar. Comparison between visual observation and pressure data shows that the dominant frequency in the signal for each tunnel corresponds to the visually observed shedding frequency except for the anodized SAFL foil where the gas content is approximately 13 ppm. The frequency from the visual observation for the SAFL foil where the gas content is 13 ppm does not match the pressure data but is closer to the case of low gas content (approximately 7 ppm), as will be discussed later. The conclusion can be made, therefore, that the difference between data is not solely attributed to the difference in measurement locations but also corresponds to differences in actual cavitation behavior.

The difference in spectra between tunnels is remarkable, despite

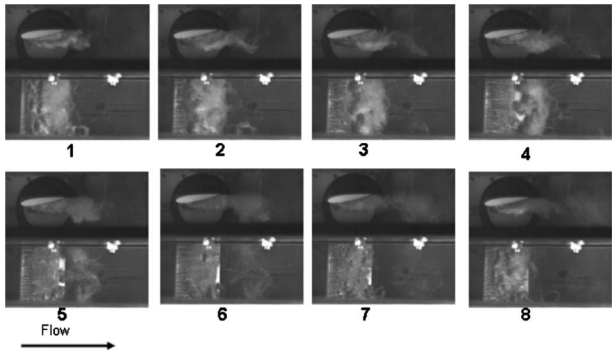

Fig. 7 Cavitation cycle for anodized foil σ=1.0, α=8 deg ($\sigma/2\alpha$=3.58), and gas content ~13 ppm in the SAFL tunnel (plan and profile view)

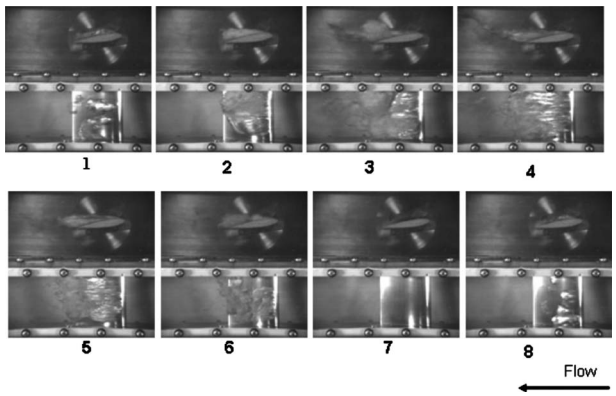

Fig. 8 Cavitation cycle for σ=1.0 and α=8 deg ($\sigma/2\alpha$=3.58) in the Osaka tunnel (plan and profile view)

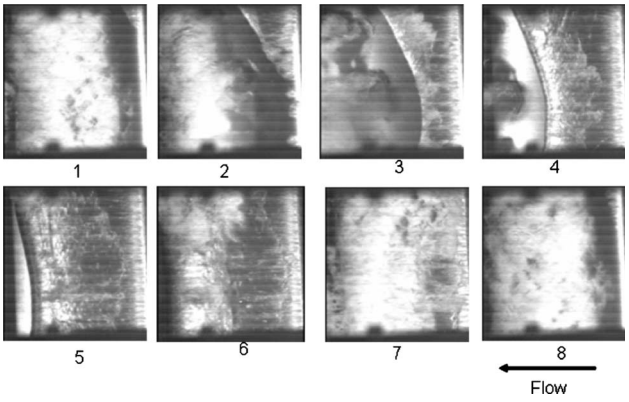

Fig. 9 Cavitation cycle for σ=1.0 and α=8 deg ($\sigma/2\alpha$=3.58) in the Obernach tunnel (plan view). Note the leading edge is visible on the right edge of each image.

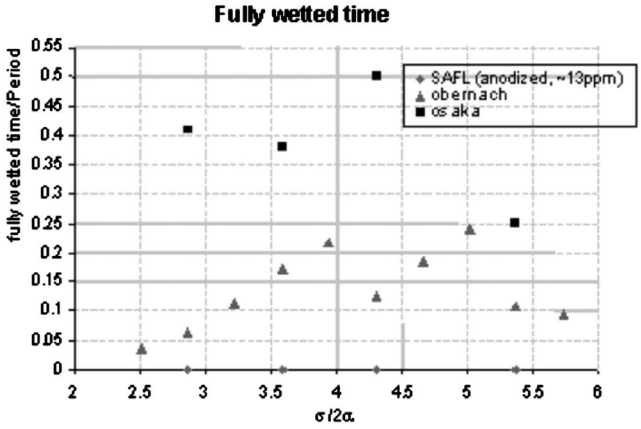

Fig. 10 NACA0015 fully wetted time normalized by period for three tunnels (Note: SAFL results show no fully wetted leading edge)

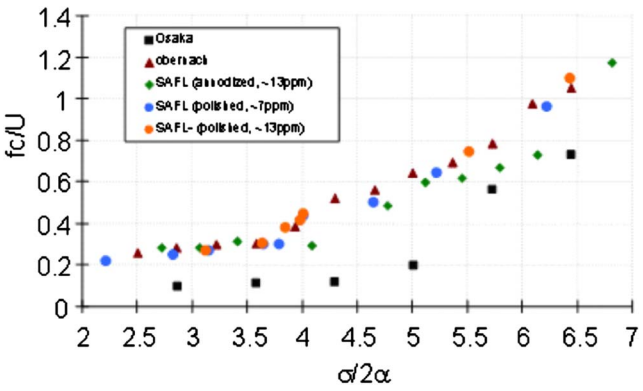

Fig. 11 Observed shedding frequency for three tunnels

the data being for the same foil at the same angle of attack. Unlike the high-speed video data, a similar trend does not exist in the spectral data. In the case of the Obernach lift data, a transition occurs at $\sigma/2\alpha \sim 4$ signifying the transition between Regions I and II, as shown in Fig. 2. The SAFL and Osaka data, however, show no sign of transition occurring, but rather a nearly constant dimensionless frequency between ~0.10 and 0.15. Without knowledge of the tunnel and foil dimensions, the data infer that the SAFL tunnel is more geometrically similar to the Osaka tunnel than the Obernach tunnel when, in fact, the opposite is true.

In the case of the Osaka tunnel, harmonics exist at integer multiples of the dominant frequency. This may be a result of the relatively small size of the Osaka water tunnel. Since the Osaka tunnel is much smaller than both the SAFL and Obernach tunnels, the pressure fluctuations caused by cloud cavitation will not be damped out, as is the case with the larger tunnels. The result is a system instability that is seen only in the Osaka tunnel because of its small size. The results suggest these system instabilities dominate to the point that perhaps the intrinsic instabilities are significantly altered.

In a study performed at SAFL, gas content was found to profoundly affect cavitation dynamics. Figure 13 contains spectral data taken for different gas contents, but identical flow conditions at the SAFL tunnel. The difference is remarkable. In the high gas content case, little spectral activity exists for $\sigma/2\alpha > 4$. In addition, for $\sigma/2\alpha < 4$, the dominant frequency is constant in the case of high gas content, but appears to linearly decrease with a decrease in σ in the low gas content case. For $\sigma/2\alpha$ values around 4, the difference in frequency in the low gas content case is over double the frequency of the high gas content case.

Two trends are noted. The low gas content case appears to be similar to the Obernach data. The high gas content case, however, corresponds more closely to the Osaka data. While still acknowledging the system instabilities present in the Osaka tunnel, it can be argued that cavitation observed at the Osaka tunnel was under very high gas content conditions and mimics Fig. 13(*a*). In the Obernach tunnel, cavitation is observed in water with low gas content similar to the trend in Fig. 13(*b*).

To explore the effect of the type of instrumentation on the spectrum, lift data taken at SAFL using a lift balance were compared with measurements made using the instrumented foil for two similar gas contents (Fig. 14). A discussion of this procedure is given in Kjeldsen et al. [1]. The lift and pressure data show remarkable similarity, suggesting that the difference in measurement location and type of instrumentation is most likely not the cause of the spectrum difference.

In the case of the high gas content, Figs. 14(*a*) and 14(*b*) are similar. For $2 < \sigma/2\alpha < 4$, both show two dominant peaks. For $\sigma/2\alpha > 4$, the instrumented foil shows the high frequency behavior observed by Kjeldsen et al. [1], while the lift balance data do

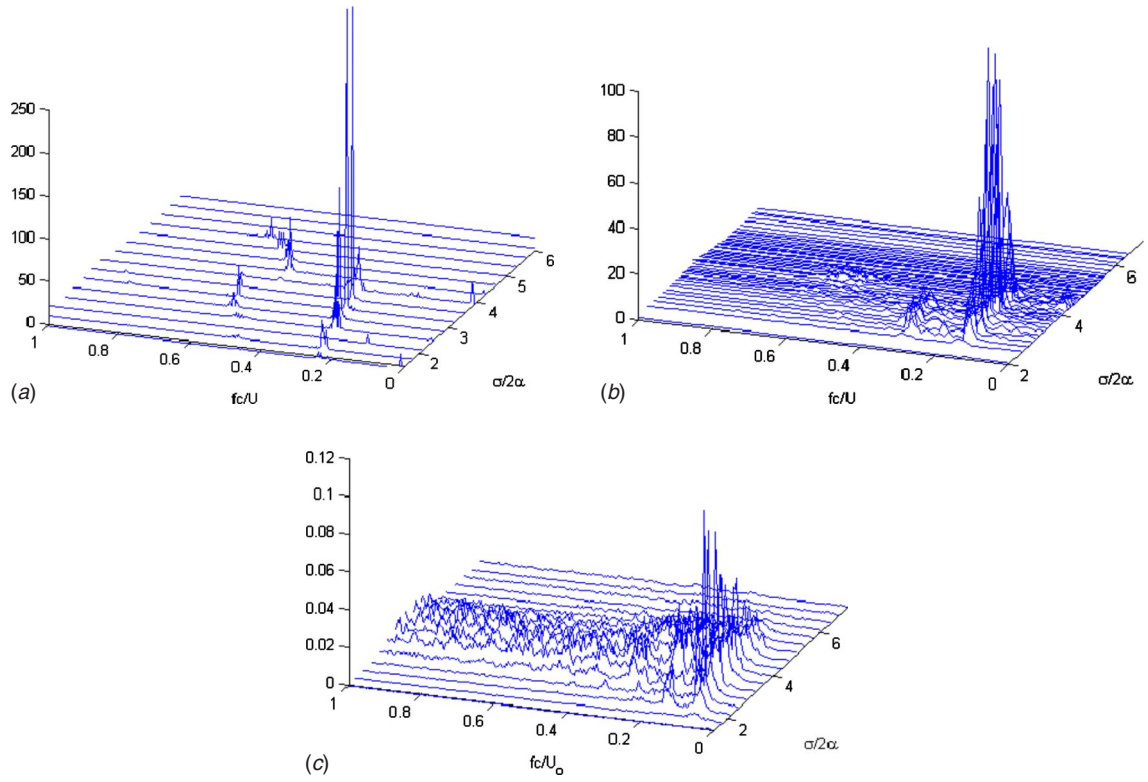

Fig. 12 Comparison of pressure and lift spectra for the NACA0015 foil observed in three tunnels: (*a*) unsteady lift—Obernach tunnels; (*b*) Unsteady lift—SAFL tunnel (anodized, ~13 ppm); (*c*) upstream strain gage—Osaka tunnel

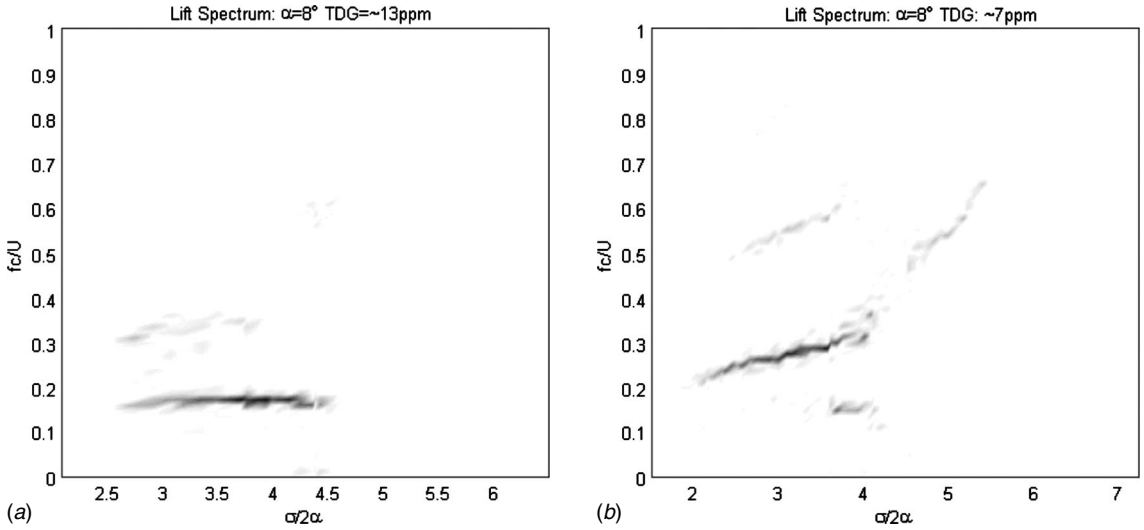

Fig. 13 Comparison of SAFL anodized foil unsteady lift spectra for high and low gas content. The intensity of shading corresponds to amplitude: (*a*) high gas content (*b*) low gas content

not. Presumably, the high spectral content in the instrumented foil data is due to a higher frequency response of the pressure sensors. For the low gas content case, Figs. 14(*c*) and 14(*d*) look remarkably similar. The difference between the cases of low and high gas contents cannot be fully explained at this time.

Discussion

A number of observations have been made that require explanation. It has been shown, using high-speed video, that a given cavitation shedding cycle on a NACA0015 foil appears very dif-

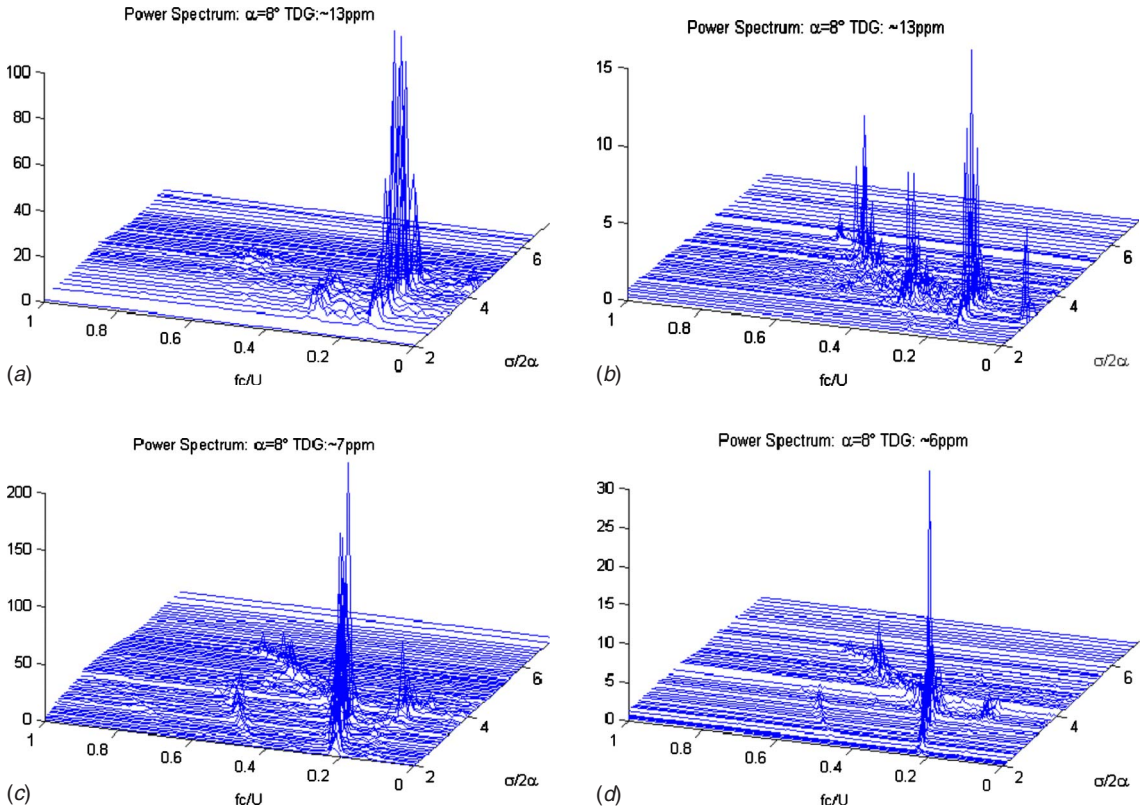

Fig. 14 Comparison between lift spectrum and suction side surface pressure fluctuations for high and low gas contents: (*a*) high gas content—SAFL lift balance; (*b*) High gas content—SAFL instrumented foil; (*c*) low gas content—SAFL lift balance; (*d*) low gas content—SAFL instrumented foil.

ferent in different water tunnels. In particular, remarkably different fully wetted time data were recorded in the three tunnels utilized in this study. Note that the foils were made using different machining processes and of different materials, which may explain the difference in fully wetted time. The question arises whether surface characteristics have an effect on the intrinsic instability of the cavity. Guennoun et al. [18] noted that both gas content and leading edge surface characteristics affect both cavitation inception and behavior.

Analysis of the spectral characteristics of the shedding process show similar trends in the visually observed shedding frequency across tunnels, but very different detailed spectral characteristics. The Osaka tunnel has a smaller test section and aspect ratio. The hypothesis is made that, due to the geometric differences in the Osaka tunnel, the pressure fluctuations caused by the cavity collapse induces harmonics in the system that are not seen in the other two larger tunnels. It is important to note that the system instability appears to have an effect on the behavior of the intrinsic instability. This is especially important to consider when performing model tests.

While the smaller Osaka tunnel has some system instabilities that alter the cavitation behavior, the question of why such a large difference is observed between the SAFL and Obernach tunnel, which have nearly the same aspect ratio and are geometrically similar, requires explanation. Since the SAFL and Obernach foils share similar manufacturing processes[1] and are much larger tunnels, it is reasonable to believe that the results should be similar. However, numerous differences exist. In particular, the observed shedding frequencies shown Fig. 11 suggest that the SAFL and Obernach shedding behavior are more similar as compared with the Osaka shedding behavior. Alternatively, a look at the fully wetted data suggests the Osaka and Obernach shedding to be more similar to each other than to the SAFL data. Given the data, foil, and tunnel information, an argument can be made with equal merit as to which two tunnel results appear more similar. Noting the spectral comparison, the conclusion could even be made that, despite having the same foil at the same angle of attack, the shedding characteristics across the three tunnels are more dissimilar than similar. This places special emphasis on the care necessary to make comparisons between experimental and numerical data.

In the cases of high gas content, the observed shedding frequency (Fig. 11) does not match the surface pressure and lift frequency plots (Fig. 14). For low gas content, however, the plots appear to match very well. One hypothesis is that in the case of low gas content, the cloud is mainly vapor and the collapse causes a "shock wave." The frequency of the collapse governs both the visual and surface pressure and lift data. In high gas content, the cloud is mainly gaseous, the collapse is less intense, and the effects of the weaker shock wave are mitigated by the gaseous bubbles. Perhaps some other mechanism governs the surface pressure and lift frequency in this case.

Since a fully wetted time is never observed, the inception process does not reoccur every time, and other flow parameters dominate the surface pressure and lift fluctuation. It still is unsettling, however, that, in the high gas content case, there is no evidence of the visual and surface pressure and lift fluctuation in the same plot. In essence, one frequency is observed visually, while another, slightly lower frequency is measured with the force balance and pressure transducers.

Conclusions

Observations of a cavitating NACA0015 foil in three different water tunnels revealed remarkably different cavity shedding appearances and behaviors. Some of the differences were attributed to system instabilities. Harmonics in the shedding spectrum observed in the Osaka tunnel are attributed to the small size of the tunnel. In the much larger Obernach and SAFL tunnels, the harmonics are not observed. This difference is attributed to system instability since the harmonics are unique to the small Osaka tunnel. The effect of harmonics on the shedding behavior should be given careful consideration when studying cavitation instabilities in small water tunnels and inferring cavitation behavior on a full-scale model. Table 2 summarizes the observed differences and the hypothesized factor contributing to the difference.

Table 2 Summary of observed phenomena and the factors accounting for the difference

Observed difference	Contributing factors
Fully wetted time	Gas content Surface characteristics
Spectral characteristics	Gas content Aspect ratio
Visual shedding frequency	Aspect ratio

In addition to a different cavitation behavior attributed to system instabilities, differences in gas content were found to significantly alter the lift spectrum of a cavitating foil. For a certain range of $\sigma/2\alpha$ near 4, the dominant frequency appears to double when the gas content is reduced by a half. This difference can be used to explain some of the discrepancies observed between tunnels.

It is also argued that surface effects can have a significant influence on fully wetted time during cavity shedding. The apparent contradiction of a long fully wetted time but high gas content in the case of the Osaka tunnel can be explained by separating inception and developed cavity observations. Surface effects play an important role in the initial inception of a fully wetted hydrofoil. Once a cavity sheet is developed, gas content is the main factor influencing cavitation behavior.

The hope is that knowledge of the effect of gas content, surface characteristics, and system characteristics will be more closely monitored in future cavitation studies. This becomes especially important when comparisons are made between water tunnels or when cavitation behavior in a water tunnel is studied in order to predict cavitation in actual applications. A more careful monitor of these parameters will lead to a better understanding of the basic mechanisms affecting cavitation instabilities.

Acknowledgment

The National Science Foundation, Division of Chemical and Transport Systems in the Engineering Directorate and the Office of International Programs, supported most of this research. Dr. Michael Plesniak and Dr. Mark Suskin were the program managers. The research in Japan was supported by a Grand-in-Aid for Science Research of the Ministry of Education, Science, Sports, and Culture through a joint agreement with the National Science Foundation. Dr. Andreas Keller of the Versuchsanstalt für Wasserbau of the Technical University Munich graciously participated in this study by making available his laboratory and assisting in the research. Special thanks go to Dr. Martin Wosnik, currently of the Alden Research Laboratory, for thoughtful discussions and countless hours of help obtaining and analyzing high-speed video.

Nomenclature

c = chord length of hydrofoil [m]
g = gravitational acceleration (m/s^2)
h = span of hydrofoil [m]
l = length of cavity [m]
p_v = vapor pressure of liquid (N/m^2)
p_∞ = freestream static pressure (N/m^2)
Re = cU_∞/ν, Reynolds number
St = fc/U_∞, Strouhal number

[1]They were manufactured in the same shop by the same machinist.

U = streamwise velocity (m/s)
U_∞ = freestream velocity (m/s)
α = angle of attack (deg)
ρ = fluid density (kg/m^3)
σ = $2(p_\infty - p_v)/\rho U_\infty^2$, cavitation number based on vapor pressure

References

[1] Kjeldsen, M., Arndt, R. E. A., and Effertz, M., 2000, "Spectral Characteristics of Sheet/Cloud Cavitation," ASME J. Fluids Eng., **122**, pp. 481–487.

[2] Reisman, G. E., Wang, Y.-C., and Brennen, C. E., 1997, "Observation of Shockwaves in Cloud Cavitation," J. Fluid Mech., **355**, pp. 255–283.

[3] Arndt, R. E. A., Song, C. S. S., Kjeldsen, M., He, J., and Keller, A., 2001, "Instability of Partial Cavitation: A Numerical/Experimental Approach," *Proceedings of the Twenty-Third Symposium on Naval Hydrodynamics*, Val de Reul, France, Office of Naval Research, Naval Studies Board, National Research Council, National Academies Press.

[4] Pham, T. M., Larrarte, F., Fruman, and D. H., 1999, "Investigation of Unsteady Sheet Cavitation and Cloud Cavitation Mechanisms," ASME J. Fluids Eng., **121**, pp. 289–296.

[5] Kawanami, Y., Kato, H., Yamaguchi, H., Tagaya, Y., and Tanimura, M., 1996, "Mechanism and Control of Cloud Cavitation," *Proceedings ASME Symposium on Cavitation and Gas-Liquid Flows in Fluid Machinery and Devices*, Paper No. FED-236, 29–336.

[6] Arndt, R. E. A., Ellis, C. R., and Paul, S., 1995, "Preliminary Investigation of the Use of Air Injection to Mitigate Cavitation Erosion," ASME J. Fluids Eng., **117**, pp. 498–504.

[7] Amromin, E., Arndt, R. E. A., Kopriva, J., and Wosnik, M., 2006, "Hydrofoil Drag Reduction by Partial Cavitation," ASME J. Fluids Eng., **128**(5), pp. 931–936.

[8] Kopriva, J., Arndt, R. E. A., Wosnik, M., and Amromin, E., 2005, "Comparison of Hydrofoil Drag Reduction by Natural and Ventilated Partial Cavitation," *Proceedings of 2005 ASME Fluids Engineering Division Summer Meeting and Exhibition*, Houston, TX, Jun. 19-23, FEDSM2005-77131.

[9] Watanabe, S., Tsujimoto, Y., and Furukawa, A., 2001, "Theoretical Analysis of Transitional and Partial Cavity Instabilities," ASME J. Fluids Eng., **123**, pp. 692–697.

[10] Callenaere, M., Franc, J. P., Michel, J. M., and Riondet, M., 2001, "The Cavitation Instability Induced by the Development of a Re-Entrant Jet," J. Fluid Mech., **444**, pp. 223–256.

[11] Franc, J. P., 2003, "Partial Cavity Instabilites and Re-Entrant Jet," *Proceedings of the Fourth International Symposium on Cavitation*, Pasedena, CA.

[12] Sato, K., Tanada, M., Monden, S., and Tsujimoto, Y., 1999, "Observations of Oscillating cavitation on a Flat Plate Hydrofoil," JSME Int. J., Ser. B, **65**(639), pp. 3659–3667.

[13] Arndt, R. E. A., and Keller, A. P., 2003, "A Case Study of International Cooperation: 30 Years of Collaboration in Cavitation Research," *Proceedings of Fourth ASME_JSME Joint Fluids Engineering Conference*, Honolulu, HI, Jul. 6–10, Keynote Paper.

[14] Sakoda, M., Yakushiji, R., Maeda, M., and Yamaguchi, H., 2001, "Mechanism of Cloud Cavitation Generation on a 2-D Hydrofoil," *Proceedings of the Fourth International Symposium on Cavitation*, Pasadena, CA.

[15] Kawakami, D. T., Qin, Q., and Arndt, R. E. A., 2003, "Can Water Quality affect the Lift Dynamics of Cavitating Hydrofoils?," *Proceedings of the Fifth International Symposium on Cavitation*, Osaka, Japan.

[16] Arndt, R. E. A., Paul, S., and Ellis, C. R., 1997, "Application of Piezoelectric Film in Cavitation Research," J. Hydraul. Eng., **123**(6), 539–548.

[17] Fujii, A., Kawakami, D. T., Tsujimoto, Y., and Arndt, R. E. A., 2007, "Effect of Hydrofoil Shape on Cavity Oscillation," ASME J. Fluids Eng., **129**(6), pp. 669–674.

[18] Guennoun, F., Farhat, M., Ait Bouziad, Y., and Avellan, F., 2003, "Experimental Investigation of a Particular Traveling Bubble Cavitation," *Proceedings of the Fifth International Symposium on Cavitation*, Osaka, Japan.

Cavitation Analogy to Gasdynamic Shocks: Model Conservativeness Effects on the Simulation of Transient Flows in High-Pressure Pipelines

Alessandro Ferrari
Michele Manno
Antonio Mittica

IC Engines Advanced Laboratory,
Politecnico di Torino,
Corso Duca degli Abruzzi 24,
Torino 10129, Italy

A comparison between conservative and nonconservative models has been carried out for evaluating the influence of conservativeness on the prediction of transient flows in high-pressure pipelines. For the numerical tests, a pump-line-nozzle Diesel injection system was considered because the pipe flow presented interesting cases of cavitation. The validity of a conservative model in the simulation of cavitating transient flows was substantiated by the comparison between computed pressure time histories and experimental results at two pipeline locations in the injection system. Although nonconservative models can assure satisfactory accuracy in the evaluation of the wave propagation phenomena, they introduce fictitious source terms in the discretized equations. Such terms are usually negligible, but can play a significant role in the presence of acoustic cavitation, i.e., pressure-wave-induced cavitation, producing errors in the pressure-wave speed prediction. A theoretical analysis based on unsteady characteristic lines was carried out, showing that the cavitation desinence is a shock gas-dynamic-like event, whereas cavitation inception is a supersonic expansion. The Rankine–Hugoniot jump conditions were applied to evaluate the shock wave speed in the presence of cavitation. Analytical relations to calculate the flow property variations across the cavitation-induced discontinuities were also derived. A previously published analytical expression of the sound speed in a homogeneous two-phase flow model was also derived from the eigenvalues of the Euler flow equations for the two distinct phases and a comparison was made with Wallis' formula, which is commonly applied to cavitating flow simulation in transmission lines. Finally, a novel algorithm for calculating the shock speed, as is predicted by nonconservative models, was presented and applied to Burgers' equation, pointing out the contribution of internal fictitious fluxes in the shock-speed wrong estimation.
[DOI: 10.1115/1.2842226]

Introduction

In hydraulic transmission lines, as a consequence of strong compression- and rarefaction-wave-induced pressure gradients, the liquid pressure can decrease up to the local vapor tension. This leads to the liquid vaporization, i.e., to acoustic cavitation.

Cavitation occurrence affects the wave propagation speed, which can significantly change [1–3]. Discontinuities in the fluid dynamic quantities at the boundaries between vaporization zone and liquid field arise [4]. Numerical simulations can be very helpful to understand the complex physical phenomena, which take place at cavitation region boundaries. A theoretical evaluation of the flow property variations across the boundary between vaporization zone and liquid field is relevant to the fluid-dynamic characterization of acoustic cavitation processes. This is an important issue for a correct numerical simulation of acoustic cavitation traveling.

Discrete-bubble cavitation models that take bubble inertial effects into account are very difficult to numerically handle, mainly for flows with high-pressure gradients [2,3]. Besides, these models imply many parameter assumptions that can hardly be assessed by experiments, making the study of the basic phenomena uncertain [3,5]. The main difficulty in the application of such an approach to situations of engineering relevance resides in the fact that the Rayleigh–Plesset-type equations refer only to single bubbles [6,7]. In fact, nucleation events occur just before vaporous cavitation takes place. After reaching a critical radius, vacancies between liquid molecules or microbubbles of contaminant gas become unstable and liquid ruptures occur, leading to the development of macroscopic bubbles. Therefore, in order to couple the Euler or the Navier–Stokes equations, which represent the continuous model, to the Rayleigh–Plesset equation, accurate models for the nucleation process are needed [8,9]. Furthermore, one should know the analytical expression of the nuclei size distribution function $\chi(R)$ [7] for the specific application. This function, for a given value of the initial void fraction, specifies how the bubble initiators distribute in size [7]. Such initiators consist of microbubbles of undissolved gas, which can be adsorbed in the crevices of the system walls or on the surface of microscopic solid particles suspended in the liquid. Analytical expressions for $\chi(R)$ can be derived from experimental analysis, for example, by means of holograms of the liquid field [10]. Tests in water tunnels [11,12] and other observations on water [13] have produced nuclei size distributions of similar shape (roughly $\chi \propto R^{-4}$). However, no data on liquid fuels and oils are available in the literature. Furthermore,

Contributed by the Fluids Engineering Division of ASME for publication in the JOURNAL OF FLUIDS ENGINEERING. Manuscript received April 3, 2006; final manuscript received October 12, 2007; published online March 12, 2008. Review conducted by Georges L. Chahine. Paper presented at the 7th Biennial ASME Conference on Engineering Systems Design and Analysis (ESDA2004), Manchester, UK, July 19–22, 2004.

the authors are mainly interested in macroscopic effects that acoustic cavitation has on injection-system performance [3].

Homogeneous bubbly-flow barotropic models reduce both the complexity of the physical description and of the parameter assumptions with respect to discrete-bubble models, contributing to the understanding of phenomena at a macroscopic level [3,6,14]. In particular, only the specification of thermodynamic evolution, which the fluid is subjected to, is required to assess the sound speed either in liquid or cavitation regions.

In high-pressure fuel injection systems, the pressure-wave propagation in the liquid flow is close to occur under isentropic conditions, consistent with negligible heat transfer and viscous power losses [3,15]. The pure liquid isentropic sound speed in the pressure and temperature range of interest for the Diesel oil is between a minimum and a maximum of 1400–2000 m/s. Since the pipe average-cross-sectional oil velocities occurring in traditional and innovative Diesel injection systems are less than 150 m/s, at any working condition, the flow is subsonic, with Mach number values less than 0.1. However, in spite of the low Mach numbers, the compressibility of the liquid must be taken into account to correctly simulate the system dynamic response to injections [3].

To determine the sound speed in liquid-vapor mixtures along specified transformations, an accurate cavitating flow model is required. In transmission pipelines and in high-pressure injection systems, the hypothesis of local thermodynamic equilibrium is accurate for macroscale models [3,6]. Cavitation barotropic models based on the Wallis works have been extensively applied to high-pressure injection-system transient flows [1,2,15–18]. Nevertheless, as is shown in Ref. [3], the Wallis expression is not consistent with cavitation description, because it does not allow the simulation of any mass transfer across the cavity walls.

A comprehensive thermodynamic approach to acoustic cavitation of general application, including the simulation of both gaseous and vaporous cavitation, was reported in Ref. [3]. The developed two-phase flow barotropic model was capable of accurately predicting the cavitating-fluid sound speed along different thermodynamic processes (isothermal, isentropic, or isenthalpic), as well as the gas dissolution and entrainment effects. Actually, gaseous release from liquid fuels needs periods of time, which are considerably higher than mean life period of vaporous cavitation-induced bubbles [19]. Therefore, in the analysis of fast transients related to compression and rarefaction waves subsequent to an injection event, gaseous cavitation, that is, passage from dissolved to undissolved gas and vice versa, can be neglected [20]. Furthermore, the pressure peak reached during the process of vaporous-bubble collapse increases if the amount of undissolved gas reduces [21]. As a consequence, neglecting any amount of undissolved gas in numerical simulations leads to a conservative estimation of the maximum pressure at the end of bubble collapse, and also removes bubble oscillatory behavior, in discrete-bubble cavitation models [6].

An application of the characteristic-line aerodynamics theory to unsteady cavitating flows in a high-pressure pump-line-nozzle injection system has been carried out. The Rankine–Hugoniot conditions have been applied to compute the speed of the traveling compression waves in the presence of cavitation. The convenience of developing conservative models for the accurate prediction of transient flows in the presence of liquid vaporization phenomena was pointed out and discussed. In particular, the effects of nonconservative forms of either partial differential equation (PDE) or numerical schemes on cavitation inception and desinence simulation were analyzed.

Conservative and Nonconservative Models

One dimensional pipe-flow conservation laws are expressed by the following hyperbolic PDE:

$$\frac{\partial \mathbf{w}}{\partial t} + \frac{\partial \mathbf{F}}{\partial x} = \mathbf{H} \tag{1}$$

where $\mathbf{w}$ is the conserved variable vector, $\mathbf{F}=\mathbf{F}(\mathbf{w})$ is the vector of physical fluxes, and $\mathbf{H}$ is a source term.

Equation (1) can also be expressed in quasilinear form by applying the chain rule to the gradient of the vector $\mathbf{F}$:

$$\frac{\partial \mathbf{w}}{\partial t} + \mathbf{A}(\mathbf{w})\frac{\partial \mathbf{w}}{\partial x} = \mathbf{H} \tag{2}$$

where $\mathbf{A}$ is the Jacobi matrix of the flux function $\mathbf{F}(\mathbf{w})$.

Equations (1) and (2) are mathematically equivalent, but for nonlinear fluxes, their numerical implementation is not [22]. Indeed, in the presence of shocks, the discretization of Eq. (2) can lead to significant errors in the prediction of weak (discontinuous) solutions. More specifically, sensible inaccuracies can occur in the shock-speed evaluation [23,24].

Actually, in order to have the computed shock located in the right position, it is required that the discretized equations have the following conservative form:

$$\mathbf{w}_j^{n+1} = \mathbf{w}_j^n - \frac{\Delta t}{\Delta x}(\mathbf{\Phi}_{j+1/2}^{n+1/2} - \mathbf{\Phi}_{j-1/2}^{n+1/2}) + \Delta t \mathbf{H}_j^{n+1/2} \tag{3}$$

where the subscript j indicates the spatial grid node, the superscript n designates the time level, and $\mathbf{\Phi}$ is the so-called numerical flux function. In particular, the numerical flux $\mathbf{\Phi}_{j+1/2}^{n+1/2}$ is an estimation of the time-averaged physical flux $\mathbf{F}\ (x_{j+1/2},t)$ over the time interval $[t_n,t_{n+1}]$:

$$\mathbf{\Phi}_{j+1/2}^{n+1/2} \approx \frac{1}{\Delta t}\int_{t_n}^{t_{n+1}} \mathbf{F}[\mathbf{w}(x_{j+1/2},t)]dt \tag{4}$$

Two aspects should be considered in the discussion of conservativeness: the first is related to the form of the PDE and the second to the features of the selected numerical scheme. A simple way to derive difference analogous to PDE in the form of Eq. (3) consists in discretizing the hyperbolic conservation law in divergence form, i.e., Eq. (1), with conservative schemes.

Conservative and Nonconservative Models of Shock Speed

The Lax–Wendroff theorem assures that if the solution $\mathbf{w}_j^n$ of Eq. (3) converges to an almost everywhere bounded function $\mathbf{w}(x,t)$ as Δx, Δt tend to zero, then $\mathbf{w}(x,t)$ is a weak solution of Eq. (1). It means that in the presence of shocks, the conservative discretization implies that the computed solution fulfills the Rankine–Hugoniot conditions [25].

With reference to a traveling-shock problem, Fig. 1 shows qualitative numerical distributions of $\mathbf{w}_j$ at instants of time t^n (dashed line) and t^{n+1} (solid line). Summing Eq. (3) over the N adjacent mesh cells, centered in $x_1,x_2,\ldots,x_N$, one obtains

$$\sum_{j=1}^{N} \mathbf{w}_j^{n+1} = \sum_{j=1}^{N} \mathbf{w}_j^n - \frac{\Delta t}{\Delta x}(\mathbf{\Phi}_{N+1/2}^{n+1/2} - \mathbf{\Phi}_{1/2}^{n+1/2}) + \Delta t \sum_{j=1}^{N} \mathbf{H}_j^{n+1/2} \tag{5}$$

In the presence of shocks, the last term on the right hand side of Eq. (5) can be neglected, so that Eq. (5) simplifies as follows

$$\sum_{j=1}^{N} (\mathbf{w}_j^{n+1} - \mathbf{w}_j^n)\Delta x \approx -\Delta t(\mathbf{\Phi}_{N+1/2}^{n+1/2} - \mathbf{\Phi}_{1/2}^{n+1/2}) \tag{6}$$

The first member of Eq. (6) approximates the difference of the integrals of the numerical solution $\mathbf{w}_j$ over the interval $(x_{1/2},x_{N+1/2})$ at time instants t^{n+1} and t^n. In Fig. 1, this quantity is given by the difference of the areas subtended by the solid-line and dashed-line curves with respect to the x axis, so that

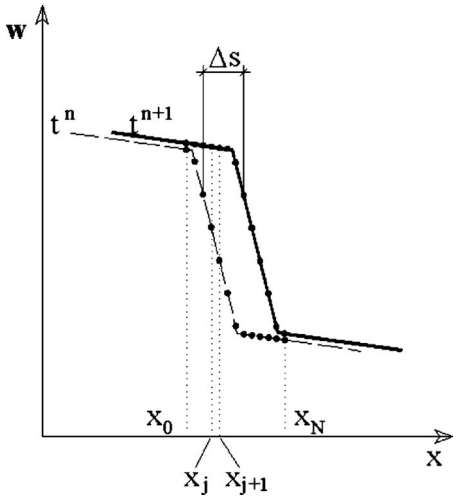

Fig. 1 Shock traveling scheme

$$\sum_{j=1}^{N} (\mathbf{w}_j^{n+1} - \mathbf{w}_j^n)\Delta x \approx -\Delta s[\mathbf{w}] \tag{7}$$

In Eq. (7), $[\mathbf{w}]$ is the finite variation of the vector $\mathbf{w}$ across the discontinuity, i.e., $\mathbf{w_N} - \mathbf{w_0}$, and can be indifferently evaluated at time t^n or t^{n+1}, and Δs is the distance covered by the shock during the time interval Δt. Combining Eq. (6) with Eq. (7), one has

$$\Delta s[\mathbf{w}] \approx \Delta t(\mathbf{\Phi}_{N+1/2}^{n+1/2} - \mathbf{\Phi}_{1/2}^{n+1/2}) \tag{8}$$

For a scalar conservation equation ($\mathbf{w} \Rightarrow u, \mathbf{\Phi} \Rightarrow \Phi$), from Eq. (8), one obtains that the numerical shock speed is equal to

$$\frac{\Delta s}{\Delta t} \approx \frac{(\Phi_{N+1/2}^{n+1/2} - \Phi_{1/2}^{n+1/2})}{[u]} \tag{9}$$

Since the numerical flux $\mathbf{\Phi}$ is an approximation of the function $\mathbf{F}$, Eq. (8) is consistent with the Rankine–Hugoniot shock-speed condition. This, for a scalar conservation equation ($\mathbf{F} \Rightarrow f, \mathbf{w} \Rightarrow u$), is given by

$$v_s = \frac{[f]}{[u]} \tag{10}$$

where ν_s is the exact shock velocity.

Reapplying to nonconservative discretized scalar equations the procedure leading to Eqs. (5)–(8), the following relation can be obtained instead of Eq. (9):

$$\frac{\Delta s}{\Delta t} \approx \frac{\sum_{j=1}^{N} (\Phi_{R_{j+1/2}}^{n+1/2} - \Phi_{L_{j-1/2}}^{n+1/2})}{[u]} \tag{11}$$

In Eq. (11), $\Phi_{Rj+1/2}$ and $\Phi_{Lj-1/2}$ are, respectively, the right and left fluxes relative to the elemental cell centered on x_j and having amplitude Δx. When the discretized equation is not in the form given by Eq. (3), Eq. (5) contains also flux contributions from inside the total control volume. In fact, performing the sum of the discretized equations over the N adjacent mesh cells, left and right fluxes relative to two bordering cells do not cancel each other, because the telescoping property [26] is not satisfied. As a result, Eq. (11) does not match the Rankine–Hugoniot condition given by Eq. (10). Actually, all consistent numerical schemes approximately meet this condition on the shock speed, but only the schemes with the telescopic property do it exactly because of exact term cancellation. The lack of the telescoping property leads to mistakes in the prediction of the shock speed. In particular, the shock can be either in delay or in advance with respect to its exact location, depending on the particular structure of the adopted scheme.

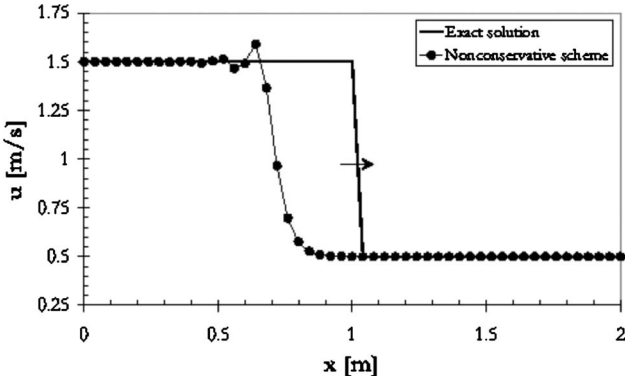

Fig. 2 Forward traveling shock: exact solution and nonconservative numerical solution

Equation (11) is of general application and can be used to predict the behavior of numerical algorithms in discontinuous flows. It allows for the evaluation of the nonconservativeness effects of both the PDE form and the numerical scheme.

Application of the Developed Shock-Speed Calculation Algorithm to Burgers' Equation. A simple nonconservative implicit algorithm of first-order accuracy for solving Burgers' inviscid scalar equation has the following quasilinear form:

$$u_j^{n+1} = u_j^n - \frac{\Delta t}{2\Delta x} u_{j+1}^{n+1}(u_{j+1}^{n+1} - u_{j-1}^{n+1}) \tag{12}$$

Since this numerical method is space centered, it can be applied to simulate waves, which propagate in both negative and positive directions of x axis [24].

For Riemann's initial data, Figs. 2 and 3 compare the exact and numerical solutions after time $\Delta t_1 = 1$ s for a forward and a backward propagation problem, respectively. In both cases, the initial position of the shock is at $x = 0$, and the comparison between exact and nonconservative solution is performed when the shock is expected to have traveled for a length $\Delta x_1 = 1$ m.

The numerical solution presented in Fig. 2 is affected by some oscillations located upstream of the discontinuity, which are absent in Fig. 3. Such a difference is due to the asymmetric structure of the considered numerical scheme. In fact, this is particularly suitable for backward traveling waves, because in Eq. (12), the Jacobi matrix ($\mathbf{A} \Rightarrow u$ for scalar Burgers' inviscid equation) has

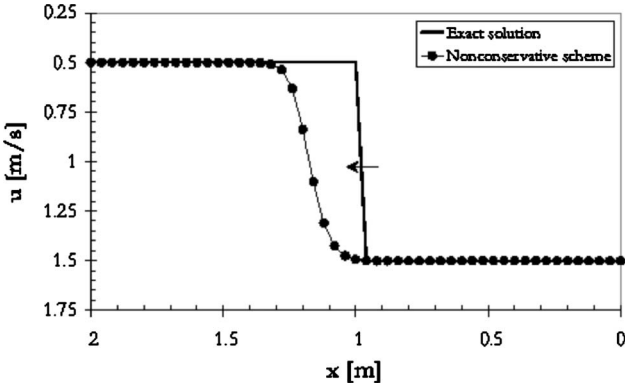

Fig. 3 Backward traveling shock: exact solution and nonconservative numerical solution

Table 1 Forward and backward traveling shock

Point J	Forward traveling shock		Backward traveling shock	
	X_j (m)	U_j (m/s)	X_j (m)	U_j (m/s)
0	0.4	1.4999	−1.48	−0.5000
1	0.44	1.4917	−1.44	−0.5001
2	0.48	1.5026	−1.4	−0.5004
3	0.52	1.5126	−1.36	−0.5020
4	0.56	1.4652	−1.32	−0.5090
5	0.6	1.4897	−1.28	−0.5374
6	0.64	1.5899	−1.24	−0.6319
7	0.68	1.3656	−1.2	−0.8381
8	0.72	0.9653	−1.16	−1.1018
9	0.76	0.6987	−1.12	−1.3096
10	0.8	0.5765	−1.08	−1.4247
11	0.84	0.5282	−1.04	−1.4752
12	0.88	0.5102	−1	−1.4941
13	0.92	0.50361	−0.96	−1.5000
14	0.96	0.5012	−0.92	−1.5012
15	1	0.5004	−0.88	−1.5010
16	1.04	0.5001	−0.84	−1.5006
17	1.08	0.5000	−0.8	−1.5003
18	1.12	0.5000	−0.76	−1.5002
19	1.16	0.5000	−0.72	−1.5000
20	1.20	0.5000	−0.76	−1.5000

been evaluated as u_{j+1}.

In both Figs. 2 and 3, the numerical solution predicts a shock traveling at a wrong speed, which can be calculated, according to Eq. (11), by the following formula:

$$v_{\text{ns}} \approx \sum_{j=1}^{N} \frac{1}{2}(u_{j+1}^2 - u_{j+1}u_{j-1}) \tag{13}$$

In Eq. (13), u_{j-1}, u_{j+1} $(j=1,\ldots,N)$ indicate the values taken by the numerical solution after time $\Delta t_1=1$ s at the grid nodes that are involved in the transition from the upstream (point 0) to the downstream level (point N) of the discontinuity.

In particular, introducing in Eq. (13) the values reported in the third column of Table 1 ($N=17$), it results in

$$v_{\text{ns}} \approx 0.72 \text{ m/s}$$

with a percentage error of 28% with respect to the exact shock-speed value ($v_s=1$ m/s).

In the case of Fig. 3, taking values in the last column of Table 1 ($N=19$), from Eq. (13), one obtains

$$v_{\text{ns}} \approx -1.18 \text{ m/s}$$

the percentage error being equal to 18% in this case.

As can be easily inferred from Figs. 2 and 3, a rather accurate pattern of the shock is predicted by the nonconservative scheme of Eq. (12), but, in both cases, the numerical solution, to which the scheme converges, sensibly differs from the exact solution.

Figure 4 illustrates the results of the convergence analysis for this nonconservative scheme. The convergence error E, which is evaluated as the sum of absolute differences, normalized to v_s, between exact and numerical solutions at grid nodes after time Δt_1, is reported as a function of the control-volume number n. The grid nodes were uniformly distributed on the spatial domain, whose length was $L=2$ m. In all the performed tests, the Courant number σ was constant and equal to 1. The results of the numerical tests are plotted by circular symbols, while the data-interpolating curve by solid line.

Figure 4(a) refers to the propagation of a sinusoidal wave for the linear advection equation case, whereas Fig. 4(b) reports the convergence study for inviscid Burgers' equation with Riemann's initial data. As can be seen from Fig. 4(a), the scheme is numerically consistent because E reduces with n, the order of accuracy being virtually equal to 1. Besides, Fig. 4(b) shows that the inaccuracy of the numerical method in the prediction of discontinuous solutions, which Figs. 2 and 3 refer to, does not disappear by refining the grid, in agreement to what is reported in Refs. [23,25] for nonconservative schemes.

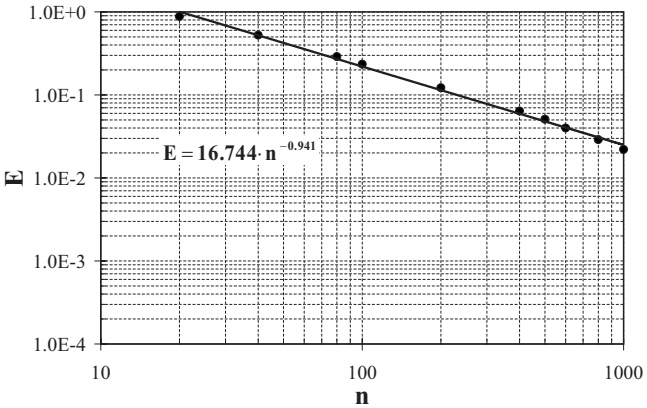

a – Linear advection equation with sinusoidal initial data

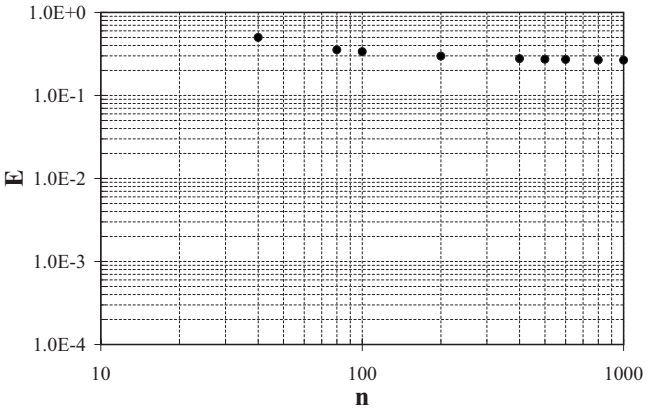

b – Burgers' inviscid equation with Riemann's initial data

Fig. 4 Convergence studies for the nonconservative scheme

Fuel Injection System

For cavitation analysis in a case of technical interest and for conservative versus nonconservative model comparison, a pump-line-nozzle Diesel injection system was considered, for which experimental data were available. Cavitation can take place in the pipe subsequently to the spill port opening, because of the depression wave protraction and intensification due to the delivery valve configuration. In fact, in order to avoid injector-nozzle reopening, the pump was equipped with a delivery valve of the relief-volume type. A snubber valve downstream to it, in the forward flow direction, was set for attenuating cavitation occurrence in the pipe. However, in spite of the snubber-valve presence, the system underwent operating conditions of local intense cavitation, mainly at partial loads.

Figure 5 shows a schematic of the injection-system layout with measurement quantities and locations. More specifically, the experimental data used for comparison with computational results consisted in pressure time histories at two pipe locations: one close to the pump outlet (p_{up}) and the other close to the injector inlet (p_{dp}).

Computational Model. The pipe connecting the pump to the injector was treated as a slender transmission line for which a one dimensional flow model is suitable. A lumped mass model was

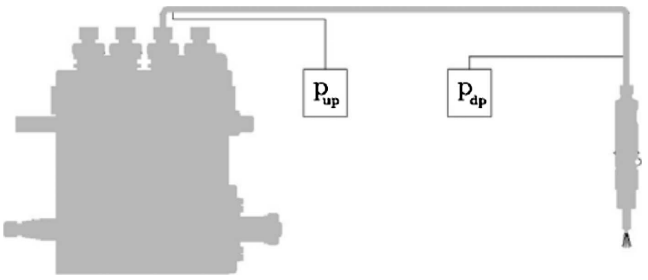

Fig. 5 Injection-system layout and measured quantities

used to write the continuity equations for pump and injector isobaric chambers. Details on the injection-system model are reported in Ref. [27].

The fuel flowing in the high-pressure pipe was modeled as a pure phase in both liquid zones and cavitation regions. Mass-averaged local intensive properties of the vapor-liquid mixture were taken in the latter regions, void fractions being generally lower than 3% [3], so that the vapor was homogeneously distributed within each of the computational cells. Whenever the pressure decreased up to the vapor-tension level at the local temperature, the fluid was modeled as a homogeneous mixture of liquid and vapor without any amount of undissolved gas. In fact, due to measures taken to reduce the dissolved gas portion in the Diesel oil and due to the relatively high temperature of the fuel in the tank (40°C), the amount of dissolved gas could be neglected.

The surface tension effects at the interface of the cavitation area were neglected. For bubble radii between 10 μm and 200 μm [5], a pressure difference lower than 50 mbars can be estimated across cavity walls, oil surface tension being $\sigma \approx 27 \times 10^{-3}$ N/m. Such a difference is of several orders lower than the pressure variations along the pipe connecting the pump to the injectors (Figs. 9–11) and hence can be neglected without any inaccuracy in keeping macroscopic phenomena.

As stated before, the liquid flow was assumed as isentropic. Temperature variations due to the fluid compressibility were taken into account. For the specific thermodynamic evolution in the cavitating region, it was verified that pressure distributions in the liquid field were not significantly influenced by the void fraction variations due to different thermodynamic paths [28]. Therefore, an isothermal cavitation was considered, consistent with the negligible thermal effects related to the tiny amount of fuel usually involved in vaporization processes, the conservative void fraction peak prediction [28], and simple implementation.

In order to obtain a conservative algorithm, the pipe-flow Euler PDE was expressed in terms of *conserved variables*, namely, ρ and ρu for mass-conservation and momentum-balance equations (the energy equation having been reduced to the heat power fundamental thermodynamic equation). Hence, according to the notations of Eq. (1), one has

$$\mathbf{w} = \begin{bmatrix} \rho \\ \rho u \end{bmatrix}, \quad \mathbf{F}(\mathbf{w}) = \begin{bmatrix} \rho u \\ p + \rho u^2 \end{bmatrix}, \quad \mathbf{H} = \begin{bmatrix} 0 \\ -4\tau_w/d \end{bmatrix} \tag{14}$$

In Eq. (14) ρ, u, and p are, respectively, the average pipe-cross-sectional density, velocity, and pressure of either the liquid or the cavitating mixture; τ_w is the wall shear stress; and d is the pipe diameter. Since density and momentum have been chosen as unknown variables, the same equation can be applied both in the presence and in the absence of cavitation. The wall shear stress was evaluated using the following formula [29,30]:

$$\tau_w = \frac{1}{8} f \rho |u| u + \delta \frac{16}{d^2} \mu \int_0^t \frac{\partial u(x,\lambda)}{\partial t} W(t-\lambda) d\lambda \tag{15}$$

The first term on the right hand side of Eq. (15) is due to the stationary friction component and the second term represents the frequency dependent component of τ_w, where the coefficient δ takes the turbulence effect into account. It is worth pointing out that in 1D flow equations, turbulence models can be used to link fluid velocity and its time derivative to wall friction. Therefore, Eq. (15) includes the turbulence model in the present application and allows simulating the interaction between turbulence and cavitation. Whenever present, turbulence introduces an increase of the wall shear stress that can promote cavitation.

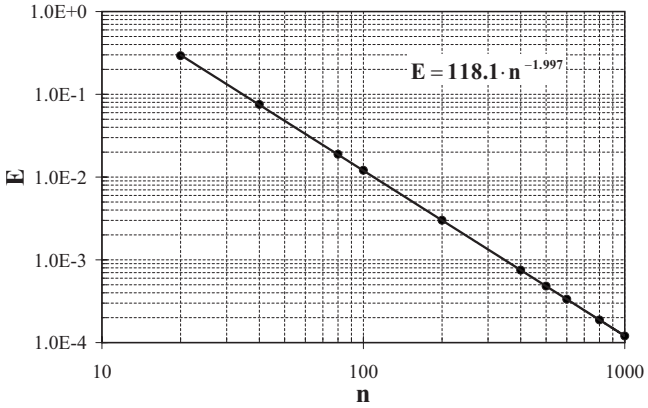

a – Linear advection equation with sinusoidal initial data

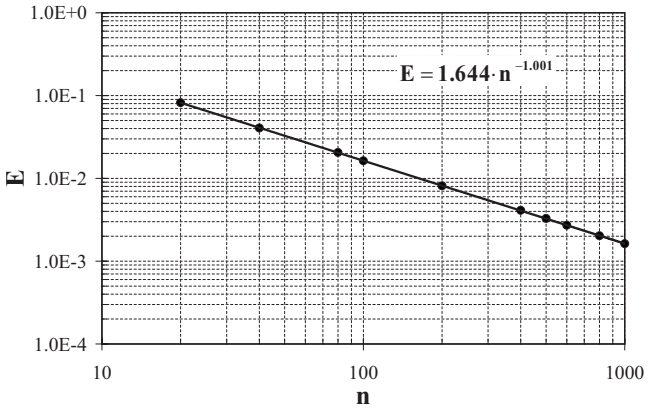

b – Burgers' inviscid equation with Riemann's initial data

Fig. 6 Convergence studies for the ICOST scheme

The proposed numerical scheme for discretizing Eq. (1) is an implicit, conservative one-step scheme of the second-order accuracy in both space and time, whose acronym is ICOST [3]. The discretized Euler equations are expressed by Eq. (3), the numerical flux $\mathbf{\Phi}$ being defined as follows:

$$\begin{aligned} \mathbf{\Phi}_{j+1/2}^{n+1/2} &= \frac{1}{2}(\mathbf{F}_{j+1}^n + \mathbf{F}_j^n) - \frac{1}{2}\left(\frac{\Delta t}{\Delta x}\right)[\mathbf{A}_{j+1/2}^{n+1}(\mathbf{F}_{j+1}^{n+1} - \mathbf{F}_j^{n+1})] \\ \mathbf{\Phi}_{j-1/2}^{n+1/2} &= \frac{1}{2}(\mathbf{F}_j^n + \mathbf{F}_{j-1}^n) - \frac{1}{2}\left(\frac{\Delta t}{\Delta x}\right)[\mathbf{A}_{j-1/2}^{n+1}(\mathbf{F}_j^{n+1} - \mathbf{F}_{j-1}^{n+1})] \end{aligned} \tag{16}$$

where

$$\mathbf{A}(\mathbf{w}) = \begin{bmatrix} 0 & 1 \\ a^2 - u^2 & 2u \end{bmatrix}$$

Figure 6(*a*) shows the convergence test carried out on the ICOST scheme for the linear advection equation in the case of the propagation of a sinusoidal wave (spatial domain $L=2$ m, Courant number $\sigma=1$). The precision order is virtually equal to 2. However, it should be pointed out that the precision order becomes lower in the presence of shocks. For the same L and σ values of Fig. 6(*a*), Fig. 6(*b*) reports the convergence results for Burgers'

inviscid equation with Riemann's initial data. In this case, the precision order reduces to 1. Such a behavior is common to every second-order conservative scheme.

For a barotropic flow model, the total energy conservation equation can be reduced to a state relation among the fluid variables. Coupling this relation to the state equation of the liquid yields the mathematical closure of Eq. (1). For the pure liquid flow, under isentropic evolution, the following relation can be obtained linking pressure and temperature variations [3]:

$$\frac{dp}{\rho} = \frac{c_{pl}}{\beta_l}\frac{dT}{T} \tag{17}$$

where

$$\beta_l = \frac{1}{v}\left(\frac{\partial v}{\partial T}\right)_p = -\frac{1}{\rho}\left(\frac{\partial \rho}{\partial T}\right)_p \tag{18}$$

is the *isobaric thermal expansivity*. The pressure can be evaluated by the state equation of the liquid, which can be expressed in the following differential form:

$$dp = a_T^2(d\rho + \beta_l \rho dT) \tag{19}$$

The analytical expressions, which provide the isobaric thermal expansivity, the isothermal sound speed, and the specific heat at constant pressure of the liquid fuel, as functions of pressure and temperature, were detailed in Refs. [27,28].

Mixture Sound Speed. In order to derive a general expression for the sound speed of the cavitating mixture, one should determine the eigenvalues of the Euler equations for the two-phase flow. The mass-conservation PDEs for liquid and vapor phases are expressed by

$$\begin{aligned} \frac{\partial(\rho_l \alpha_l)}{\partial t} + \frac{\partial(\rho_l \alpha_l u)}{\partial x} &= -\Gamma_v \\ \frac{\partial(\rho_v \alpha_v)}{\partial t} + \frac{\partial(\rho_v \alpha_v u)}{\partial x} &= \Gamma_v \end{aligned} \tag{20}$$

In Eq. (20), the term

$$\Gamma_v = \rho \frac{d\mu_v}{dt} \tag{21}$$

represents the rate of production of vapor per unit volume due to cavitation phenomena, μ_v being the mass vapor fraction, and α_v and α_l are the vapor and liquid volume fractions defined as

$$\alpha_v = \frac{V_v}{V}, \quad \alpha_l = \frac{V_l}{V}$$

Vapor mass and volume fractions are related by $\mu_v = \rho_v \alpha_v / \rho$.

Developing the partial derivatives in Eq. (20), one obtains

$$\begin{aligned} \alpha_l \frac{\partial \rho_l}{\partial t} + \rho_l \frac{\partial \alpha_l}{\partial t} + \rho_l u \frac{\partial \alpha_l}{\partial x} + \alpha_l u \frac{\partial \rho_l}{\partial x} + \alpha_l \rho_l \frac{\partial u}{\partial x} &= -\Gamma_v \\ \rho_v \frac{\partial \alpha_v}{\partial t} + \alpha_v \frac{\partial \rho_v}{\partial t} + \rho_v u \frac{\partial \alpha_v}{\partial x} + \alpha_v u \frac{\partial \rho_v}{\partial x} + \alpha_v \rho_v \frac{\partial u}{\partial x} &= \Gamma_v \end{aligned} \tag{22}$$

Since, according to a barotropic model, a thermodynamic evolution law has been introduced for each phase, the liquid and vapor densities can be expressed as functions of pressure only. Therefore, the following differential relations hold:

$$\begin{aligned} \frac{\partial \rho_l}{\partial y} &= \frac{d\rho_l}{dp}\frac{\partial p}{\partial y} = \frac{1}{a_l^2}\frac{\partial p}{\partial y} \\ \frac{\partial \rho_v}{\partial y} &= \frac{d\rho_v}{dp}\frac{\partial p}{\partial y} = \frac{1}{a_v^2}\frac{\partial p}{\partial y} \end{aligned} \tag{23}$$

where y refers to either the time (t) or the spatial coordinate (x) and a_l, a_v are the sound speeds for liquid and vapor phases.

Coupling Eq. (22) to Eq. (23), one obtains

$$\left(\frac{\alpha_v}{\rho_v a_v^2} + \frac{1-\alpha_v}{\rho_l a_l^2}\right)\frac{\partial p}{\partial t} + \frac{\partial u}{\partial x} + \left(\frac{\alpha_v}{\rho_v a_v^2} + \frac{1-\alpha_v}{\rho_l a_l^2}\right) u \frac{\partial p}{\partial x} = \frac{\Gamma_v}{\rho_v}\left(1 - \frac{\rho_v}{\rho_l}\right) \tag{24}$$

Being $\mu_v = \mu_v(p)$ for a barotropic flow, the total time derivatives of μ_v leads to

$$\Gamma_v = \rho \frac{d\mu_v}{dt} = \rho \frac{d\mu_v}{dp}\left(\frac{\partial p}{\partial t} + u\frac{\partial p}{\partial x}\right) \tag{25}$$

Replacing Γ_v in Eq. (24) by Eq. (25) and rearranging, one has

$$\frac{\partial p}{\partial t} + u\frac{\partial p}{\partial x} + \left[\frac{\alpha_v}{\rho_v a_v^2} + \frac{1-\alpha_v}{\rho_l a_l^2} - \rho\left(\frac{1}{\rho_v} - \frac{1}{\rho_l}\right)\frac{d\mu_v}{dp}\right]^{-1}\frac{\partial u}{\partial x} = 0 \tag{26}$$

The mixture momentum-balance equation can be written in the following nonconservative form:

$$\frac{\partial u}{\partial t} + u\frac{\partial u}{\partial x} + \frac{1}{\rho}\frac{\partial p}{\partial x} = -\frac{4\tau_w}{\rho d} \tag{27}$$

Equations (26) and (27) make up a system of two equations in the form given by Eq. (2), where

$$\mathbf{w} = \begin{bmatrix} p \\ u \end{bmatrix}, \quad \mathbf{H} = \begin{bmatrix} 0 \\ -4\tau_w/\rho d \end{bmatrix}$$

$$\mathbf{A} = \begin{bmatrix} u & 1/\rho a^2 \\ 1/\rho & u \end{bmatrix}$$

The variable a is defined as follows:

$$\frac{1}{\rho a^2} = \frac{\alpha_v}{\rho_v a_v^2} + \frac{1-\alpha_v}{\rho_l a_l^2} - \rho\left(\frac{1}{\rho_v} - \frac{1}{\rho_l}\right)\frac{d\mu_v}{dp} \tag{28}$$

As can be verified, the eigenvalues λ of the Jacobian $\mathbf{A}$ are

$$\lambda_{1,2} = u \pm a \tag{29}$$

where a is the sound speed of the two-phase mixture. The first two terms on the right hand side of Eq. (28) are related to the elasticity properties of each component of the mixture, whereas the last term refers to the vaporization or condensation process.

The specification of the thermodynamic process, which the cavitating fluid is subjected to, allows the vapor source term modeling, i.e., $d\mu_v/dp$ in Eq. (28). In particular, for an isentropic process, one has from the energy equation

$$\frac{d\mu_v}{dp} = \frac{1}{r}\left\{\left[\frac{1}{\rho} - \frac{1-\mu_v}{\rho_l}(1-\beta_l T)\right] - c_p\frac{dT}{dp}\right\} \tag{30}$$

whereas for an isenthalpic process, one obtains

$$\frac{d\mu_v}{dp} = -\frac{1}{r}\left\{\frac{1-\mu_v}{\rho_l}(1-\beta_l T) + c_p\frac{dT}{dp}\right\} \tag{31}$$

In Eqs. (30) and (31), r is the vaporization heat per unit mass of the fuel and c_p is the mixture specific heat at constant pressure

$$c_p = (1-\mu_v)c_{pl} + \mu_v c_{pv}$$

The oil vapor tension, as a function of the temperature, was measured at ICE Laboratory of Politecnico and is reported in Fig. 7. Its experimental uncertainty is below $\pm 1\%$. Being the oil, a multicomponent substance, its isothermal vaporization occurs in a vapor pressure range, rather than at constant pressure. At each temperature, the vapor tension, which has been reported in Fig. 7, should be regarded as a mean vapor tension in the void fraction range of interest for high-pressure injection systems. Since this range is particularly narrow ($\alpha_v < 3\%$), the hypothesis of constant vapor tension at each temperature is still accurate. As can be in-

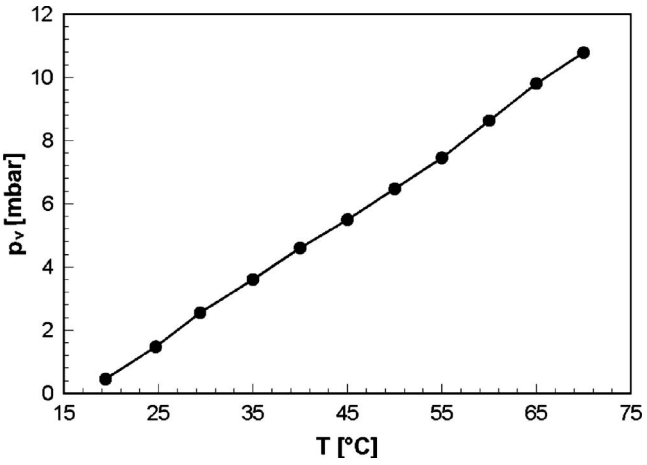

Fig. 7 ISO4113 vapor tension versus temperature

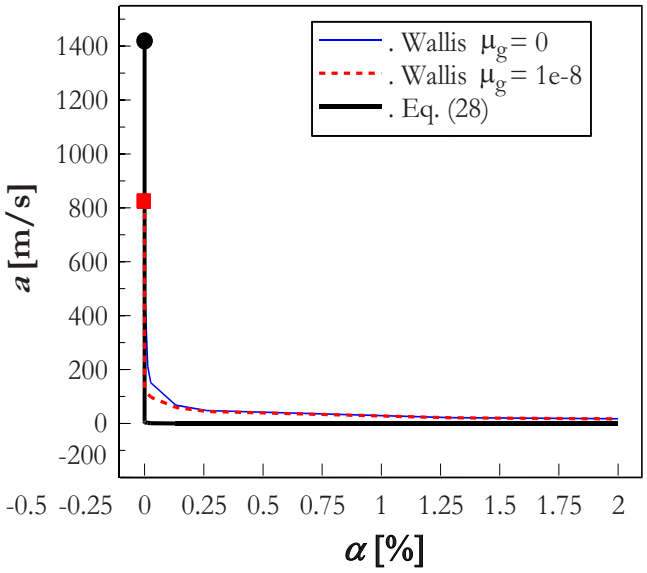

Fig. 8 Comparison between Eq. (28) and Wallis' formula

ferred from Fig. 7, the plotted vapor pressure varies almost linearly with the temperature in the range 20–70°C, so that dT/dp in Eqs. (30) and (31) is virtually independent of T.

If an isothermal cavitation is assumed, the pressure keeps constant at the vapor-tension value for the specific temperature, so that taking the limit $d\mu_v/dp \to \infty$, Eq. (28) leads to

$$a = a_T \to 0 \tag{32}$$

In this case, compression and rarefaction waves propagate inside the cavitating regions with the local velocity u of the mixture according to Eq. (29).

Comparison With Wallis Formula Results. Wallis' expression for the sound speed in two-phase flows is given by

$$\frac{1}{\rho a^2} = \frac{\alpha_v}{\rho_v a_v^2} + \frac{1-\alpha_v}{\rho_l a_l^2} \tag{33}$$

With respect to Eq. (28), Eq. (33) does not include any term that accounts for mass transfer across the cavities. This is due to the fact that in Wallis' work [1], the sound speed was obtained by considering the rate of vapor production Γ_v per unit volume as a source term to be separately modeled. It is worth recalling that considering Γ_v as a source term in the evaluation of eigenvalues of Eq. (20) means to regard it as a variable independent of the gradient of **w**. This would be right if the appearance of any vapor fraction in the fluid was due to an external aeriform source, whose dynamics could be governed independent of the flow evolution. However, in the case of cavitation, the aeriform source is internal to the fluid, since its dynamics depends on the fluid evolution history. Therefore, it is not physically consistent to ignore the term Γ_v in the calculation of the eigenvalues of Eq. (20). Evidence of this is given by the fact that Eq. (33) does not yield a null speed of sound, for the case of isothermal vaporous cavitation, as results from Eq. (28), instead, as well as directly from the basic definition of sound speed for a homogeneous flow $a = \sqrt{dp/d\rho}$ (for isothermal cavitation, p keeps constant and therefore $a \to 0$).

For a homogeneous cavitating mixture, Fig. 8 compares the isentropic sound speed a given by Eq. (33) to that expressed by Eq. (28) as functions of vapor void fraction at a temperature of 40°C. The thick solid-line curve refers to Eq. (28), $d\mu_v/dp$ being given by Eq. (30), whereas the thin solid-line and dashed-line curves refer to Eq. (33). The value that the solid-line curves take for $\alpha_v = 0$ is the same and corresponds to the liquid isentropic sound speed at 40°C (solid circle symbol). Besides, Eqs. (28) and (33) give virtually the same value of sound speed for vapor void fractions higher than 2%.

The sound speed a abruptly decreases as soon as cavitation takes place. However, for the case of Eq. (28), it is the vaporous cavitation occurrence that causes the drop in sound speed values, whereas in the case of Eq. (33), significant reductions of a also occur when the vaporization process proceeds (e.g., at $\alpha_v = 0.1\%$, Eq. (33) gives $a \approx 110$ m/s, while Eq. (28) $a \approx 5$ m/s; at $\alpha_v = 1\%$, Eq. (33) yields $a \approx 25$ m/s, whereas Eq. (28) $a \approx 2$ m/s).

In the α_v range of Fig. 8, the third term on the right hand side of Eq. (28) keeps much higher values than the other two terms, which are related to the mixture elasticity properties. Therefore, the values of a drastically reduce as soon as cavitation inception occurs. Furthermore, although the first two terms on the right hand side of Eq. (28) gradually change with the void fraction of fluid, a is practically unaffected by the α_v value. Thus, Eq. (28) induces a discontinuity at $\alpha_v = 0$. On the other hand, in Eq. (33), a is more sensible to α_v changes, showing a smooth distribution around the abscissa $\alpha_v = 0$.

All these considerations are also useful to analyze the effect of the presence of undissolved gas on the mixture sound speed during vaporous cavitation. The undissolved gas modifies the elasticity properties of the fluid during cavitation. Therefore, for $\alpha_v > 0$, the presence of a fixed amount of undissolved gas is expected to sensibly modify the values of a given by Eq. (33) but not those achieved by Eq. (28), where the dominant term is $d\mu_v/dp$ and the role of this is not significantly influenced by the presence of a very small amount of undissolved gas.

The dashed-line curve in Fig. 8 reports Wallis' sound speed distribution during vaporous cavitation in the presence of a fixed undissolved mass fraction of gas ($\mu_g \approx 10^{-8}$). The plotted values of a were obtained by adding the term $\alpha_g/\rho_g a_g^2$ on the right hand side of Eq. (33). The resulting graph is shifted below the curve, which refers to the case $\mu_g = 0$. In particular, for $\alpha_v = 0$, the isentropic speed of sound (square symbol) is much lower than the value it takes for $\mu_g = 0$ (circle symbol). For $\alpha_v > 0$, the addition of the term $\alpha_g/\rho_g a_g^2$ in Eq. (28) does not determine any perceptible variation in the diagram with respect to the case $\mu_g = 0$. The differences of the cavitating-fluid sound speeds computed by Eq. (28) with respect to values given by Eq. (33) tend to reduce when appreciable undissolved gas quantities are present in the oil.

In conclusion, the application of Wallis' formula can lead to appreciable inaccuracies in the prediction of the two-phase flow sound speed, when spread vaporous cavitation occurs with low vapor void fractions, even in the presence of very small amounts of undissolved gas.

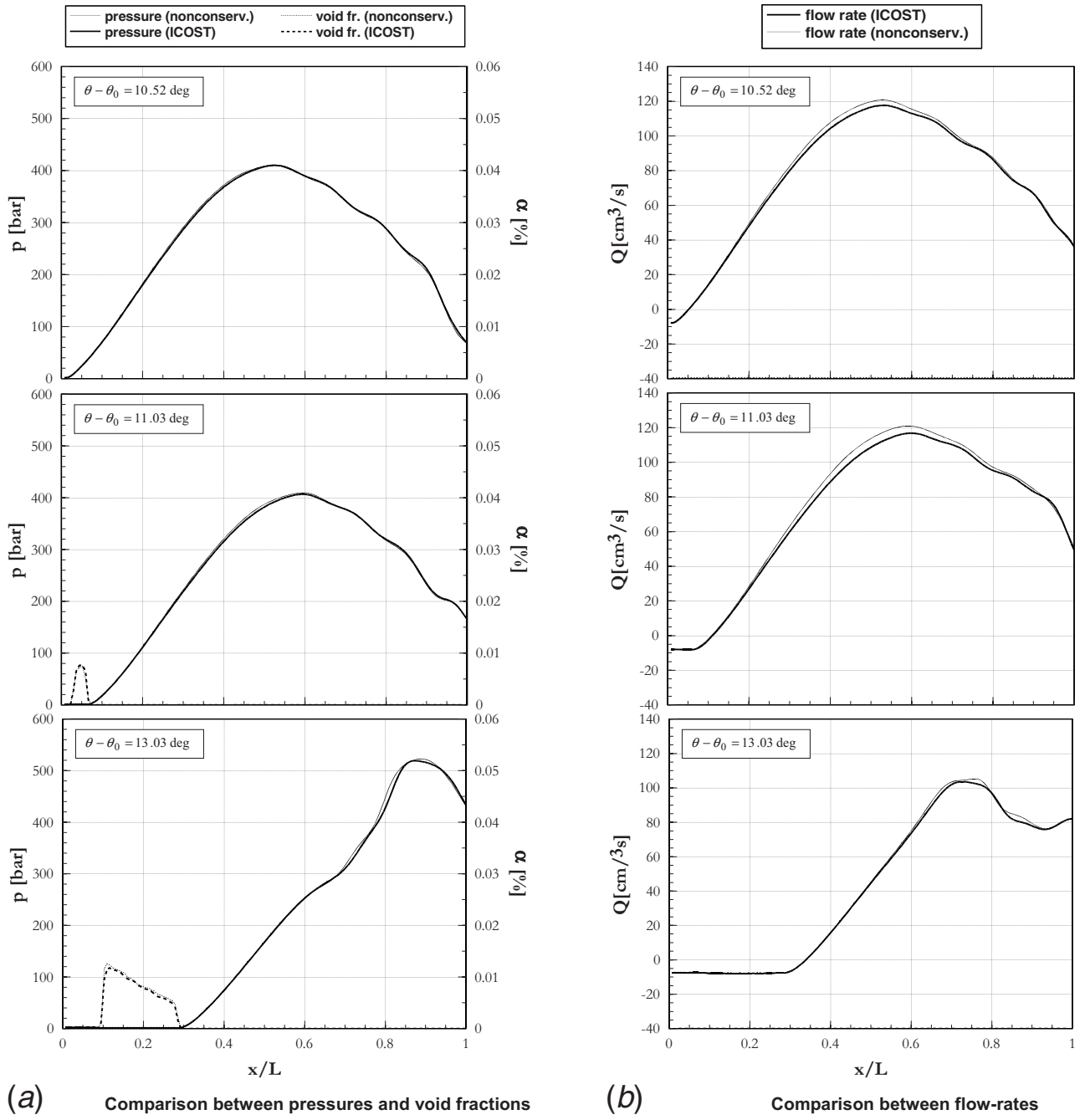

Fig. 9 Comparison between pressures and void fractions (*a*) and comparison between flow rates (*b*)

Conservative Versus Nonconservative Models in the Simulation of Acoustic Cavitation

A comparison between conservative and nonconservative models was carried out in the simulation of pump-line-nozzle transient pipe flows in the presence of cavitation at part load for two different pump speeds.

Figures 9–11 report sequences of flow rate, pressure, and void fraction distributions along the pipe and injector-drilled passages at different time instants corresponding to the indicated $(\theta-\theta_0)$ cam angles, θ_0 being a reference value. The abscissa reports the distance from the pump outlet normalized to the length (L) of the connecting pipe including the injector-drilled passages. The distributions obtained by Eqs. (3) and (16) are plotted along with those achieved using the implicit first-order accuracy nonconservative scheme, which had already been applied to Burgers' test case, by Eq. (12). The nonconservative discrete analogous to the mass-conservation and momentum-balance PDEs is expressed by

$$\mathbf{w}_j^{n+1} = \mathbf{w}_j^n - \frac{\Delta t}{\Delta x}[\mathbf{A}]_{j+1}^{n+1}(\mathbf{w}_{j+1}^{n+1} - \mathbf{w}_{j-1}^{n+1}) + \Delta t \mathbf{H}_j^{n+1} \tag{34}$$

where

$$\mathbf{w} = \begin{bmatrix} \rho \\ u \end{bmatrix}, \quad A(\mathbf{w}) = \begin{bmatrix} u & \rho \\ a^2/\rho & u \end{bmatrix}, \quad \mathbf{H} = \begin{bmatrix} 0 \\ -4\tau_w/\rho d \end{bmatrix}$$

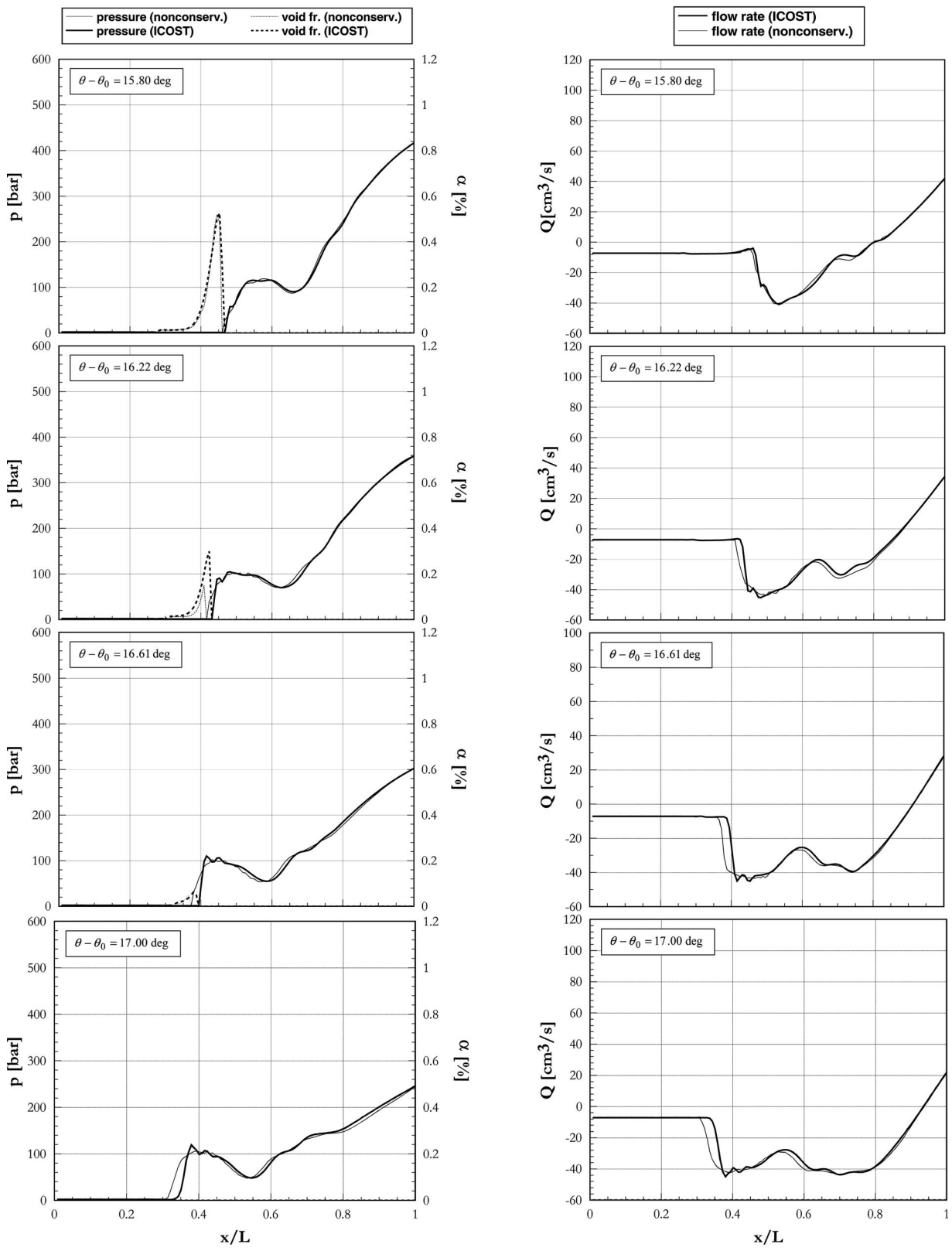

Fig. 10 Comparison between pressures and void fractions (*a*) and comparison between flow rates (*b*)

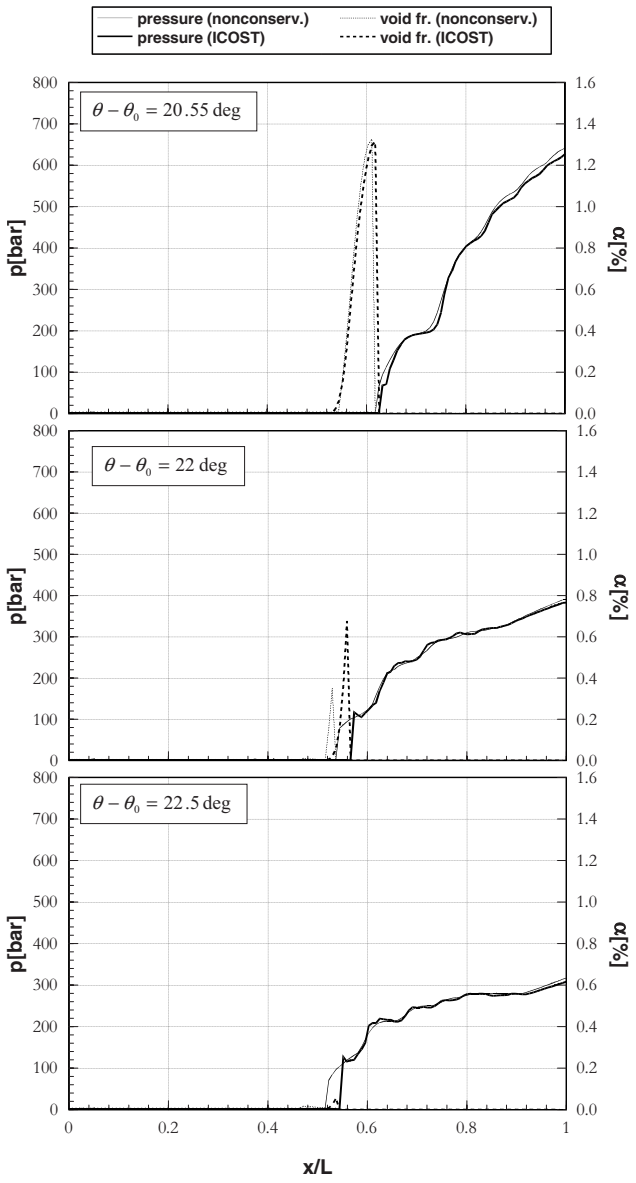

Fig. 11 Comparison between pressures and void fractions

The ICOST scheme and the nonconservative algorithm have different accuracy order. Therefore, some preliminary tests on Burgers' equation with sinusoidal initial data were carried out, in order to determine two distinct grid-data sets, one for each scheme, which gave the same convergence error. Based on the results of such numerical experiments, the following mesh sizes were selected for the comparisons made in Figs. 9–11: $\Delta x = 20$ mm, $\Delta t = 20$ μs for Eqs. (3) and (16) and $\Delta x = 1$ mm, $\Delta t = 1$ μs for Eq. (34). With the abovementioned grid data, approximately 5 min were needed by the ICOST scheme to perform an overall injection cycle ($\Delta\theta = 180$ deg) on a Pentium 4 CPU. The simulation time was sensibly higher for the nonconservative algorithm because of the much lower values of Δx and Δt.

Figure 9 refers to a case of cavitation inception at $n = 1300$ rpm. Fuel vaporization is subsequent to the spill port opening, which determines the ending of the fuel delivery phase. As soon as the spill port opens, a depression arises in the pumping chamber. This makes the flow reversed at the beginning of the pipe, so that the fuel velocity becomes negative. In Fig. 9(*b*), for $\theta - \theta_0 = 10.52$ deg, the flow-rate spatial distribution crosses the axis $Q = 0$ at the point $x_i/L \approx 0.05$. Since $Q_{i+1/2} > 0$ and $Q_{i-1/2} < 0$ ($Q_i = 0$), the density ρ_i is subjected to a strong reduction. Thus, being the pressure p_i close to the vapor-tension level (Fig. 9(*a*), $\theta - \theta_0 = 10.52$ deg), cavitation takes place, as can be seen from the void fraction at $x_i/L \approx 0.05$, for $\theta - \theta_0 = 11.03$ deg. Once the cavitation region has taken place, it travels toward the injector and enlarges with time in its initial development stage.

In fact, point x at which the flow rate Q is equal to zero proceeds ahead of the cavitation zone (Fig. 9(*a*), $\theta - \theta_0 = 11.03$ deg and $\theta - \theta_0 = 13.03$ deg) and is responsible for the right boundary of the cavitating region to move forward through the pipe. The cavitation zone leaves a low-pressure noncavitating one behind it. This is due to the presence of a snubber valve, which produces a slight pressure increase, upstream of it, in the backflow from the pipe to the pumping chamber [27]. Thus, a pressure wave of small amplitude arises in the chamber ahead of the snubber valve and propagates toward the pipe reaching the cavitation zone from the left side. Consequently, the left boundary of the cavitating region moves toward the injector as $\theta - \theta_0$ increases (Fig. 9(*a*)).

As is shown in Fig. 9, fuel vaporization occurs without any discontinuity in the flow properties. Pressure, void fraction, and flow-rate distributions, resulting from the nonconservative and ICOST algorithms, are virtually coincident. The most noticeable differences occur in the flow rates (Fig. 9(*b*)), but the discrepancy between the conservative and nonconservative results is always smaller than 5%. This is not related to conservativeness, being caused by the different round-off errors that the discretization schemes introduce and can be further reduced by reducing the computational mesh sizes.

Figure 10 illustrates cavitation decrease and desinence. At early stages ($\theta - \theta_0 = 15.80$ deg), the flow property distributions computed by the two algorithms are almost coincident, but, as condensation proceeds, differences in the boundary locations of the cavitating region arise. Purposely carried out numerical tests showed that these differences persist by reducing temporal and spatial dimensions of the computational mesh.

As shown by Fig. 10(*a*), the cavitating region is swept away by a compression wave moving toward the pump. This occurs in a cam angle interval $\Delta\theta = 1.20$ deg, i.e., from $\theta - \theta_0 = 15.8$ deg to $\theta - \theta_0 = 17.0$ deg, and this interval corresponds to a period of time $\Delta t_2 = \Delta\theta/n = 0.1538$ ms, being $n = 1300$ rpm. In Fig. 10, the time-averaged shock velocity predicted by the nonconservative model results to be approximately 1.2 times that computed by the conservative algorithm. Therefore, the percentage error introduced by the nonconservative scheme is of the same order as those in Figs. 2 and 3.

The phase shift occurs mainly close to the compression wave front, where discontinuities in the flow properties, void fraction included, arise. This behavior is consistent with the presence of a discontinuity similar to an aerodynamic shock [22,24]. The presence of fictitious source terms, of numerical derivation, in the nonconservative discretized equations, is responsible for the inaccuracy shown by the nonconservative algorithm.

The nonconservative shock fronts are in advance of the conservative ones. This outcome is coherent with the result in Fig. 3 for backward traveling waves. The predicted shock speed can be obtained by applying Eq. (11) to each scalar quantity in Eq. (34).

The phase shift between conservative and nonconservative solutions is less remarkable in Fig. 10 than in Figs. 2 and 3 because the observation time Δt_2 and the traveled distance $\Delta x_2 = \nu_C \Delta t_2$ in Fig. 10(*b*) are much lower than Δx_1 and Δt_1 in Fig. 3. The snubber valve limits the cavitation region extent and, consequently, the period of time Δt_2. In the absence of the snubber valve, the left boundary of cavitation zone would stay fixed at $x/L \approx 0$. As a result, the cavitation region would persist until the compression wave (Fig. 10) reaches the pump outlet. In such a case, the inaccuracy introduced by the nonconservative algorithm in the shock-speed prediction would last for a time much longer than Δt_2,

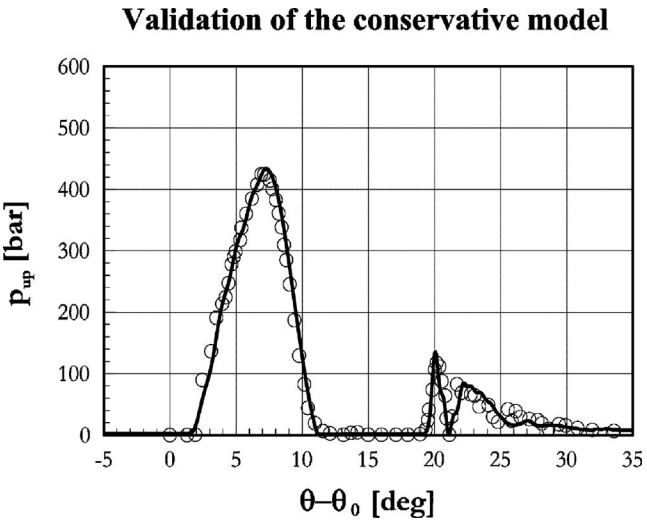

Fig. 12 Pipe pressure at the delivery outlet [3]

producing a sensibly higher shift between conservative and nonconservative pressure spatial distributions at cavitation end. However, only experimental data in the presence of the snubber valve were available.

Figure 11 compares pressure and void fraction distributions resulting from the nonconservative and ICOST algorithms for a cavitation desinence event, occurring at part load and at a pump speed of 2000 rpm. Severely cavitating flow conditions were obtained, with void fraction values higher than 1%. The phase shift between the two pressure distributions grows faster than in Fig. 10(*a*) because of the increased shock intensity. In general, the higher the void fraction peak in front of the pressure wave is, the more intense the shock induced by cavitation collapse is and thus the higher is the inaccuracy that nonconservativeness introduces.

Figures 12 and 13 [3] are reported to show the accuracy of the conservative model, using ICOST scheme, in predicting macroscopic features of the fuel injection-system behavior in the presence of cavitation. Numerical distributions (solid line) are compared to experimental data (circle symbol), versus the camshaft angle $\theta-\theta_0$. The measured data refer to part load and to a pump speed $n=1300$ rpm, i.e., the same working conditions of Figs. 9 and 10. The diagrams show how the compression wave arisen in the pumping chamber (first peak in Fig. 12) reaches the injector inlet (Fig. 13) and is partially reflected, traveling back toward the pump as a compression wave. Figure 12 shows cavitation occurrence at the pump outlet. The pressure reaches the value of the

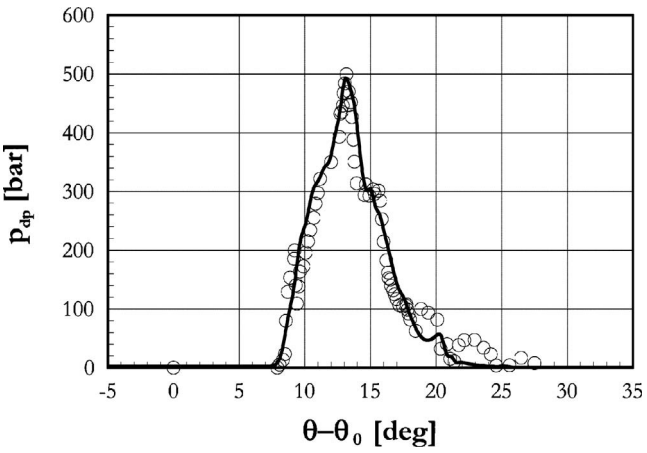

Fig. 13 Pipe pressure at the injector inlet [3]

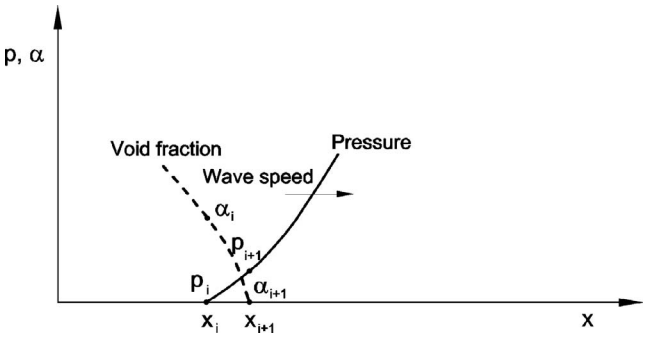

Fig. 14 Cavitation inception: pressure and void fraction distributions at the boundary of the liquid zone

vapor tension at the cam angle $\theta-\theta_0\approx 11$ deg at the transit of the cavitation region, which keeps on advancing in the pipe until the pressure wave from the injector reaches it. A sensible pressure raise occurs at the pump outlet for $\theta-\theta_0\approx 19$ deg.

Analysis of Cavitation Transients

Figure 14 expands the pressure (solid line) and void fraction (dashed line) spatial distributions around the boundary between cavitating and liquid regions. The scheme refers to the case of cavitation inception at a given time instant. The abscissas x_i and x_{i+1} indicate grid nodes of the computational mesh, while p_i and p_{i+1}, and α_i and α_{i+1} are the values of pressure and void fraction at these points. Having been a PDE numerical solution worked out, the values of the variables at the grid nodes are known at any instant of time. At the postprocessing stage, cubic splines were used to interpolate the discrete data obtained by the numerical algorithm, leading to continuous patterns of the fluid-dynamic quantities. The obtained pressure and void fraction distributions show an intersection point at the boundary of the cavitation region, as is shown in Fig. 14. This is due to discretization error arising from the interpolation of numerical data. The simulation code eliminates such a discrepancy by forcing the void fraction to zero wherever the pressure is greater than the vapor-tension level. All the diagrams reported in Figs. 9–11 were plotted by making this graphical rectification.

With reference to Fig. 14, the PDE characteristic lines were schematically reported outside the interval (x_i, x_{i+1}) in Fig. 15. Since for an isothermal evolution the sound speed of the liquid-vapor mixture is equal to zero, according to Eq. (33), the eigenvalues expressed by Eq. (29) become equal to the local fluid velocity u inside cavitation regions.

In the pure liquid zone, only the characteristic lines pertaining to the eigenvalue $u+a_l$ are reported in Fig. 15. In fact, as the rarefaction wave is traveling toward the injector, the liquid characteristic lines with negative slope are irrelevant to the following

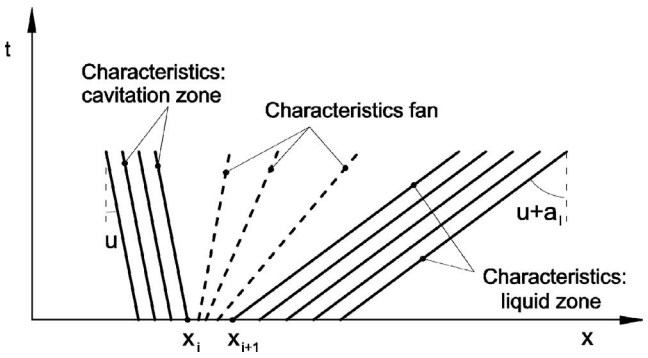

Fig. 15 Cavitation inception: characteristics of the PDE

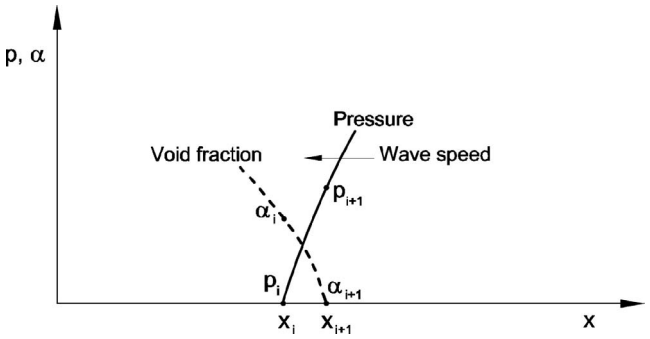

Fig. 16 Cavitation desinence: pressure and void fraction distributions at the boundary of the liquid zone

considerations. Since the sound speed value falls in the passage from liquid to cavitating flow, the characteristics belonging to the region under vaporization and to the zone of the pure liquid have different slope and, in particular, they diverge. Thus, no shock occurs in the flow during cavitation inception, but only discontinuities in the first derivative of flow property spatial distributions (Fig. 9). This kind of discontinuity is typical of flows accelerated up to supersonic conditions. In the space interval (x_i, x_{i+1}), a transition from subsonic to supersonic flow should occur through a gradual continuous rarefaction, which reduces the sound speed from a_l up to zero. This gives rise to a fan of characteristic lines whose slope changes from the value $u_{i+1}+a_{i+1}$ at point x_{i+1} to the value u_i at point x_i. As already explained, the flow velocity in the cavitation region is negative and so is the slope of the corresponding characteristics.

Figure 16 reports the pattern of pressure and void fraction distributions at a certain time instant for the case of cavitation desinence, taking place in the interval (x_i, x_{i+1}). It schematically reproduces what happens in Figs. 10(*a*) at the right boundary of the region subjected to vaporization, where a compression wave traveling toward the pump sweeps gradually away the formerly developed cavitation.

Figure 17 reports the characteristics corresponding to the eigenvalues $u-a_l$ and u, belonging to the liquid and cavitation zones, respectively, outside the interval (x_i, x_{i+1}). These converge and intersect, giving rise to a shock occurrence.

Cavitation desinence occurs through a supersonic-subsonic shock in Figs. 10 and 11. Since in the cavitation region $a=a_T=0$, the supersonic flow at a pipe location within the vaporization region becomes subsonic as the compression wave proceeds crossing this location. If a thermodynamic evolution different from the isothermal process is considered, the cavitation sound speed is higher than zero and the flow can be either supersonic or transonic, depending on the local Mach number. However, the fact that the characteristic lines diverge in the case of cavitation inception and intersect in the case of cavitation desinence is independent of the specific thermodynamic transformation. In fact, whatever barotropic evolution law is considered, Eq. (28) predicts a strong diminution of the sound speed passing from liquid to cavitation zones.

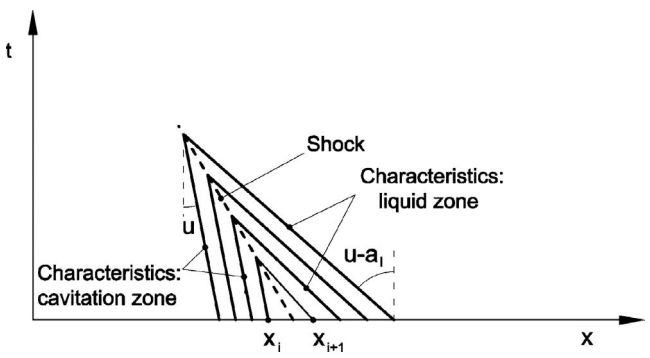

Fig. 17 Cavitation desinence: characteristics of the PDE

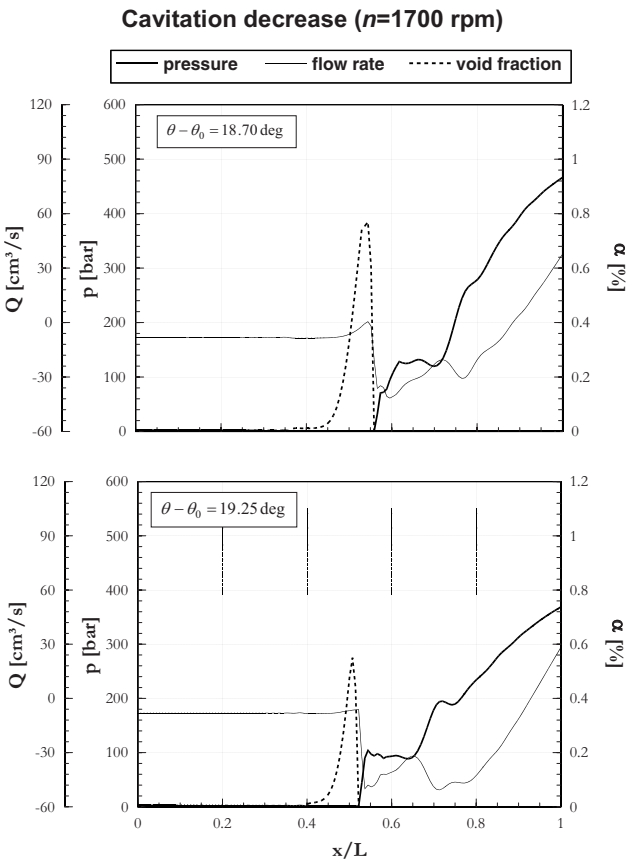

Fig. 18 Numerical distributions by the conservative model

Shock-Speed Evaluation by Rankine–Hugoniot Jump Conditions. Figures 10 and 18 illustrate cases of cavitation desinence and collapse at part load and for two different pump speeds equal to $n=1300$ rpm and $n=1700$ rpm, respectively. Having shown that cavitation desinence is a shock event, in Figs. 10 and 18, the speed at which the compression wave front travels should be well predicted by the Rankine–Hugoniot relations. For the Euler equation system of mass conservation and momentum balance, these are provided by [24,25]

$$v_s = \frac{[\rho u]}{[\rho]} = \frac{[p + \rho u^2]}{[\rho u]} \tag{35}$$

Table 2 reports the value of the liquid pressure close to the shock (p_l), as well as the values of densities and flow rates at both sides of the shock (subscript l for the liquid field and subscript c for the cavitation region). It is worth recalling that the pressure level in the cavitation region is taken equal to the vapor-tension level at the considered temperature. The values of the thermo-fluid-dynamic properties in Table 2 derive from the theoretical distributions plotted in Figs. 10 and 18. The values of $|v_s|$, which are reported in the last column of Table 2, have been obtained by applying Eq. (35) for each of the considered camshaft angles. In particular, the shock-speed value calculated from the mass-conservation equation is reported in the upper part of every cell in the $|v_s|$ column, whereas the lower part of cell reports the $|v_s|$ value calculated from the momentum-balance equation. The two values are always close to each other, with a percentage error

Table 2 Upstream and downstream shock flow properties

rpm	$\theta-\theta_0$	p_l (bar)	ρ_l (kg/m^3)	Q_l (cm^3/s)	ρ_c (kg/m^3)	Q_c (cm^3/s)	$\lvert v_s\rvert$ (m/s)
1300	15.8	55	807.95	−30	800.9	−2.9	882 893
1300	16.22	94	809.95	−41	802.59	−4.7	1135 1138
1300	16.61	110	810.75	−45	804.35	−8	1332 1305
1700	18.70	71	808.75	−36	798.85	+0.6	848 855
1700	19.25	104	810.45	−50	800.7	−6	1039 1041

smaller than 2%, consistent with Eq. (35). From Figs. 10 and 18, it can be deduced that slower shock speeds are reached when the void fraction peak values are higher and lower liquid pressure values occur upstream of the shock. Actually, being the sound speed null inside the cavitation region, the pressure wave front has to condense the vapor zone in front of it before proceeding forward. The phase change takes more time to complete when the void fraction peak is higher and the traveling compression wave has lower intensity.

It is interesting to study the discontinuity with respect to a reference frame moving with the negative shock speed v_s. In this case, the fluid penetrates the discontinuity surface with an upstream velocity $(u_c-v_s)>0$ and leaves it with a lower downstream velocity $(u_l-v_s)>0$. Besides, the pressure and density upstream of the shock (p_c,ρ_c) are lower than those downstream from it (p_l,ρ_l). All these features are consistent with the classic steady shock theory. For the mass and momentum conservation in a reference frame moving with shock, the following conditions are satisfied at the cavitation region boundary:

$$p_l - p_c = \rho_l \mathrm{Ma}_l a_l (u_c - u_l)$$

$$\frac{\rho_l}{\rho_c} = 1 + \frac{(u_c - u_l)}{\mathrm{Ma}_l a_l} \tag{36}$$

where a_l is the speed of sound evaluated in the liquid region downstream from the shock and Ma_l is the corresponding Mach number:

$$\mathrm{Ma}_l = \frac{u_l - v_s}{a_l}$$

The entropy increase due to the presence of shock could be neglected in the present investigation. As is well known, aerodynamic shocks can be treated as isentropic processes only when the pressure ratio across the shock is close to 1. In the present application, such a ratio can be higher than 100. Nevertheless, the supersonic to subsonic flow transition across the boundary of cavitation zones is not due to a strong and irreversible viscosity induced flow deceleration, like an aerodynamic shocks, but it is due to the drastic variation of the sound speed subsequent to the condensation of the fuel. Therefore, the cavitation desinence can be regarded as a virtually nondissipative phenomenon here.

Conclusion

A novel algorithm for calculating the speed of numerically predicted shocks has been proposed and applied to Burgers' equation with Riemann's initial data, as well as to Euler's equations during the occurrence of acoustic cavitation desinence and collapse in high-pressure pipelines. For nonconservative models, the developed procedure points out the contribution of the internal fictitious fluxes, which derive from the failure of the telescoping property, in the inaccurate estimation of the shock speed.

The influence of conservativeness of computational models in the cavitation prediction has been investigated in a pipe-line-nozzle Diesel injection system, undergoing operating conditions of relatively intense fuel vaporization, mainly at part loads. As soon as fuel condensation processes take place, discrepancies arise between the predictions of conservative and nonconservative algorithms, due to the onset of an aerodynamiclike shock, with differences in the shock-speed estimation of up to 20–25%. The resulting phase shift between conservative and nonconservative pressure spatial distributions at the edge of the reentrant cavitation zone increases with both the intensity of the cavitation event and the dimensions of the region subjected to fuel vaporization.

Cavitation inception and growth is shown to be a smooth phenomenon, whereas cavitation desinence has the features of a discontinuous event. However, when Wallis' expression for two-phase flow sound speed evaluation is applied to cavitating mixtures, the flow property patterns during cavitation collapse become numerically continuous. Actually, this expression is not consistent with the presence of any mass transfer across the cavity walls. The physical reasons of such inconsistency were analyzed by deriving the sound speed in a two-phase cavitating homogeneous mixture from the eigenvalues of Euler's equations by linking the vapor-mass production density to the flow evolution, thus showing that such a vapor production term cannot be considered as a pure source term in accordance with Wallis' expression derivation procedure.

Based on the gasdynamic theory of unsteady characteristics, an exhaustive analysis has been carried out at the boundaries of the cavitation region. For the liquid vaporization case, the PDE characteristics outside the cavitating region are divergent giving rise to a fan. However, for the vapor condensation processes, these were convergent and intersect, as generally occurs for aerodynamic shocks, which arise from initially smooth flow properties. The Mach number value inside the region subjected to vaporization depends on the thermodynamic evolution taken for cavitation modeling. Nevertheless, the differences due to the specific evolution did not significantly affect the nature and the main features of the investigated fluid-dynamic events.

The Rankine–Hugoniot conditions were finally applied for accurately evaluating the speed of the traveling compression waves in the presence of cavitation, as well as for deriving in analytical form the links existing between the flow properties across the cavitation-induced discontinuities.

Acknowledgment

Financial support to this research was provided by Ministry of University and Research (MUR) under PRIN-COFIN'04 Program.

Nomenclature

a = sound speed
$\mathbf{A}$ = Jacobian matrix

c = specific heat
d = pipe diameter
E = bulk modulus of elasticity; convergence error
f = scalar flux, Darcy–Weisbach friction coefficient
$\mathbf{F}$ = flux vector
h = enthalpy per unit mass
$\mathbf{H}$ = source vector
ICE = internal combustion engine
L = length of pipe and injector-drilled passage
n = control-volume number; pump speed
p = pressure; average-cross-sectional pressure
PDE = partial differential equation
Q = volumetric flow rate
r = vaporization heat per mass unit
R = bubble radius
t = time
T = temperature
u = average-cross-sectional velocity
v = velocity of the shock
$\mathbf{w}$ = conservative variable vector
W = weight function in the frequency dependent friction
x = axial distance along pipe
α = void fraction; average cross-sectional void fraction
β = thermal expansivity
Γ = rate of vapor production per volume unit of fluid
Δt = time increment
Δs = shock trajectory increment
Δx = distance increment
θ = cam angle
χ = bubble initiator distribution function
λ = Jacobian matrix eigenvalue
μ = mass fraction; dynamical viscosity
ρ = density; average-cross-sectional density; mixture density
σ = surface tension; Courant number
τ_w = wall shear stress
$\mathbf{\Phi}$ = numerical flux vector

Subscripts

0 = reference value
c = cavitation
C = conservative
g = undissolved gas
l = liquid phase
ns = nonconservative shock speed
p = at constant pressure
s = shock
T = at constant temperature
v = vapor phase; at constant volume

References

[1] Wallis, W., 1975, *One dimensional Two-Phase Flow*, McGraw-Hill, New York.
[2] Iben, U., Wrona, F., Munz, C. D., and Beck, M., 2002, "Cavitation in Hydraulic Tools Based on Thermodynamic Properties of Liquid and Gas," ASME J. Fluids Eng., **124**, pp. 1011–1017.
[3] Catania, A. E., Ferrari, A., Manno, M., and Spessa, E., 2006, "A Comprehensive Thermodynamic Approach to Acoustic Cavitation Simulation in High-Pressure Injection Systems by a Conservative Homogeneous Two-Phase Barotropic Flow Model," ASME J. Eng. Gas Turbines Power, **128**, pp. 434–445.
[4] Catania, A. E., Dongiovanni, C., Mittica, A., Spessa, E., and Lovisolo, F., 1994, "Study of Unsteady Flow Phenomena in an Automotive Diesel Injection System," *Proceedings of XXV FISITA Congress*, International Academic, Beijing, Vol. 1, pp. 124–137.
[5] Nguyen-Schaefer, H., and Sprafke, H., 1998, "Numerical Study on Interaction Effects of Bubbles Induced by Air-Release and Cavitation in Hydraulic Systems," *Tenth Bath International Fluid Power Workshop*, Research Studies Press, Hertfordshire, UK/Wiley, New York.
[6] Catania, A. E., Ferrari, A., and Manno, M., 2006, "Acoustic Cavitation Thermodynamic Modeling in Transmission Pipelines by an Implicit Conservative High-Resolution Algorithm," *ASME Fluid Engineering Summer Meeting*, Miami, FL, July 17–20, Paper No. FEDSM06-98272.
[7] Yi, W. C., 2000, "Stability Analysis of One-Dimensional Steady Cavitating Nozzle Flows With Bubble Size Distribution," ASME J. Fluids Eng., **122**, pp. 425–430.
[8] Delale, C. F., Hruby, J., and Marsik, F., 2003, "Homogeneous Bubble Nucleation in Liquids: The Classical Theory Revisited," J. Chem. Phys., **118**, pp. 792–906.
[9] Blander, M., and Katz, J., 1975, "Bubble Nucleation in Liquids," AIChE J., **21**, pp. 833–848.
[10] Gates, E. M., and Bacon, J., 1978, "Determination of Cavitation Nuclei Distribution by Holography," J. Ship Res., **22**(1), pp. 29–31.
[11] Katz, J., 1978, "Determination of Solid Nuclei and Bubble Distributions in Water by Holography," Division of Engineering and Applied Science, California Institute of Technology, Report No. 183-3.
[12] Van Wijngaarden, L., 1972, "One-Dimensional Flow of Liquids Containing Small Gas Bubbles," Annu. Rev. Fluid Mech., **4**, pp. 369–396.
[13] Billet, M. L., 1985, "Cavitation Nuclei Measurement, A Review," *Proceedings of ASME Cavitation and Multiphase Flow Forum*, pp. 31–38.
[14] Mor, M., and Gany, A., 2004, "Analysis of Two-Phase Homogeneous Bubbly Flows Including Friction and Mass Addition," ASME J. Fluids Eng., **126**, pp. 102–109.
[15] Catalano, L. A., Tondolo, V. A., and Dadone, A., 2002, "Dynamic Rise of Pressure in the Common Rail Fuel Injection System," SAE Paper No. 2002-01-0210.
[16] Chaudhry, M. H., Bhallamudi, S. M., Martin, C. S., and Naghash, M., 1990, "Analysis of Transient Pressures in Bubbly, Homogeneous, Gas-Liquid Mixtures," ASME J. Fluids Eng., **112**, pp. 225–231.
[17] Young, F. R., 1989, *Cavitation*, McGraw-Hill, London.
[18] Kolev, N. I., 1986, *Transiente Zweiphasen Strömung*, Springer-Verlag, Berlin.
[19] BHRA Fluid Engineering Center, 1987, *Cavitation and Aeration in Hydraulic Systems*, Technical Report, Bedford.
[20] Akhatov, I., Lindau, O., Topolnikov, A., Mettin, R., Vakhitova, N., and Lauterborn, W., 2001, "Collapse and Rebound of a Laser-Induced Cavitation Bubble," Phys. Fluids, **13**, pp. 2805–2819.
[21] Rayleigh, L., 1917, "On the Pressure Developed in a Liquid During the Collapse of a Spherical Cavity," Philos. Mag., **34**, pp. 94–98.
[22] Anderson, D., Tannehill, J. C., and Pletcher, R. H., 1984, *Computational Fluid Mechanics and Heat Transfer*, McGraw-Hill, New York.
[23] LeVeque, R. J., 2002, *Finite Volume Methods for Hyperbolic Problems*, Cambridge University Press, New York.
[24] Hirsch, C., 1988, *Numerical Computation of Internal and External Flows* (Computational Methods for Inviscid and Viscous Flows), Vol. 2, Wiley, New York.
[25] Toro, E. F., 1997, *Riemann Solvers and Numerical Methods for Fluid Dynamics: A Practical Introduction*, Springer-Verlag, Berlin.
[26] Hirsch, C., 1988, *Numerical Computation of Internal and External Flows (Fundamentals of Numerical Discretization)*, Vol. 1, Wiley, New York.
[27] Ferrari, A., 2004, "Development of a Model for Thermo-Fluid Dynamic Transient Simulation in High-Pressure Injection Systems. Equipment of a High-Performance Test Bench for Diesel Fuel Injection Systems: First Experimental Results on Common Rail System Dynamics," Ph.D. thesis, Politecnico di Torino, Italy.
[28] Catania, A. E., Ferrari, A., Manno, M., and Spessa, E., 2004, "Thermal Effect Simulation in High-Pressure Injection System Transient Flows," *SAE 2004 World Congress*, Detroit, MI, March 8–12, SAE Paper No. 2004-01-0532, pp. 44–59.
[29] Zielke, W., 1968, "Frequency-Dependent Friction in Transient Pipe Flow," ASME J. Basic Eng., **90**, pp. 109–115.
[30] Catania, A. E., Ferrari, A., and Manno, M., 2005, "Development and Application of a Complete Common-Rail Injection System Mathematical Model for Hydrodynamics Analysis and Diagnostics," *ASME ICED Spring Technical Conference*, Chicago, IL, April 5–7, Paper ICES2005-1018, ASME J. Eng. Gas Turbines and Power, submitted.

Hydrodynamics and Sound Generation of Low Speed Planar Jet

Victoria Suponitsky
e-mail: v.suponitsky@qmul.ac.uk

Eldad Avital
e-mail: e.avital@qmul.ac.uk

Mike Gaster
e-mail: m.gaster@qmul.ac.uk

Department of Engineering,
Queen Mary, University of London,
London, E1 4NS, UK

Hydrodynamics and sound radiation of a low speed planar jet with Re=3000 *have been studied by large eddy simulation combined with Lighthill's acoustic analogy. Jets evolving from both well-developed (parabolic) and undeveloped (top-hat) mean velocity profiles have been simulated. The results showed the following: (i) initial domination of a symmetrical mode for jets evolving from top-hat profiles and prevailing of an antisymmetrical mode resulting in a sinuous distortion of the potential core for jets evolving from parabolic profiles, and (ii) shape of a mean velocity profile has some effect on mean flow characteristics; however, the major differences were observed in the development of the fluctuations. Velocity fluctuations were significantly higher for jets evolving from a parabolic profile in the region beyond the end of the potential core before the flow reached a self-preserving state. To calculate the basic sound radiation, the sources in Lighthill's equation were treated either as compact in all directions or as noncompact in the spanwise direction. The spanwise length of the computational domain was found to have a little effect on the results obtained with compact in all directions solution provided that spanwise length exceeds the correlation length. Results showed that the majority of sound was generated by the region beyond the end of the potential core.*
[DOI: 10.1115/1.2844581]

1 Introduction

The planar jet has been extensively studied experimentally from the late 1950s. The studies were motivated by both practical and academic goals, because planar jets occur in various industrial applications and also represents a fundamental problem in fluid dynamics. The first and most complete experimental study on transition of the plane jet was conducted by Sato [1], where the effect of the shape of mean exit velocity profile on transition and the resulting mean flow characteristics were thoroughly addressed. In the vicinity of the nozzle, disturbances were found to be amplified according to inviscid linear stability theory, followed by a nonlinear stage involving the vortex roll-up process. Two classes of unstable modes, symmetrical and antisymmetrical, were detected, and the dominance of a particular mode was highly dependent on the shape of the exit mean velocity profile. For *undeveloped* (top-hat) exit mean velocity profiles, *symmetrical* modes were found to prevail, whereas for *well-developed* parabolic exit profiles, *asymmetrical* modes were reported to dominate, although their dominance seemed to weaken with an increase of Reynolds number. A random switching between the modes was also observed in experiments of the water planar jet using flow visualization [2]. Application of linear stability analysis to a planar jet, where the mean velocity profile was prescribed by the hyperbolic secant function, also supported the existence of two unstable modes, where the symmetrical mode was characterized by the higher amplification factor [3]. The near-field region of the planar jet has been further investigated in Refs. [4–7]. These experiments were conducted for *top-hat* exit mean velocity profiles and mainly focused on the flow reconstruction from the symmetrical structures prior to the end of the potential core to the array of antisymmetric vortices downstream. A wide range of measurements of the flow characteristics in the self-preserving region of a planar jet can be found in the experimental studies [8–12]. One of the features of planar jets in the self-preserving region is the occurrence of the negative correlation between longitudinal-velocity fluctuations obtained simultaneously from laterally separated probes on opposite sides of the jet centerline. This phenomenon has been termed "flapping," a term that stems from the early interpretations that associated the jet motion to a flapping flag [13,14]. Later on, the occurrence of this negative correlation has been linked to the existence of large-scale coherent structures in the self-preserving region of a planar jet [5,15–19]. Measurements showed "quasiperiodic" behavior of the correlation function [14]. A corresponding correlation frequency (often termed the fundamental mode) was observed to remain nearly constant when it was scaled by the centerline mean velocity and the local width of the jet ($St_b \approx 0.11$). Despite numerous experimental studies, only a limited number of numerical studies have been carried out for planar jets: large eddy simulation (LES) and direct numerical simulation (DNS) of a planar jet can be found in Refs. [20–24].

In the present work, incompressible LES combined with the acoustic analogy are used to study hydrodynamics and sound radiation of a planar jet. The effect of the nozzle's exit mean velocity profile has been investigated. Two formulations of Lighthill's acoustic analogy were used to calculate the sound radiation: (i) the acoustic source was treated as compact in all three directions and (ii) the acoustic source was assumed to be noncompact in homogeneous spanwise direction.

2 Numerical Formulation

2.1 Hydrodynamics. Incompressible Navier–Stokes equations were solved by the inhouse code LITHIUM in its structured finite-difference staggered grid form. The projection method was applied to ensure continuity, where an elliptic solver based on fast fourier transform was used for the solution of the pressure equation [25]. The convection and diffusive terms were evaluated by the fourth order upwind biased and fourth order central schemes [26], respectively, while time marching was achieved by a third order Runge–Kutta scheme. A mixed time scale model [27], which relates the eddy viscosity to a kinetic energy in a test level, was used to calculate subgrid stress. In the base case, the simula-

Contributed by the Fluids Engineering Division of ASME for publication in the JOURNAL OF FLUIDS ENGINEERING. Manuscript received March 16, 2007; final manuscript received October 3, 2007; published online March 3, 2008. Assoc. Editor: Paul Durbin.

tions were performed for the computational domain with dimensions of $Lx/h=Ly/h=30$ and $Lz/h=8$ (h is the slot width) in the streamwise, transverse, and spanwise directions, respectively, with the corresponding number of grid points of $256\times300\times64$. The effect of the spanwise length of the computational domain was studied by carrying out simulations with $Lz/h=4$ and 16 with the corresponding number of grid points $nz=33$ and 129. A uniform grid was used in the streamwise and spanwise directions, while in the transverse direction a greater density ($\Delta y=0.062h$) was used around the jet centerline. The grid resolution was checked by performing the simulations with $513\times451\times129$ number grid points on computational domain with dimensions $Lx/h=Ly/h=36$ and $Lz/h=8$.

To define various mean velocity profiles at the nozzle exit, part of the nozzle was included into computations. In the base case, the simulated part of the nozzle had a length of $2h$. Increase of the nozzle length to $5h$ had no effect on the results obtained from simulations of isolated jet. At the inflow boundary (entrance to the nozzle), the mean streamwise velocity was prescribed. A well-developed flow was specified by a *parabolic* profile. An undeveloped flow was prescribed by top-hat velocity profile that was smoothed by including boundary layers inside the nozzle. The velocity distribution inside these boundary layers was given by a Pohlhausen polynomial with the momentum thickness of $\theta/h=0.035$. Simulations were performed for the jet with $\mathrm{Re}_h=3000$ and the flow inside the nozzle remained laminar. A sinusoidal disturbance containing 20 equally spaced frequencies within the range of Strouhal numbers $0.1\leqslant \mathrm{St}_h\leqslant 0.5$ and a peak intensity of 2% was added to the streamwise velocity at the inflow boundary. Each of the frequencies composing an inflow disturbance had a randomized phase in the y and z directions.

A simple convection boundary condition was applied at the outflow boundary where a buffer zone of 15% of the streamwise length of the computational domain was added. In the buffer zone, the calculation of the convection terms was smoothly replaced by a first order upwind scheme and the source term in the pressure equation was damped [28]. A constant pressure boundary condition was set on the boundaries in the transverse direction. Periodic boundary conditions were used in the spanwise direction to simulate a two-dimensional jet geometry.

2.2 Acoustics. Sound radiation was calculated by Lighthill's acoustic analogy. Two different assumptions in the solution of Lighthill's equation (Eq. (1)) can be applied to problems with two-dimensional geometries. The first one is a widely used assumption that the sound source is compact (i.e., $\lambda_{\mathrm{acoustic}}\gg L$) in all directions, which is generally true at the limit of $M\to0$. The results obtained from this formulation can be interpreted as the basic radiation per the largest eddy, provided that the spanwise length of the computational domain is larger than the correlation length. Alternatively, the results can be applicable to the high aspect ratio rectangular jets provided that edge effects do not play a significant role. The second formulation mimics the real two-dimensional geometry (imposed in the numerical simulations by the periodic boundary conditions) and thus the sound source is assumed to be noncompact in the homogeneous spanwise direction.

$$\frac{\partial^2\rho}{\partial t^2}-a_o^2\nabla^2\rho=\frac{\partial^2T_{ij}}{\partial y_i\partial y_j},\quad T_{ij}=\rho u_iu_j+p_{ij}-a_0^2\rho\delta_{ij} \tag{1}$$

In the above equation, ρ is the fluid density, a_0 is the speed of sound, $p_{ij}=p\delta_{ij}-2\mu(e_{ij}-(1/3)e_{kk}\delta_{ij})$, where μ is the fluid viscosity, $e_{ij}=1/2[(\partial u_i/\partial x_j)+(\partial u_j/\partial x_i)]$, and $e_{kk}=\partial u_k/\partial x_k$.

2.2.1 Compact Source Solution. When the source is treated as being compact in all directions, the solution of Eq. (1) results in the following expression for the far-field sound [29]:

$$\rho'(x_1,x_2,x_3,t)=\frac{1}{4\pi a_0^4r}\left(\frac{x_ix_j}{r^2}\right)\times\int\int\int\frac{\partial^2}{\partial t^2}T_{ij}\left(y_1,y_2,y_3,t-\frac{r}{a_0}\right)dy_1dy_2dy_3 \tag{2}$$

where $r=\sqrt{x_1^2+x_2^2+x_3^2}$. For cold jets at very small Mach numbers, T_{ij} can be approximated as $\rho_ou_iu_j$, where ρ_o is the density of ambient fluid. At the limit of $M\to0$, solution given by Eq. (2) can be further simplified as

$$\rho'(x_1,x_2,x_3,t)=\frac{\rho_0}{4\pi a_0^4r}\left(\frac{x_ix_j}{r^2}\right)\underbrace{\frac{\partial^2}{\partial t^2}\int\int\int u_iu_jdy_1dy_2dy_3}_{\ddot{Q}_{ij}\ \textit{quadrupole}} \tag{3}$$

A part of the expression in Eq. (3) is generally referred to as Lighthill's quadrupole source and is denoted by $\ddot{Q}_{ij}$. Quadrupoles $\ddot{Q}_{ij}$ are calculated from the hydrodynamic field. Boundary corrections were added to solution to account as much as possible for the vortical structures leaving the outlet of the computational domain [30]. An acoustic spectrum is further calculated by taking the frequency spectrum of the total acoustic power output:

$$P=\int_0^{2\pi}d\phi\int_0^{\pi}Ir^2\sin\theta d\theta \tag{4}$$

where I is an acoustic intensity defined as $I=a_o^3\overline{\rho^2}/\rho_o$, and ϕ and θ are the spherical and polar angles, respectively.

2.2.2 Noncompact in the Spanwise Direction Source Solution. Here, we follow the approach similar to Hu et al. [31] and solve Lighthill's equation (Eq. (1)) in Fourier space in time and spanwise direction. After some manipulations and assuming a compact source in the streamwise-transverse plane (Appendix), one gets

$$\hat{\rho}(x_1,x_2,k_z,\omega)=-\frac{i\hat{k}^2}{4a_o^2}\frac{x_mx_n}{r^2}H_o^{(1)}(\hat{k}r)\cdot\int\int\hat{T}_{mn}dy_1dy_2-\frac{ik_z\hat{k}}{2a_o^2}\frac{x_m}{r}\times H_o^{(1)}(\hat{k}r)\cdot\int\int\hat{T}_{m3}dy_1dy_2+\frac{ik_z^2}{4a_o^2}\times H_o^{(1)}(\hat{k}r)\cdot\int\int\hat{T}_{33}dy_1dy_2$$

where

$$\hat{k}^2\equiv\omega^2/a_o^2-k_z^2 \tag{5}$$

In the above equation, the hat sign denotes a Fourier transform in time and spanwise direction, $H_o^{(1)}$ is Hankel's function of the first kind, $m,n=1,2$ and $r=\sqrt{x_1^2+x_2^2}$. For a positive $\hat{k}^2$, the mode is radiative because it decays algebraically in the far field. In the case of negative $\hat{k}^2$, the mode is referred as nonradiative as it decays exponentially in the far field. The acoustic spectrum is calculated by taking the frequency spectrum of the total acoustic power output P,

$$P=\int_o^{L_z}dx_3\int_o^{2\pi}Ird\phi,\quad I=\frac{a_o^3\overline{\rho^2}}{\rho_o} \tag{6}$$

3 Results

The simulations were carried out for $\mathrm{Re}_h=3000$. For the results presented here, the point $x/h=0$ corresponds to the nozzle exit. The slot width h and the half-jet width b are used as the reference length scales. Time is normalized by the slot width and maximum

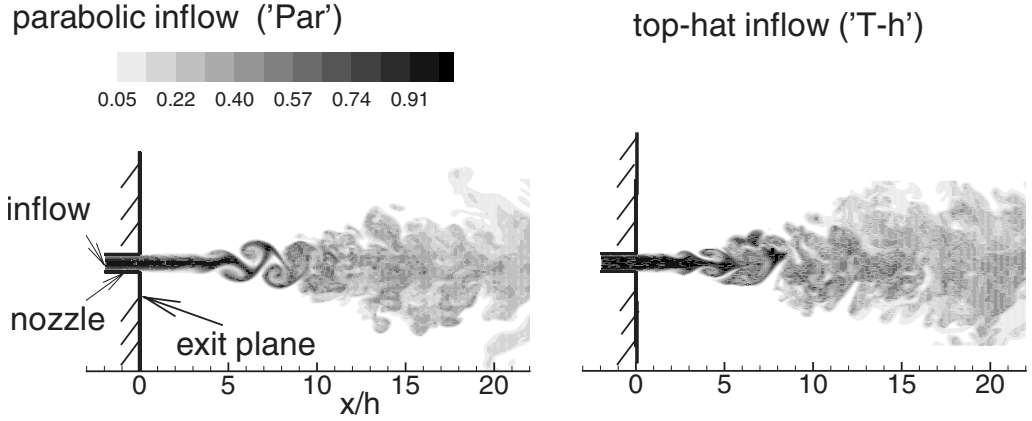

Fig. 1 Instantaneous flow field shown by the contours of the passive scalar at the midplane of the computational domain

jet velocity at the inflow $T=t/(h/U_o)$. In the rest of the paper, the simulations with a parabolic and top-hat inflow profiles are termed as "Par" and "T-h," respectively. To analyze the mean and (root mean square) (rms) flow characteristics, the statistics were accumulated for the time period of five domain flow-through times given by $L_x/(U_0/2)$ and averaged in a homogeneous spanwise direction.

3.1 Hydrodynamics. A typical instantaneous flow field corresponding to the various exit mean velocity profiles is shown by the contours of the passive scalar in Fig. 1. One can see that for a parabolic profile, the antisymmetric mode is dominant, resulting in a "snaky" distortion of a potential core, whereas for the top-hat profiles, a symmetric mode prevails, leading to jet "puffing." These results support the experimental findings reported by Sato [1], who was the first and the only one to conduct detailed measurements of planar jets exiting from both very long and short nozzles.

The decay of the centerline velocity and the downstream growth of the jet half-width are shown in Figs. 2(*a*) and 2(*b*), respectively. It can be seen that in the region relatively close to the nozzle exit ($x/h \leqslant 10$), the jet developing from a parabolic exit profile is characterized by a more rapid decay of the centerline velocity and a slightly higher spreading rate of the jet width. The same trends were observed in the experiments conducted by Sato [1]. Analysis of the self-preserving region of planar jets predicts linear and inverse-squared relationships between streamwise coordinate and jet width and centerline velocity, respectively (see Eq. (7)).

$$\frac{b}{h} = K_1(x/h + K_2), \quad \left(\frac{U_0}{U_{c.l.}}\right)^2 = C_1(x/h + C_2) \tag{7}$$

where K_1, K_2, C_1, C_2 are constants. The rates of the centerline velocity decay (expressed by the constant C_1) obtained from the current simulations for $x/h \geqslant 10$ are $C_1=0.324$ and $C_1=0.24$ for the parabolic and top-hat inflow profiles, respectively. For the top-hat inflow profile, the value of C_1 is inside the values obtained in the previous experimental and numerical studies ($0.143 \leqslant C_1 \leqslant 0.25$, see Refs. [4,5,8,10–12,14,18,22,24]), while for the parabolic inflow, it is noticeably higher. The jet width growth rate (expressed by the constant K_1) is $K_1=0.122$ for the parabolic inflow and $K_1=0.113$ for the top-hat one. Here again, the value obtained for the top-hat inflow is well inside of the previously reported data and value for the parabolic profile is slightly higher.

Figure 3 shows the normalized streamwise and transverse mean velocity profiles for several streamwise locations. Hollow and full symbols refer to the parabolic and top-hat inflow velocity profiles. It can be seen that in both cases, all profiles of the streamwise velocity collapse to a self-preserving profile from about $x/h=10$, and they compare well with the experimental results. For the transverse velocity, it takes longer to develop into a self-similar shape, and profiles approach the self-preserving state at about $x/h=20$. It can be also seen that at about $x/h=10$, the transverse velocity attains higher values in the case of a parabolic inflow profile.

Normalized rms values of the streamwise and transverse velocity fluctuations at the jet centerline and along the nozzle lip line ($y=\pm h/2$) are shown, respectively, by black and gray lines at Fig. 4. DNS results by Stanley et al. [24] and experimental measurements of Browne et al. [4] at the jet centerline are added for comparison. One can see that for a parabolic inflow profile, the region $7 \leqslant x/h \leqslant 12$ is characterized by significantly higher values of the fluctuation intensities. Comparing the present results with

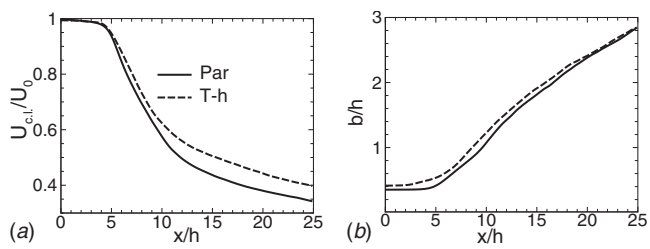

Fig. 2 Jet mean flow characteristics: (*a*) centerline mean velocity decay; (*b*) downstream growth of the jet's half-width

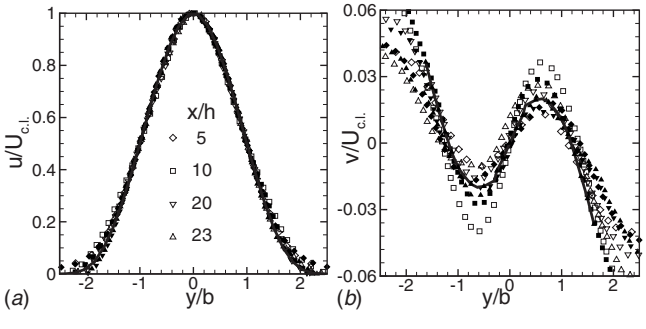

Fig. 3 Normalized mean velocity profiles for a parabolic (hollow symbols) and top-hat (full symbols) inflow profiles. (*a*) u velocity; (*b*) v velocity. Experimental data obtained by Bradbury [8] are shown by the thick solid lines.

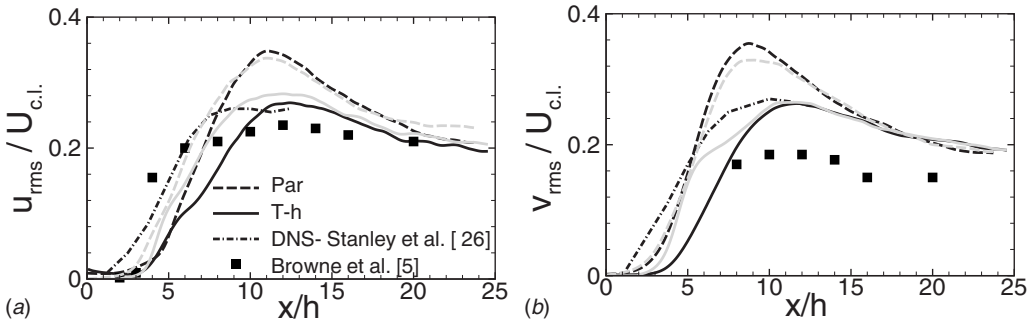

Fig. 4 rms values of velocity fluctuations at the jet centerline (black lines) and along the nozzle lip line $y=\pm h/2$ (gray lines). (*a*) streamwise velocity fluctuations; (*b*) transverse velocity fluctuations.

those obtained in a DNS study [24] for similar top-hat inflow profiles, it can be seen that the growth rate of fluctuations, as well as their values, are pretty close to each other. The only difference is that the starting point of the rapid growth of fluctuations is delayed in our simulations because of the difference in the inflow fluctuations between the two studies. It should be noted that the maximum rms values, as well as their growth rates, vary significantly between experiments (see, for example, Tables 4 and 5 in Stanley et al. [24]) and present calculated results are well within these values. Comparing fluctuations evolution at jet centerline with that along the nozzle lip line, little differences are observed for a parabolic inflow profile. For a top-hat profile, however, fluctuation evolution along the nozzle lip line is characterized by more rapid growth rate for $x/h \leqslant 5$ (in particular, for the transverse velocity component). Normalized profiles of the rms values of velocity fluctuations for several streamwise locations are shown in Fig. 5. Experimental data obtained by Bradbury [8] for the self-preserving jet region are also plotted by the thick solid lines. One can see that at about $x/h=20$, the profiles approach the self-preserving state and compare well with the experimental results. In the region around $x/h=10$, the planar jet evolving from the parabolic inflow profile exhibits much higher velocity fluctuations in the vicinity of the centerline.

One of the issues to be addressed in numerical simulations of two-dimensional geometries is the choice of a spanwise length of the domain, because only a flow segment of a finite width is simulated. This is directly related to the length scales occurring in a particular flow. To provide a realistic simulation of a two-dimensional geometry, a spanwise length sufficient to allow two-point correlations to decay significantly at large separation is required. The effect of the spanwise length of the domain on the extent of spanwise correlations calculated from u fluctuations is shown in Fig. 6 for the parabolic inflow profile. The results are presented for two streamwise locations of $x/h=5$ and 20. The first point is in the region characterized by a relatively strong two dimensionality of the vortical structures and the second point is placed in the self-preserving flow region. It can be seen that while the spanwise length of $Lz=8h$ is sufficient to ensure that the two-point correlations decay adequately, the spanwise length of $Lz=4h$ is a bit short. Integral scales in each direction were also calculated and the results were found to be in a good agreement with the existing experimental data.

To follow the spectral development of the fluctuations, time-correlation function and coherency spectra were calculated for points located on the opposite sides of the jet centerline. The use of the coherency spectra accentuates the discrete frequencies present on each side of the jet, while the influence of the broad-band background energy is reduced. Figure 7 presents time-correlation function and coherency spectra calculated from the v-velocity fluctuations for the points located at the opposite side of the jet centerline ($y/b \approx 1$, where b is the jet half-width) for $x/h=10$ and 20 and for the parabolic inflow profile. The influence of inflow conditions (known to be strong in the jet near field) is expected to weaken for the above downstream locations and the results look similar for the parabolic and top-hat inflow profiles. It can be seen that the correlation function exhibits a quasiperiodic behavior and the correlation frequencies are about $St_h \approx 0.1$ at $x/h=10$ and $St_h \approx 0.02$ at $x/h=20$. Scaling the correlation frequency with the jet half-width b and the centerline velocity leads to $St_b \approx 0.17$ at $x/h=10$ and $St_b \approx 0.12$ at $x/h=20$. The value of $St_b \approx 0.12$ is very close to that of the fundamental mode ($St_b \approx 0.11$) observed in the self-preserving region of a planar jet.

3.2 Acoustics

3.2.1 Compact Sound Source. Acoustic power spectra (Eq. (4)) obtained for different spanwise lengths of the computational domain are shown in Fig. 8 for the parabolic inflow profile. Experimental results by Kouts and Yu [32] are added for the comparison. The results presented are normalized by the total acoustic

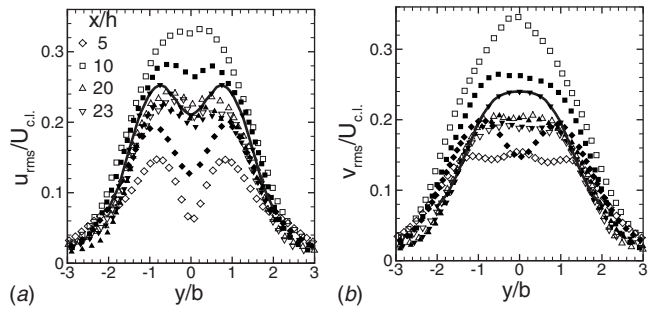

Fig. 5 Normalized profiles of rms values of velocity fluctuations for a parabolic (hollow symbols) and top-hat (full symbols) inflow profiles. (*a*) u-velocity fluctuations; (*b*) v-velocity fluctuations. Experimental data by Bradbury et al. [8] are shown by the thick solid lines.

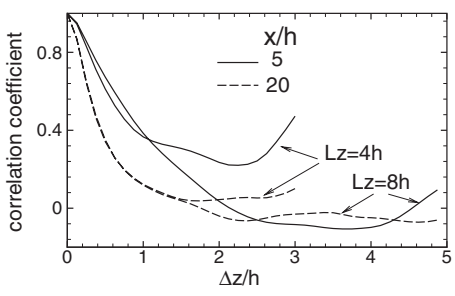

Fig. 6 Spanwise correlation coefficient calculated from *u* fluctuations at the jet centerline for the parabolic inflow profile

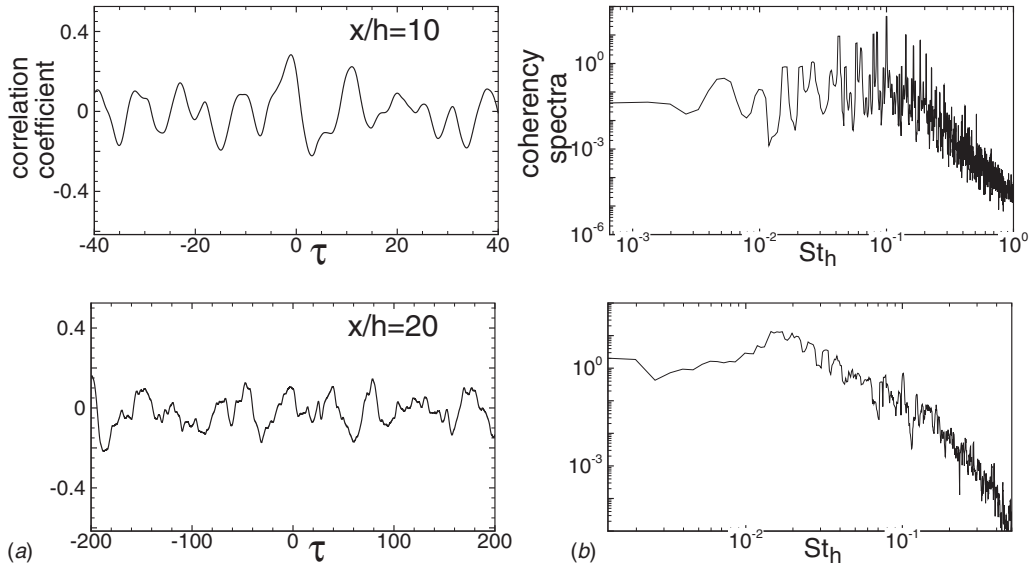

Fig. 7 Time-correlation function (*a*) and coherence spectra (*b*) calculated from the v-velocity fluctuations for the points on the opposite sides of the jet ($y/b \approx 1$) in the case of a parabolic inflow profile

power and scaled with the parameters used in experiments ($U_o = 123$ m/s and $h = 0.01422$ m). It can be seen that the results obtained are not strongly influenced by varying the spanwise length of the computational domain or by increasing the grid resolution. The majority of the acoustic power is concentrated at the low frequencies with a peak occurring at about $St_h \approx 0.1$. At low frequencies, the results obtained compare quite well with experimental data, although in the vicinity of the peak the numerical prediction is slightly high. This is probably because of some differences in the aerodynamic fluctuations, which are further exaggerated in the calculation of the acoustic source. At high frequency, the decay of the computed spectra is much steeper. The differences at high frequency between spectra computed from LES and those obtained from experiments are known and usually attributed to the effect of the subgrid model. Intensity spectra obtained at polar angles $\theta = 30$ deg and 90 deg are plotted in Fig. 9 for a spherical angle $\phi = 90$ deg. The results are presented for both parabolic and top-hat inflow profiles and compared with experimental data [32]. To take into account the effect of the spanwise length of the computational domain, the experimental data were normalized by the slot area and the numerical results by $h \cdot Lz$. It can be seen that here again the low frequency part of the spectra compares well with experimental measurements, whereas the significant differences occur at the high frequency range. The results show that at smaller polar angles (in the direction close to the jet axis) low frequency noise is higher. The results also indicate that while the overall shape of the spectra is similar for parabolic and top-hat inflow profiles, for the latter the sound radiation is slightly higher.

Directivities of OAPSL's obtained from numerical simulations with $Lz = 4h$ and $8h$ are shown at $\phi = 0$ deg and $\phi = 90$ deg in Fig. 10 for a parabolic inflow profile. The results are compared with experimental data by Kouts and Yu [32] and Munro and Ahuja [33]. Numerical data are scaled (including the influence of the Doppler effect) with the parameters used in experiments: $U_o = 123$ m/s, $h = 0.01422$ m, distance from the source $r = 3.048$ m, and aspect ratio $A\mathfrak{R} = 10$ in Ref. [32] and $U_o = 202$ m/s, $h = 0.001016$ m, $r = 2.74$ m, and $A\mathfrak{R} = 750$ in Ref. [33]. It was found [33] that for rectangular jets with $A\mathfrak{R} \geqslant 200$, the best fit to account for slot dimensions is to scale the results with $h^{3/2} \cdot Lz^{1/2}$, in contrast to the jets with lower aspect ratio, which are usually scaled with the slot area $h \cdot Lz$. The above scaling was applied for experimental and numerical results. One can see that at small polar angles, there is a little difference in directivities obtained at $\phi = 0$ deg and 90 deg and the results compare well with the experimental data. At larger polar angles, at which high frequency noise

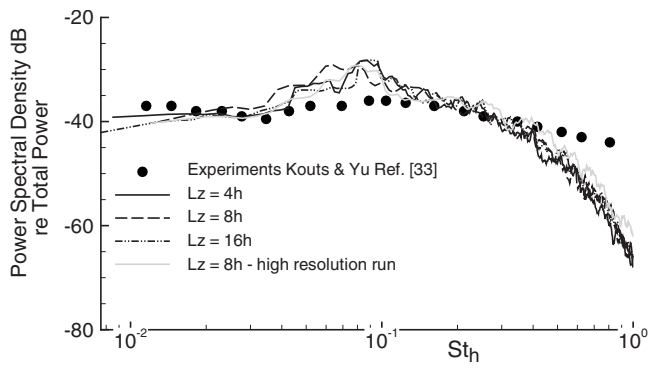

Fig. 8 Acoustic power spectral density obtained in the case of a parabolic inflow profile (compact solution)

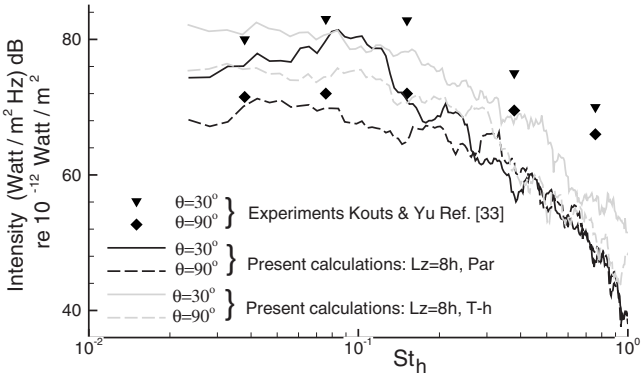

Fig. 9 Intensity spectra obtained for $\phi = 90$ deg (compact solution)

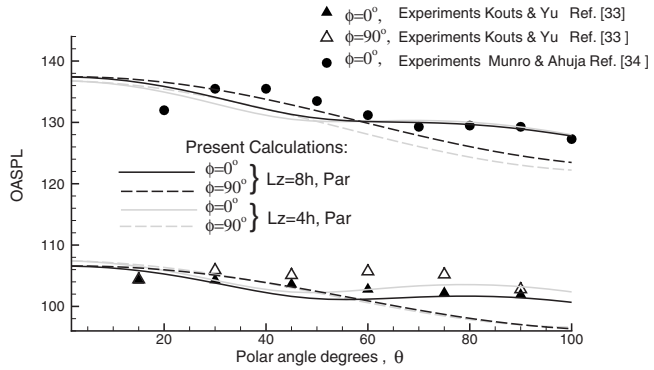

Fig. 10 Direcivities of OASPL's for the case of the parabolic inflow profile (compact solution)

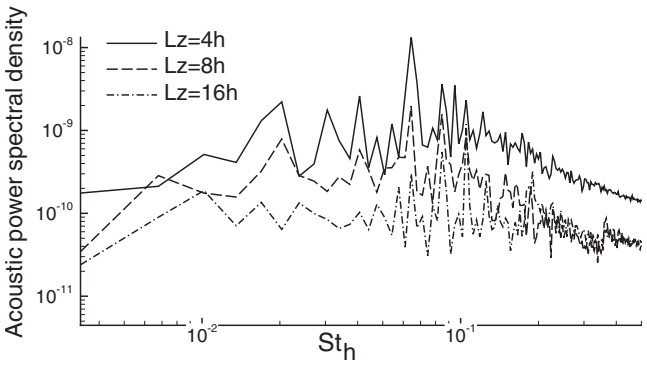

Fig. 13 Acoustic power *P* (Eq. (6)) obtained from the noncompact in the spanwise direction solution. Results are shown for *M*=0.35.

plays an important role, the differences between results obtained at $\phi=0$ deg and 90 deg become noticeable and are probably attributed to the less accurate numerical prediction of high frequency radiation.

Contours of the rms values of the Q_{xx} quadrupoles obtained are shown in Fig. 11 for a parabolic inflow profile. The figure indicates that the majority of the sound is generated by the region following the end of the potential core, which is characterized by the large-scale vortical structures and their further breakdown into smaller ones.

3.2.2 Noncompact Sound Source. The spectra of Q_{xx} and Q_{zz} quadrupoles obtained for several wave numbers k_z are shown in Fig. 12. The results presented are for the parabolic inflow profile obtained from the high resolution simulation with $L_z=8h$. The plot shows that as expected, the amount of power at low frequencies, in particular, decreases with an increase in the wave number k_z. It can be also seen that more energy is contained at higher frequencies for large wave numbers k_z. It should be noted that the spectra presented contain both radiative and nonradiative parts and in general resemble the hydrodynamic spectra. Acoustic power spectra (Eq. (6)) are presented in Fig. 13 for the different spanwise lengths of the computational domain. It can be seen that while overall shape of the spectra remains similar, the spanwise length of the domain Lz has an effect on the power levels. In this case, the increase in Lz results in the decrease of the acoustic power. It should be noted that in this formulation parameters Lz and nz are directly related to the wave numbers kz, and at this stage the exact effect of the latter is unclear and requires further investigation. The plot also indicates that most of the acoustic power comes from the frequencies around $St_h \approx 0.1$ similar to the results obtained from the compact solution.

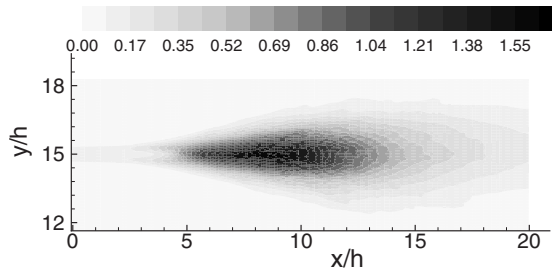

Fig. 11 Spanwise averaged contours of rms values of Q_{xx} quadrupole obtained from the compact source solution for a parabolic inflow profile

4 Conclusions

LES combined with Lighthill's acoustic analogy was used to study an incompressible planar jet with the $Re_h=3000$. Sources treated either as compact in all directions or as noncompact in the spanwise direction were used with Lighthill's analogy to calculate sound radiation. The results showed that for jets evolving from well-developed profiles, a sinuous instability mode dominates, resulting in a snaky distortion of the potential core. For jet evolving from undeveloped profiles, a *symmetrical* mode dominates within the jet near field resulting in a jet puffing. A fundamental mode of the planar jet was clearly observed in the self-preserving region for both shapes of the inflow profiles. The mean flow characteristics, i.e., centerline velocity decay and jet width growth rate, are influenced by the shape of the inflow profile; however, the major differences are observed in the development of the fluctuations. The sound radiation results obtained with the solution compact in all directions showed little dependence on the spanwise length of

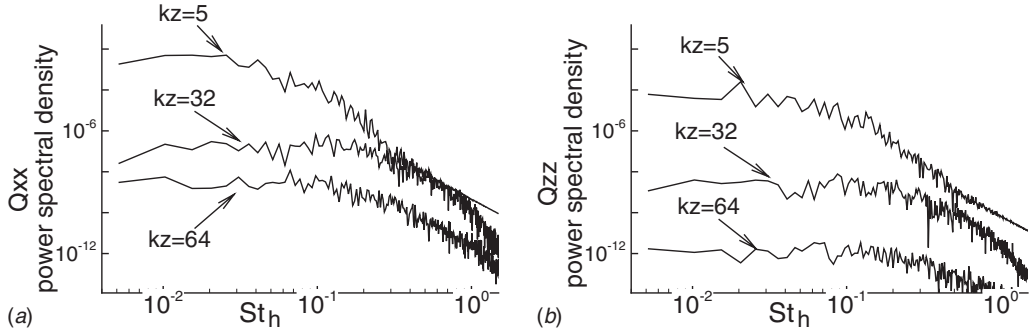

Fig. 12 Spectra of Q_{xx} (*a*) and Q_{zz} (*b*) quadrupoles for the noncompact in the spanwise direction solution at several wave numbers k_z ($Lz/h=8$)

the computational domain or increase in the grid resolution. At low frequencies, the results showed good agreement with the experimental data, while larger differences occurred at high frequencies. It was also shown that the majority of generated sound comes from the region beyond the end of the potential core. The results obtained with the solution using noncompact source in the spanwise direction appeared to be more sensitive to numerical issues.

Acknowledgment

The authors would like to thank the EC Marie Curie programme for supporting this study under Grant No. 011415 and UK EPSRC for providing national computing time under Grant No. EP/D044073/1.

Appendix

Solution of Lighthill's equation (Eq. (A1)) with the assumption that sound source is noncompact in the spanwise direction can be obtained as follows:

$$\frac{\partial^2 \rho}{\partial t^2} - a_0^2 \nabla^2 \rho = \frac{\partial^2 T_{mn}}{\partial y_m \partial y_n}, \quad m,n = 1,2,3 \tag{A1}$$

Apply Fourier transform in time and z direction,

$$\hat{\rho} = \hat{\rho}(y_1, y_2, k_z, \omega), \quad \hat{T}_{mn} = \hat{T}_{mn}(y_1, y_2, k_z, \omega) \tag{A2}$$

This leads to

$$-\omega^2 \hat{\rho} + a_0^2 k_z^2 \hat{\rho} - a_0^2 \nabla_{12}^2 \hat{\rho} = \frac{\partial^2 \hat{T}_{mn}}{\partial y_m \partial y_n} + 2ik_z \frac{\partial \hat{T}_{m3}}{\partial y_m} - k_z^2 \hat{T}_{33} \tag{A3}$$

where $\nabla_{12}^2 = (\partial^2/\partial y_1^2) + (\partial^2/\partial y_2^2)$, $m,n = 1,2$ and $\hat{T}_{m3} = \hat{T}_{3m}$. Equation (A3) can be further rewritten as

$$\nabla_{12}^2 \hat{\rho} + \hat{k}^2 \hat{\rho} = -\frac{1}{a_0^2} \frac{\partial^2 \hat{T}_{mn}}{\partial y_m \partial y_n} - \frac{2ik_z}{a_0^2} \frac{\partial T_{m3}}{\partial y_m} + \frac{k_z^2}{a_0^2} \hat{T}_{33} \tag{A4}$$

where $m,n = 1,2$ and $\hat{k}^2 = \omega^2/a_o^2 - k_z^2$. Taking into account only the radiative components, i.e., $\hat{k}^2 > 0$ and using Green's function $G(x_1, x_2) = (1/4i) H_0^{(1)}(\hat{k}|\vec{x}|)$, where $|\vec{x}| = \sqrt{(x_1^2 + x_2^2)}$ and $H_0^{(1)}$ is Hankel's function of the first kind, we get

$$\hat{\rho} = \underbrace{-\frac{1}{4ia_0^2} \int\int \frac{\partial^2 \hat{T}_{mn}}{\partial y_m \partial y_n} H_0^{(1)}(\hat{k}r) dy_1 dy_2}_{I}$$

$$\underbrace{-\frac{k_z}{2a_0^2} \int\int \frac{\partial \hat{T}_{m3}}{\partial y_m} H_0^{(1)}(\hat{k}r) dy_1 dy_2}_{II}$$

$$\underbrace{-\frac{k_z^2}{4ia_0^2} \int\int \hat{T}_{33} H_0^{(1)}(\hat{k}r) dy_1 dy_2}_{III} \tag{A5}$$

where

$$r \equiv \sqrt{(x_1 - y_1)^2 + (x_2 - y_2)^2}$$

i.e., $\hat{\rho} = I + II + III$, where I is a quadrupole directivity in 2D, II is a dipolelike directivity in 2D, and III is a monopolelike directivity in 2D. From Eq. (A5), we follow Mitchell et al. [34] and obtain for the far-field sound expression given by Eq. (5) in Sec. 2.2 (note that all contributions decay as $1/\sqrt{r}$). The overall ρ can be further obtained by an inverse Fourier transform in space and time. In order to derive outflow conditions, we assume that the quadrupole decays as a wave packet outside the computational domain, i.e.,

$$\hat{T}_{mn}(x > x_{\text{out}}) = \hat{T}_{mn}(x = x_{\text{out}}) e^{-ik_0 x} e^{-\varepsilon(x - x_{\text{out}})} \tag{A6}$$

where

$$\varepsilon \ll 1 \text{ and } k_o \cong \omega/U_c$$

$$\Downarrow$$

$$\int_{-\infty}^{\infty} dy_2 \int_{-\infty}^{\infty} \hat{T}_{mn} dy_1 = \int_{-\infty}^{\infty} dy_2 \int_{0}^{L_x} \hat{T}_{mn} dy_1 + \int_{-\infty}^{\infty} dy_2 \int_{-\infty}^{0} \hat{T}_{mn} dy_1 + \int_{-\infty}^{\infty} dy_2 \int_{L_x}^{\infty} \hat{T}_{mn} dy_1 \tag{A7}$$

where

$$\int_{-\infty}^{0} \hat{T}_{mn} dy_1 \cong -\frac{1}{ik_o} \hat{T}_{mn}(x=0) e^{-ik_o x} \Big|_{-\infty}^{0} = \frac{1}{k_o} \hat{T}_{mn}(x=0) \tag{A8}$$

$$\int_{L_x}^{\infty} \hat{T}_{mn} dy_1 \cong -\frac{1}{ik_o} \hat{T}_{mn}(x = x_{\text{out}}) e^{-ik_o x} \Big|_{L_x}^{\infty}$$

$$= \frac{1}{ik_o} \hat{T}_{mn}(x = x_{\text{out}}) = -\frac{i}{k_o} \hat{T}_{mn}(x = x_{\text{out}}) \tag{A9}$$

Thus, using Eqs. (A8) and (A9) in Eq. (A7) leads to

$$\int_{-\infty}^{\infty} dy_2 \int_{-\infty}^{+\infty} \hat{T}_{mn} dy_1 = \int_{-\infty}^{\infty} dy_2 \int_{0}^{L_x} \hat{T}_{mn} dy_1 + \int_{-\infty}^{\infty} dy_2 \frac{i}{k_o} \Big(\underbrace{\hat{T}_{mn}(x=0)}_{\approx 0 \text{ usually small}} - \hat{T}_{mn}(x = L_x) \Big) \tag{A10}$$

where the bracket term on the right hand side of Eq. (A10) is the boundary correction. It is similar in its form to the boundary correction based on the frozen structure used in the time-space domain in Ref. [30].

References

[1] Sato, H., 1960, "The Stability and Transition of a Two-dimensional Jet," J. Fluid Mech., **7**, pp. 53–80.
[2] Rockwell, D. O., and Niccolls, W. O., 1972, "Natural Breakdown of Planar Jets," ASME J. Basic Eng., **94**, pp. 720–730.
[3] Mattingly, G. E., and Criminale, W. O., 1971, "Disturbance Characteristics in a Plane Jet," Phys. Fluids, **14**, pp. 2258–2264.
[4] Browne, L. W. B., Antonia, R. A., and Chambers, A. J., 1984, "The Interaction Region of a Turbulent Plane Jet," J. Fluid Mech., **149**, pp. 355–373.
[5] Thomas, F. O., and Goldschmidt, V. W., 1986, "Structural Characteristics of a Developing Turbulent Planar Jet," J. Fluid Mech., **163**, pp. 227–256.
[6] Thomas, F. O., and Chu, H. C., 1989, "An Experimental Investigation of the Transition of a Planar Jet: Subharmonic Suppression and Upstream Feedback," Phys. Fluids A, **1**, pp. 1566–1587.
[7] Thomas, F. O., and Prakash, K. M. K., 1991, "An Experimental Investigation of the Natural Transition of an Untuned Planar Jet," Phys. Fluids A, **3**, pp. 90–105.
[8] Bradbury, L. J. S., 1965, "The Structure of a Self-Preserving Turbulent Plane Jet," J. Fluid Mech., **23**, pp. 31–64.
[9] Heskestad, G., 1965, "Hot-Wire Measurements in a Plane Turbulent Jet," ASME J. Appl. Mech., **32**, pp. 721–734.
[10] Gutmark, E., and Wygnanski, I., 1976, "The Planar Turbulent Jet," J. Fluid Mech., **73**, pp. 465–495.
[11] Hussain, A. K. M. F., and Clark, A. R., 1977, "Upstream Influence on the Near Field of a Plane Jet," Phys. Fluids, **20**, pp. 1416–1426.
[12] Everitt, K. W., and Robins, A. G., 1978, "The Development and Structure of Turbulent Plane Jets," J. Fluid Mech., **88**, pp. 563–583.
[13] Goldschmidt, V. W., and Bradshaw, P., 1973, "Flapping of a Plane Jet," Phys. Fluids, **16**, pp. 354–355.
[14] Cervantes de Gortari, J., and Goldschmidt, V. W., 1981, "The Apparent Flapping Motion of a Turbulent Plane Jet—Further Experimental Results," ASME J. Fluids Eng., **103**, pp. 119–126.

[15] Goldschmidt, V. W., Moallemi, M. K., and Oler, J. W., 1983, "Structures and Flow Reversal in Turbulent Plane Jets," Phys. Fluids, **26**, pp. 428–432.
[16] Oler, J. W., and Goldschmidt, V. W., 1982, "A Vortex-street Model of the Flow in the Similarity Region of a Two-dimensional Free Turbulent Jet," J. Fluid Mech., **123**, pp. 523–535.
[17] Mumford, J. C., 1982, "The Structure of the Large Eddies in Fully Developed Turbulent Shear Flows. Part 1. The Plane Jet," J. Fluid Mech., **118**, pp. 241–268.
[18] Thomas, F. O., and Brehob, E. G., 1986, "An Investigation of Large-scale Structure in the Similarity Region of a Two-dimensional Turbulent Jet," Phys. Fluids, **29**, pp. 1788–1795.
[19] Antonia, R. A., Chambers, A. J., Britz, D., and Browne, L. W. B., 1986, "Organized Structures in a Turbulent Plane Jet: Topology and Contribution to Momentum and Heat Transport," J. Fluid Mech., **172**, pp. 211–229.
[20] Dai, Y., Kobayashi, T., and Taniguchi, N., 1994, "Large Eddy Simulation of Plane Turbulent Jet Flow Using a New Outflow Velocity Boundary Condition," JSME Int. J., Ser. B, **37**, pp. 242–253.
[21] Weinberger, C., Rewerts, J., and Janicka, J., 1997, "The Influence of Inlet Conditions on a Large Eddy Simulation of a Turbulent Plane Jet," *Proceedings of the 11th Symposium on Turbulent Shear Flows*, Springer-Verlag, Grenoble, France, Vol. 3, pp. 25.17–25.22.
[22] Ribault, C. L., Sarkar, S., and Stanley, S. A., 1999, "Large Eddy Simulation of a Plane Jet," Phys. Fluids, **11**, pp. 3069–3083.
[23] Ribault, C. L., Sarkar, S., and Stanley, S. A., 2001, "Large Eddy Simulation of Evolution of a Passive Scalar in Plane Jet," AIAA J., **39**, pp. 1509–1516.
[24] Stanley, S. A., Sarkar, S., and Mellado, J. P., 2002, "A Study of the Flow-Field Evolution and Mixing in a Planar Turbulent Jet Using Direct Numerical Simulation," J. Fluid Mech., **450**, pp. 377–407.
[25] Avital, E. J., 2005, "A Second Look at the Role of the Fast Fourier Transform as an Elliptic Solver," Int. J. Numer. Methods Fluids, **48**(9), pp. 909–927.
[26] Kim, W. W., and Menon, S., 1999, "An Unsteady Incompressible Navier–Stokes Solver for Large Eddy Simulation of Turbulent Flow," Int. J. Numer. Methods Fluids, **31**, pp. 983–1017.
[27] Inagaki, M., Kondoh, T., and Nagano, Y., 2002, "A Mixed-Time-Scale SGS Model for Practical LES," Trans. Jpn. Soc. Mech. Eng., Ser. B, **68**(673), pp. 2572–2579.
[28] Mittal, R., and Balachandar, S., 1996, "Direct Numerical Simulation of Flow Past Elliiptic Cylinders," J. Comput. Phys., **124**, pp. 351–367.
[29] Crighton, D. G., 1975, "Basic Principles of Aerodynamic Noise Generation," Prog. Aerosp. Sci., **16**(1), pp. 31–96.
[30] Avital, E. J., Sandham, N. D., Luo, K. H., and Musafir, R. E., 1999, "Calculation of Basic Sound Radiation of Axisymmetric Jets by Direct Numerical Simulation," AIAA J., **37**(2), pp. 161–168.
[31] Hu, H., Morfey, C. L., and Sandham, N. D., 2003, "Sound Radiation in Turbulent Channel Flows," J. Fluid Mech., **475**, pp. 269–302.
[32] Kouts, C. A., and Yu, J. C., 1975, "Far Noise Field of a Two-Dimensional Subsonic Jet," AIAA J., **13**, pp. 1031–1035.
[33] Munro, S. E., and Ahuja, K. K., 2003, "Aeroacoustics of a High Aspect-Ratio Jet," *Ninth AIAA/CEAS Aeroacoustics Conference and Exhibit*, Hilton Head, South Carolina, May 12–14, AIAA Paper No. 2003–3323, pp. 1–17.
[34] Mitchell, B. E., Lele, S. K., and Moin, P., 1995, "Direct Computation of the Sound from a Compressible Co-rotating Vortex Pair," J. Fluid Mech., **285**, pp. 181–202.

Inhomogeneous Multifluid Model for Prediction of Nonequilibrium Phase Transition and Droplet Dynamics

A. G. Gerber
Associate Professor
Department of Mechanical Engineering,
University of New Brunswick,
Fredericton, NB, E3B5A3, Canada
e-mail: agerber@unb.ca

A pressure based Eulerian multifluid model for application to phase transition with droplet dynamics in transonic high-speed flows is described. It is implemented using an element-based finite-volume method, which is implicit in time and solves mass and momentum conservation across all phases via a coupled algebraic multigrid approach. The model emphasizes treatment of the condensed phases, with their respective velocity and thermal fields, in inertial nonequilibrium and metastable gas flow conditions. The droplet energy state is treated either in algebraic form or through transport equations depending on appropriate physical assumptions. Due to the complexity of the two-phase phenomena, the model is presented and validated by exploring phase transition and droplet dynamics in a turbine cascade geometry. The influence of droplet inertia on localized homogeneous nucleation is examined. [DOI: 10.1115/1.2844580]

Keywords: multifluid, droplet slip, homogeneous nucleation, steam turbines

Introduction

The present study arises out of ongoing efforts to develop a comprehensive multiphase computational-fluid-dynamics (CFD) model for the low pressure stages in a steam turbine. The influence of droplets on both thermodynamic efficiency and blade erosion has made this an important topic, but the related thermofluid dynamic phenomena surrounding phase transition, droplet collection, and reentrainment are a complex subject area for CFD analysis. It is only recently that tools have become mature enough to tackle these flow situations in a comprehensive manner. This possibility comes from the maturity of underlying CFD solvers and from a long history of theoretical and computational studies related to two-phase flow phenomena in steam turbines. The computational/theoretical history has been reviewed in several recent publications [1–3], and the current work relies heavily on this framework. The present work makes a significant contribution in generalizing the models for implementation (and release) into a widely used commercial CFD solver ANSYS-CFX, utilizing its capabilities for solving inhomogeneous multiphase flows at all speeds. This work follows on a history of development [4,5] before adoption into its present form for inertial and thermal nonequilibrium predictions. The model to be presented here has also been applied to a large multistage turbine with multiple phase transition sites along the flow passage [6]. However, this work emphasizes the numerical details underlying the applications.

Source Specific Representation of Droplets

Before introducing the governing equations, it is useful to discuss how the dispersed (or condensed) phases in a multifluid model can be distributed to accommodate phase transition at different locations in the flow path and possibly initiated at significantly different sizes (many orders apart). For example, improved accuracy is possible by considering the introduction of the phases on the basis of their "source" (i.e., homogeneous, heterogeneous, secondary droplets reentrained, etc.) and "specific location" in the flow. Since droplets initiated under similar conditions experience a common history during transport, they can be reasonably represented by a monodispersed distribution. This approach can be applied to machines such as steam turbines, where phase transition is a complex process that occurs at several points throughout the flow path and depends on load conditions. An example of results obtained using a "source specific" approach is shown in Figs. 1(*a*)–1(*c*) [6].

A representation of the source specific distribution of phases is given (topologically) in Fig. 1(*d*). In this example, P1 is the gas phase, P2 is a condensed phase that can only be generated in S1 (stator 1) through S2 (knowing that at design, primary moisture formation begins in stator 2), and phase P3 can only be generated in R2 (rotor 2), phase P4 only in S3, and, finally, phase P5 only in R3 and DIF (the diffuser). A phase P6 is also shown to represent droplets that are generated at solid boundaries. All of the phases are free to interact with the gas phase (by heat, mass, and momentum transfer) in any location of the domain. A particular condensed phase (in this example, any of P2–P6) involving a similar droplet source and location can then be represented reasonably with a monodispersed droplet assumption as already noted. In this manner, at the exit of the turbine, five mass fraction (or wetness) values are predicted, each with its own mean droplet size. Each phase can be tied to a particular source/location in the turbine. The result is a considerable increase in detail of the moisture formation in the turbine. Results of this type are described in Ref. [6] (except that P6 is not included in the calculations) and provide a framework for applying the model equations to be discussed next.

Model Equations

The model equations are implemented in an Eulerian multifluid framework allowing for a treatment of each phase with its own velocity and energy levels. Table 1 has been prepared to provide an overview of the system of Reynolds averaged transport equations solved in space (x_j) and time (t). In Table 1, subscript d refers to the dispersed (condensed) phases of which there can be nd of them, and c refers to the continuous phase of which there is only one. The transported quantities ϕ have contributions from terms not associated with interphase exchange and are listed under

Contributed by the Fluids Engineering Division of ASME for publication in the JOURNAL OF FLUIDS ENGINEERING. Manuscript received February 13, 2007; final manuscript received December 5, 2007; published online March 11, 2008. Assoc. Editor: Rajat Mittal. Paper presented at the 2006 ASME Fluids Engineering Division Summer Meeting and Exhibition (FEDSM2006), Miami, FL, July 17–20, 2006.

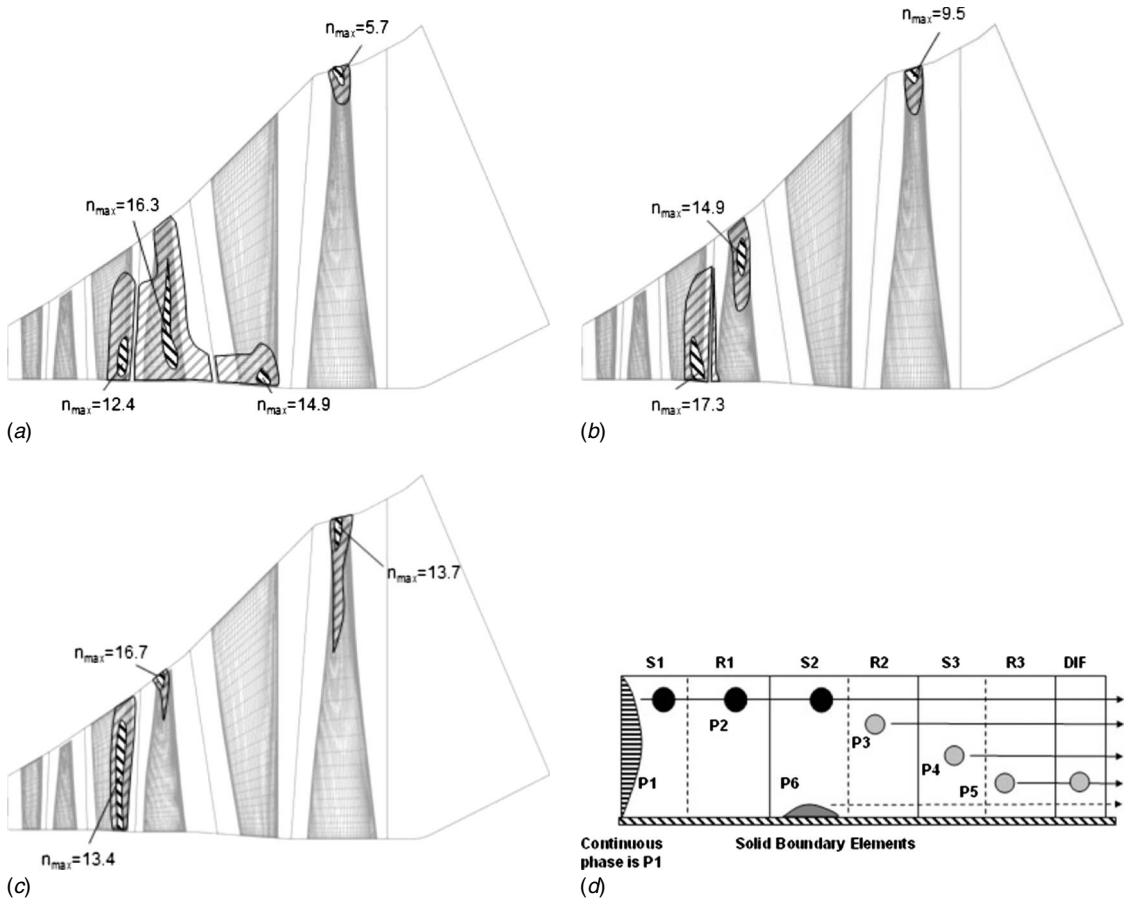

Fig. 1 Homogeneous phase transition at (*a*) part-load, (*b*) design, and (*c*) overload conditions presented in Ref. [6] where $n_{max}=\log(J_{max})$. The cross-hatched regions represent the approximate ranges of $n_{max}:n_{max}-1$ for the inner and $n_{max}-1:n_{max}-9$ for the outer. A topological representation of the multifluid model phases is given in (*d*). Each condensed phase is introduced into the flow using a source specific approach.

columns $S_{c\phi 1}$ and $S_{d\phi 1}$. Columns $S_{c\phi 2}$ and $S_{d\phi 2}$ describe additional terms related to interphase transfer and phase transition. In columns $S_{c\phi 1}$ and $S_{d\phi 1}$, terms are present for pressure (P) gradients, viscous stress tensor (τ_{ij}), and heat diffusion (Q). The remaining term M incorporates additional contributions to the energy equation, including viscous dissipation, which is activated for the transonic flow conditions considered.

The continuous and dispersed phase transport equations for momentum conservation, u_i, total energy level, H, and mass conservation are given in Table 1. For each condensed phase, a number density N is also solved with contributions from the nucleation model through the nucleation rate J. Note that the nucleation model can be activated for different regions of the flow according to the source specific approach outlined earlier in Fig. 1. The droplet number N has a unit of number/m^3 space, and the nucleation rate has a unit of number/m^3 vapor s. Note that in Table 1 the transport of droplet number uses material mass flows so that volume fraction α_d is removed from all terms indicated by setting $\phi=N/\alpha$. For the determination of the pressure active across all phases, mass conservation for each phase is summed to obtain a mixture expression shown in Table 1. Included with the mixture conservation equations is turbulent kinetic energy κ and dissipation ε associated with the κ-ε two-equation turbulence model with scalable wall functions [7]. This near wall treatment allows for an arbitrarily fine mesh resolution while maintaining correct log-law-based estimates of the wall shear stress. In Table 1 the incorporation of turbulent viscosity (μ_t) into momentum transport equations when expanding τ_{ij} and the definition of an effective diffusivity (Γ_{eff}) for related scalar equations (including energy when expanding Q) assume that the Reynolds stresses are linearly related to mean flow variables. This standard eddy-viscosity model approach introduces turbulence into the prediction of the mean flow field.

In the presented calculations, the volume fractions are generally much less than 1×10^{-5}, and droplet sizes are studied in a range up to 5 μm. In this range, the droplet volume loading and inertia are low such that the modulation of the gas phase would be minimal. In light of this, a homogeneous mixture treatment of turbulence across the phases is relevant and implies that turbulence in the continuous phase dominates (since its volume fraction is ~1) turbulent activity in the dispersed phases with no return coupling.

For the continuous phase, source term contributions to $S_{c\phi 2}$ for mass, momentum, and energy exist from all *nd* condensed phases. Summations of the dispersed phase $S_{d\phi 2}$ sources for mass, momentum, and energy are equal and opposite to $S_{c\phi 2}$ except for the latent heat liberation implicit in the formulation of the energy equations and the droplet number equation that is necessary for extracting size information from the particle size distribution (which is treated as monodispersed for each source specific phase).

In the dispersed phase energy treatment, an option exists for algebraically specifying the droplet temperature T_d as a function of its radius r_d, a formulation based on droplet capillarity [8]. The algebraic equation is given in Table 1 as energy (2), where T_s is the saturation temperature at pressure P, T_{sc} the supercooling level in the gas phase, and r^* the critical radius at the formation of the

Table 1 Governing equations

Continuous phase	$\frac{\partial(\rho\alpha\phi)_c}{\partial t}+\frac{\partial}{\partial x_j}(\rho\alpha u_j\phi)_c=S_{c\phi1}+S_{c\phi2}$		
	ϕ	$S_{c\phi1}$	$S_{c\phi2}$
Mass	1	0	$-\sum_{d=1}^{n_d} S_{d\phi2}$
Momentum	u_i	$-\alpha_c\frac{\partial P}{\partial x_i}+\frac{\partial\alpha_c\tau_{ijc}}{\partial x_j}$	$-\sum_{d=1}^{nd} S_{d\phi2}$
Energy	H	$-\alpha_c\frac{\partial P}{\partial t}+\frac{\partial\alpha_c Q_{jc}}{\partial x_j}+M_c$	$-\sum_{d=1}^{nd} S_{d\phi2}$
Dispersed phases	$\frac{\partial(\rho\alpha\phi)_d}{\partial t}+\frac{\partial}{\partial x_j}(\rho\alpha u_j\phi)_d=S_{d\phi1}+S_{d\phi2}\ d=1,\ldots,n_d$		
	ϕ	$S_{d\phi1}$	$S_{d\phi2}$
Mass	1	0	$\dot{m}_d+m^*\alpha_c J_d$
Momentum	u_i	$-\alpha_d\frac{\partial P}{\partial x_i}+\frac{\partial\alpha_d\tau_{ijd}}{\partial x_j}$	$\dot{m}_d u_{id}^U-C_D/8\,\beta_D\rho_c\lvert u_{id}-u_c\rvert(u_{id}-u_c)$
Energy (1)	H	$-\alpha_d\frac{\partial P}{\partial t}+\frac{\partial\alpha_d Q_{jd}}{\partial x_j}+M_d$	$\dot{m}_d H^U+\beta_d q_d$
Energy (2)		$T_d=T_s(P)-T_{sc}\frac{r_d^*}{r_d}$ for $2r_d\leqslant 1\ \mu$m	
Number	N/α	0	$\alpha_c\rho_d J_d$
Mixture conservation	$\frac{\partial\rho\phi}{\partial t}+\frac{\partial}{\partial x_j}(\rho u_j\phi)=\frac{\partial}{\partial x_j}\left(\Gamma_{\text{eff}}\frac{\partial\phi}{\partial x_j}\right)+S$		
	ϕ	Γ	S
Mass (pressure)	1	0	0
Turbulent kinetic energy	κ	μ_t/Pr_k	κ-ε model with scalable wall functions [7]
Turbulence dissipation	ε	$\mu_t/\text{Pr}_\varepsilon$	

dispersed phase obtained from the nucleation model. In the present calculations, this equation is also applied to droplet diameters in the $1-5\ \mu$m range and tested against results obtained by solving a transport equation described with Energy (1) in Table 1. As droplets become larger, significant differences develop between the droplet internal temperature and its surface, and the algebraic representation is no longer appropriate. Additionally, convective heat transfer from the droplet surface increases with larger droplet sizes.

A number of models governing the interphase contributions are present in $S_{c\phi2}$ and $S_{d\phi2}$. The models for nucleation rate, droplet drag, and heat and mass transfer are outlined in the following section.

Phase Transition and Metastable States

In order for $S_{c\phi2}$ and $S_{d\phi2}$ exchange terms to be active, droplets must be introduced into the flow domain either at boundaries or through homogeneous/heterogeneous nucleation sources. In the present case, droplets enter the domain at the inlet or are created due to phase transition by homogeneous nucleation. Phase transition based on classical nucleation theory requires metastable state information, and in the present calculations, this has been supplied by the IAPWS property formulation [9]. For computational efficiency, essential dispersed and continuous phase properties have been tabulated at the beginning of the solution as functions of pressure and/or temperature. The tabulated properties have associated spinodal and saturation information to demarcate metastable regions. The extent of metastable conditions in the flow is measured by the supercooling level

$$T_{\text{sc}} = T_{\text{sat}}(P) - T_c \tag{1}$$

The appearance of a second phase out of its vapor is governed by the process of homogenous nucleation. A detailed description of the development of nucleation models for steam turbine applications is given in Ref. [1] and provides the basis for the nucleation model used here. At significant levels of supercooling, the critical droplet radius is very small as given by the equation

$$r^* = \frac{2\sigma}{\rho_d \Delta G_c} \tag{2}$$

where ΔG_c is the Gibbs free energy of the continuous phase (and is calculated from the equation of state), σ the bulk surface tension, and ρ_d the density of the dispersed phase. The number of droplets formed is as follows:

$$J = \frac{z}{1+\eta}\left(\frac{2\sigma}{\pi m^3}\right)^{1/2}\frac{\rho_c^2}{\rho_d}\exp\left(-\frac{4\pi r^{*2}\sigma}{3KT_c}\right) \tag{3}$$

where

$$\eta = 2\frac{\gamma-1}{\gamma+1}\frac{L}{RT_c}\left(\frac{L}{RT_c}-\frac{1}{2}\right) \tag{4}$$

and z is a condensation coefficient generally taken as 1, ρ_c the gas phase density, K the Boltzmann's constant, m the mass of one water molecule, R the gas constant for water, γ the specific heat ratio, and L the equilibrium latent heat.

Interphase Exchange

The interphase exchange of mass, momentum, and energy depends on the droplet surface area density (β_d) for a given phase d relative to the surrounding continuous phase,

$$\beta_d = \frac{3\alpha_d}{r_d} \tag{5}$$

and is calculated as a function of the volume fraction and droplet radius for that phase. The same volume fraction, in conjunction with droplet number, is used to calculate the mean droplet radius

$$r_d = \left(\frac{3\alpha_d}{4\pi N_d}\right)^{1/3} \tag{6}$$

The droplet radius is an important input to momentum and heat transfer correlations used in the calculations.

Momentum Transfer. In order to predict flow behavior such as droplet collection or entrainment near solid surfaces, inertial nonequilibrium (characterized by droplet Reynolds number Re_d based on a vapor-droplet slip velocity) must be considered in conjunction with thermal nonequilibrium. For the cases considered in this study, spherical droplets are present in the diameter range from $\sim$0.001 μm to 5 μm, providing an opportunity to examine the influence of large droplets, relative to those generated homogeneously, on phase transition. The drag coefficient C_D applied for condensed phases of nominally 1 μm or larger is the Schiller–Naumann [10] having the form

$$C_D = \frac{24}{\mathrm{Re}_d}(1 + 0.15\,\mathrm{Re}_d^{0.687}) \tag{7}$$

and is applicable to droplets in the range of $0.1 < \mathrm{Re}_d < 1000$. At Re_d values larger than 1000, i.e., in the Newton's regime, C_D is clipped to 0.44. For submicron droplets, a constant and large value for C_D is set to maintain the droplets close to the gas phase velocity. In such cases, having a fixed C_D value helped convergence stability.

Heat and Mass Transfer

Small Droplet Model for Water. For condensed water droplets operating in a size range below 1 μm, a small droplet model is applied to govern heat and mass transfer. This model is best explained by considering Fig. 2(a), which describes the temperature field in and around a spherical droplet for the case of evaporation or condensation. Temperature gradients coincide with heat flow from the continuous phase (q_c) or the dispersed phase (q_d) to support phase change at the interface. Based on Fig. 2(a), the heat fluxes are

$$q_c = \frac{k_c}{2r_d}\mathrm{Nu}_c(T_s - T_c) \tag{8}$$

$$q_d = 0 \tag{9}$$

Note that in the case of the small droplet model, gradients in internal droplet temperature (T_d) can be assumed negligible, allowing the surface temperature T_s to be equated to T_d. Furthermore, because of the small size and capillarity, it is possible to relate the droplet temperature to its size, as shown for energy (2) in Table 1. The net result is that internal heat flow is zero and all heat transfer to support either condensation or evaporation from the droplet surface is with the continuous phase through flux q_c.

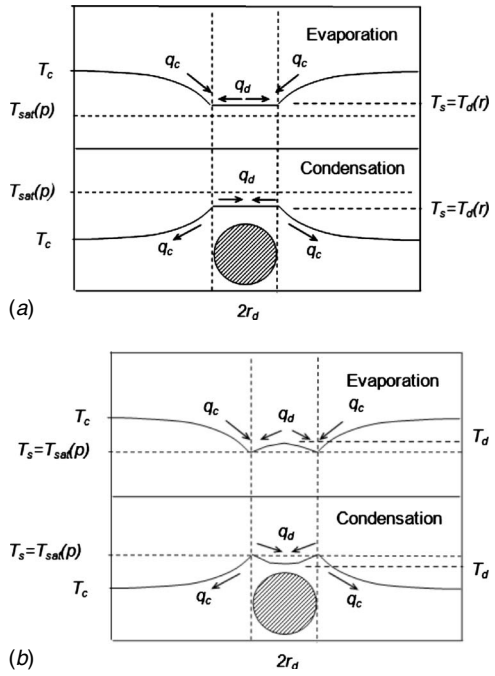

Fig. 2 Depiction of droplet (T_d) and continuous phase (T_c) temperatures (T_c), for either evaporation or condensation, versus radius emanating from the droplet center. Conditions for (a) a small droplet model nominally in the range $2r_d \leq 1$ μm, and (b) a large droplet model in the nominal range $2r_d > 1$ μm. Note that for case (a), droplet temperature T_d is treated algebraically as a function of r_d, as described for energy (2) in Table 1.

The Nusselt number applied for the continuous phase is based on a model by Gyarmathy [8],

$$\mathrm{Nu}_c = \frac{2}{1 + c\mathrm{Kn}} \tag{10}$$

where c is given a value of 3.18 and the Knudsen number Kn is evaluated from the vapor mean free path and droplet radius. This Nusselt formulation is applicable to water droplets formed at very small sizes by nucleation processes.

The mass transfer associated with phase change is determined by applying a heat flow balance at the droplet surface in Fig. 2(a) so that

$$\dot{m}_d = \frac{q_c + q_d}{(h_c - h_d)} \tag{11}$$

where static enthalpy h_d is determined using T_d along with pressure P from property tables. In addition, h_c is available from the solution of the continuous phase total energy using $h_c = H_c - U^2/2$, where U is the velocity magnitude for the continuous phase.

Large Droplet Model. For droplet sizes larger than 1 μm, internal temperatures can begin to deviate from the surface temperature T_s, as shown in Fig. 2(b), and coincides with the droplet trajectory beginning to deviate from the gas phase. This requires a more general treatment of the droplet surface heat transfer, including solving a transport equation for the droplet energy level, h_d, obtained through the solution of H_d and droplet velocity in Table 1.

By referring now to Fig. 2(b), the surface heat fluxes for either condensation or evaporation become

$$q_c = \frac{k_c}{2r_d}\mathrm{Nu}_c(T_s - T_c) \tag{12}$$

$$q_d = \frac{k_d}{2r_d}\mathrm{Nu}_d(T_s - T_d) \tag{13}$$

and $T_s = T_d$ can no longer be specified and Nu_c is based on a Ranz–Marshall correlation [11] of the form

$$\mathrm{Nu}_c = 2 + 0.6\,\mathrm{Re}_d^{1/2}\,\mathrm{Pr}_d^{1/3} \tag{14}$$

For the internal droplet heat flow, $\mathrm{Nu}_d = 6$ is applied as a reasonable approximation. Note that Eq. (14) now includes the increased heat transfer associated with droplet slip as seen by the droplet Reynolds number influence. The determination of the interphase mass transfer again uses Eq. (11), but now q_d is not zero and h_d is determined from a transport equation (Energy (1) in Table 1).

Secondary Fluxes. For the droplet related source terms $S_{c\phi 2}$ and $S_{d\phi 2}$ in Table 1, secondary flux terms are present, associated with the mass transfer between phases determined on the basis of Eq. (11). Equation (11) can be related to the droplet area density and growth rate by

$$\dot{m}_d = \rho_d \frac{dr_d}{dt}\beta_d \tag{15}$$

The secondary mass transfer flux uses an upwind approach for determining which transported quantity is removed from the originating phase and carried into the receiving phase (this quantity is designated with superscript U in Table 1). The direction of $\dot{m}$ is determined by its sign and is taken as positive into the receiving phase. The application of the upwind approach is straightforward for momentum but is more complicated in the case of energy. For energy, the saturation condition is always used for the property entering a receiving phase. This approach ensures that the enthalpy difference (between originating and receiving phases) is always close to the latent heat value and will always be stable.

Numerical Model

The conservation equations described above are discretized using an element-based finite volume method [12]. The mesh may consist of tetrahedral, prismatic, pyramid, and hexahedral elements. A control volume is constructed around each nodal point of the mesh, as illustrated in Fig. 3. The subface between two control volumes within a particular element is associated with an integration point (ip); it is at integration points that the fluxes are discretized. Integration point quantities such as pressure and velocity gradients are obtained from nodal values using finite-element shape functions, with the exception of advected variables that are obtained using an upwind-biased discretization. The discretization is fully conservative and time implicit. The conservation equations are integrated over each control volume; volume integrals are converted to surface integrals using Gauss' divergence theorem, and surface fluxes are evaluated in exactly the same manner for the two control volumes adjacent to an integration point. This process is now described in more detail for mass continuity and momentum.

The discrete conservation equations for the dispersed phase continuity may be viewed as evolution equations for the volume fractions,

$$\frac{V}{\partial t}((\rho\alpha)_d^{n+1} - (\rho\alpha)_d^n) + \sum_{\mathrm{ip}} (\rho u_i)_d^{n+1} A_i \alpha_d^{n+1} = 0 \tag{16}$$

where V represents the control volume, $\mathbf{A}_i^i$ the area, and ∂t the time step, and the superscripts $n+1$ and n indicate that the quantity is evaluated at the new and old time steps, respectively.

The advection scheme used to evaluate α_{ip} in terms of neighboring vertex values must give solutions that are both bounded and accurate. This is written as

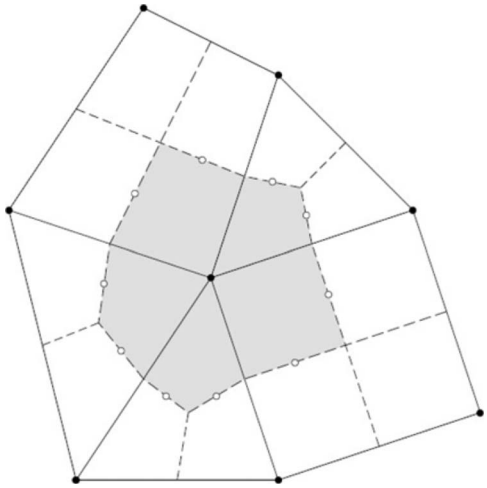

Fig. 3 Element-based finite-volume discretization of the spatial domain. Solid lines define element boundaries, and dashed lines divide elements into sectors. Solution unknowns are colocated at the nodal points (●), and surface fluxes are evaluated at integration points (○). Control volumes are constructed as unions of element sectors (shaded region).

$$(\alpha_d)_{\mathrm{ip}}^{n+1} = (\alpha_d)_{\mathrm{up}}^{n+1} + \lambda \nabla \alpha_d \cdot \mathbf{R} \tag{17}$$

where the subscript "up" refers to the upwind vertex value and $\mathbf{R}$ is the vector from the upwind vertex to the integration point. If $\lambda = 0$, this scheme recovers the first-order upwind scheme, which is bounded but excessively diffusive. If $\lambda = 1$, this scheme is a second-order upwind-biased scheme, but unbounded. A bounded high-resolution scheme can be obtained by making λ as close to 1 as possible, but reducing where necessary to prevent overshoots and undershoots from occurring. A method similar to that described by Barth and Jesperson [13] is used. Note that the description here for dispersed phase volume fraction applies to the continuous phase and that the advection scheme implied by Eq. (17) is applied to all conservation equations with a transported variable.

The mass flows must be discretized in a careful manner to avoid pressure-velocity decoupling. This is performed by generalizing the interpolation scheme proposed by Rhie and Chow [14], such that the advecting velocity for each phase is evaluated as follows:

$$(ui)_{\mathrm{ip}} = (\bar{u}\bar{i})_{\mathrm{ip}} + d_{\mathrm{ip}}\left(\frac{\partial P}{\partial x_i} - \overline{\frac{\partial P}{\partial x_i}}\right)_{\mathrm{ip}} \tag{18a}$$

where

$$d_{\mathrm{ip}} \propto -V/a$$

$$a \propto \rho_m V/\partial t + b \tag{18b}$$

and b represents the sum of advection and viscous coefficients in the discretized momentum equation. The overbar denotes the average of the control volume values adjacent to the integration point.

The discretized dispersed phase momentum equations may be viewed as an evolution equation for the velocity field,

$$\frac{V}{\partial t}((\rho\alpha u_i)_d^{n+1} - (\rho\alpha u_i)_d^n) + \sum_{\mathrm{ip}} (\rho\alpha u_j)_d^{n+1} A_j (u_i)_d^{n+1}$$

$$= -\sum_{\mathrm{ip}} (P\alpha_d)^{n+1} A_i + \sum_{\mathrm{ip}} (\tau_{ji}\alpha)_d^{n+1} A_j + S_{du2} V \tag{19}$$

A high-resolution scheme based on Eq. (17) is used for the advected velocity in this equation, and finite-element shape func-

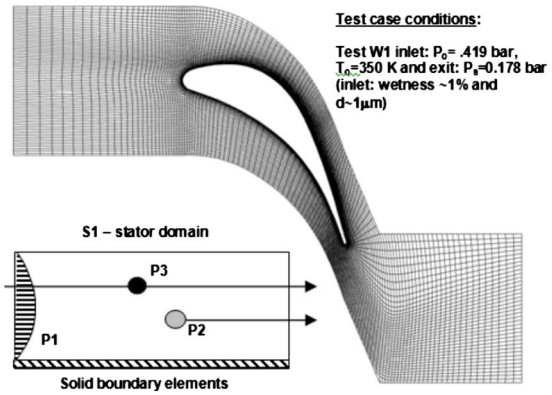

Fig. 4 Cascade blade geometry taken from Ref. [16] along with mesh. The inset (bottom left) gives the topology of the solution phases with P1 as the continuous phase, P2 as droplets formed within the domain by homogeneous nucleation, and P3 as a phase containing larger droplets formed upstream of the inlet.

tions are used to evaluate the gradients for the pressure and viscous forces. A similar treatment applies to the continuous phase momentum equation.

Finally, it remains to derive a discrete equation for pressure. This is obtained by integrating the phasic mass equations in Table 1 over the control volume and summing across all phases,

$$\sum_{a=1}^{n_d+1} \frac{1}{\rho_a}\left(\frac{V}{\partial t}((\rho\alpha)_a^{n+1} - (\rho\alpha)_a^n) + \sum_{\text{ip}} (\rho u_i)_a^{n+1} A_i \alpha_a^{n+1} = 0\right) \quad (20)$$

which yields a diagonally dominant equation for pressure because of the special interpolation used for $(ui)_{\text{ip}}$. In Eq. (20), subscript a is used to represent summation over all the phases both continuous and dispersed.

The algebraic equations (Eqs. (16), (19), and (20)), once assembled into a final coefficient form, represent equations for the volume fraction, velocity, and pressure fields. With n_d+1 phases then, $3(n_d+1)$ momentum and one pressure equations are solved directly at each nodal point. This is applied in the context of solving the overall linear system of equations using the coupled algebraic multigrid technique described by Raw [15]. In this process, Eq. (16) is decoupled from the pressure-velocity system and treated in a segregated manner, as are the remaining equations described in Table 1.

In light of the above discussion, the solutions to follow were obtained with a rms convergence setting of 1×10^{-5} across all variables. Global imbalances for each transport equation upon convergence were typically 0.01% or lower. An unstructured hexahedral mesh, with ~81,000 nodes, was employed due to its superior qualities in the near wall regions of the flow where the mesh was refined. The solutions obtained were all steady state with a time step of $\sim5\times10^{-5}$ s chosen in an implicit formulation. The time step was chosen as a bit lower than the average advection time for the flow to pass through the device.

Demonstration Case: 2D Cascade Section

To demonstrate the application of the model, the influence of inertial nonequilibrium on local homogeneous phase transition in a steam turbine cascade row is examined. For this, the cascade geometry and flow conditions in Ref. [16] can be used (shown along with mesh in Fig. 4) and, in particular, focus on the subset of experimental data where large droplets are present in conjunction with very small droplets produced by homogeneous phase transition. For example, case W1 in Ref. [16] gives measured inlet droplet size (~1 μm) and mass fraction (~1% wetness) along with measurements for blade static pressure profile and schlieren photographs of the flow structure where homogeneous phase transition is present. These data are used as a base line validation, and then the influence of droplet size, and associated slip, on the phase transition process is examined. In addition, the influence of the treatment of the energy equation for the dispersed phase on the results is studied.

Following the source specific approach described in Fig. 1, a similar schematic is provided in Fig. 4 (bottom left). Relative to the full turbine previously described in Fig. 1, the setup is obviously much simplified. Only three phases are considered, with P1 representing the continuous parent phase, P2 any droplets formed in the blade passage by homogeneous nucleation, and P3 larger droplets formed previously upstream (indicated by the arrow originating upstream of the inlet). The base line calculation to follow uses an energy (2) treatment along with small droplet heat transfer model (Eqs. (8) and (9)) for both phases P2 and P3. This eliminates the need for transport equations. The effect of this assumption, which may not be suitable for the larger P3 droplets (convective heat transfer becomes important with the appearance of slip), is tested subsequently.

Baseline Solution. The case W1 solution is described in Figs. 5–8, beginning with a description of the flow conditions in the region where homogeneous nucleation is active. The relatively large droplets formed upstream of the inlet, at a level of about 1% mass fraction, are carried into the blade passages, and with sizes of ~1 μm develop slip relative to the vapor phase. This is apparent by the mass fraction deficit on the blade suction side, as seen in Fig. 5(*a*). The decrease in droplet surface area enables critical supercooling levels (Wilson line) to be reached earlier, as seen in Fig. 5(*b*) and further indicated by the nucleation zone impinging the suction surface in Fig. 5(*c*). The phase transition is followed by a rapid increase in the presence of phase P2, as shown by the mass fraction field in Fig. 5(*d*). The solution therefore predicts two monodispersed size groups, one for each phase, as well as two volume fractions presented in terms of mass fractions. The transport of phase P3 through the blade passages in this base line case is nearing a threshold since only minor increases in droplet size beyond 1 μm will lead to significant inertial nonequilibium conditions, as will be shown in calculations to follow. Homogeneous no-slip assumptions for turbine cascade or rotor calculations historically rely on assuming that droplets are smaller than 1 μm. The calculation here supports this, but what is also apparent is that the presence of another earlier formed droplet group can influence the strength and location of any homogeneous phase transition in the blade passages.

Case W1 results can be validated using shock and condensation fronts viewed by schlieren photographs and static pressure profiles measured over the blade surfaces [16]. Figure 6 gives the comparison of the flow structures. Figure 6(*a*) shows features of the predicted Mach number distribution, where a strong oblique shock is shown to sit off the suction side of the blade (S_s) evaporating a significant portion of P2, as shown in Fig. 5(*d*). The larger P3 droplets are less responsive to abrupt changes in flow properties, but still show a slight reduction in mass fraction levels in Fig. 5(*a*). A condensation front is also present (S_c) following the region of peak supercooling, as indicated by the Wilson line in Fig. 5(*b*). The location and angle of the S_s and S_c fronts highlighted in Fig. 6(*a*) compare well with the schlieren photographs given in Fig. 6(*b*). Further, in this comparison for case W1, the predicted blade pressure profile is given in Fig. 7, where it is apparent that the suction side pressure rise is well located, and generally of the right strength. Droplet size predictions for phases P2 and P3 are also shown in Fig. 8, and show slow growth of phase P3 in Fig. 8(*a*) compared to the rapid droplet growth associated with phase P2.

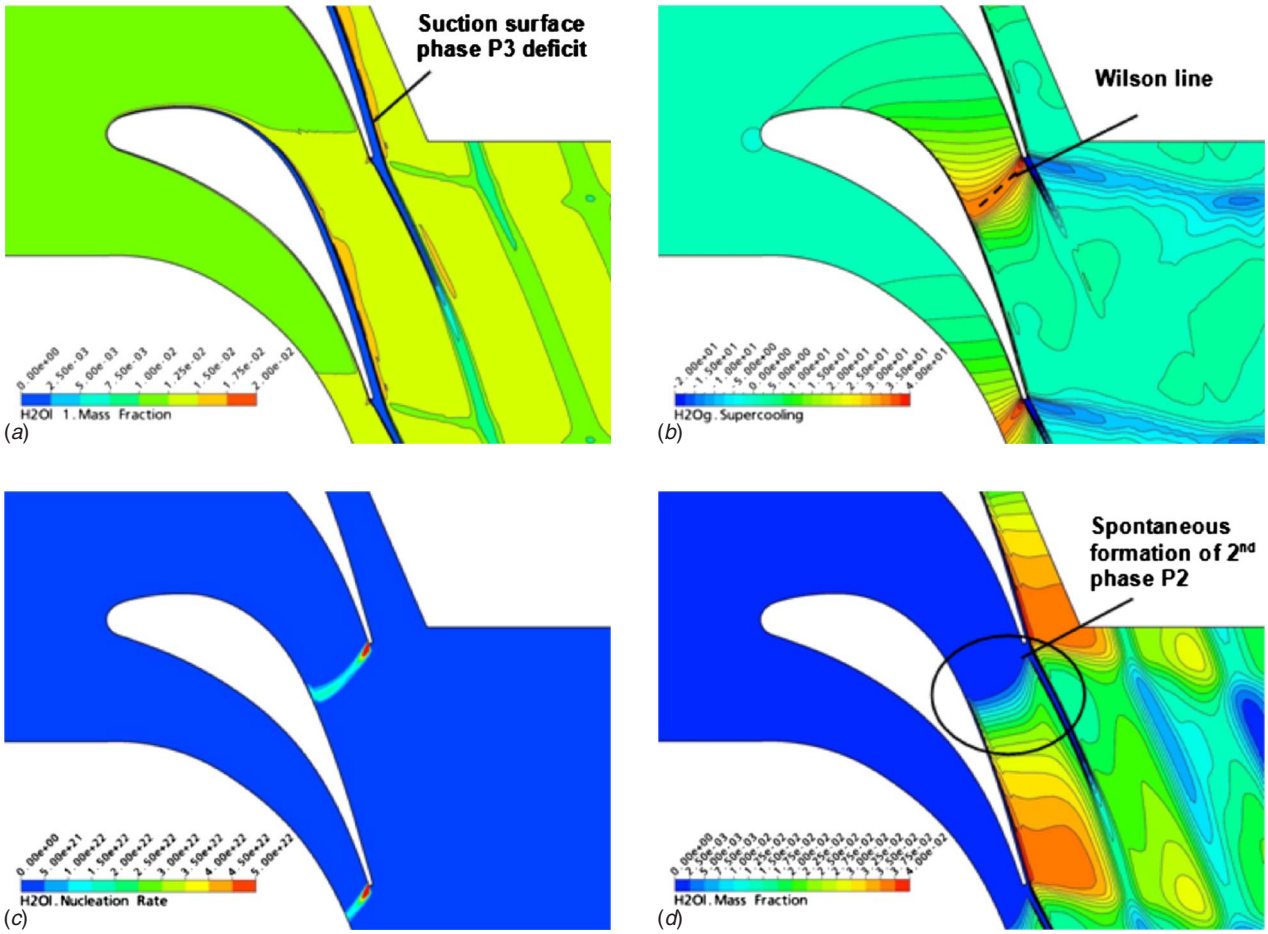

Fig. 5 Case W1 [16] results with (*a*) mass fraction of phase P3 highlighting deviation of droplets from equilibrium trajectory, (*b*) supercooling level with the Wilson line indicated, (*c*) location and strength of nucleation front, and (*d*) location of formation of phase P2 mass fraction

Large quantities of small droplets (~0.001 μm) at nucleation for P2 respond rapidly in the supercooled vapor, bringing the flow closer to equilibrium (as seen in Fig. 5(*b*)) following the Wilson line.

Influence of Droplet Size on Phase Transition. An additional aim in the present work was to apply the model to the influence of inertial nonequilibrium on local homogeneous phase transition and the influence of treatment of the dispersed phase energy equation on predictions. Using the base line results as part of the investigation, a series of calculations with inlet droplet size of 0.5 μm, 2 μm, and 5 μm was undertaken. These calculations used the same treatment of the dispersed phase energy equation and droplet heat transfer as in the base line case.

Figures 9(*a*) and 9(*b*), in conjunction with Fig. 5(*c*), show the positioning of peak nucleation as the droplet size is increased. This is also demonstrated by plotting the suction side pressure profiles, as shown in Fig. 9(*c*). Clearly, as the P3 inlet droplet sizes are increased, the pressure rise associated with the impinging nucleation front moves further upstream. The influence of smaller sizes delays and weakens nucleation, and would ultimately, if sizes were reduced below 0.1 μm, begin to approach an equilibrium pressure profile.

The movement of the nucleation zone, as described in Fig. 9, is tied to the degree of inertial nonequilibrium of phase P3 in the intervening blade passages. This is shown in Fig. 10 where the droplet trajectories are visible from the mass fraction fields for three different inlet sizes. As alluded to earlier, size changes beyond 1 μm at the inlet quickly lead to a significant droplet slip relative to the vapor. This is apparent when comparing results in Fig. 10(*a*) for 0.5 μm to those in Figs. 10(*b*) and 10(*c*) at diameters of 2 μm and 5 μm (the result for 1 μm is shown in Fig. 5(*a*)), where larger droplets cannot follow the vapor phase along the blade suction side. The resulting reduction of the overall droplet surface area in the suction region enables peak supercooling, and associated nucleation, to move upstream. At 5 μm, P3 droplets almost entirely bypass the critical suction region and explain the diminishing influence of increased size on the pressure profile in Fig. 9(*c*). At even larger droplet sizes, no droplets enter the suction region, and homogeneous nucleation will proceed in generating P2 almost as if P3 was not present. In other words, the strength and location of the homogeneous nucleation front will be independent of the P3 inlet droplet size.

A further test was undertaken to determine the influence of the P3 energy equation on predictions. The first test was to reproduce Fig. 9(*c*) results with P3 energy obtained using the energy (1) form in Table 1 along with the large droplet model for heat transfer (Eqs. (12) and (13)). This showed only a minor influence on the suction side pressure profiles in Fig. 9(*c*). Following this, pitchwise results at the exit plane were compared for the 1 μm and 5 μm cases, each obtained with P3 using energy (2)/small droplet and energy (1)/large droplet settings. Such a comparison becomes relevant since with increasing slip, droplet heat transfer includes convection effects, which is included in the large droplet model. The comparison of these predictions is given in Fig. 11. Here, all results are normalized by inlet conditions, for the droplet

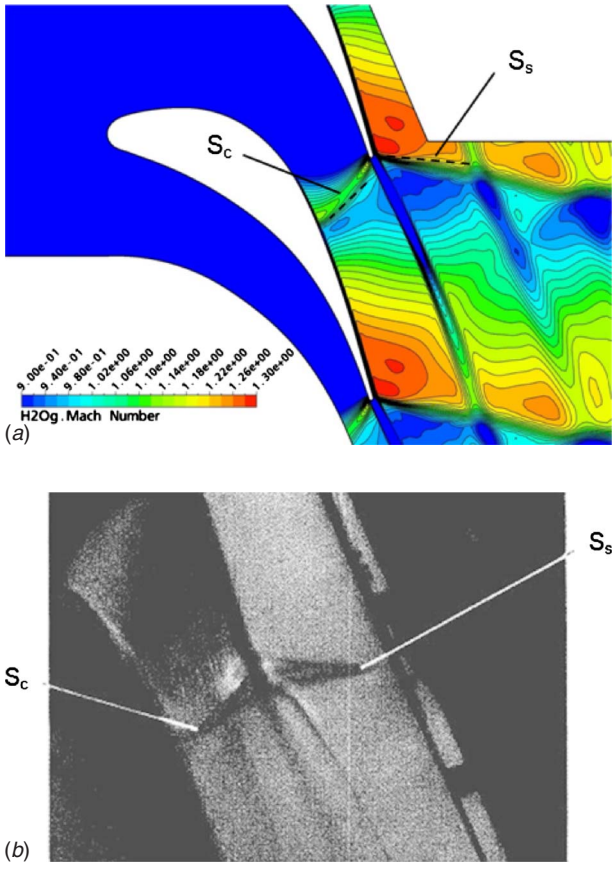

Fig. 6 Comparison of predicted suction side (S_s) oblique shock and condensation front (S_c) locations, as given in (*a*), with schlieren photographs given in (*b*) for case W1 in Ref. [16]

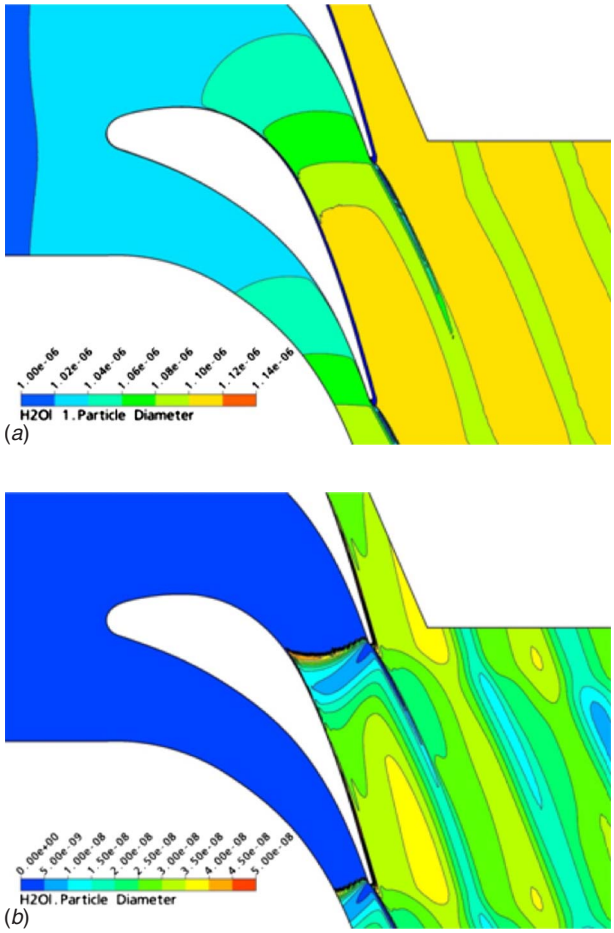

Fig. 8 Predicted droplet size distributions for case W1 [16]

diameter (D) and droplet mass fraction (y), and saturation temperature based on the exit pressure for dispersed phase P3 temperature (T).

The comparison shows that in either treatment, the predicted droplet temperatures are almost identical; however, there are significant changes in the mass fraction and droplet size predictions. In the cases where a transport equation is applied with large droplet heat transfer, the predicted mass fraction is higher, as is the associated droplet size. For 5 μm, the mass fraction is higher by about 5% in the core of the P3 droplet wake. Overall, the droplets are typically about 1% larger. Since the inlet mass fraction is held constant between the two cases tested, the smaller inlet droplet size case (of 1 μm) has a larger overall surface area leading to a more responsive P3 phase. Here also the mass fraction and droplet size obtained with the transport equation and large droplet model are higher, about 15% and 7%, respectively. For both cases tested, the results are consistent with the increased heat transfer when convective effects are included in the underlying Nusselt correlation. However, in both cases, droplet temperatures are very similar. This result suggests that for a certain range of droplet sizes of the order of 1 μm or larger, a good approximation to reduce problem complexity would be to retain the algebraic form for droplet temperature (energy (2) in Table 1) and include the large droplet heat transfer correlation in Eq. (8). This treatment is, of course, not applicable for droplet sizes well beyond 1 μm since internal droplet temperatures will begin to deviate significantly from the surface values.

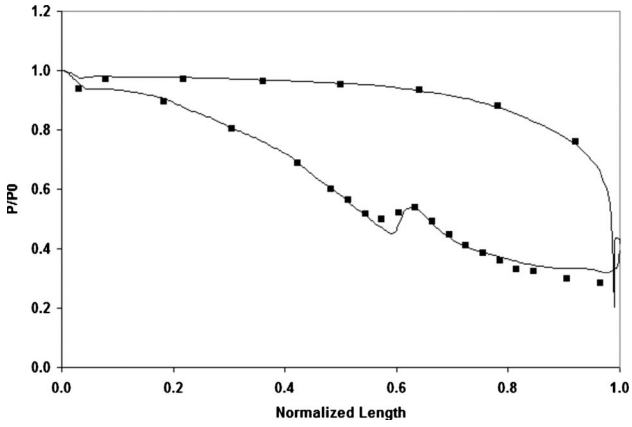

Fig. 7 Predicted blade static pressure profiles for case W1 [16]

Influence of Back Pressure on Efficiency Predictions. The previous section highlighted the use of an algebraic approach (energy (2) in Table 1) for determining the energy state of a dispersed phase versus solving a transport equation directly. The algebraic prescription is a desirable choice in that the droplet temperature to size relationship has been shown to enforce the surface energy requirements in forming small droplets [8]. Furthermore, not requiring an energy transport equation, in a highly nonlinear system as encountered in transonic flows with homogeneous nucleation, improves convergence behavior considerably. However, since the total energy of the droplet is not conserved explicitly by the solu-

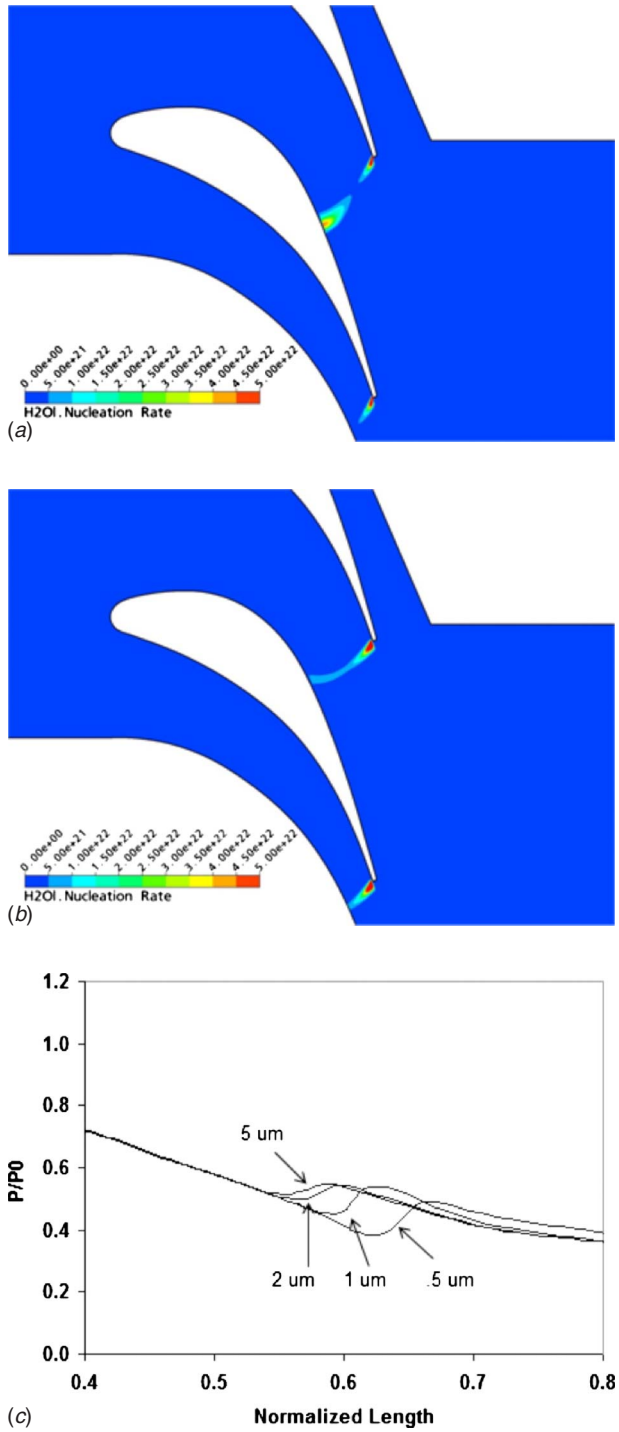

Fig. 9 Change in phase transition location with (*a*) P3 droplet size 0.5 μm and (*b*) 5 μm. As shown in (*c*), the suction side static pressure rise moves upstream with increasing P3 inlet size.

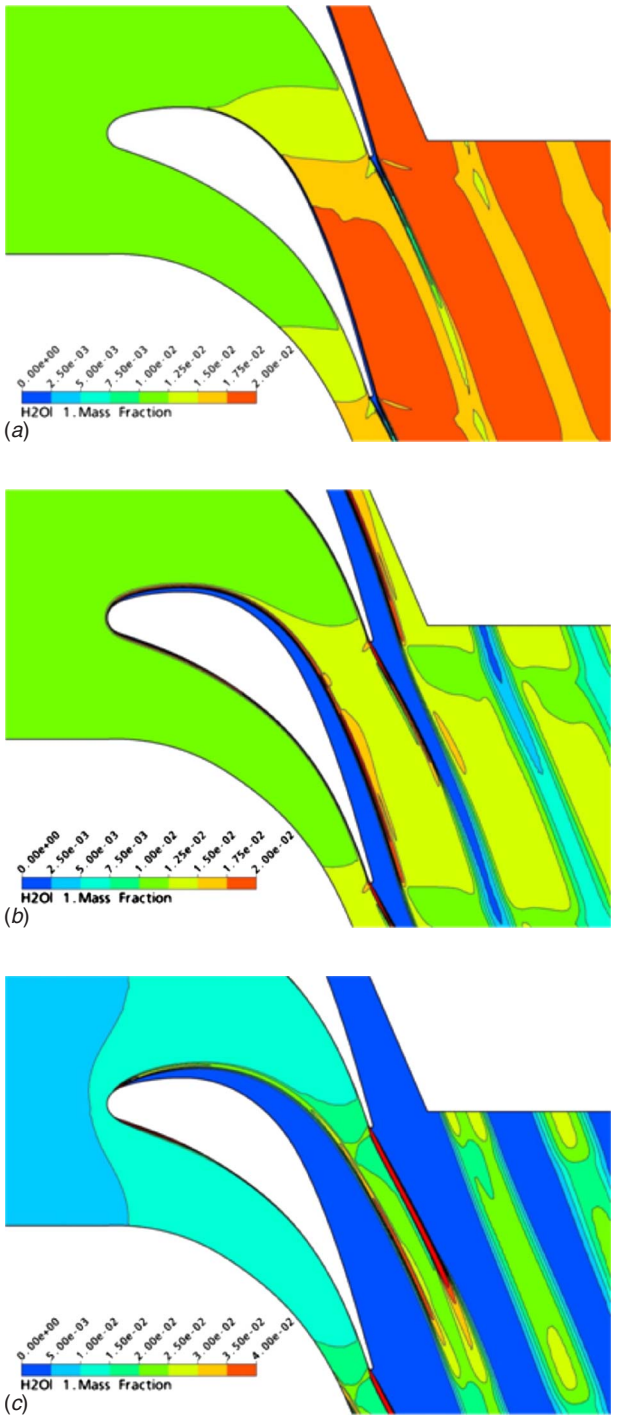

Fig. 10 Dispersed phase (P3) droplet trajectory for inlet diameters of (*a*) 0.5 μm, (*b*) 2 μm, and (*c*) 5 μm. Note that the 1 μm case is already given in Fig. 5(*a*).

tion of a transport equation, the droplet enthalpy based on the algebraic temperature is not the best choice for use in calculating efficiency. Other quantities directly derived from conserved variables in the formulation would be a better choice. For example, for this study, the isentropic efficiency is based on using the mixture kinetic energy divided by the isentropic mixture enthalpy drop. The appropriate equation would be

$$\eta = \frac{1}{2}\sum_{i=1}^{n_d+1} y_i U_i^2/(H_1 - h_{2s})_{\text{mix}} \tag{21}$$

For rotating components where work is extracted from the flow, an isentropic efficiency should be based on power output calculated from the pressure and viscous stresses on rotating boundaries.

Presently, the use of a total energy transport equation for the nucleating phase is problematic in that iteration is required to extract droplet temperature from the transported variable, in this

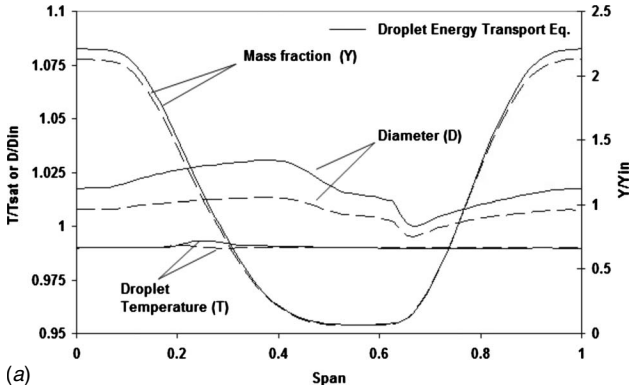

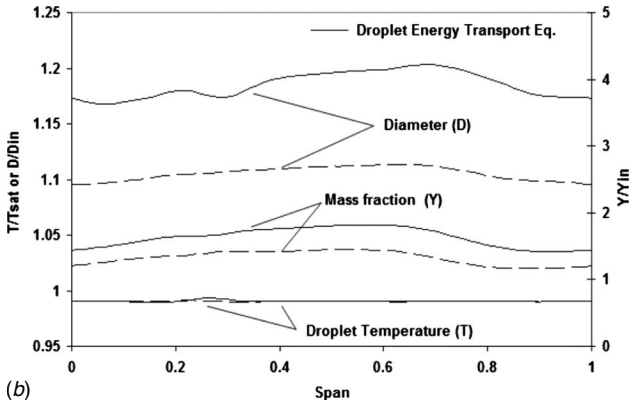

Fig. 11 Influence of dispersed phase energy equation treatment on exit temperature/mass fraction/size predictions for the case of P3 inlet diameters of (*a*) 5 μm and (*b*) 1 μm. Solid lines are obtained with energy (1), and dashed lines with an algebraic treatment energy (2), as shown in Table 1.

case total enthalpy, when surface energies are also included (which are a function of both r and T_d). For our calculation, all nucleating phases are treated with an algebraic form, taking advantage of the benefits outlined above. When surface energy terms are not important, a transport equation can be used, as in the results shown for Fig. 11.

The isentropic efficiency was also calculated for the cascade used in this study and compared to the calculated results reported in Ref. [16]. Figure 12 shows the predicted efficiencies for the W test set, all of which have inlet droplet sizes of approximately 1 μm at a level of approximately 1.6% wetness. Also shown is the L test set, which is dry at the inlet with approximately 4–5 deg of superheat. The primary parameter variation within both the W and L sets is the change in back pressure, also shown in Fig. 12 as the ratio of inlet total pressure to exit static pressure (P_{O1}/P_e). The calculation method used in Ref. [16] is based on an Euler–Lagrangian formulation for predicting nonequilibrium phase change and is indicated with CFD-LA in Fig. 12. The calculations in this study are based on the Eulerian multifluid approach indicated with CFD-MF.

Comparing the efficiency predictions of the two approaches, it is apparent in Fig. 12 that the presented model compares very well. The CFD-MF approach generally predicts a slightly lower value than the CFD-LA, for both the W and L test sets. These results are encouraging, given that considerably different algorithms have been used to predict similar results. It should be noted, however, that the CFD-LA results do not include viscous losses (or slip for larger droplets as in CFD-MF in the W set) and that in order to make comparisons, viscous loss estimates have been added from the experimental loss components tabulated in Ref. [16]. The experimental efficiency numbers from Ref. [16] have not been included as the authors are very tentative about their accuracy and provide no experimental error estimates. However, they, in general, coincide with the CFD trends shown in Fig. 12 to within approximately $\pm 1\%$.

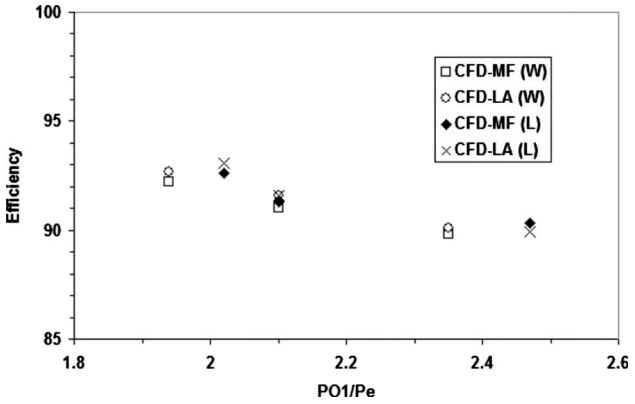

Fig. 12 Predicted efficiency using the present Eulerian multifluid model (CFD-MF) and the Eulerian–Lagrangian (CFD-LA) approach reported in Ref. [16]. Two test sets (W and L) are considered from Ref. [16].

Conclusions

A comprehensive model for treating nonequilibrium phase transition, including nonequilibrium droplet inertia relative to the gas phase, in transonic flow conditions has been outlined. Emphasis has been given on treating multiple phase transition sites, and associated bimodel size distributions that result using a source specific approach. Each phase, or source, in the present case is treated as monodispersed in droplet size and transported with its own droplet number and velocity. The approach is flexible enough to consider machines such as steam turbines with a variety of nucleation sources. The application of the model to the steam turbine cascade section illustrates this approach on a smaller scale, but in the present case, it includes a study of the influence of droplet inertia on local homogeneous phase transition. The study shows that the strength and location of the nucleation zone is affected by the droplet size of a phase, with fixed mass fraction, created upstream. Furthermore, the treatment of the energy equation for the dispersed phase with slip should include a Nusselt correlation including convective effects. The results show that although a predicted droplet temperature, using an algebraic form or transport equation, does not change much, the resulting mass fraction and size distributions show considerable differences. These differences will have an impact on the important problem of droplet collection in blade passages in steam turbine applications. The model also compares well to published computational results for efficiency predictions, although, as highlighted, care needs to be taken in the form of the efficiency equation used when algebraic energy states are used. In particular, the equation should use conserved quantities associated with governing transport equations in the solution. The model has been applied with homogeneous phase transition; further work may include other sources such as heterogeneous nucleation or surface entrainment. In addition, the treatment of the droplet size distributions using a moment based methodology is also a possibility [17].

Acknowledgment

The author would like to acknowledge the many helpful suggestions of Drs. Dan Williams and Phil Zwart at ANSYS Canada in the implementation of the model.

Nomenclature

A = area
C_D = drag coefficient
H = total enthalpy
J = nucleation rate
K = Boltzmann's constant (=1.3087×10^{-23} J/K)
Kn = Knudsen number
L = latent heat
M = secondary energy terms
N = droplet number density
Nu = Nusselt number
P = pressure
Pr = Prandtl number
Q = heat diffusion
R = gas constant (=461.4 J kg/K)
Re = Reynolds number
S = source term
T = temperature
U = velocity magnitude
V = volume
ΔG = Gibbs free energy change
$\mathbf{R}$ = upwind to ip space vector
b = sum advection/diffusion coefficients
h = static enthalpy
k = thermal conductivity
m = mass of one water molecule
$\dot{m}$ = mass transfer rate
q = heat flux
r = droplet radius
r^* = critical radius
t = time
u = velocity components
x = Cartesian coordinates
y = mass fraction
z = condensation coefficient (=1.0)

Greek

Γ = diffusion coefficient
α = volume fraction
β = area density
ϕ = transport (dependent) variable
ε = turbulent dissipation
γ = specific heat ratio
κ = turbulent kinetic energy
λ = high-resolution blending function
μ = dynamic viscosity
ρ = density
σ = surface tension
τ = viscous stress tensor
η = efficiency

Subscript/Superscript

a = index over all phases
i,j = stress tensor indices
ip = integration point
d = index over dispersed phases
eff = effective diffusivity
c = continuous phase
n = time level
n_d = number of dispersed phases
s = droplet surface quantity
sat = saturation property
sc = Supercooling
t = turbulent viscosity
up = upwind quantity

References

[1] Bakhtar, F., Young, J. B., White, A. J., and Simpson, D. A., 2005, "Classical Nucleation Theory and Its Application to Condensing Steam Flow Calculations," Proc. Inst. Mech. Eng., Part C: J. Mech. Eng. Sci., **219**, pp. 1315–1333.
[2] Bakhtar, F., White, A. J., and Mashmoushy, H., 2005, "Theoretical Treatments of Two Dimensional Two-Phase Flows of Steam and Comparison With Cascade Measurement," Proc. Inst. Mech. Eng., Part C: J. Mech. Eng. Sci., **219**, pp. 1335–1355.
[3] Bakhtar, F., 2005, "Special Issue on Wet Steam. Part 2," Proc. Inst. Mech. Eng., Part C: J. Mech. Eng. Sci., **219**, pp. 1301–1436.
[4] Gerber, A. G., 2002, "Two-Phase Eulerian/Lagrangian Model for Nucleating Steam Flow," ASME J. Fluids Eng., **124**, pp. 465–475.
[5] Gerber, A. G., and Kermani, M. J., 2004, "A Pressure Based Eulerian-Eulerian Multiphase Model for Condensation in Transonic Steam Flows," Int. J. Heat Mass Transfer, **47**, pp. 2217–2231.
[6] Gerber, A. G., Sigg, R., Völker, L., Casey, M. V., and Sürken, N., 2007, "Predictions of Nonequilibrium Phase Transition in a Model Low Pressure Steam Turbine," Proc. Inst. Mech. Eng., Part A, **221**, pp. 825–835.
[7] Esch, T., and Menter, F. R., 2003, "Heat Transfer Predictions Based on Two-Equation Turbulence Models With Advanced Wall Treatment," in *Turbulence, Heat and Mass Transfer 4*, K. Hanjalic, Y. Nagano, and M. J. Tummers, eds., Begell House Inc., New York.
[8] Gyarmathy, G., 1976, "Condensation in Flowing Steam," in *Two-Phase Steam Flow in Turbines and Separators*, M. J. Moore and C. H. Sieverding eds., Hemisphere, London, pp. 127–189.
[9] Wagner, W., and Kruse, N., 2000, "The IAPWS Industrial Formulation 1997 for the Thermodynamic Properties of Water and Steam," ASME J. Eng. Gas Turbines Power **122**, pp. 150–184.
[10] Schiller, L., and Naumann, A., 1933, VDI Z. (1857-1968), p. 318–320.
[11] Ranz, W. E., and Marshall, W. R., 1952, "Evaporation From Drops," Chem. Eng. Prog., **48**, pp. 141–146;
[12] Schneider, G. E., and Raw, M. J., 1987, "Control Volume Finite-Element Method for Heat Transfer and Fluid Flow Using Colocated Variables 1. Computational Procedure," Numer. Heat Transfer, **11**, pp. 363–390.
[13] Barth, T. J., and Jesperson, D. C., 1989, "The Design and Application of Upwind Schemes on Unstructured Meshes," AIAA Paper No. 89-0366.
[14] Rhie, C. M., and Chow, W. L., 1983, "Numerical Study of the Turbulent Flow Past an Airfoil With Trailing Edge Separation," AIAA J., **21**, pp. 1525–1532.
[15] Raw, M. J., 1996, "Robustness of Coupled Algebraic Multigrid for the Navier-Stokes Equations," AIAA Paper No. 96-0297.
[16] White, A. J., Young, J. B., and Walters, P. T., 1996, "Experimental Validation of Condensing Flow Theory for a Stationary Cascade of Steam Turbine Blades," Philos. Trans. R. Soc. London, **354**, pp. 59–88.
[17] Gerber, A. G., and Mousavi, A., 2007, "Application of Quadrature Method of Moments to the Polydispersed Droplet Spectrum in Transonic Steam Flows With Primary and Secondary Nucleation," Appl. Math. Model., **31**, pp. 1518–1533.

Design of the Dense Gas Flexible Asymmetric Shock Tube

P. Colonna[1]
Energy Technology Section,
Process and Energy Department,
Delft University of Technology,
Leeghwaterstraat 44,
2628 CA Delft, The Netherlands
e-mail: p.colonna@tudelft.nl

A. Guardone
Dipartimento di Ingegneria Aerospaziale,
Politecnico di Milano,
Via La Masa 34,
20158 Milano, Italy

N. R. Nannan

C. Zamfirescu

Energy Technology Section,
Process and Energy Department,
Delft University of Technology,
Leeghwaterstraat 44,
2628 CA Delft, The Netherlands

This paper presents the conceptual design of the flexible asymmetric shock tube (FAST) setup for the experimental verification of the existence of nonclassical rarefaction shock waves in molecularly complex dense vapors. The FAST setup is a Ludwieg tube facility composed of a charge tube that is separated from the discharge vessel by a fast-opening valve. A nozzle is interposed between the valve and the charge tube to prevent disturbances from the discharge vessel to propagate into the tube. The speed of the rarefaction wave generated in the tube as the valve opens is measured by means of high-resolution pressure transducers. The provisional working fluid is siloxane D_6 *(dodecamethylcyclohexasiloxane,* $C_{12}H_{36}O_6Si_6$*). Numerical simulations of the FAST experiment are presented using nonideal thermodynamic models to support the preliminary design. The uncertainties related to the thermodynamic model of the fluid are assessed using a state-of-the-art thermodynamic model of fluid* D_6*. The preliminary design is confirmed to be feasible and construction requirements are found to be well within technological limits.*
[DOI: 10.1115/1.2844585]

1 Introduction

A research project [1] is currently underway at the Delft University of Technology, the Netherlands—in collaboration with the Politecnico di Milano and the University of Brescia, Italy, and with industrial partners from the United States, the Netherlands, and Italy—to investigate the possible technical applications of so-called dense gas dynamics, namely, the flows of compressible dense vapors near the liquid-vapor saturation curve and critical point. Research activities encompass different aspects of dense gas dynamics, including new accurate thermodynamic models for dense vapors [2,3], the development of the computational fluid dynamics (CFD) software ZFLOW for compressible multidimensional flows of real vapors [4], and preliminary studies on turbomachinery applications benefiting from the peculiar phenomena occurring in the dense gas regime [5]. Experimental activities are devoted to the design and construction of a dense gas Ludwieg tube, i.e., the flexible asymmetric shock tube (FAST), aimed at demonstrating the existence of nonclassical gasdynamic phenomena in the dense gas flow of complex molecules [6,7].

Nonclassical gasdynamic phenomena, including rarefaction or mixed shock waves, can possibly occur provided that the fundamental derivative of gasdynamics [9], namely,

$$\Gamma(s,v) = -\frac{v}{2}\left(\frac{\partial^2 P}{\partial v^2}\right)_s \Bigg/ \left(\frac{\partial P}{\partial v}\right)_s, \tag{1}$$

where $P=P(s,v)$ is the pressure and v and s are the specific volume and entropy, respectively, becomes negative. According to state-of-the-art thermodynamic models, a region of negative Γ exists for molecularly complex vapors, such as hydrocarbons [10], perfluorocarbons [10–12], and siloxanes [2,13] near the liquid-vapor critical point and close to the liquid-vapor saturation curve. Fluids exhibiting a $\Gamma<0$ region in the vapor phase are usually referred to as Bethe–Zel'dovich–Thompson or BZT fluids, after the names of the three scientists who first theorized their existence. Figure 1 shows the saturation curve and the nonclassical ($\Gamma<0$) region of the cyclic siloxane D_6 (dodecamethylcyclohexasiloxane, $C_{12}H_{36}O_6Si_6$) in the reduced volume-pressure plane. From basic gasdynamic theory [9,14], an expansion wave entirely embedded in the $\Gamma<0$ region necessarily evolves as a discontinuity, namely, as a nonclassical rarefaction shock, whereas a compression wave disintegrates into an isentropic nonclassical compression wave.

Nonclassical flowfields [9,15–17] have already been observed experimentally for fluid states encompassing the liquid-vapor [18–21] and solid-solid [22] transition curves. The first attempt to provide experimental evidence of the existence of nonclassical rarefaction shock waves in the vapor phase was performed in 1983 by Borisov et al. [23] A steep rarefaction wave in Freon-13 (Chlorotrifluoromethane, $CClF_3$) was observed, propagating with no distortion, and it was therefore claimed to be a nonclassical rarefaction shock. However, these results have been challenged by many authors [24–27]. In 2003, a nonclassical shock-tube facility [27] was constructed and tested at the University of Colorado at Boulder, but many technological problems, including the imperfect burst of the shock-tube diaphragm and the thermal decomposition of the working fluid, prevented the observation of a rarefaction shock wave in fluid PP10 (Pf-perhydrofluorene, $C_{13}F_{22}$).

In the present research, the existence of nonclassical rarefaction shocks is to be proved by measuring the speed of propagation of a rarefaction shock wave in a still fluid, as attempted in the Boulder experiment. From the knowledge of the speed of sound in the unperturbed state—which can be measured very accurately prior to the experiment in ad hoc facilities—one can compute the Mach number of the propagating wave: If the Mach number is greater than 1, i.e., supersonic, the wave is a nonclassical one. Conversely, if the wave is sonic with respect to unperturbed conditions, then it is a classical rarefaction wave.

The design and analysis of an experimental facility in which a rarefaction shock wave is generated and measured are the focus of this study. In Sec. 2, an overview of the experimental strategy is given and the preliminary design of the facility is described. The preliminary design is validated by means of numerical simula-

[1]Corresponding author.

Contributed by the Fluids Engineering Division of ASME for publication in the JOURNAL OF FLUIDS ENGINEERING. Manuscript received December 12, 2006; final manuscript received August 20, 2007; published online March 11, 2008. Assoc. Editor: Malcolm J. Andrews. Paper presented at the Ninth AIAA/ASME Joint Thermophysics and Heat Transfer Conference, San Francisco and European Conference on Computational Fluid Dynamics ECCOMAS CFD 2006, Egmond aan Zee, The Netherlands.

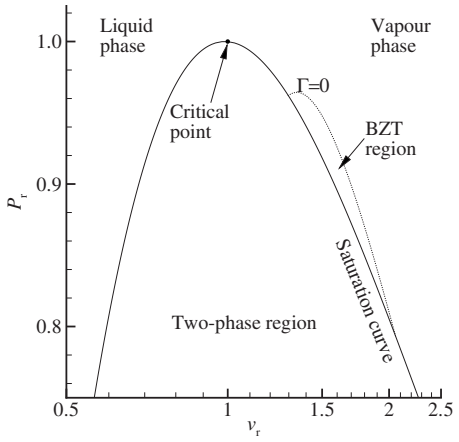

Fig. 1 Saturation and $\Gamma=0$ curves for siloxane D_6 in the v_r-P_r plane of reduced specific volume and pressure, as computed by the PRSV thermodynamic model. [8] Reduced thermodynamic variables are made dimensionless by their critical point values. The nonclassical region (BZT region) is bounded by the saturation curve and the $\Gamma=0$ curve.

Table 1 Pre- and postshock States A and B computed by the PRSV EOS

		Value Units	Description
RSW	u_W	35.00 m/s	Velocity
	M_W	1.023	Mach number
State A	P_A	9.124 bar	Pressure
	ρ_A	188.34 kg/m^3	Density
	T_A	368.97°C	Temperature
	Γ_A	−0.1218	Fundam. deriv.
	u_A	0.0 m/s	Velocity
	c_A	34.21 m/s	Speed of sound
	M_A	0	Mach number
State B	P_B	8.017 bar	Pressure
	ρ_B	127.28 kg/m^3	Density
	T_B	363.71°C	Temperature
	Γ_B	0.1386	Fundam. deriv.
	u_B	16.79 m/s	Velocity
	c_B	51.79 m/s	Speed of sound
	M_B	0.324	Mach number

tions. The dependence of the results on the chosen thermodynamic model is also assessed. In Sec. 3, the wave velocity measurement technique is discussed.

2 Preliminary Design of the Experimental Facility

The concept of the FAST setup is depicted in Fig. 2. The Ludwieg-tube facility is composed of a high-pressure charge tube connected to a low-pressure reservoir. The charge tube and the reservoir are separated by a fast-opening valve (FOV). The fluid is initially at rest and the temperature is kept uniform by a suitable thermal control system.

The experiment starts when the FOV is opened, thus connecting the charge tube to the reservoir. For suitable initial states A (charge tube) and R (reservoir), a rarefaction shock wave (RSW) is expected to form and to propagate into the charge tube. Through the RSW, the fluid is accelerated from rest conditions A to postshock conditions B. The fluid flows into the reservoir through a nozzle. The nozzle is designed to work in choked conditions, namely, at sonic conditions S at the nozzle throat, to prevent disturbances to propagate from the reservoir into the charge tube. Two dynamic pressure transducers are flush mounted close to the end wall of the charge tube in order to measure the incident RSW. A time-of-flight method is used to determine the speed of the rarefaction wave; if the speed is greater than the local speed of sound, then the wave moves at supersonic speed with respect to unperturbed conditions and it is indeed a nonclassical RSW, see Sec. 3 for further details.

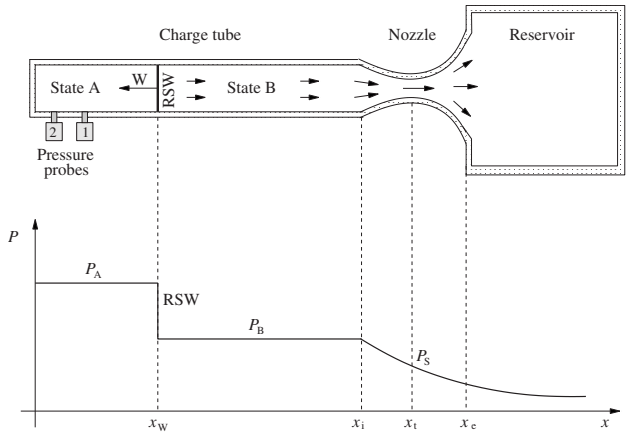

Fig. 2 The FAST dense gas Ludwieg tube setup: concept and pressure profile after the opening of the FOV separating the charge tube from the reservoir (qualitative). A RSW propagates into the charge tube at supersonic speed. Past the RSW, the fluid is accelerated from rest conditions A to postshock conditions B and flows into the reservoir through the nozzle. At the nozzle throat, sonic conditions S are attained.

The choice of the working fluid for the experiment is of the outmost importance, as previous failed attempts demonstrate. The experiment of Borisov et al. [23] has been questioned because the chosen fluid, Freon-13, is made of molecules that are not sufficiently complex to induce nonclassical gas dynamic behavior, at least in the thermodynamic region in which Γ is negative, outside the so-called scaling-law region. The Boulder experiment [27] encountered major problems due to the decomposition of the fluid at high temperature. Currently three classes of fluids are believed to exhibit a $\Gamma<0$ region in the vapor phase and outside the scaling-law region, namely, hydrocarbons [10], perfluorocarbons [10–12] and siloxanes [2,13]. Siloxanes have been selected for this project. The thermodynamic modeling of siloxanes is in an advanced stage with respect to perfluorocarbons and their thermal stability in conditions similar to the foreseen experiment has already been tested. Thermal decomposition of siloxanes leads to polymerization and the polymer product is not toxic, whereas thermal decomposition of perfluorocarbons may result in hydrofluoric acid (HF) and possibly other very toxic compounds. Flammability of siloxanes is far lower than hydrocarbons. The simpler molecules of the siloxanes' class are currently utilized in organic Rankine cycle turbines, which is the first application proposed for the envisaged results of the current research project. All the mentioned reasons lead to the choice of siloxanes as the working fluids to be tested in the proposed experiment. In particular, the cyclic siloxanes have proved to be more thermally stable than their linear counterparts and are therefore preferred.

Siloxane fluid D_6 is chosen here as a compromise between thermal stability and the size of the thermodynamic region—in terms of pressure and temperature ranges—in which nonclassical gas dynamic phenomena can possibly occur according to current models. Pre and postshock conditions leading to the RSW with maximum Mach number have been computed according to the procedure presented in Ref. [28] and are reported in Table 1. Figure 3 shows the RSW and the expansion up to the nozzle throat in the reduced volume-pressure plane and the Mach profile along the

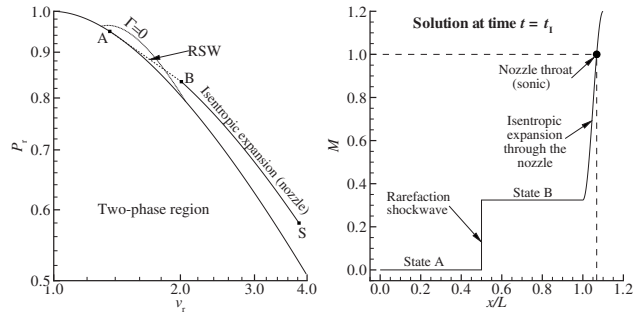

Fig. 3 Left: Expansion in the charge tube up to the nozzle throat in the v_r-P_r plane. Right: Mach profile at time $t=t_I$ for a fully formed RSW.

charge tube at time $t=t_I$, see Sec. 2.1. The possibility of using different siloxane fluids in the FAST setup is discussed in Ref. [6]. The design of the critical subsystems of the FAST experiment is detailed in the following.

2.1 Fast-Opening Valve and Charge Tube Length. Due to the finite opening time of the FOV, the RSW is not instantaneously formed but instead a finite time—or, equivalently, space—is required for all disturbances to coalesce into a single shock front. An estimate of the maximum allowed opening time can be obtained by imposing that the RSW is completely formed at Point I located at x_I. The domain of dependence of Point I is given by the region in the x-t plane bounded by the characteristic curves C_A^- and C_B^-. The opening time Δt_{open} is therefore obtained by computing $x=x_e$ line, where x_e is the location of the nozzle outlet, as follows:

$$\Delta t_{\text{open}} = (x_I - x_e)\left(\frac{1}{\lambda_A} - \frac{1}{\lambda_B}\right)$$

where $\lambda_A=-c_A$ and $\lambda_B=u_B-c_B$ are the characteristic velocities. This procedure is expected to give a good estimate of Δt_{open}, provided that no shocks are formed during the opening process and that the influence of the nozzle is negligible.

In the FAST setup, the intersection point x_I has been chosen to be located 5 m from the FOV, which immediately gives $\Delta t_{\text{open}} \simeq 3.31$ ms. Such a relatively low value of the opening time is considered technically feasible, even at the very high temperature of operation of the experiment, and a FOV fulfilling the present requirements is currently under construction. The RSW is to be completely formed at measurement Stations 1 and 2 close to the tube end wall. To allow for slightly higher opening times, which may possibly be caused by the relatively high temperature of operation of the FOV, a total tube length of 9 m has been chosen.

2.2 Charge Tube Diameter. The choice of the charge tube diameter is influenced by different requirements. On the one hand, since the working fluid is expensive and the purification process is time consuming, the diameter should be chosen as small as possible to reduce the amount of fluid to be used. On the other hand, the tube diameter should be large enough to allow for the cleaning of the charge tube and to reduce viscous dissipation past the RSW, which leads to the weakening the RSW itself. As a compromise, a charge tube diameter of 40 mm has been chosen. The total volume inside the charge tube is therefore 0.0113 m^3, which, from the initial density $\rho_A=188.34$ kg/m^3 from Table 1, results in a total of 2.13 kg of fluid.

To estimate the effect of viscosity and thermal conductivity on the experiment, a simple one-dimensional approximation has been adopted. In the postshock state, the dense gas viscosity model of Chung et al. [29], which is deemed to be 10% accurate in the dense gas region, gives $\mu_B=17.3\times10^{-6}$ Pa s at $P_B=8.017$ bar and $T_B=363.71\,^\circ$C. Hence, substituting $u_B=16.79$ m/s from Table 1, the local Reynolds number reads $\text{Re}(x)=(\rho_B u_B x)/\mu_B \simeq 1.82\times10^8\times x$. Remarkably enough, the Reynolds number is very high also at locations very close to the RSW. Since transition to turbulence in these kind of flows [30] can be located at $\text{Re}(x)\sim5\times10^4$, which in the present case gives $x\sim0.2$ mm, one can assume that the flow is fully turbulent past the leading shock wave. Therefore, the Fanning friction factor [31] f depends only on the relative surface roughness. In the present computations, $f=0.008$ since the charge tube is electrolytically polished. Under the above assumption, the flow between the RSW and the nozzle inlet can be modeled as a steady one-dimensional flow with friction, namely, as a Fanno flow [31,32]. At the tube end wall ($x=L=9$ m), the pressure drop ΔP between Point B immediately after the RSW and the inlet of the nozzle is therefore computed as $\Delta P=(1/2)f(L/D)\bar{\rho}\bar{u}^2\simeq0.336$ bar, where $\bar{\rho}$ and $\bar{u}$ respectively. The pressure drop due to the viscous dissipation is therefore quite relevant, namely, about 30% of the pressure difference across the RSW. However, the pressure difference between State A and the nozzle throat is controlled by the nozzle cross-sectional area, see next section, which can be changed to compensate for the viscous losses. Our computations predict that a 2.1% increase of the diameter at the nozzle throat section is sufficient to counterbalance viscous losses.

It is remarkable that the Reynolds number past the shock wave is very high, namely, about 10^8/m, whereas the wave Mach number is as low as 1.023. On the one hand, this is due to the very low value of the kinematic viscosity $\nu=\mu/\rho$, which in turn is related to the very high density of the states characterizing the experiment. Note that the dynamic viscosity μ is comparable to that of air at standard conditions. On the other hand, the flow velocity past the shock is very high. This is due to the high compressibility of the fluid, which results in a density jump of about 51 kg/m^3, or 27% of ρ_A, even though the shock wave is very weak. For mass conservation, this leads to high values of the postshock velocity.

2.3 Nozzle and Reservoir Design. The nozzle connecting the charge tube to the reservoir works in choked conditions, namely, the local Mach number, is unity at the nozzle throat, to prevent disturbances from the reservoir to propagate into the charge tube.

To compute the ratio of the area of the nozzle throat section to the charge tube cross-sectional area, the flow is assumed to be steady and therefore both the total enthalpy and the entropy are conserved from State B to the sonic State S. The entropy S_B in State B is computed via the well-known Rankine–Hugoniot relations. Critical (sonic) conditions are then computed by solving for v_S the equation $h(s_B,v_S)+\frac{1}{2}c^2(s_B,v_S)=h_B^t$, where $h_B^t=h_A^t$ is the total specific enthalpy per unit mass of State B and v and c indicate the specific volume and the speed of sound; one therefore obtains

$$\frac{A_S}{A_{\text{tube}}} = \frac{\rho_B u_B}{\rho_S c_S}$$

or $A_S/A_{\text{tube}}\simeq0.423$ for the chosen initial States A and B, see Table 1. For a 40 mm diameter tube, $A_S\simeq531.2$ mm^2, which corresponds to a throat diameter of $D_S\simeq26$ mm. The fluid state at the sonic throat is summarized in Table 2.

The reservoir size and initial conditions must be chosen in such a way that during the discharge process the pressure at the nozzle outlet, namely, the discharge pressure, is always lower than the pressure at the nozzle throat. In this way, the nozzle remains choked during the experiment. For simplicity and to avoid disturbances due to the temperature gradients along the charge tube, the reservoir initial temperature is chosen to be equal to the charge tube temperature T_A, namely, the whole FAST setup is isothermal. Moreover, to limit the overall size of the experimental apparatus, the total volume of the reservoir is limited to 0.1 m^3. The mass flowing from the charge tube into the reservoir is obtained as the product of the mass flow $\rho_B u_B A_{\text{tube}}=\rho_S c_S A_S$ times the duration of the experiment. The latter is slightly higher than the time required

Table 2 Sonic State S computed by the PRSV EOS from the value in Table 1

		Value Units	Description
State S	P_S	5.572 bar	Pressure
	ρ_S	66.87 kg/m^3	Density
	T_S	356.70°C	Temperature
	Γ_S	0.6176	Fundam. deriv.
	u_S	75.50 m/s	Velocity
	c_S	75.50 m/s	Speed of sound
	M_S	1	Mach number

for the RSW to reach the second measurement station or, for simplicity, the charge tube end wall, or $x_e - x_1 = u_W(t_{\text{end}} - t_1)$, where $x_1 = 5$ m and $t_1 = x_1/\lambda_A$, so that $t_{\text{end}} = 0.289$ s and therefore $\Delta m = \dot{m}\Delta t = [\rho_S c_S A_S]t_{\text{end}} = 0.776$ kg. Neglecting pressure losses due to the viscosity, the enthalpy per unit volume in the reservoir is therefore increased by the quantity $\Delta(\rho_R h_R) = h_S^t \Delta m$, with h_S^t total specific enthalpy per unit mass at the nozzle throat. The reservoir pressure at the end of the experiment is then computed from the final value of the specific enthalpy $h_{R,\text{end}}$ and specific volume $v_{R,\text{end}}$ as $P_{R,\text{end}} = P(h_{R,\text{end}}, v_{R,\text{end}}) = 1.083$ bar, where $h_{R,\text{end}} = (\rho_{R,0} h_{R,0} + h_S^t \Delta m)/m_{R,\text{end}}$ and $v_{R,\text{end}} = V_R/m_{R,\text{end}}$, with V_R the volume of the reservoir and m_R the total mass in the reservoir, $m_{R,\text{end}} = m_{R,0} + \Delta m$, and with the subscript 0 indicating initial conditions. The maximum discharge pressure $P_{R,\text{end}}$ is therefore always lower than the sonic pressure $P_S = 5.572$ bar.

2.4 Numerical Simulation of the Flexible Asymmetric Shock Tube Experiment. Numerical simulations were performed to verify the preliminary design of the FAST setup. In particular, the steady flow assumption, which has been made in designing the nozzle, is verified against the unsteady flow computations of the experimental facility. All simulations are performed with the CFD solver ZFLOW [4] using the PRSV thermodynamic model and under the assumption of a quasi-one-dimensional flow, namely, the FAST setup is modeled as a variable-cross sectional area tube in which the local multidimensional effects are negligible with respect to the main axial flow.

A grid sensitivity study was also performed, to investigate the dependence of the numerical results on the computational grid used in the computations. Three different grids with increasing number of nodes, namely, 835, 1669, and 3336 nodes, respectively, were considered. The grid spacing is not uniform, with nodes clustered in the regions where the cross-sectional area varies the most, i.e., inside the nozzle and at the nozzle discharge section; in the charge tube, the grid spacing is uniform. To avoid numerical spurious oscillation due to the abrupt change in the cross-sectional area at the nozzle discharge section, a smooth area variation is artificially introduced to connect the nozzle outlet to the reservoir: the cross-sectional area is assumed to vary smoothly from the nozzle throat value of 531.2 mm^2 to a value of 0.196 m^3 over a distance of 0.5 m.

The numerical results are reported in Fig. 4, where the pressure signals at the throat location and at measurement Station 1 are shown as a function of the elapsed time for the three considered grids. Numerical results are found to be almost independent from the grid resolution and to converge to the "exact" solution. The exact solution is, in fact, computed by assuming that the flow in the nozzle connecting the charge tube to the reservoir is steady and choked for the entire duration of the experiment. Moreover, the RSW is assumed to be completely formed at the exit of the nozzle, with no perturbations resulting from the interaction with the nozzle itself. The above assumptions are relaxed in the simulation to investigate their correctness. In fact, the pressure at the nozzle throat reaches its steady-state choked value almost immediately, that is about 4 ms after the FOV opening—which is assumed here to open instantaneously—and the influence of the interaction with the nozzle on the RSW propagation time is found to be negligible, see Fig. 4 (right).

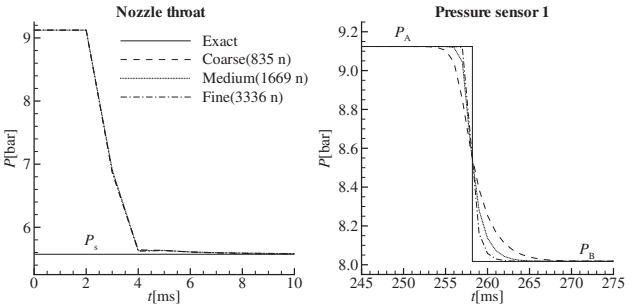

Fig. 4 Pressure signals at the nozzle throat (left) and at measurement station 1 (right) as computed using three different grid resolutions. Numerical results are compared to the "exact" solution, in which the flow inside the nozzle is assumed to be steady.

The preliminary design is therefore confirmed by the present numerical simulations, in terms of both initial conditions leading to the occurrence of a RSW propagating in the charge tube, and to the characteristic dimensions and times of the experiment. The intermediate grid made of 1669 nodes is therefore used in the following section to assess the uncertainties due to the thermodynamic model of the fluid.

2.5 Uncertainties Due to the Thermodynamic Model. The preliminary design obtained using the PRSV thermodynamic model is validated against the more complex Span–Wagner (SW) model of D_6 [3,33,34]. For the sake of the present discussion, the SW model is assumed to provide the exact thermodynamic properties of D_6, of which the PRSV provides an approximation. It should be recalled that none of the models is validated as far as the determination of the value of the fundamental derivative of gas dynamics Γ is concerned and therefore the present analysis is to be intended only as an initial evaluation of the criticalities due to the uncertainties in the thermodynamic model, similar to the study presented in Ref. [35].

According to the experimental procedure [6], the initial State A is chosen along the vapor saturation line at the initial pressure P_A. As shown in Fig. 5, a RSW fulfilling the Rankine–Hugoniot jump relation is predicted to be formed also by the SW model, which, in this case, moves at a slightly higher speed. The postshock pressure

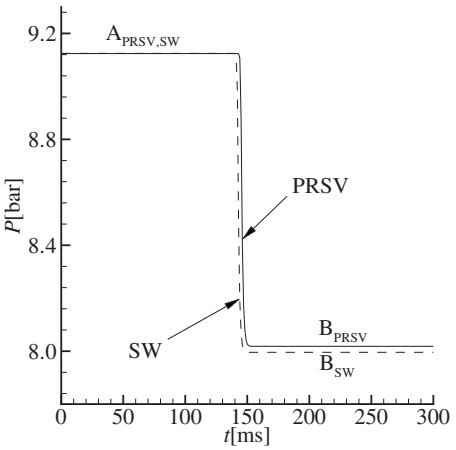

Fig. 5 FAST experiment according to the PRSV and SW models

level is 7.996 bar according to the SW model, which is only 0.3% lower than that predicted by the PRSV (8.018 bar) EOS. The pressure jump across the RSW computed using the SW model is therefore about 2% higher than that obtained from the PRSV EOS.

3 Wave Speed Measurement

The wave speed W of the propagating RSW is to be measured by comparing the time of arrival of the RSW at two different measurement stations, namely, Stations 1 and 2, as discussed in the Introduction. Many technical problems affect the measurement of the speed of a shock wave and these are addressed exhaustively in Ref. [27]. Here, we focus mainly on the two issues that are peculiar of nonclassical shock waves, namely, the possibly nonnegligible shock wave thickness and the correct estimation of the wave Mach number, being very close to unity.

In practice, a shock wave from State A to State B in a viscous fluid is not a discontinuity but a steep profile, though continuous, in which all thermodynamic quantities vary smoothly from State A to State B, over a shock thickness Δ_{shock}. Thompson and Lambrakis [10] proposed to define the shock thickness as the distance for which the velocity across the shock changes with 98.7% and they obtained the following dimensional expression:

$$\Delta_{\text{shock}} = \frac{10}{\Gamma} \frac{\alpha \rho_A c_A^2}{P_B - P_A} \frac{\mu}{\rho_A c_A}$$

where $\rho_A c_A^2 = (15-35) \times 10^4$ kg/m s^2 and $\alpha \equiv 4/3 + \mu_\nu/\mu + (\gamma - 1)P/P_c$ is the dimensionless form of the Kirchoff diffusivity, with γ the specific heat ratio and μ_ν and μ the bulk and the dynamic viscosity coefficients, respectively. The quantity $\mu/\rho_A c_A$ has the dimension of length and represents an effective mean free path of the molecules. Substituting $\mu_B = 17.3 \times 10^{-6}$ Pa s from Sect. 2.2 gives $\mu/(\rho_A c_A) \sim 10^{-9}$ m. Due to the large uncertainty in μ_ν, it is difficult to accurately estimate α. Thompson and Lambrakis proposed $\alpha = 2$, using this value for α. For a pressure jump across a RSW of approximately 1 bar, one has

$$\Delta_{\text{shock}} \sim \frac{1}{|\Gamma|} 10^{-7} \text{ m}$$

Note that as Γ goes to zero, the shock thickness goes to infinity. However, for a fluid with a relatively large BZT region, a value of $\Gamma = -0.1$ is reasonable. This gives an estimate of the rarefaction shock thickness on the order of 1 μm, which would make the discontinuity thickness appreciable. In terms of time span from the shock head to the shock tail, one has $\tau \simeq W \Delta_{\text{shock}} \simeq 0.035$ ms.

A relevant source of uncertainty is associated with sound speed measurements. To provide a conclusive proof that the measured rarefaction wave is indeed a RSW, the wave speed W should be higher than the sound speed c_A in the unperturbed State A. Since the highest expected wave Mach number to be observed is about 1.023, the relative difference between W and c_A is very low, namely, $(W - c_A)/c_A \simeq 0.023$. For the comparison to be possible, the uncertainties in the measurement of both W and c_A should be therefore lower than about 1%. In Fig. 6, the speed of the rarefaction wave and the sound speed for different saturated states is plotted. For unperturbed states in the vicinity or inside the nonclassical region, an RSW is formed and the wave speed exceeds the speed of sound, as shown in Fig. 6, where the error bars associated with a 0.5% uncertainty in both W and c_A are shown. Figure 6 also suggests an alternative experimental procedure in which the speed of sound and the wave speed are both measured in the FAST facility. Sound speed measurements can be performed by including an oscillator in the setup or by opening the FOV with $P_R \simeq P_A$, to produce a very weak (ideally acoustic) rarefaction wave propagating into the charge tube. Then, the pressure P_B in the reservoir is lowered to design value and the experiment is rerun.

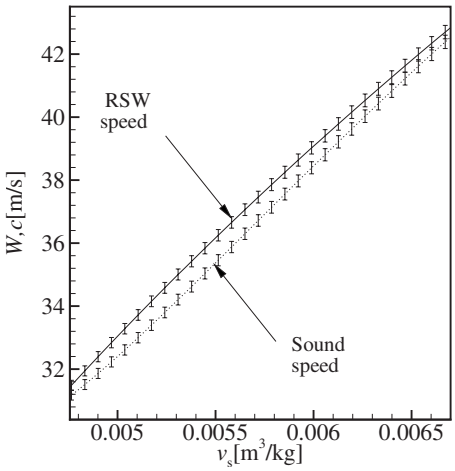

Fig. 6 Dimensional wave speed *W* and sound speed *c* as a function of the reduced volume along the vapor side of the saturation curve. The error bars represent an error of 0.5% in the evaluation of *W* or *c*.

4 Conclusions

The preliminary design of the FAST nonclassical Ludwieg-tube setup currently under construction at the Delft University of Technology has been presented. The experimental facility is designed to produce a nonclassical rarefaction shock wave moving in siloxane D_6. The (expected) supersonic speed of the rarefaction wave will provide a definite proof of the existence of nonclassical phenomena in dense vapor made of complex molecules. Due to the nonideal character of the working fluid and operating conditions, a nonideal thermodynamic model has been used in the computations. Further work is underway to improve the thermodynamic model of the fluid [3,34] and to investigate the feasibility of the chosen setup and its sensitivity to off-design conditions [7].

The preliminary design of the FAST setup has been validated by means of numerical simulations of the experiment. The numerical results confirm the choice of the initial conditions for the experiment; in particular, the assumption of considering a steady flow inside the nozzle connecting the charge tube to the reservoir has been found to be realistic.

Finally, a rough estimate of the sensitivity of the present design with respect to the accuracy of the thermodynamic model is provided by comparing the results obtained by two different thermodynamic models of D_6. Very small differences in the (computed) experimental output have been found in this case. Further work is currently underway to improve the SW model and to validate it against the experimental results. In particular, a measurement campaign aimed at filling the gaps in the knowledge of the thermodynamic properties of siloxanes has been recently carried out and includes measurements of speed of sound as well as ab initio computations of the specific heat capacity in the ideal-gas state [36].

Acknowledgment

This research is supported by the Dutch Technology Foundation STW, Applied Science Division of NWO and the Technology Program of the Ministry of Economic Affairs, DSF 6573.

References

[1] Colonna, P., 2004, "Experimental and Numerical Investigation of Dense Gas Fluid Dynamics and BZT Fluids Exploitation for Energy Conversion Applications," NWO-VIDI Project Proposal, Energy Technology Section, Delft University of Technology, February.

[2] Colonna, P., and Silva, P., 2003, "Dense Gas Thermodynamic Properties of Single and Multicomponent Fluids for Fluid Dynamics Simulations," ASME J.

Fluids Eng., **125**, pp. 414–427.
[3] Colonna, P., Nannan, N. R., Guardone, A., and Lemmon, E. W., 2006, "Multiparameter Equations of State for Selected Siloxanes," Fluid Phase Equilib., **244**, pp. 193–211.
[4] Colonna, P., and Rebay, S., 2004, "Numerical Simulation of Dense Gas Flows on Unstructured Grids With an Implicit High Resolution Upwind Euler Solver," Int. J. Numer. Methods Fluids, **46**, pp. 735–765.
[5] Colonna, P., Rebay, S., Harinck, J., and Guardone, A., 2006, "Real-Gas Effects in ORC Turbine Flow Simulations: Influence of Thermodynamic Models on Flow Fields and Performance Parameters," *ECCOMAS CFD 2006 Conference, Egmond aan Zee*.
[6] Zamfirescu, C., Guardone, A., and Colonna, P., 2006, "Preliminary Design of the FAST Dense Gas Ludwieg Tube," *Ninth, AIAA/ASME Joint Thermophysics and Heat Transfer Conference*, San Francisco, CA.
[7] Zamfirescu, C., Guardone, A., and Colonna, P., 1986, "Numerical Simulation of the FAST Dense Gas Ludwieg Tube Experiment," *ECCOMAS CFD 2006 Conference*, Egmond aan Zee.
[8] Stryjek, R., and Vera, J. H., 1986, "PRSV: An Improved Peng–Robinson Equation of State for Pure Compounds and Mixtures," Can. J. Chem. Eng., **64**, pp. 323–333.
[9] Thompson, P. A., 1971, "A Fundamental Derivative in Gas Dynamics," Phys. Fluids, **14**(9), pp. 1843–1849.
[10] Thompson, P. A., and Lambrakis, K. C., 1973, "Negative Shock Waves," J. Fluid Mech., **60**, pp. 187–208.
[11] Cramer, M. S., 1989, "Negative Nonlinearity in Selected Fluorocarbons," Phys. Fluids A, **1**(11), pp. 1894–1897.
[12] Guardone, A., and Argrow, B. M., 2005, "Nonclassical Gasdynamic Region of Selected Fluorocarbons," Phys. Fluids, **17**(11), pp. 116102-1-17.
[13] Colonna, P., Guardone, A., and Nannan, N. R., 2007, "Siloxanes: A New Class of Candidate Bethe–Zel'dovich–Thompson Fluids," Phys. Fluids, **19**, pp. 086102-1-12.
[14] Hayes, W. D., 1960, "The Basic Theory of Gasdynamic Discontinuities," *Fundamentals of Gasdynamics (High Speed Aerodynamics and Jet Propulsion)*, H. W. Emmons, ed., Princeton University Press, Princeton, NJ, Vol. 3, pp. 416–481.
[15] Bethe, H. A., 1942, "The Theory of Shock Waves for an Arbitrary Equation of State," Office of Scientific Research and Development, Technical Report 545.
[16] Zel'dovich, Y. B., 1946, "On the Possibility of Rarefaction Shock Waves," Zh. Eksp. Teor. Fiz., **4**, pp. 363–364.
[17] Menikoff, R., and Plohr, B. J., 1989, "The Riemann Problem for Fluid Flow of Real Material," Rev. Mod. Phys., **61**(1), pp. 75–130.
[18] Thompson, P. A., and Kim, Y., 1983, "Direct Observation of Shock Splitting in a Vapor-Liquid System," Phys. Fluids, **26**(11), pp. 3211–3215.
[19] Thompson, P. A., Carofano, G. A., and Kim, Y., 1986, "Shock Waves and Phase Changes in a Large Heat Capacity Fluid Emerging From a Tube," J. Fluid Mech., **166**, pp. 57–96.
[20] Gulen, S. C., Thompson, P. A., and Cho, H. A., 1989, "Rarefaction and Liquefaction Shock Waves in Regular and Retrograde Fluids With Near-Critical End States," *Adiabatic Waves in Liquid-Vapor Systems*, Springer-Verlag, pp. 281–290.
[21] Simões-Moreira, J. R., and Shepherd, J. E., 1999, "Evaporation Waves in Superheated Dodecane," J. Fluid Mech., **382**, pp. 63–86.
[22] Ivanov, A. G., and Novikov, S. A., 1961, "Rarefaction Shock Waves in Iron and Steel," Zh. Eksp. Teor. Fiz., **40**(6), pp. 1880–1882.
[23] Borisov, A. A., Borisov, Al. A., Kutateladze, S. S., and Nakaryakov, V. E., 1983, "Rarefaction Shock Waves Near the Critic Liquid-Vapour Point," J. Fluid Mech., **126**, pp. 59–73.
[24] Cramer, M. S., and Sen, R., 1986, "Shock Formation in Fluids Having Embedded Regions of Negative Nonlinearity," Phys. Fluids, **29**, pp. 2181–2191.
[25] Kutateladze, S. S., Nakoryakov, V. E., and Borisov, A. A., 1987, "Rarefaction Waves in Liquid and Gas-Liquid Media," Annu. Rev. Fluid Mech., **19**, pp. 577–600.
[26] Fergason, S. H., Ho, T. L., Argrow, B. M., and Emanuel, G., 2001, "Theory for Producing a Single-Phase Rarefaction Shock Wave in a Shock Tube," J. Fluid Mech., **445**, pp. 37–54.
[27] Fergason, S. H., Guardone, A., and Argrow, B. M., 2003, "Construction and Validation of a Dense Gas Shock Tube," J. Thermophys. Heat Transfer, **17**(3), pp. 326–333.
[28] Zamfirescu, C., Colonna, P., and Guardone, A., 2007, "Maximum Wave Mach Number of Rarefaction Shocks in Selected BZT Fluids," *Proceedings of the Fifth International Conference on Heat Transfer, Fluid Mechanics and Thermodynamics (HEFAT2007)*, Sun City, South Africa, Jul. Paper No. ZC1, pp. 1–6.
[29] Chung, T.-H., Ajlan, M., Lee, L. L., and Starling, K. E., 1988, "Generalized Multiparameter Correlation for Non-Polar and Polar Fluid Transport Properties," Ind. Eng. Chem. Res., **27**, pp. 671–679.
[30] Mirels, H., 1955, "Laminar Boundary Layer Behind Shock Advancing Into Stationary Fluid," National Advisory Committee for Aeronautics, Technical Note TN 3401.
[31] Thompson, P. A., 1988, *Compressible Fluid Dynamics*, McGraw-Hill, New York.
[32] Cramer, M. S., Monaco, J. F., and Fabeny, B. M., 1994, "Fanno Processes in Dense Gases," Phys. Fluids, **6**(2), pp. 674–683.
[33] Span, R., 2000, *Multiparameter Equations of State*, Springer-Verlag, Berlin.
[34] Colonna, P., Nannan, N. R., and Guardone, A., 2008, "Multiparameter Equations of State for Siloxanes: $[(CH_3)_3\text{-Si-}O_{1/2}]_2\text{-}[O\text{-Si-}(CH_3)_2]_{i=1\ldots3}$, and $[O\text{-Si-}(CH_3)_2]_6$," Fluid Phase Equilib., **263**(2), pp. 115–130.
[35] Guardone, A., Vigevano, L., and Argrow, B. M., 2004, "Assessment of Thermodynamic Models for Dense Gas Dynamics," Phys. Fluids, **16**(11), pp. 3878–3887.
[36] Nannan, N. R., Colonna, P., Tracy, C. M., Rowley, R. L., and Hurly, J. J., 2007, "Ideal-Gas Heat Capacities of Dimethylsiloxanes From Speed-of-Sound Measurements and Ab Initio Calculations," Fluid Phase Equilib., **257**(1), pp. 102–113.